Illuminating tidal disruption events with a time-dependent theory of relativistic accretion discs

Andrew Mummery

Wadham College

University of Oxford

A thesis submitted for the degree of

Doctor of Philosophy

Trinity 2022

Statement of Originality

The work presented in this thesis was completed during a Doctor of Philosophy (DPhil) degree at the University of Oxford, funded by a Science and Technology Facilities Council Studentship through the Science and Technology Facilities Council. This degree was completed between October 2018 and May 2022.

I assert that the work contained in this thesis is my own, and that any results used to supplement my research that are not my own have been properly cited. None of the work in this thesis has been submitted as part of another degree at the University of Oxford, or any other university.

The chapters of this thesis are based on works published in peer reviewed academic journals, or from works in preparation to be submitted to peer reviewed academic journals, as indicated at the beginning of each chapter and below.

Chapter 2 is based upon:
Balbus and Mummery 2018, MNRAS, 481, 3348
Mummery and Balbus 2019a, MNRAS, 489, 132
Mummery and Balbus 2019b, MNRAS, 489, 143

Chapter 3 is based upon:
Mummery and Balbus 2020a, MNRAS, 492, 5655
Mummery and Balbus 2020b, MNRAS, 497, L13

Chapter 4 is based upon:
Mummery and Balbus 2021a, MNRAS, 505, 1629
Mummery and Balbus 2021b, MNRAS, 504, 4730
Mummery 2021a, MNRAS, 504, 5144
Mummery 2021b, MNRAS, 507, L24.
Mummery 2022, submitted.

Chapter 5 is based upon:
Mummery and Balbus, 2022, submitted.
Mummery et al., 2022, in prep.

This thesis is dedicated to the memory of
Margaret 'G' Peterson
14th November 1930 – 21st April 2021
who would have been so proud to read it.

Acknowledgements

I am extremely grateful to my supervisor, Steven Balbus, for all of his advice and guidance over the last five years. A walking Mathematica module, I have learnt a huge amount from our meetings over the years: from the Weierstrass substitution to Watsons lemma. I will always have fond memories of the time we spent at the blackboard talking physics.

The completion of this thesis would not have been possible without the incredible support of Pip Beck, who saw far too much of it being formulated from across our one table during numerous lockdowns. From teaching me the various intricacies of the English language, to keeping me well stocked with cups of tea, this thesis, and I, are all the better for your input.

To my family, without you all I would not have made it this far. I would like to thank my Mum for her endless belief in me, and for all her support. My Dad, for igniting a passion for science in me as a young man, and my younger sister Alice, for always being a legend.

To 'Robs group', and in particular Rob Fender and Adam Ingram, thank you for putting up with me presenting some work-in-progress mathematics at your meetings, and for reading my paper drafts. A big thank you also goes to the Oxford astrophysics office team – Laurence, Jamie, Ed, Sean and Lauren: you have made the completion of this thesis a great deal of fun.

To Braddy, Pete, and Stu, and all my friends from eight fantastic years at Oxford: Cheers, it's been a blast.

Finally, to members of the tidal disruption event community, in particular Nick Stone, Thomas Wevers, Sjoert van Velzen, Peter Jonker, DJ Pasham, Richard Saxton, Jason Hinkle, Adelle Goodwin, Adam Malyali and Matt Middleton; thank you for replying to my various emails over the years, and for sharing your data with me.

Abstract

At the centre of every large galaxy in the Universe lurks a supermassive black hole, weighing in at a mass ranging from millions to tens of billions that of the Sun. The study of these monsters is by necessity an indirect science, as a black hole itself emits no detectable radiation: if one wants to learn about the properties of black holes, one must understand in great detail their effect on their surroundings. Historically, the primary approach to inferring the existence of black holes and determining their properties has been through the detection and study of bright X-ray emitting accretion discs, in our Galaxy and at cosmological distances. The name "accretion disc" is given to the structures formed by gas as it spirals slowly into a black hole, never to return. Accretion discs are turbulent, and phenomenally bright, systems which can outshine entire galaxies. In this thesis I present my contributions to the field of accretion disc physics, in particular to the study of time-dependent and relativistic accretion discs.

One particularly interesting type of astrophysical black hole–accretion disc system, and the focus of much of this thesis, are called tidal disruption events. The stellar densities of galactic centres are high, and the orbits of individual stars are continuously perturbed by the combined gravitational interactions of the galaxy's stellar population. Very unfortunate stars can, on a rare occasion, be perturbed onto a near-radial orbit about the galaxy's central black hole. Should this orbit take the star within a critical separation called the tidal radius, the star's gravitational attraction to the black hole will become larger than its own self-gravity. Upon entering this region the star is destroyed, *in its entirety*, by the black hole's tidal gravitational force, scattering stellar debris onto a series of different orbits. Some fraction of this stellar debris subsequently rains back onto the supermassive black hole, and fuels an accretion disc which is observed as a bright flare from an otherwise quiescent galactic centre. These flares, which typically outshine their entire host galaxy, last for timescales of months-to-years and have been observed at frequencies across the entire electromagnetic spectrum. The current population of known tidal disruption events stands at roughly 40 sources, and their study is taking on a growing importance in the field of transient astronomy.

Tidal disruption events are intrinsically relativistic and time dependent accretion disc systems, and must therefore be described by a relativistic and time dependent theory. However, despite the great success of *steady-state* relativistic disc models, and the myriad practical uses found for Newtonian time-dependent disc theory, the theory of relativistic, time-dependent, accretion discs is a hugely underexplored field. In Chapter 2 of this thesis I derive and then present the first analytical and numerical solutions of the evolution equations describing relativistic thin discs. I show that these solutions represent much more than simple refinements of the Newtonian theory, and display a mathematically rich and physically interesting set of behaviours. The *global* properties of time-dependent relativistic discs are shown to be sensitive to the physical properties of the disc's very innermost regions, and in particular to the behaviour of the disc stress at the innermost stable circular orbit. The question of whether the dynamical disc stress vanishes at the innermost stable circular orbit of a black hole disc has a controversial history as old as the field of black hole accretion itself. In this thesis I develop and explore a number of observational probes that may have already offered insight into the answer to this long controversial question.

The solutions of the relativistic disc equations developed in Chapter 2 are put to the test in Chapter 3, where I develop models which describe the evolving luminosities observed from two tidal disruption events named ASASSN-14li and ASASSN-15lh. So named after the All Sky Automated Survey for SuperNovae which discovered them, ASASSN-14li and ASASSN-15lh show rather distinct observed properties, here chosen to span the broad range of observed tidal disruption event phenomenology. Despite their very different properties, the luminosity from both sources are extremely well described as resulting from evolving relativistic discs. In addition to providing an excellent description of the observations, the disc models measure and constrain the physical parameters of the tidal disruption event system. As a result of this analysis, observations of the luminosity emergent from tidal disruption events can be used as probes of the properties of the black holes at their hearts.

The numerical models of Chapter 3 are complimented by an asymptotic analysis of the emitted luminosity of relativistic thin discs. I demonstrate a profound dependence of the properties of tidal disruption event light curves on observing band. This dependence can be understood entirely analytically, and in particular the X-ray luminosity emergent from supermassive black hole discs is extremely simple to describe. I show that a simple power-law decay of the bolometric disc luminosity, when appropriately filtered by bandpass, is observed to be near-time-independent in the ultra-violet, while simultaneously exponentially decaying at X-ray energies. These particular properties are observed in numerous tidal disruption event light curves.

In Chapter 4 this analysis of the X-ray luminosity of relativistic thin discs is extended so as to model tidal disruption events from across the entire parameter space likely to be spanned by these remarkable objects. This includes the development of the first self-consistent models for the time evolution of "hard state" nonthermal X-ray emission from black hole accretion discs. By extending classical disc scaling relationships into the time-dependent regime, I highlight that time dependent accretion discs have a temperature profile which is far more sensitively dependent on their black hole and disc parameters than their steady state counterparts. This sensitive dependence of the temperature on system parameters, in particular the black hole mass, coupled with the exponential dependence of the X-ray luminosity on disc temperature results in diverse, quantitative predictions for the properties of a population of tidal disruption event sources. I compare these predictions to the current observed population of tidal disruption events, and demonstrate that, while we are in the early days of population studies, the initial evidence suggests that these predictions are in excellent accord with the data.

In addition to seeking to answer a number of questions of interest to the study of accretion disc physics and tidal disruption events, this thesis will, I hope, highlight a number of interesting avenues for further research. In Chapter 5 I highlight two areas in which I believe the analysis in this thesis can be refined, or extended, and some initial progress in those directions. The first of these is the future inclusion of the emission resulting from material within the innermost stable circular orbit of a black hole disc. Before the properties of the emission from this region can be understood, the underlying dynamical equations of motion describing the intra-ISCO inspiral must first be solved. I present a universal form of the discs inflow velocity in Chapter 5, in addition to explicit solutions of the full inspiralling trajectory of test particles. The solutions for maximally rotating Kerr black holes are, in particular, remarkably simple. Finally, I highlight how the late-time ultra-violet luminosity emergent from tidal disruption events represents potentially the most powerful probe of the properties of their black holes. In fact, strong constraints on a tidal disruption event's black hole mass can be placed with just a single measurement of its late-time luminosity. This opens up the possibility of utilising the full power of tidal disruption events as a probe of galactic dynamics. I conclude by presenting updated galactic scaling relationships which have been extended with the addition of 41 tidal disruption event black hole masses.

Contents

List of Figures

List of Tables

Gravity... Is working against me...
And gravity... Wants to bring me down...

— John Mayer's *Gravity*

1 Black holes, accretion discs and tidal disruption events

1.1 Black holes

Black holes are perhaps the most mysterious objects in the Universe: we do not understand the finer details of their internal structure and we cannot see them directly, yet they contain information about the fundamental laws of physics and the true nature of space and time itself.

Theoretical discussion of objects with the characteristic properties of what we now call black holes has a surprisingly long history. It was John Michell (1784) who first proposed that, if light followed Newton's corpuscular theory, a sufficiently massive 'star' would prevent the light emitted from its surface from escaping, this light instead being forced to return back towards the star's surface. This idea was, perhaps unsurprisingly, not widely accepted at the time, principally due to the limited understanding of the phenomenon of gravity and the apparent impossibility of demonstrating the existence of such objects experimentally. Once the consensus that light was an electromagnetic wave took hold, Michell's ideas were no longer widely considered plausible.

Only over 100 years later, when Einstein (1915), (1916) developed his theory of general relativity, were the theoretical foundations laid for a rigorous treatment of these 'black' stars. Einstein (1916a) himself showed that gravitational fields do indeed modify the motion of light rays, and a year after the field equations of general relativity

were published, they were solved by Schwarzschild (1916), who found the vacuum solution valid external to a non-rotating point mass. The space-time metric of such a system contained two apparent singularities, one at the location of the point mass, and one at a radial distance $2GM/c^2$ from the point mass (the Schwarzschild radius). Of course, a metric singularity does not necessarily imply a physical singularity of the spacetime, and debate over the exact physical properties of this boundary raged for some time. Eddington (1924) demonstrated that the $2GM/c^2$ singularity disappeared after a change of co-ordinates (into the so-called Eddington-Finkelstein coordinates), but it was not until the work of Lemaitre (1933) that it was realised that this implied that $2GM/c^2$ did not represent a physical singularity of the spacetime. In hindsight, by computing the Kretschmann scalar $R^{\alpha\beta\gamma\delta}R_{\alpha\beta\gamma\delta}$ of Schwarzschild's spacetime, it is relatively simple to show that the metric singularity at the location of the point mass is indeed a physical one, whereas the singularity at the Schwarzschild radius is a coordinate one. A free falling body can cross this outer radial boundary without any indication that this surface in spacetime was special.

To a distant observer however, the Schwarzschild radius would indeed appear to be special. An observer at rest at infinity watching an object fall towards the Schwarzschild radius would observe an ever increasing, and eventually infinite, red-shift as the object approached $2GM/c^2$. In fact, the Schwarzschild radius is the radius at which, in order to escape from the central mass, an object must move away at precisely the speed of light. Thus within the Schwarzschild radius objects must fall towards $r = 0$ ("the singularity"), and even light cannot escape. Once matter or light has passed beyond the Schwarzschild radius, it is completely cut off from larger radii, and a distant observer could not communicate in any way with an object within the Schwarzschild radius.

These mathematical black hole solutions of Einstein's equations were for many years treated as such, mathematical curiosities which were not expected to correspond to any real physical object in our universe. It was thought at the time that no massive body could 'collapse' under its own gravity to become smaller than its own Schwarzschild radius. Evidence to the contrary was growing however. Chandrasekhar (1931) calculated that above a mass of $\sim 1.4M_{\odot}$, matter supported by electron degeneracy pressure has no stable solutions, and must ultimately collapse. The neutron was later discovered, and it was assumed that neutron degeneracy pressure would prevent this singular fate. Proponents of these ideas were partially correct, stable neutron stars can and do exist, but they too are limited in their maximum mass. Tolman (1939), along with

Oppenheimer and Volkoff, showed that neutron stars above a mass now believed to be $\sim 2-3M_{\odot}$ would collapse further for the reasons proposed by Chandrasekhar. They correctly concluded that no known law of physics could intervene and prevent at least some massive stars collapsing into black holes.

The final theoretical pieces of the black hole puzzle fell into place in the 1960s (the so-called "golden age" of General Relativity). Roy Kerr (1963) found the black hole solution corresponding to a point mass which had angular momentum, a solution of considerable astrophysical interest, although this was not realised at the time. Shortly thereafter Ezra Newman (1965) found the black hole solution for a point mass which is both rotating and electrically charged. This Kerr-Newman metric turns out to be the ultimate description of a black hole: the work of Israel (1967), (1968) and Carter (1971) lead to the formulation of the "no-hair theorem", which states that the most general black hole solution is completely described by just three parameters: its mass, angular momentum and electric charge. The final theoretical argument against the formation of black holes in nature was the following: it was suggested that the peculiar properties of these solutions might simply be pathological artefacts of the imposed symmetries, which would not occur in a generic gravitational collapse. This notion was dispelled by the singularity theorems of Penrose and Hawking. In brief, Penrose (1965) demonstrated that once a 'trapped surface' has formed during gravitational collapse (defined analogously to the region within $2GM/c^2$ in the Schwarzschild metric: a region of spacetime within which light rays must be converging), a singularity at the centre of this surface must inevitably form. Thus singularities, and therefore black holes, are completely general end points of gravitationally collapsing bodies.

The first observational evidence for black holes did not lag far behind these rapid theoretical developments. In the early 1970s consensus grew that the bright Galactic X-ray source Cygnus X-1 was in fact a black hole. First detected in 1964 by a sub-orbital rocket mission, Cygnus X-1 is a source of bright radio and X-ray emission, located within half a degree on the sky of the bright star Eta Cygni. At the location of Cygnus X-1 is a supergiant blue star named HDE 226868, which is not by itself capable of producing the observed X-ray luminosity, and therefore some dark companion must be present which is capable of heating the gas given off by HDE 226868's stellar wind to the millions of degrees required to produce copious amounts of X-ray radiation. Followup observations found variability in the X-ray emission from the centre of Cyg-X1 at the millisecond level, implying that the maximum size of the X-ray emitting region was

much smaller than the radius of the sun. Meanwhile, measurements of the Doppler shift of HDE 226868's spectrum confirmed the dark companions presence, and determined a lower bound of its mass, which was substantially super solar $M \gtrsim 10M_{\odot}$. This combination of a substantially sub-solar radius and super-solar mass ultimately led to Cyg-X1 being the first black hole widely accepted by the community.

Fast forward 50 years and black holes are now a mainstay of modern physics and astrophysics. There are dozens of Galactic X-ray binary systems like Cyg-X1 now known, while analogous systems of a central black hole and a surrounding gaseous disc power some of the most luminous objects in the universe: active galactic nuclei and quasars. Quasars and AGN are situated in the centres of some galaxies, and consist of a supermassive black hole of mass ranging from millions to tens of billions of solar masses, surrounded by a large gaseous disc which feeds it. The accretion of matter onto a black hole is an extremely efficient way of liberating the rest mass energy of the disc, and the luminosities of these quasars are extreme: many thousands of times the total luminosity of the milky way.

Entirely new approaches to studying black holes have also been developed, with teams led by Reinhard Genzel (2003) and Andrea Ghez (2005) resolving and revealing the properties of the orbits of individual stars about the massive black hole at the centre of our Milky Way Galaxy, known as Sgr A*. These teams have demonstrated that the population of stars closest to Sgr A* are orbiting the galactic centre on highly elliptical orbits. These orbits have now been tracked in exquisite detail for over 20 years and reveal a dark (not seen in visible light) mass of $\sim 10^6 M_{\odot}$ which is contained within a region of maximum radius ~ 100 AU. While formally outside of the Schwarzschild radius of a $10^6 M_{\odot}$ black hole, the high density and dark nature of the central mass is compelling evidence for our own Galaxy hosting a supermassive black hole at its centre.

The LIGO (Laser Interferometer Gravitational-Wave Observatory) collaboration has borne fruit with the spectacular (now routine) direct detection of the gravitational radiation from merging black holes and neutron stars at cosmological distances. First detected on the 14th of September 2015 (Abbott et al. 2016), the total number of binary mergers found during the first three LIGO runs now stands in the tens of sources, and will likely grow into the hundreds in the coming years. Finally, 2019's astronomical show-stopping image of the event horizon environment of the black hole in the galaxy M87 captured the worlds attention (Event Horizon Telescope Collaboration et al. 2019a). Found using data from several very-long-baseline interferometry stations

covering an entire side of the globe, the EHT image appears to be consistent with predictions of the 'shadow' of a Kerr black hole.

The study of astrophysical black holes has progressed immeasurably over the past 50 years, but at its heart it remains a field of indirect study. If one wants to learn about the properties of black holes, one must understand in great detail their effect on their surroundings. The primary approach to inferring the existence of black holes and determining their properties has been through the detection and study of bright X-ray emitting accretion discs, in our Galaxy and at cosmological distances. It is to these objects that we now turn our attention.

1.2 Accretion discs

A particle on a circular orbit in a central gravitational potential will remain on that orbit, prevented from falling onto the central object by its specific angular momentum. If angular momentum is slowly removed from the particle's orbit it will spiral in towards the central object (recall that the angular momentum of a particle on a circular orbit scales with the square root of the particle's distance from a point mass central potential). If, rather than a single orbiting particle, gas is in orbit around a central object and angular momentum can be efficiently rearranged within this gas, then some of this gas can fall in towards the centre of the gravitational potential, with the remaining gas moving outwards to soak up this angular momentum. The conserved total angular momentum of the orbiting gas, a vector quantity, naturally sets a plane within which this radial motion takes place. Thus, the accretion of gas onto a central object is naturally mediated by disc-like structures. In an astronomical setting, these 'accretion discs' are extremely common, and form some of the most luminous objects in the night sky.

While the dynamical and observed properties of accretion discs are fundamentally governed by the simple concepts of mass, energy and angular momentum conservation, they nonetheless display a rich and varied behaviour. The theoretical study of accretion discs was developed by some of the most prominent astrophysical theorists of the 1970s: Nikolai Shakura, Rashid Sunyaev, Donald Lynden-Bell, James Pringle, and Martin Rees all played seminal roles. At a time when the existence of black holes was still a matter of controversy, the hope was that a robust theory of accretion would allow X-ray observations to reveal their presence. Alas, the theory of black hole accretion, replete with magnetohydrodynamical turbulence and relativistic jet-like

outflows, turned out to be too complicated to be used as an unambiguous observational tool. Instead, the problem turned around: accretion discs emerged from this era as fascinating astronomical objects in their own right, worthy of their own field of study.

The dynamics of an individual fluid element within an accretion disc is simple to qualitatively describe. The fluid element has angular momentum, and follows a near circular orbit around the central mass. In isolation this fluid element would happily stay on this circular orbit, a situation which is hydrodynamically stable. However, angular momentum may be redistributed between neighbouring fluid elements, and by giving up some of its angular momentum to the surrounding gas, an individual fluid element may move onto another near-circular orbit at a smaller radii, closer to the black hole. Two circular orbits at different radii differ not just in their specific angular momentum, but also in their gravitational potential energy. Thus, in moving between these two orbits, the fluid element must have given up some of its potential energy, and this liberated energy heats the disc and is then radiated away. The exchange of angular momentum within an accretion flow is the fundamental physical process which ultimately leads to the bright X-ray sources which light up our night's sky.

Accretion discs are phenomenally bright. By slowly releasing the gravitational potential energy[1] of a series of circular orbits the accretion process can achieve a mass-to-radiated-energy efficiency of $\epsilon \sim GM/R_{\rm in}c^2$, where $R_{\rm in}$ is the radius of the final, innermost, circular orbit of the disc. For a black hole, $R_{\rm in}$ is given by the so-called Innermost Stable Circular Orbit (ISCO), which is of order GM/c^2, and efficiencies can reach up to $\sim 42\%$. The luminosity of a black hole accretion disc fed just one billionth of a solar mass per year will reach levels of $\sim 10^{38}$ erg/s, roughly 100,000 times the luminosity of the sun.

The extreme efficiency of the accretion process ultimately results in a maximum luminosity attainable by a disc. Known as the Eddington limit, this luminosity scale represents the point at which the radiation pressure of the disc photon field becomes sufficient to overcome the gravitational attraction of the black hole-accretion flow itself. Above this limit, the radiation pressure is sufficient to halt the flow of material towards the compact object, thus cutting off the accretion disc's 'fuel supply', and the luminosity quickly falls to sub-Eddington levels. Given explicitly by

$$L_{\rm edd} = \frac{4\pi c G M m_p}{\sigma_T} \simeq 10^{38} \left(\frac{M}{M_\odot}\right) \text{ erg/s} \tag{1.1}$$

[1]More precisely, the free energy of the disc shear is released.

the Eddington limit is formally only applicable for spherically symmetric accretion, which accretion through a disc is clearly not. Thus super-Eddington accretion is neither unprecedented or unexpected (e.g., so-called "ultraluminous" X-ray sources). Nonetheless, the Eddington luminosity sets a natural (black hole mass dependent) scale for accretion disc physics, one we shall repeatedly return to.

All of the preceding discussion relies implicitly on there existing some process by which angular momentum can be efficiently redistributed within an accretion flow. The exact physical nature of this process was however a long controversial topic of debate. Early pioneering analysis of accretion disc systems (Lynden-Bell and Pringle 1974) all contain a diffusion coefficient proportional to an ad hoc 'turbulent viscosity'. The need for some turbulent enhancement of ordinary particulate viscosity was known from the very beginning of accretion disc studies, as the timescales of variability in compact object accretion discs are observed to be many orders of magnitude shorter than would be expected from typical fluid kinematic viscosities. The fact that accretion discs do actually accrete was a real theoretical problem for the field for a number of years. It was only much later that this problem was resolved, when Steven Balbus and John Hawley demonstrated in a series of seminal papers (Balbus and Hawley 1991, 1992; Hawley and Balbus 1991, 1992) that an ionised fluid undergoing Keplerian circular orbits is in fact unstable in the presence of even vanishingly weak magnetic fields. This instability, known as the magneto-rotational instability, rapidly redistributes angular momentum within the disc, and is the ultimate physical mechanism by which accretion proceeds.

Therefore, accretion discs are fundamentally turbulent, not viscous, systems. Fortunately, the governing evolutionary equations of a turbulent disc have the same functional form as the Lynden-Bell & Pringle equations, without the need of introducing an explicit viscosity (Balbus and Papaloizou 1999). By writing the velocity field as a sum of a mean plus a turbulent fluctuation, an effective diffusion coefficient emerges, which is proportional to the correlation in the radial and azimuthal turbulent velocity fluctuations. Magnetic fields can themselves be incorporated into this formalism, with an additional contribution to the turbulent stress resulting from correlations between the radial and azimuthal magnetic field components. While a simple replacement of a classical 'disc viscosity' by a 'turbulent stress tensor' may appear to place classical accretion disc theory on solid foundations, it is important to remember that a turbulent flow is not equivalent to a viscous flow, no matter how large the "coefficient of viscosity" is made. In certain physical regions, for example at the very inner edge

of a black hole accretion disc, turbulence has fundamentally different properties to an enhanced viscosity, and may be able to transfer angular momentum in physical situations where a viscosity could not.

The first principles approach to studying the turbulent evolution of black hole accretion flows is to numerically solve the equations of magnetohydrodynamics in a curved space time. Such General Relativistic MagnetoHydroDynamical (GRMHD) simulations have greatly enhanced our understanding of accretion physics. The growth of this field from the very earliest 2-dimensional MHD simulations, which confirmed the importance of the magneto-rotational instability (Hawley and Balbus 1991), to the current state of the art has, like any computationally driven field, been immense. Numerous code packages now exist, which all differ in their precise implementation and simplifying assumptions (e.g., McKinney 2006; Stone et al. 2008; White et al. 2016; Porth et al. 2017; Liska et al. 2018; Jiang et al. 2019). Modern simulations have now progressed to the stage of testing higher order predictions of the properties of accretion flows in general relativity, including the effects of frame dragging (Liska et al. 2021), while a huge effort has gone into understanding the mechanisms by which jets are launched from black hole disc systems (Liska et al. 2018; Parfrey et al. 2019), and their subsequent stability (McKinney and Blandford 2009). GRMHD simulations played a central role in interpreting the event horizon telescope data of M87 (Event Horizon Telescope Collaboration et al. 2019c), including in the production of the final black hole image itself (Event Horizon Telescope Collaboration et al. 2019b).

Unfortunately, it is only very recently (Jiang et al. 2019) that GRMHD codes have been published which model the radiation field emitted from the disc as a dynamical variable. The vast majority of the analysis of the emergent spectrum of GRMHD disc simulations therefore involves 'post-processing' the emission from the flow. While GRMHD simulations capture to an impressive degree the complex physics of magneto-hydrodynamical turbulence, the huge expense involved in running a single simulation means that the detailed modelling of the observed spectra of accretion disc sources remains a field completely dominated by simpler, more phenomenological, analysis.

Like any mature academic discipline, the study of accretion discs is by now an incredibly broad subject. In this thesis I will focus on those discs which are geometrically thin and optically thick. This means that I will study objects which rapidly radiate away the heat generated by the accretion process as photons, and do not store this energy internally. There is wide world of disc solutions outside of these thin-disc assumptions,

principally those which advect a significant degree of the liberated accretion energy. Such models include "slim" discs (Abramowicz et al. 1988), which are believed to occur at very high luminosities $L \gg L_{\rm edd}$, and so-called "two-temperature" flows (Narayan and Yi 1994), which are believed to occur at very low luminosities $L \lesssim 0.01 L_{\rm edd}$. Thin disc models, therefore, are chiefly appropriate for black hole systems in their bright (but not too bright) phase, with luminosities roughly $L_{\rm edd} \gtrsim L \gtrsim 0.01 L_{\rm edd}$. The models constructed in this thesis will therefore be suitable for comparison with only a certain class of black hole-disc systems, to which we shall restrict our attention. I shall not discuss advection dominated accretion flows further.

Phenomenological studies of thin accretion discs proceed from the following simple statements: the fluid elements in an accretion disc move on nearly circular orbits, with a small radial drift velocity correction term $v^R \ll v^\phi$; there exists some "viscosity" which can re-distribute the angular momentum of the flow; this same "viscosity" locally extracts the free energy of the disc shear; this locally liberated energy is then locally radiated away. One then writes down the equations of mass, angular momentum and energy conservation within the flow, subject to these constraints, and solves.

It was Lynden-Bell (1969) who first wrote down the steady state solutions of these equations, valid in a Newtonian theory of gravity. Lynden-Bell found what would prove to be a crucial result, the properties of the radiation emitted from a steady accretion flow are *independent* of the "viscosity" of the flow. This good fortune results from the same "viscosity" term appearing in both the equations of angular momentum and energy conservation, from which it can be eliminated in the steady state. Lynden-Bell's temperature profile can be written

$$\sigma T^4 = \frac{3GM\dot{M}}{8\pi R^3}\left[1 - \left(\frac{R_0}{R}\right)^{1/2}\right], \tag{1.2}$$

where M is the central mass, $\dot{M}$ is the steady mass accretion rate through the disc, R is the cylindrical distance from the centre, and R_0 is an integration constant, chosen to represent the inner radius of the disc where the temperature is assumed to vanish. The characteristic temperature fall off $T \sim R^{-3/4}$, a consequence of the liberation of gravitational potential energy, means that every disc annuli emits with both a different temperature and a different emitting area. The total disc flux at a given observed frequency comes from summing these different contributions over the entire disc surface

$$L_\nu(\nu) = 4\pi \int R\, B_\nu(\nu, T(R))\, {\rm d}R, \tag{1.3}$$

where B_ν is the Planck function $B_\nu = 2h\nu^3/c^2\,[\exp(h\nu/kT) - 1]$. Therefore one only needs to specify the mass of the central object M, and the rate at which material is accreting onto it $\dot{M}$, to compute the observed spectrum of a steady-state disc.

Unfortunately, if one wants to do physics beyond just the emitted spectrum of a steady-state accretion disc then one must compute various thermodynamic disc quantities (the disc density and pressure, for example) which do in fact depend explicitly on the turbulent stress, or "viscosity", of the flow. Even with explicit numerical studies however, the properties of disc turbulence remains at best poorly understood. There is no consensus fundamental theory that allows one, for example, to express a stress tensor in terms of background mean disc properties. There remains an ongoing requirement therefore for some form of phenomenological 'closure' relationship, which expresses the disc stress tensor in terms of thermodynamic disc quantities. The closure relationship which is used throughout the disc community is the so-called α-disc model of Shakura and Sunyaev (1973). Shakura & Sunyaev noted that turbulent velocity fluctuations (which I shall notate δv^i) will be limited by the local speed of sound within the disc $\delta v^i \leq c_s$. The reason for this is that super-sonic fluctuations will result in the formation of shocks within the disc, which will then quickly reduce the velocity fluctuation to sub-sonic values. The alpha-parameterisation is formally written as[2]

$$W^{r\phi} = \left\langle \delta v^r \delta v^\phi \right\rangle \lesssim c_s^2 \equiv \alpha c_s^2, \quad \alpha \leq 1. \tag{1.4}$$

The term on the far left of this expression encapsulates the correlations between the radial and azimuthal turbulent velocity fluctuations within the flow, and is this 'stress tensor' which ultimately causes accretion.

Of course, the fact that the fluid's velocity fluctuations must be less than c_s does not necessarily imply that they are equal to a number less than one (α) *multiplied* by the speed of sound. The α-parameterisation should therefore be considered primarily an informative scaling relationship, but is unlikely to capture the full behaviour of MHD turbulence. For MHD turbulence, α can be thought of as an indication of the amplitude of the rms turbulent fluctuations. In analytic modelling α is generally assumed to be constant, but there is no compelling justification for this, and numerical simulations show a highly complex spatio-temporal structure for α (e.g., Nelson and Papaloizou 2003).

[2]Another common (equivalent) parameterisation of the α-model is the following $\nu = \alpha c_s H$, where H is the height scale of the disc, and ν a 'turbulently enhanced kinematic viscosity'. The idea being that c_s plays the role of the random velocity scale of the turbulence, and H its typical length scale.

In addition, the Shakura and Sunyaev (1973) stress parameterisation has an unfortunate property, first pointed out by Lightman and Eardley (1974): it is formally unstable (the effective "diffusion coefficient" of the disc becomes negative) when the radiation pressure of the disc is larger than its thermal pressure. What precisely it means for an already turbulent system to be unstable is not clear, and observations of real accretion disc systems (in the so-called "soft" state) are entirely compatible with stable thermal discs (e.g. Done et al. 2007). Most practical implementations of the α-model therefore only use the gas pressure to compute the sound speed in equation 1.4, which highlights some of the limitations of this phenomenological analysis.

Nonetheless, the α-parameterisation facilitates the derivation of the full solutions to the thermodynamic equations of the disc (e.g., Shakura and Sunyaev 1973; Frank et al. 2002), and has therefore become a cornerstone of analytic disc theory. The α-parameterisation is of particular utility in out-of-equilibrium studies of accretion discs, the regime relevant for disc systems which are yet to reach a steady state. The reason for this is that the evolution of the disc's surface density, and therefore radiative temperature, is explicitly dependent on the disc's "viscosity" when out of equilibrium, as the equation of angular momentum conservation is no longer sufficient to eliminate all viscosity-dependent terms.

The classical theory of out-of-equilibrium thin accretion discs was developed by Lynden-Bell and Pringle (1974). In their seminal work, the constraints of mass and angular momentum conservation were shown to lead to a diffusion-like equation for the evolution of the disc's surface density. On energetic and angular momentum arguments alone, Lynden-Bell & Pringle showed that the minimum energy configuration of a disc is a limit in which one particle of infinitesimal mass carries all the angular momentum out to a circular orbit at infinity, while all the remaining mass aggregates at the centre. This quite generally then is the limiting solution one would expect from the disc equations, and indeed the Greens function solutions of the Lynden-Bell & Pringle equation are in exact agreement with these energetic arguments. While the intricacies of the Greens function solutions themselves depend on the exact viscosity parameterisation, the gross mass-in angular momentum-out behaviour is independent of the exact microphysics of the specification of the disc's turbulent "viscosity".

The classical solutions of Lynden-Bell (1969) and Shakura and Sunyaev (1973) and Lynden-Bell and Pringle (1974) are all only valid in Newton's theory of gravity. The extension of the steady state solutions of the equations of mass, angular momentum

and energy conservation to the relativistic Kerr geometry was, shortly thereafter, first written down by Page and Thorne (1974). The crucial solution for the dissipation (and thus σT^4) has qualitatively the same features as equation 1.2: an overall scaling of $M\dot{M}/R^3$, and an inner boundary condition set so that the inner-disc temperature is zero. There are, naturally, relativistic correction terms important in the very inner regions of the flow, which include terms dependent on the black hole's spin, time-dilation effects and terms relating to the explicit deformation of the metric from flat space.

The relativistic 'upgrade' of the Shakura-Sunyaev α-model was presented in Novikov and Thorne (1973), who derived closed-form, algebraic, solutions of the full thermodynamic equations of a disc about a Kerr black hole. These solutions have been of great practical utility to the astronomical community. When combined with relativistic 'ray-tracing' calculations, these equations form the basis for the modelling of the X-ray spectra observed from Galactic X-ray binaries (Li et al. 2005). The explicit dependence of these solutions on the black hole's spin allows, in principal (and often in practice), for direct spectral measurements of the spin of a black hole (McClintock et al. 2014). The spin of a black hole is a quantity of intense astrophysical interest. Representing the integrated angular momentum flux onto the black hole over its lifetime, it contains information on the formation and evolution of black holes. Furthermore, these equations form the foundations upon which more complex models are built, such as those describing the quasi-periodic oscillations observed in the power spectra of many Galactic X-ray binaries (Nathan et al. 2022).

Given the great success of steady-state relativistic disc models, and the myriad practical uses found for Newtonian time-dependent disc theory (e.g., in dwarf nova eruptions (Frank et al. 2002) and protoplanetary discs (Fromang et al. 2002)) it is extremely surprising that relativistic, time-dependent, accretion disc theory is in effect a completely unexplored field. In one of the appendices of a paper studying magnetic stresses in accretion discs, Eardley and Lightman (1975) first presented the form of this relativistic evolutionary equation appropriate for the Kerr spacetime, but did not explore the properties of its solutions. Except for a brief numerical analysis in Garofalo and Reynolds (2005), this equation was then left completely unexplored until Balbus (2017) rediscovered it and presented a formal WKB modal analysis of its properties. Occupying the middle ground between computational rigour and Newtonian modelling, the Kerr evolution equation promises to be a practical theoretical tool, particularly for the analysis of intrinsically time-dependent and relativistic systems.

It is the purpose of this thesis to derive the first numerical and analytical solutions to this governing equation, and then use it to model one such astrophysical system: the accretion of tidally disrupted stellar debris onto a supermassive black hole.

1.3 Tidal disruption events

It is believed that a supermassive black hole ($M_{\rm BH} > 10^6 M_\odot$) lurks at the centre of every massive galaxy. The properties of these objects appear to be correlated with many characteristics of the host galaxy itself (e.g., Magorrian et al. 1998), suggesting that the presence of these black holes has a profound effect on the evolution of the galaxy itself. While some of these supermassive black holes are continuously fed by large discs of material, the majority of those in the local universe are starved of fuel and lie quiescent. A novel method for studying these quiescent black holes at cosmological distances from the milky way: observing the emitted radiation produced when the stellar debris from a tidally disrupted star accretes onto the central black hole, is taking on a growing importance in the field of transient astronomy.

The stellar concentration of galactic centres are high, and perturbations of the orbits of individual stars by the combined gravitational interactions of the remaining stellar population can occasionally set an unfortunate star onto a near-radial orbit about the central black hole. There is a critical separation, the so-called tidal radius r_T, where the star's gravitational attraction to the black hole first becomes larger than its own self-gravity. Upon entering this region the star is destroyed, *in its entirety*, by the black hole's gravitational force, scattering stellar debris onto a series of different orbits. Some fraction of this stellar debris subsequently rains back onto the supermassive black hole, and drives accretion which causes bright flares from these otherwise quiescent galactic centres. These flares, which typically outshine their entire host galaxy, last for timescales of months-to-years and have been observed at frequencies across the entire electromagnetic spectrum, including hard X-rays (e.g. Cenko et al. 2012), soft X-rays (e.g. Greiner et al. 2000), optical (e.g. Gezari et al. 2008), U.V (e.g., van Velzen et al. 2019b), infrared (e.g. Jiang et al. 2016, van Velzen et al. 2016) and radio waves (e.g., Alexander et al. 2016, Goodwin et al. 2022). First discovered in the late 1990s (Bade et al. 1996), the current population of observed tidal disruption events stands at around 40.

Tidal disruption events (or "TDEs") offer a truly novel probe of the properties of supermassive black holes, the majority of which are only observable during these (rare) events. The population of supermassive black holes probed by TDEs will be unique in a number of ways. TDE black holes will encompass the lower mass end of the total supermassive black hole mass distribution (black holes above $10^8 M_\odot$ swallow stars whole, rather than tidally disrupt them (Hills 1975)), a region of parameter space which is only very sparsely populated by other observational techniques (see e.g., McConnell and Ma 2013). Furthermore, TDEs represent the best avenue by which the first 'intermediate' mass black holes $10^2 M_\odot < M < 10^6 M_\odot$ may be discovered.

Fundamentally, TDEs represent one of only a very small number of physical systems where we can watch the accretion process itself 'switch on'. AGN, Galactic X-ray binaries and quasars have all typically been accreting for millions of years before they are first observed, whereas a TDE system can go from effectively non-luminous to shining brighter than an entire galaxy over a timescale as short as a week. After reaching peak brightness, TDE emission decays away over the following months to years, a timescale much shorter than other supermassive black hole disc systems (AGN discs typically evolve over thousands of years), and therefore represent the best environment for testing whether the physics of accretion is scale (black hole mass) invariant. It is well-established that Galactic X-ray binaries undergo dramatic 'state transitions' when their luminosity in Eddington units is of order $\sim 1\%$ (e.g. Fender and Belloni 2004, Maccarone 2003). Although there is evidence that AGN discs undergo similar state transitions (Maccarone et al. 2003), the significantly longer evolution timescales of typical AGN discs generally prevents such transitions from being directly observed. Tidal disruption events will test whether supermassive black hole discs undergo these very same transitions. A reliable model for describing the evolution of the post-disruption debris and the transient luminosity of these sources would therefore represent a vitally important addition to the wider study of supermassive black holes, and of accretion disc physics itself.

The canonical model for the evolution of post-disruption debris is due to Martin Rees (1988), and proceeds as follows. Roughly half of the debris is assumed to be ejected onto parabolic orbits, while the remaining debris remain gravitationally bound to the black hole, with a distribution of energies, ϵ, due to the disruption event. This bound matter is then assumed to accrete onto the black hole by a simple 'fallback mechanism'. The idea is that a typical particle will have energy $\epsilon \sim GM_{BH}/R$ (G is Newton's constant,

M_{BH} the black hole mass, R the distance from the black hole). Applying Kepler's third orbital law $R \propto t^{2/3}$, and assuming that equal mass fractions are scattered into each energy interval ($\mathrm{d}M/\mathrm{d}\epsilon \sim$ cst), a characteristic mass fall-back rate of

$$\dot{M}_{\rm fb} = \frac{\mathrm{d}M}{\mathrm{d}\epsilon}\frac{\mathrm{d}\epsilon}{\mathrm{d}R}\frac{\mathrm{d}R}{\mathrm{d}t} \propto t^{-5/3}, \tag{1.5}$$

is found. The assumption was that the luminosity, L, of the source would follow this behaviour at large times. Indeed for many years this behaviour was used as an observational diagnostic of TDEs (Esquej et al. 2008), with the functional form $L \propto (t - t_0)^{-5/3}$ fit to many TDE-candidate light curves.

If one knows what one is looking for, it is often all too easy to find. Thus, when the initial searches for TDEs not only found candidates, but apparent fits to $-5/3$ power laws (Esquej et al. 2008), the theory seemed validated. Matters turned out to be more complicated, however. One never sees an outburst at inception, so the initial time t_0 is unknown, and different choices of t_0 in the real world of messy data give different indices. (By fitting $L \propto (t - t_0)^{-5/3}$ to a light curve with unknown start date, one is really fitting for t_0, a quantity which can never be retrospectively measured and thus confirmed. This exact point was well demonstrated in Bright et al. (2018), Figure 3.) In addition, there are theoretical concerns with this Ressian picture. A TDE accretion flow is necessarily out of equilibrium, as such the mass flux back to the pericentre of the disrupted stars orbit (the fall-back rate calculated above) is not equal to the rate at which material will flow across the black hole's event horizon. Out of equilibrium, angular momentum must be redistributed within this flow before it can be accreted, a process which is by no means instantaneous. As such the 'mass accretion rate' is a dynamic quantity, varying at every radius and time within the flow. Uncritically substituting $L \propto \sigma T^4 \propto \dot{M}_{\rm acc} \propto \dot{M}_{\rm fb} \propto t^{-5/3}$ into equations from disc theory will result in large (total) systematic errors. Finally, and this is an extremely important point, even if the *bolometric* luminosity were to follow $\sim t^{-5/3}$, what is the evolution of the luminosity *as observed at a particular frequency band* (e.g., with an X-ray telescope)? One never observes all of the emission from an event with, for example, the *Swift* X-ray telescope only picking up the emission between 0.3 and 10 keV. TDE emission has been detected spanning 4 orders of magnitude in energy, from the infra-red $E_{\rm IR} \sim 10^{-4}$ keV up to X-rays $E_{\rm X} \sim 1$ keV, not a simple factor of a few. It transpires that the effects of this partial sampling of the total luminosity are profound, as will be demonstrated in Chapter 3.

The theoretical study of TDE emission over the previous decades has largely been tied to this original Reesian picture. A huge amount of effort has gone into the simulation of the initial stages of the stellar disruption, and into computing the spatial distribution, and rate of return, of the scattered debris (e.g., Kochanek 1994, Guillochon and Ramirez-Ruiz 2015, Bonnerot et al. 2016). The realisation that returning debris streams will likely intercept and shock on themselves (Piran et al. 2015), has lead to the development of models of shock-powered TDE emission (Ryu et al. 2020). A different and popular approach to computing TDE observables is to assume that the observed emission results from the re-processed Reesian accretion luminosity (equation 1.5) by an unbound outflowing 'atmosphere' which is either produced in the initial disruption or by large radiation pressures. Analytical (Metzger and Stone 2016), or numerical (Guillochon and Ramirez-Ruiz 2013), calculations of the fall-back rate are then converted into observed luminosities by using $\sigma T^4 \propto \dot{M}_{\rm fb}(t)$, to get an 'intrinsic luminosity' which is then folded through a 'reprocessing layer' on the way to the observer.

The black hole masses computed from fitting these models to observed TDE light curves do not correlate with the masses of the galaxies they come from (Hammerstein et al. 2022), a surprising result given that the mass of a black hole is known to correlate tightly with the mass of its galaxies bulge (Magorrian et al. 1998, McConnell and Ma 2013), and it is known that TDE host galaxies have prominent bulges typically of mass half that of the total galaxy mass (Law-Smith et al. 2017). An additional problem with the current state of the art is that neither shock-powered or reprocessing models of TDE emission make any predictions of, or equivalently take into account, the properties of the X-ray emission from a given TDE source. Some TDEs shine phenomenally brightly at X-ray frequencies $L_X \sim 10^{43} - 10^{44}$ erg/s (i.e., roughly ten billion solar luminosities), while others are X-ray dim with only upper detection limits. It seems likely that information gleaned from the X-ray properties of a given TDE will be extremely constraining of its physical parameters.

Progress on the observational TDE front has been more rapid however. The first few TDE candidates were discovered by the ROSAT X-ray telescope in the late 1990s (Bade et al. 1996), but the real step change in observational studies of TDEs came with the advent of optical all-sky surveys hunting for supernovae. The All Sky Automated Survey for SuperNovae (or ASASSN) discovered, while looking for supernovae, a number of TDE candidates starting from 2014 (Holoien et al. 2014, Holoien et al. 2016a, Holoien et al. 2016b). Other optical surveys like OGLE (Wyrzykowski et al. 2017),

and the X-ray slew survey of the XMM satellite (Saxton et al. 2019) contributed to the trickle of sources which culminated in the ~ 40 sources known to the community at the beginning of the 2020s. An acceleration in the discovery rate of TDEs began in the last year, with the ZTF survey discovering 30 TDEs (van Velzen et al. 2021, Hammerstein et al. 2022), while the all-sky X-ray satellite eRosita expects to discover $\sim$ 1000s of TDEs in the near future (Khabibullin et al. 2014), and has already released detections of its first 13 sources (Sazonov et al. 2021). Some of the earliest source detections of these two surveys are included in this thesis, but many of the most recent (late 2021 to 2022) detections are not. It is likely, and an exciting reality, that many of the figures in this thesis will quickly become out of date, as huge amounts of new data on these fascinating sources are discovered.

In effect this thesis asks the following question: what if TDE accretion is not by direct fall back onto the hole, but by the formation and mediation of a disc? The necessity of the presence of an accretion disc has been recognised in the TDE community as the physical source of the X-ray emission detected from some TDEs (e.g., Bright et al. 2018), but the theoretical descriptions of these X-ray emitting discs have been strictly steady state (e.g., Miller et al. 2015), when of course a TDE disc will in fact be far from inflow equilibrium. A pioneering study of out-of-equilibrium accretion discs in the context of TDEs was performed by Cannizzo et al. (1990) in the very early days of TDE theory, but has since been superseded by different models of TDE emission. Cannizzo et al's study focussed on the bolometric luminosity emergent from a disc evolving in Newton's gravity. Of course, the observed X-ray luminosity of a TDE represents only a (potentially small) fraction of the bolometric luminosity from a disc, and the innermost regions of a TDE disc will be resolutely relativistic, not Newtonian. A proper calculation of the X-ray luminosity emergent from a relativistic disc represents a step change in the descriptive power of TDE disc models, resolving simultaneously the problems associated with existing steady-state, or bolometric Newtonian, modelling.

Before the observed luminosity of TDE sources can be modelled by an evolving relativistic disc, I must first derive, solve and analyse the relativistic disc evolution equation. These solutions, the first found for the relativistic disc equation, are presented in Chapter 2. With the machinery of a new time dependent relativistic disc theory at hand, Chapter 3 demonstrates that the detailed modelling of the observed light curves of two TDE sources provides both excellent fits to the data, a deeper understanding of the physical processes at play in a TDE, and strong constraints on the physical

properties of the black holes at the TDEs centre. Chapter 4 then extends these ideas, analysing the properties of TDE discs, as observed at X-ray energies, across the entire physical parameter space likely to be spanned by the black holes and stars involved in tidal disruption events. I will argue that the properties of the black holes and discs at the heart of a TDE are of fundamental importance to understanding a TDE's gross observed properties, and demonstrate how the early signs from population studies of TDEs are inkeeping with the predictions of fundamental disc theory. In Chapter 5, I conclude, and look forward to potential extensions of the ideas presented in this thesis. Both theoretical extensions and how best to utilise the forthcoming explosion of TDE data sets are discussed.

2

A time dependent theory of relativistic thin discs

The work in this chapter is based upon the following peer-reviewed journal articles
Balbus and Mummery 2018, MNRAS, 481, 3348
Mummery and Balbus 2019a, MNRAS, 489, 132
Mummery and Balbus 2019b, MNRAS, 489, 143

2.1 Introduction

In the classical theory of thin accretion discs, the constraints of mass and angular momentum conservation lead to a diffusion-like equation for the turbulent evolution of the disc's surface density. In its original implementation, the equation contains a diffusion coefficient proportional to an ad hoc turbulent viscosity (Lynden-Bell and Pringle 1974). The precise microphysical origin of this turbulent viscosity is not discussed in these early works, but Balbus and Papaloizou (1999) later showed how the same evolution equation emerges without the need to introduce an explicit viscosity. By writing the velocity field as a sum of a mean plus a fluctuation, an effective diffusion coefficient emerges, which is proportional to the correlation in the

radial and azimuthal velocity fluctuations[1].

With the governing equation in place, the evolution of these thin accretion discs is then generally studied via techniques first developed by Lynden-Bell and Pringle (1974) (see Pringle (1981) for a review). The solutions of the disc equation show that matter in accretion discs drifts inward, while angular momentum is transported outward, sustained by a vanishingly small mass fraction of the disc. This behaviour is independent of the exact microphysics of the specification of the disc's turbulent 'viscosity'. The classical (Newtonian) disc evolutionary equation has found practical use in many astrophysical systems, including dwarf nova eruptions (Frank et al. 2002), protoplanetary discs (Fromang et al. 2002) and, the topic of much of this thesis, tidal disruption events (Cannizzo et al. 1990). While equilibrium relativistic thin disc theory was developed nearly half a century ago, the ability to study *relativistic* disc evolution by the methods similar to those introduced by Lynden-Bell & Pringle is only now being developed.

In one of the appendices of a paper studying magnetic stresses in accretion discs, Eardley and Lightman (1975) first presented the form of this relativistic evolutionary equation appropriate for the Kerr spacetime. Following the Novikov and Thorne (1973) and Page and Thorne (1974) equilibrium models, the viscosity (in reality turbulent transport) is represented by an anomalous stress tensor. First invoked by Shakura and Sunyaev (1973), the anomalous stress both enhances the transport of angular momentum and drives significant dissipative heating. Emerging in the form of radiative losses, the latter energy source is the mechanism by which X-ray emitting accretion discs are ultimately observed. Very little was done by way of investigating explicit solutions of the Eardley–Lightman equation until very recently, when Balbus (2017), unaware of the earlier derivation, rediscovered the Kerr evolutionary equation (in slightly different coordinates). As an alternative to the much more expensive direct numerical simulation, the one-dimensional relativistic equation promises to be a practical theoretical tool, occupying the middle ground between computational rigour and phenomenological modelling.

The analysis of the 'relativistic upgrade' of the classical Lynden-Bell & Pringle disc evolution equation presented in this Chapter represents an important addition to the literature. First, a relativistic and time-dependent theory of thin accretion discs

[1]The presence of a magnetic field can be further incorporated into this formalism, with the product of the radial and azimuthal Alfvén velocities subtracted from the correlated velocity fluctuations in the diffusion coefficient – resulting in an additional positive stress.

represents the final missing piece of the simplest theoretical descriptions of thin discs: steady state Newtonian and relativistic solutions are well known, and time-dependent Newtonian theories well established. Practically, a huge number of astrophysically interesting accretion disc sources surround black holes and neutron stars, where a relativistic description is required. While the majority of the radial extent of these black hole accretion disc systems are in robustly Newtonian regions, the same is not true for the total liberated luminosity. The inner regions of an accretion disc are significantly hotter than the outer regions, and so the luminosity resulting from the highly relativistic regions of an accretion disc represent a substantial correction to the Newtonian luminosity prediction. Imprinted on this emitted luminosity are features pertinent to the theory of general relativity, as only a relativistic disc-theory can accurately capture the nature of black hole spins, the properties of the ISCO, and fluid dynamics in strong gravity regimes. These various quantities encode fundamental information about the formation and evolution of black holes across the age of our Universe.

Most importantly, and the focus of the final Chapters of this thesis, some accreting systems, for example tidal disruption events, are intrinsically time dependent and relativistic systems, and thus can only be described by the equations derived in this Chapter. In this Chapter I derive, solve and analyse the governing time dependent and relativistic thin disc equations.

2.2 Derivation of the governing disc equation

The disc evolution equation is a partial differential equation for the azimuthally-averaged, height-integrated disc surface density $\Sigma(r,t)$, and is written in terms of standard cylindrical Boyer-Lindquist coordinates for the Kerr metric: r (radial), ϕ (azimuthal), z (vertical) and t (time).

I observe the following conventions. The speed of light is set to unity throughout this chapter. Greek indices $\alpha, \beta, \gamma \ldots$ denote space–time coodinates. The exception is ϕ, which is always the azimuthal angular coordinate. The time coordinate is labelled 0. The metric in local inertial coordinates is $g_{\alpha\beta} \to \eta_{\alpha\beta} = \mathrm{diag}(-1,1,1,1)$. Other notation is standard: G is the gravitational constant, M the central black hole mass and $r_g = GM$ the gravitational radius. The black hole's angular momentum parameter is a (having dimensions of length in this choice of units).

The derivation of the disc evolution equation follows from the conservation of three key quantities, the mass, energy and angular momentum of the rotating disc fluid. In relativistic notation these conservation laws are written

$$\begin{aligned} &\nabla_\mu (\rho u^\mu) = 0 \quad \text{(mass conservation)}, \\ &\nabla_\mu \left(T^\mu_\phi\right) = 0 \quad \text{(angular momentum conservation)}, \\ &\nabla_\mu (T^\mu_0) = 0 \quad \text{(energy conservation)}. \end{aligned} \tag{2.1}$$

Here u^μ is the 4-velocity of the rotating disc fluid, ρ is the disc density, $T^{\mu\nu}$ is the stress-energy tensor of the disc and ∇_μ represents a covariant derivative with respect to co-ordinate x^μ.

2.2.1 Mass conservation

I begin with the conservation of mass, which can be more explicitly written as

$$\nabla_\mu (\rho u^\mu) = \frac{1}{\sqrt{g}}\, \partial_\mu (\sqrt{g} \rho u^\mu) = 0. \tag{2.2}$$

Here $g \equiv |\det g_{\mu\nu}|$, the absolute value of the Kerr metric determinant, and $\partial_\mu \equiv \partial/\partial x^\mu$ is the ordinary partial derivative with respect to co-ordinate x^μ. I now make the assumption that the disc is thin, with the disc quantities independent of the vertical z co-ordinate, and axisymmetric. This second assumption means that all disc quantities are independent of the ϕ azimuthal co-ordinate. The non-zero disc 4-velocity components are u^0, u^r and u^ϕ. Further expansion of the mass conservation equation in this manner gives

$$\partial_t \left(\sqrt{g}\, u^0 \rho\right) = -\partial_r \left(\sqrt{g}\, u^r \rho\right). \tag{2.3}$$

After height-integrating this equation, and defining $\Sigma(r,t)$ as

$$\Sigma(r,t) \equiv \int \rho \, \mathrm{d}z, \tag{2.4}$$

mass conservation becomes

$$\partial_t \left(\sqrt{g}\, u^0 \Sigma\right) = -\partial_r \left(\sqrt{g}\, u^r \Sigma\right). \tag{2.5}$$

Further simplifications of this expression will follow after an examination of the equation of conservation of disc angular momentum.

2.2.2 Angular momentum conservation

The stress-energy tensor of the rotating disc fluid is given by the following expression

$$T^{\mu\nu} = g^{\mu\nu}P + (\rho + P + e)u^\mu u^\nu + q^\mu u^\nu + q^\nu u^\mu, \tag{2.6}$$

where the first two terms are those of an ideal fluid, P is the isotropic pressure, and e the internal energy density of the fluid. The final two terms represent the contribution of the disc's radiation field

$$F^{\mu\nu} = q^\mu u^\nu + q^\nu u^\mu. \tag{2.7}$$

The 4-vector q^μ is the radiative energy flow vector, which satisfies $q_\mu u^\mu = 0$ (Page and Thorne 1974). Following the notation of Balbus (2017) I define

$$\sigma^{\mu\nu} = (\rho + P + e)u^\mu u^\nu + q^\mu u^\nu + q^\nu u^\mu. \tag{2.8}$$

The conservation of disc angular momentum can be expressed as

$$\nabla_\mu \left(T^\mu_\phi\right) = \frac{1}{\sqrt{g}}\,\partial_\mu\left(\sqrt{g}\sigma^\mu_\phi\right) - \Gamma^\lambda_{\mu\phi}\sigma^\mu_\lambda = 0, \tag{2.9}$$

where I have used the fact that $\nabla_\mu g^\mu_\nu \equiv 0$, $\partial_\phi P = 0$ by axisymmetry, and I have introduced the affine connection

$$\Gamma^\alpha_{\beta\gamma} \equiv \frac{1}{2}g^{\alpha\delta}\left(\partial_\beta g_{\gamma\delta} + \partial_\gamma g_{\beta\delta} - \partial_\delta g_{\beta\gamma}\right). \tag{2.10}$$

For axisymmetric metrics (like the Kerr metric) $\partial_\phi g_{\mu\nu} = 0$, and so

$$\Gamma^\lambda_{\mu\phi} = \frac{1}{2}g^{\lambda\alpha}\left(\partial_\mu g_{\phi\alpha} - \partial_\alpha g_{\mu\phi}\right), \tag{2.11}$$

meaning the combination

$$\Gamma^\lambda_{\mu\phi}\sigma^\mu_\lambda = \frac{1}{2}g^{\lambda\alpha}\left(\partial_\mu g_{\phi\alpha} - \partial_\alpha g_{\mu\phi}\right)\sigma^\mu_\lambda = \frac{1}{2}\left(\partial_\mu g_{\phi\alpha} - \partial_\alpha g_{\mu\phi}\right)\sigma^{\mu\alpha} \equiv 0, \tag{2.12}$$

vanishes for *any* symmetric tensor $\sigma^{\mu\alpha}$, since the metric derivative are anti-symmetric in μ and α, while $\sigma^{\mu\alpha}$ is symmetric in these indices. As a result of this identity, the conservation of disc angular momentum equation becomes

$$\frac{1}{\sqrt{g}}\,\partial_\mu\left(\sqrt{g}\sigma^\mu_\phi\right) = 0. \tag{2.13}$$

2.2.3 Turbulent velocity hierarchy

To make further progress these two conservation equations are expanded perturbatively in the disc 4-velocity u^μ. The disc 4-velocity (as well as the disc 4-momentum u_μ) are decomposed into a mean component U^μ and vanishing-mean fluctuating component δU^μ:

$$u^\mu = U^\mu + \delta U^\mu, \quad u_\mu = U_\mu + \delta U_\mu, \tag{2.14}$$

which satisfy asymptotic scalings

$$\delta U_\phi \ll U_\phi, \quad U^r \ll \delta U^r \sim \delta U_\phi / r \ll r U^\phi. \tag{2.15}$$

I also introduce an averaging procedure, denoted by angled brackets $\langle . \rangle$, which represents an average over a time scale Δt which is short compared to the evolutionary timescale of the disc, but long compared to the timescales of individual turbulent fluctuations:

$$\langle X(r,t) \rangle \equiv \frac{1}{\Delta t} \int_t^{t+\Delta t} X(r,t')\, \mathrm{d}t'. \tag{2.16}$$

The velocity fluctuations are defined in such a way that

$$\langle \delta U^\mu \rangle = 0, \tag{2.17}$$

while importantly

$$W^{\mu\nu} \equiv \langle \delta U^\mu \delta U^\nu \rangle \neq 0. \tag{2.18}$$

These *correlated* velocity fluctuations impart a turbulent stress on the disc, which ultimately drives accretion. In particular, this velocity hierarchy means that

$$\langle u^r u_\phi \rangle = \langle U^r U_\phi + \delta U^r \delta U_\phi + U_\phi \delta U^r + U^r \delta U_\phi \rangle = U^r U_\phi + W^r{}_\phi, \tag{2.19}$$

with the final two terms in the middle equality vanishing by definition. The final assumption is that the zeroth order flow of the disc is that of precisely circular motion, i.e., that U^0, U_0, U^ϕ and U_ϕ are equal to the test particle equatorial plane circular motion solutions of the Kerr metric. Importantly, this means that these quantities only depend on the radial metric co-ordinate r.

This velocity hierarchy expansion is the key physical premise upon which the disc evolution equation is derived: to zeroth order the fluid rotates about the origin, with fluctuations at first order due to the low-level disc turbulence. Only at second order

(in the fluctuation amplitude) does the fluid radial drift velocity emerge. The two δU fluctuations are assumed to be of comparable order, suitably dimensionalized. In common with Newtonian theory (Balbus and Papaloizou 1999), I expect $U^r U_\phi$ (the product of a zeroth order rotational velocity and a second order radial drift) to be of the same asymptotic order as $\delta U^r \delta U_\phi$ (the product of two first order fluctuations).

2.2.4 The disc evolution equation

The equation of mass conservation, when suitably expanded in the turbulent velocity hierarchy and averaged is

$$\frac{\partial \Sigma}{\partial t} = -\frac{1}{U^0 \sqrt{g}} \frac{\partial}{\partial r} \left(\sqrt{g}\, U^r \Sigma \right), \tag{2.20}$$

while the angular momentum conservation equation is (after height averaging)

$$\frac{1}{\sqrt{g}}\, \partial_\mu \left(\sqrt{g} \sigma^\mu_\phi \right) = U^0 U_\phi \partial_t \Sigma + \frac{1}{\sqrt{g}} \frac{\partial}{\partial r} \left[\sqrt{g} \Sigma \left(U^r U_\phi + {W^r}_\phi \right) \right] + U_\phi \int \partial_z q^z \, \mathrm{d}z = 0. \tag{2.21}$$

In formulating this expression I have used the fact that the thermal energy density is much smaller than the disc density $(P + e)/\rho \sim c_s^2/c^2 \ll 1$, where c_s is the speed of sound (Novikov and Thorne 1973), and that the radiation field has only one non-zero component q^z (the disc radiates out of its upper and lower surfaces). The final term is

$$U_\phi \int \partial_z q^z \, \mathrm{d}z = U_\phi \mathcal{F}_\mathcal{E}, \tag{2.22}$$

where $\mathcal{F}_\mathcal{E}$ is the energy radiated from the disc surface, a quantity I shall return to in the following section. The combination $U_\phi \mathcal{F}_\mathcal{E}$ corresponds to the *angular momentum* radiated away by the photon field, a quantity which can become significant in the relativistic inner-disc regions. Expanding equation 2.21 in full leaves

$$U_\phi \left(U^0 \partial_t \Sigma + \frac{1}{\sqrt{g}} \partial_r \left(\sqrt{g} \Sigma U^r \right) \right) + U'_\phi \Sigma U^r + \frac{1}{\sqrt{g}} \frac{\partial}{\partial r} \left(\sqrt{g} \Sigma {W^r}_\phi \right) + U_\phi \mathcal{F}_\mathcal{E} = 0, \tag{2.23}$$

where I have defined $U'_\phi \equiv \partial U_\phi / \partial r$. The first group of terms is zero as a result of mass conservation, meaning that

$$\Sigma U^r = -\frac{1}{U'_\phi} \left(\frac{1}{\sqrt{g}} \frac{\partial}{\partial r} \left(\sqrt{g} \Sigma {W^r}_\phi \right) + U_\phi \mathcal{F}_\mathcal{E} \right). \tag{2.24}$$

Grouping the mass and angular momentum conservation equations together leads to the disc evolution equation

$$\frac{\partial \Sigma}{\partial t} = \frac{1}{U^0 \sqrt{g}} \frac{\partial}{\partial r} \left(\frac{1}{U'_\phi} \left[\frac{\partial}{\partial r} \left(\sqrt{g} \Sigma {W^r}_\phi \right) + \sqrt{g} U_\phi \mathcal{F}_\mathcal{E} \right] \right). \tag{2.25}$$

2.3 Simplifying the governing equation

2.3.1 The radiated energy flux

For an equilibrium model of a relativistic accretion disc, Page and Thorne (1974) present a relationship between the disc shear, the tensor stress coupling and the energy radiated from the disc's surface. In the notation of this thesis, their relation is the following

$$\mathcal{F}_{\mathcal{E}} = -\Sigma W^{r}{}_{\phi} U^{0} \frac{\mathrm{d}\Omega}{\mathrm{d}r} \tag{2.26}$$

where

$$\Omega \equiv \frac{\mathrm{d}\phi}{\mathrm{d}t} = \frac{U^{\phi}}{U^{0}} \tag{2.27}$$

is the angular velocity as measured by an observer at infinity. In essence, this states that the energy *locally* extracted from differential rotation and put into turbulent fluctuations is *locally* radiated away at the same rate, i.e. the total energy extracted by the underlying turbulence over the local disc thickness is equal to the energy radiated through the upper and lower surfaces. It is of interest to verify that this relationship still holds in an out-of-equilibrium disc, such as those considered in this thesis.

A derivation demonstrating that equation 2.26 still holds in an out-of-equilibrium setting is presented below. Note that the derivation presented here differs from that of Balbus (2017).

I begin with the equation of energy conservation within the disc

$$\nabla_{\mu} \left(T_{0}^{\mu} \right) = \frac{1}{\sqrt{g}} \partial_{\mu} \left(\sqrt{g} \sigma_{0}^{\mu} \right) - \Gamma_{\mu 0}^{\lambda} \sigma_{\lambda}^{\mu} = 0, \tag{2.28}$$

where I remind the reader that $\sigma^{\mu\nu} \equiv (\rho + P + e) u^{\mu} u^{\nu} + q^{\mu} u^{\nu} + q^{\nu} u^{\mu}$, and I shall neglect the contribution from the thermal energy density $(P + e)/\rho \ll 1$. By the same reasoning as above (equation 2.11, 2.12), the final term in this expression ($\Gamma_{\mu 0}^{\lambda} \sigma_{\lambda}^{\mu}$) is identically zero by symmetry, and thus

$$\nabla_{\mu} \left(T_{0}^{\mu} \right) = \frac{1}{\sqrt{g}} \partial_{\mu} \left(\sqrt{g} \sigma_{0}^{\mu} \right) = 0. \tag{2.29}$$

Expanding the turbulent velocity and time-averaging leaves

$$\frac{1}{\sqrt{g}} \partial_{\mu} \left(\sqrt{g} \sigma_{0}^{\mu} \right) = \frac{1}{\sqrt{g}} \frac{\partial}{\partial x^{\mu}} \Big[\sqrt{g} \rho \left(U^{\mu} U_{0} + W_{0}^{\mu} \right) + \sqrt{g} (q^{\mu} U_{0} + U^{\mu} q_{0}) \Big] = 0, \tag{2.30}$$

which upon expanding (and neglecting the asymptotically small q_0 term) is

$$U_0\left[\frac{1}{\sqrt{g}}\partial_\mu\left(\sqrt{g}\rho U^\mu\right)\right]+\rho U^r\partial_r U_0+\frac{1}{\sqrt{g}}\partial_\mu\left(\sqrt{g}\rho W_0^\mu\right)+U_0\partial_z q^z=0. \tag{2.31}$$

The first term in square brackets in the above expression is just mass conservation within the disc, and is zero. Thus, energy conservation leads to

$$\nabla_\mu\left(T_0^\mu\right)=\rho U^r\partial_r U_0+\frac{1}{\sqrt{g}}\partial_\mu\left(\sqrt{g}\rho W_0^\mu\right)+U_0\partial_z q^z=0, \tag{2.32}$$

which is of a symmetric form to the equation of conservation of angular momentum (2.23)

$$\nabla_\mu\left(T_\phi^\mu\right)=\rho U^r\partial_r U_\phi+\frac{1}{\sqrt{g}}\partial_\mu\left(\sqrt{g}\rho W_\phi^\mu\right)+U_\phi\partial_z q^z=0. \tag{2.33}$$

To make further progress I take U^0 times the energy conservation equation, add it to U^ϕ times the angular momentum conservation equation, and then height integrate. This procedure leaves

$$\begin{aligned}\Sigma U^r\left[U^0\partial_r U_0+U^\phi\partial_r U_\phi\right]+\frac{U^0}{\sqrt{g}}\partial_\mu\left(\sqrt{g}\Sigma W_0^\mu\right)+\frac{U^\phi}{\sqrt{g}}\partial_\mu\left(\sqrt{g}\Sigma W_\phi^\mu\right)&\\ =-\left(U^0U_0+U^\phi U_\phi\right)\int\partial_z q^z\,\mathrm{d}z&\end{aligned} \tag{2.34}$$

The term on the right hand side of this equation is simply equal to $\mathcal{F}_\mathcal{E}$, as $U^\mu U_\mu=-1$. Thus the left hand side of this expression is the required term. I will deal with the two remaining terms individually, starting with

$$A=\Sigma U^r\left[U^0\partial_r U_0+U^\phi\partial_r U_\phi\right]=-\Sigma U^r\left[U_0\partial_r U^0+U_\phi\partial_r U^\phi\right], \tag{2.35}$$

where I have used $\partial_r(U^\mu U_\mu)=0$ to derive the final equality. The grouping in square brackets on the right vanishes for mean circular orbits. To prove this, consider the covariant null 4-vector

$$X_\mu=g_{\alpha\beta}U^\alpha\nabla_\mu U^\beta=\frac{1}{2}\nabla_\mu(U^\alpha U_\alpha)\equiv 0. \tag{2.36}$$

The middles equality follows as $g_{\alpha\beta}$ is symmetric and $\nabla_\mu g_{\alpha\beta}=0$. Expanding the covariant derivative in the first term on the right leaves

$$X_\mu=g_{\alpha\beta}U^\alpha\partial_\mu U^\beta+g_{\alpha\beta}\Gamma^\beta_{\sigma\mu}U^\alpha U^\sigma. \tag{2.37}$$

Writing the final term explicitly

$$g_{\alpha\beta}\Gamma^{\beta}_{\sigma\mu}U^{\alpha}U^{\sigma} = \frac{1}{2}\left(\partial_{\sigma}g_{\mu\alpha} + \partial_{\mu}g_{\sigma\alpha} - \partial_{\alpha}g_{\mu\sigma}\right)U^{\sigma}U^{\alpha}. \tag{2.38}$$

The first and third terms in the above cancel by symmetry, and therefore

$$X_{\mu} = g_{\alpha\beta}U^{\alpha}\partial_{\mu}U^{\beta} + \frac{1}{2}\left(\partial_{\mu}g_{\alpha\beta}\right)U^{\alpha}U^{\beta} = 0. \tag{2.39}$$

The final term vanishes with the help of the geodesic equation for U_{μ},

$$\frac{\mathrm{d}U_{\mu}}{\mathrm{d}\tau} = \frac{1}{2}\left(\partial_{\mu}g_{\alpha\beta}\right)U^{\alpha}U^{\beta}, \tag{2.40}$$

where τ is the particles proper time. For $\mu = r$ this term must be zero for circular orbits. Hence,

$$X_{r} = g_{\alpha\beta}U^{\alpha}\partial_{r}U^{\beta} = U_{0}\partial_{r}U^{0} + U_{\phi}\partial_{r}U^{\phi} = 0, \tag{2.41}$$

and $A = 0$. Therefore the energy flux is

$$\mathcal{F}_{\mathcal{E}} = \frac{U^{0}}{\sqrt{g}}\partial_{\mu}\left(\sqrt{g}\Sigma W^{\mu}_{0}\right) + \frac{U^{\phi}}{\sqrt{g}}\partial_{\mu}\left(\sqrt{g}\Sigma W^{\mu}_{\phi}\right). \tag{2.42}$$

To simplify this expression to its final form, use the fact that $\delta\left(U^{\mu}U_{\mu}\right) = 0$ to relate the δU_{0} and δU_{ϕ} turbulent velocity fluctuations

$$U^{\mu}\delta U_{\mu} = U^{0}\delta U_{0} + U^{\phi}\delta U_{\phi} = 0 \rightarrow \delta U_{0} = -\Omega\delta U_{\phi}, \tag{2.43}$$

and thus

$$W^{\mu}_{0} = \left\langle \delta U^{\mu}\delta U_{0}\right\rangle = -\Omega\left\langle \delta U^{\mu}\delta U_{\phi}\right\rangle = -\Omega W^{\mu}_{\phi}. \tag{2.44}$$

This leads to the final result

$$\begin{aligned}\mathcal{F}_{\mathcal{E}} &= -\frac{U^{0}}{\sqrt{g}}\partial_{\mu}\left(\sqrt{g}\Sigma\Omega W^{\mu}_{\phi}\right) + \frac{U^{\phi}}{\sqrt{g}}\partial_{\mu}\left(\sqrt{g}\Sigma W^{\mu}_{\phi}\right)\\ &= -\frac{U^{0}\Omega}{\sqrt{g}}\partial_{\mu}\left(\sqrt{g}\Sigma W^{\mu}_{\phi}\right) + \frac{U^{\phi}}{\sqrt{g}}\partial_{\mu}\left(\sqrt{g}\Sigma W^{\mu}_{\phi}\right) - U^{0}\Sigma W^{r}{}_{\phi}\frac{\mathrm{d}\Omega}{\mathrm{d}r}\\ &= -\Sigma W^{r}{}_{\phi}U^{0}\frac{\mathrm{d}\Omega}{\mathrm{d}r},\end{aligned} \tag{2.45}$$

in agreement with the Page and Thorne (1974) steady state result.

2.3.2 The governing disc equation in its simplest form

The governing equation, with the radiated energy flux substituted from above, is

$$\frac{\partial \Sigma}{\partial t} = \frac{1}{U^0\sqrt{g}}\frac{\partial}{\partial r}\left(\frac{1}{U'_\phi}\left[\frac{\partial}{\partial r}\left(\sqrt{g}\Sigma W^r{}_\phi\right) - \sqrt{g}\Sigma W^r{}_\phi U_\phi U^0 \Omega'\right]\right). \tag{2.46}$$

Defining $Y \equiv \sqrt{g}\Sigma W^r{}_\phi$, and Q by $\partial_r Q \equiv -U_\phi U^0 \Omega'$, leaves

$$\frac{\partial \Sigma}{\partial t} = \frac{1}{U^0\sqrt{g}}\frac{\partial}{\partial r}\left(\frac{1}{U'_\phi}\left[\frac{\partial Y}{\partial r} + \frac{\mathrm{d}Q}{\mathrm{d}r}Y\right]\right), \tag{2.47}$$

which equals

$$\frac{\partial \Sigma}{\partial t} = \frac{1}{U^0\sqrt{g}}\frac{\partial}{\partial r}\left(\frac{e^{-Q}}{U'_\phi}\left[\frac{\partial}{\partial r}\left(Ye^{Q}\right)\right]\right). \tag{2.48}$$

The parameter Q can be determined by the following steps. Start with

$$\frac{\mathrm{d}Q}{\mathrm{d}r} \equiv -U_\phi U^0 \Omega'. \tag{2.49}$$

Substituting

$$\Omega \equiv \frac{\mathrm{d}\phi}{\mathrm{d}t} = \frac{U^\phi}{U^0}, \tag{2.50}$$

results in

$$\frac{\mathrm{d}Q}{\mathrm{d}r} = -U_\phi (U^\phi)' + U_\phi U^\phi (U^0)'/U^0. \tag{2.51}$$

For a particle undergoing circular motion in the equatorial plane,

$$U_\mu U^\mu = U_\phi U^\phi + U_0 U^0 = -1, \tag{2.52}$$

from which I substitute for $U_\phi U^\phi$ to find

$$\frac{\mathrm{d}Q}{\mathrm{d}r} = -\left(\ln U^0\right)' - \left[U_\phi (U^\phi)' + U_0 (U^0)'\right]. \tag{2.53}$$

The final term in square brackets has been shown to be zero (equation 2.41), and thus

$$\frac{\mathrm{d}Q}{\mathrm{d}r} = -\frac{\mathrm{d}}{\mathrm{d}r}\left(\ln U^0\right) \rightarrow e^{-Q} = U^0, \tag{2.54}$$

since I am free to choose $Q \rightarrow 0$ as $U^0 \rightarrow 1$. (Note that the value of the proportionality constant is not actually needed in the governing equation.)

The governing equation is therefore

$$\frac{\partial \Sigma}{\partial t} = \frac{1}{U^0\sqrt{g}}\frac{\partial}{\partial r}\left(\frac{U^0}{U'_\phi}\left[\frac{\partial}{\partial r}\left(\frac{\sqrt{g}\Sigma W^r{}_\phi}{U^0}\right)\right]\right). \tag{2.55}$$

The turbulent stress $W^r{}_\phi$ may depend on the disc's surface density (and thus implicitly on time) and so the final equation is found by noting that

$$\frac{\partial}{\partial t}\left(\frac{\sqrt{g}\Sigma W^r{}_\phi}{U^0}\right) = \frac{\sqrt{g}}{U^0}\frac{\partial \Sigma}{\partial t}\left[W^r{}_\phi + \Sigma\frac{\partial W^r{}_\phi}{\partial \Sigma}\right], \tag{2.56}$$

and so

$$\frac{\partial}{\partial t}\left(\frac{\sqrt{g}\Sigma W^r{}_\phi}{U^0}\right) = \left(\frac{1}{U^0}\right)^2\left[W^r{}_\phi + \Sigma\frac{\partial W^r{}_\phi}{\partial \Sigma}\right]\frac{\partial}{\partial r}\left(\frac{U^0}{U'_\phi}\left[\frac{\partial}{\partial r}\left(\frac{\sqrt{g}\Sigma W^r{}_\phi}{U^0}\right)\right]\right). \tag{2.57}$$

Henceforth I shall denote this governing equation as

$$\frac{\partial \zeta}{\partial t} = \mathcal{W}\frac{\partial}{\partial r}\left(\frac{U^0}{U'_\phi}\frac{\partial \zeta}{\partial r}\right), \tag{2.58}$$

where

$$\zeta \equiv \frac{\sqrt{g}\Sigma W^r{}_\phi}{U^0}, \tag{2.59}$$

and

$$\mathcal{W} \equiv \left(\frac{1}{U^0}\right)^2\left[W^r{}_\phi + \Sigma\frac{\partial W^r{}_\phi}{\partial \Sigma}\right]. \tag{2.60}$$

2.4 The turbulent stress $W^r{}_\phi$

At this stage I am yet to discuss the physical properties of the turbulent stress tensor $W^{\mu\nu}$, and in particular the key component thereof $W^r{}_\phi$. Clearly, if one is to solve the relativistic disc equation (2.58) then one must specify a closed form parameterisation of $W^r{}_\phi$. In the following subsections I summarise the general properties of the turbulent stress present in accretion discs, before discussing canonical parameterisations, and their underlying assumptions and limitations, of $W^r{}_\phi$, which allow exact solutions of equation 2.58 to be found.

2.4.1 General properties

Perhaps the simplest property of $W^r{}_\phi$ is that it acts as a diffusion coefficient of the accretion flow. This can be seen most explicitly by defining the angular-momentum-like quantity $\mathcal{J}$ by

$$\mathrm{d}\mathcal{J} \equiv \frac{U'_\phi}{U^0}\,\mathrm{d}r, \tag{2.61}$$

which transforms the governing equation into the following clearly diffusion-like form

$$\frac{\partial \zeta}{\partial t} = \mathcal{D}_\mathcal{J}\frac{\partial^2 \zeta}{\partial \mathcal{J}^2}, \tag{2.62}$$

with 'diffusion coefficient'

$$\mathcal{D}_\mathcal{J} = \frac{U'_\phi}{(U^0)^3}\left(W^r{}_\phi + \Sigma\frac{\partial W^r{}_\phi}{\partial \Sigma}\right). \tag{2.63}$$

Equation 2.62 shows that an interesting way to think about the relativistic disc evolution equation is a diffusion equation of an angular-momentum-flux-like quantity (ζ) in angular momentum space, not radius. The physics of accretion is simply the physics of the redistribution of angular momentum.

A second important property of $W^r{}_\phi$ is that at no point in the derivation of the governing equation 2.58 have I specified the underlying physical process which causes the fluctuating velocity field δU^μ. This is an important result: provided that whatever physical mechanism at play results in correlated r–ϕ fluctuations in the disc fluids velocity field, then accretion will be driven throughout the disc. The fact that the magneto-rotational instability (Balbus and Hawley 1991; Hawley and Balbus 1991) is the ultimate cause of the underlying disc turbulence need not be known in advance of qualitatively understanding relativistic accretion solutions.

Finally, and this will be expanded on later, for stable disc evolution two conditions must be met. Stable disc evolution requires $\mathcal{D}_\mathcal{J} \geq 0$ and thus the disc's angular momentum gradient must be positive $U'_\phi > 0$. This is the relativistic analogue of Rayleigh's criterion, and is satisfied at all radii exterior to the ISCO[2] $r > r_I$. Secondly, the following condition must also be met

$$W^r{}_\phi + \Sigma\frac{\partial W^r{}_\phi}{\partial \Sigma} > 0. \tag{2.64}$$

[2]In fact, this defines the ISCO radius, $U'_\phi(r_I) = 0$.

Since all physical stress models have a positive turbulent stress ($W^r{}_\phi > 0$), this is in reality more usefully phrased as

$$\frac{\partial \ln W^r{}_\phi}{\partial \ln \Sigma} > -1. \tag{2.65}$$

While the Rayleigh criterion is satisfied throughout the disc, more care is required in how this second condition is treated. As I shall now discuss, the canonical Shakura and Sunyaev (1973) stress parameterisation of $W^r{}_\phi$ does not in fact always satisfy this second stability constraint.

2.4.2 Explicit models: the Shakura-Sunyaev α-parameterisation

Essentially all analytic and semi-analytic treatments of accretion discs rely on the use of $W^r{}_\phi$, the so-called 'anomalous stress tensor' to account for the enhanced angular momentum transport and thermal energy dissipation associated with the accretion process. First invoked by Shakura and Sunyaev (1973), a measured turbulent stress tensor may now be extracted from numerical simulations of discs, as a consequence of the magnetorotational instability (Balbus and Hawley 1991). Even with explicit numerical studies however, turbulence remains at best poorly understood. There is no consensus fundamental theory that allows one, for example, to express this stress tensor in terms of background mean disc properties. That being said, to make progress analytically one must specify a disc parameter (r, Σ) dependence of $W^r{}_\phi$.

To do this I shall follow the Shakura and Sunyaev (1973) α-prescription. In the α-model, $\widetilde{W}^{r\phi}$ (note the raised indices) is defined through the phenomenological relationship:

$$\widetilde{W}^{r\phi} = \left\langle \delta v^r \delta v^\phi \right\rangle \equiv \alpha c_s^2. \tag{2.66}$$

The original Shakura and Sunyaev notation included a factor of the surface density Σ on the right[3], but more importantly, $\widetilde{W}^{r\phi}$ should not, despite the presence and placement of the indices, be regarded as a true covariant tensor (hence the tilde notation). Following the standard formalism of Shakura & Sunyaev, α in equation (2.66) is assumed to be constant throughout the disc, and c_s is the local sound speed of the orbiting gas.

Before I discuss the implications of this assumption I will take some time to discuss the justification and plausibility of this model. Shakura and Sunyaev (1973)

[3]The dimensions of the original Shakura-Sunyaev 'stress tensor' $\widetilde{W}$ was that of a dynamic, not kinematic, stress.

noted that the turbulent stress resulting from a 'turbulently enhanced kinematic viscosity' ν_t can be expressed as

$$\widetilde{W}^{r\phi} \sim \nu_t \frac{\mathrm{d}\Omega}{\mathrm{d}\ln r} \sim \nu_t \frac{v^\phi}{r} \sim c_s^2 \left(\frac{v_t}{c_s}\right), \tag{2.67}$$

where, by invoking turbulent mixing length theory, the final equalities follow from $\nu_t \sim v_t l_t$, where v_t is the 'turbulent velocity scale' and l_t the 'turbulent length scale', assumed to be roughly $l_t \sim H \sim r c_s / v^\phi$. Here H is the scale height of the disc, and the final scaling $H \sim r c_s / v^\phi$ expresses the approximate solution of hydrostatic equilibrium.

The magnetic Maxwellian stress on the disc is similarly given by

$$\widetilde{W}^{r\phi} = -\frac{B^r B^\phi}{4\pi\rho} \sim c_s^2 \left(\frac{v_A}{c_s}\right)^2, \tag{2.68}$$

where v_A is the Alfvén velocity of the disc. Thus, the total stress from turbulence and magnetic fields satisfies

$$\widetilde{W}^{r\phi} \sim \left[\frac{v_t}{c_s} + \left(\frac{v_A}{c_s}\right)^2\right] c_s^2 \sim \alpha c_s^2, \tag{2.69}$$

which defines the α parameter. It is somewhat of a leap to suggest that the α parameter must be a constant throughout the disc, particularly as both 'terms' in α depend explicitly on the local speed of sound in the disc. Nonetheless, in analytic modelling α is generally assumed to be constant, but it is important to remember that there is no compelling justification for this[4], and numerical simulations show a highly complex spatio-temporal structure for α (e.g., Nelson and Papaloizou 2003).

As noted in the first Chapter, a core result of the Shakura-Sunyaev parameterisation is the following: turbulent velocity fluctuations (I will use δv^i to indicate an 'ordinary' velocity fluctuation) will be limited by the local speed of sound within the disc $\delta v^i \lesssim c_s$, and therefore it can be deduced that $\alpha \lesssim 1$. Any super-sonic fluctuations will result in the formation of shocks, which will quickly reduce the velocity fluctuation to sub-sonic values. While this is likely true of the turbulent 'term' in 2.69, coherent magnetic fields can of course have Alfvén velocities far exceeding the local speed of sound. Provided however that the magnetic fields in accretion discs are small scale and chaotic, it is likely that the second term in 2.69 will also be $\lesssim 1$. The α-parameterisation should be considered primarily an informative scaling relationship, but is unlikely to capture

[4]It is interesting to note that in their original paper, Shakura and Sunyaev (1973) state explicitly "*In addition, the parameter α can (and must) be a function of disc radius*".

the full behaviour of MHD turbulence. For MHD turbulence, α can be thought of as an indication of the amplitude of the rms turbulent fluctuations.

Postponing further discussions regarding the solidity of the foundations provided by the α-parameterisation, I shall now compute its implications for the governing evolution equation. As noted above, $\widetilde{W}^{r\phi}$ measures correlations between "ordinary" turbulent *velocity* fluctuations, whereas $W^r{}_\phi$ measures correlations between fluctuations in the fluid angular momentum and radial velocity, a true 4-velocity correlation. The two quantities are related by (for the remainder of this section I shall be neglecting general relativistic effects and working in the Newtonian limit)

$$\widetilde{W}^{r\phi} = W^r{}_\phi / r. \tag{2.70}$$

To determine the precise (r, Σ) dependance of $W^r{}_\phi$ I start with the statement that on extended evolutionary time scales, the energy locally extracted from the disc shear must balance the locally radiated energy:

$$W^r{}_\phi \Sigma \Omega' \propto \frac{T_c^4}{\tau} \propto \frac{T_c^4}{\kappa \Sigma}. \tag{2.71}$$

Here κ is the opacity, τ the optical depth, Σ the surface density, $W^r{}_\phi$ the turbulent stress, Ω the angular frequency, and T_c the mid-plane temperature of the disc. The speed of sound within the disc is related to the dynamic disc quantities through

$$\widetilde{W}^{r\phi} = W^r{}_\phi / r \propto c_s^2 \propto T_c. \tag{2.72}$$

In the final proportionality on the right, I have used the gas pressure to compute the sound speed, an important assumption that may, as will be discussed in a later section, break down when the total pressure is dominated by radiation. In section 2.4.3, I discuss in more detail the role of a possible viscous instability that emerges from the use of radiation pressure in (2.72).

The disc scale height H is related to the disc sound speed by

$$c_s \propto H\Omega \propto T_c^{1/2}, \tag{2.73}$$

and I will assume a disc opacity of the form

$$\kappa \propto \rho^A \, T_c^{-B}, \tag{2.74}$$

which may be used for a wide range of physically plausible models, including electron scattering $A = B = 0$, or a Kramers opacity: $A = 1, B = 7/2$. The density and surface density of the disc are trivially related through the disc scale height

$$\rho \propto \Sigma/H. \tag{2.75}$$

Finally, assuming Keplerian rotation

$$\Omega \propto r^{-3/2}, \tag{2.76}$$

these relationships suffice to define the parameter dependence of the turbulent stress. Substitution of equations (2.72 – 2.76) into equation (2.71) leads to the following result

$$W^{r}_{\ \phi} \propto \Sigma^{\eta}\, r^{\mu}. \tag{2.77}$$

Where

$$\eta = (4 + 2A)/(6 + A + 2B), \tag{2.78}$$

and

$$\mu = (3 + 2B - 2A)/(6 + A + 2B). \tag{2.79}$$

Thus, bi-powerlaw turbulent stress tensors are generic 'predictions' of the α-model. As such, the turbulent stress parameterisations used in this thesis will all be of the generic form $W^{r}_{\ \phi} \propto r^{\mu}\Sigma^{\eta}$. In particular, in this Chapter I shall derive analytical and numerical solutions of equation 2.58, for (i) $\mu = \eta = 0$, (ii) $\mu \neq 0, \eta = 0$, and then (iii) $\mu \neq 0, \eta \neq 0$. The principal results of these studies do not depend sensitively on the choice of η or μ, and thus any deficiencies in the α-parameterisation are unlikely to cause major discrepancies between theory and observation.

2.4.3 (Neglecting) The Lightman-Eardley instability

An important, and possibly consequential, simplification used in this thesis (in common with many applications of time-dependent accretion theory e.g., Cannizzo et al. 1990) is the neglect of the Lightman and Eardley (1974) instability in the inner regions of the disc, where the dynamical pressure becomes radiation-dominated. If the turbulent stress is proportional to the dominant radiation pressure, as opposed to the gas pressure, the resulting sensitive dependence on temperature leads to a formal instability in α disc

models[5]. Although local 3D disc simulations with radiative hydro do exhibit unstable behaviour (Jiang et al. 2013), as do global 2D hydro simulations (Fragile et al. 2018), observations of X-ray binaries are compatible with stable thermal discs (e.g. Done et al. 2007), as are observations of tidal disruption events, which show stable thermal X-ray spectra which persist for thousands of days (Bright et al. 2018). To what extent this process manifests as a true physical instability in real discs, and what an 'instability' on top of an already turbulent flow might mean, is unclear at the present time.

The point of view adopted in this work is that the Lightman-Eardley instability, if indeed present in nature, will result in *some* reasonably well-defined stress tensor $W^r{}_\phi$, perhaps not of the explicit α-form used here, but in any case it will not completely disrupt the inner disc. The principal conclusions of this study do not appear to be sensitive to the precise functional form of $W^r{}_\phi$: so as long as there exists some self-consistent local stress tensor, neglect of the formal Lightman-Eardley instability in the first instance seems a reasonable strategy, guided principally by the observational fact that the real disc systems I am attempting to model appear to be resolutely stable.

2.4.4 The ISCO stress

While the need for some form of anomalous stress tensor has long been understood, one of its key properties — whether or not it vanishes at the ISCO — has long been a controversial theoretical question. The presence of an innermost stable circular orbit (ISCO) within a relativistic disc implies that the disc must be in effect cut-off, since gas interior to this radius, facing no angular momentum barrier, is able to plunge toward the centre. A purely viscous stress would arguably vanish at this location (e.g. Page and Thorne 1974), as it does at a free fluid boundary. It was long thought that the turbulent stress in an accretion disc was merely some sort 'turbulently enhanced' ordinary viscosity, and it was therefore assumed in early modelling that the stress must vanish in astrophysical accretion discs. This assumption has somewhat stuck.

In reality, astrophysical discs are much more likely to be dominated by a magnetic stress, it is after all the MRI which drives angular momentum transport throughout the disc. As a magnetic stress requires only correlated (radial and azimuthal) fields to be present, there is no reason for this quantity to vanish at the ISCO. It has long

[5]With $c_s^2 \propto P_{\rm rad}/\rho \propto T_c^4 H/\Sigma$, identical reasoning as above leads to $W^r{}_\phi \propto \Sigma^{-1}$ for an electron scattering opacity (the relevant opacity when radiation dominates the total disc pressure). As such, $\mathcal{D}_\mathcal{J} < 0$, and the disc is formally unstable.

been argued on theoretical grounds (Gammie 1999, Krolik 1999, Agol and Krolik 2000) that sizeable ISCO torques would result from the magnetic coupling of matter at radii interior and exterior to the ISCO. Indeed, 3D GRMHD simulations of accretion discs invariably find a non-zero ISCO stress (Shafee et al. 2008, Noble et al. 2010, Penna et al. 2010). Despite these developments, the view that the ISCO stress must vanish on dynamical grounds has retained prominent advocates.

This continued controversy is further confounded by the lack of a clear observational discriminant for or against a non-zero ISCO stress. For example, Li et al. (2005) demonstrated that the effect of a non-zero ISCO stress on the spectrum of a steady state disc is largely degenerate with the source-observer distance and mass accretion rate, two parameters that are often only poorly constrained for a particular source. It should be noted however that the argument presented by Li et al. (2005) relied on a model which was still in effect cut off at the ISCO, with no emission included from $r < r_I$. It is not clear if the value of the ISCO stress will remain observationally hard to pin down with the future inclusion of this material in more advanced models (see Chapter 5).

Clearly, the question of whether the ISCO stress is non-zero or not is one of upmost importance, particularly if one wishes to infer quantities (such as the black hole's spin) using measurements of the very innermost disc regions. In this thesis I will take as far as is possible an agnostic view of the properties of the ISCO stress, solving the governing equation 2.58 for both finite and vanishing stress (as well as many different external stress parameterisations). I will focus on determining observational discriminants between the two cases, in the hope of finding a possible route to the answer of this question which is rooted in both theory and observation. As I shall now demonstrate, unlike the case of a steady state disc, the nature of the ISCO stress can have profound influences on the global properties of an out-of-equilibrium relativistic disc.

2.5 Solving the relativistic disc equation

2.5.1 Laplace modes & a reduced disc model

To understand the properties of the solutions of the relativistic evolution equation I analyse the behaviour of the equations Laplace modes. Laplace modes are defined by a time dependence $\tilde{\zeta} \sim e^{-st}, s > 0$, and denoted with a tilde $\tilde{\zeta}$ to distinguish these modes from the full time dependent solution ζ. By definition

$$\frac{\partial \zeta(r,t)}{\partial t} \to -s\,\tilde{\zeta}(r,s). \tag{2.80}$$

Each Laplace mode then satisfies its own evolution equation

$$-s\,\tilde{\zeta}(r,s) = \mathcal{W}\,\frac{\mathrm{d}}{\mathrm{d}r}\left(\frac{U^0}{U'_\phi}\frac{\mathrm{d}}{\mathrm{d}r}\tilde{\zeta}(r,s)\right), \tag{2.81}$$

and the $\zeta(r,t)$ distribution at a specified time t is given by a superposition over all modes, with a weighting function $f(s)$:

$$\zeta(r,t) = \int_0^\infty f(s)\,e^{-st}\,\tilde{\zeta}(r,s)\;\mathrm{d}s, \tag{2.82}$$

this weighting function is set entirely by the initial conditions. As a second order ordinary differential equation, equation (2.81) will have two linearly independent solutions, which take the form of spatial amplitudes $\tilde{\zeta}_1$ and $\tilde{\zeta}_2$:

$$\tilde{\zeta}(r,s) = C_1(s)\,\tilde{\zeta}_1(r,s) + C_2(s)\,\tilde{\zeta}_2(r,s). \tag{2.83}$$

To make further progress I analyse the Laplace mode solutions of a 'reduced disc model'. This involves adopting a simple piecewise continuous form for the important angular momentum gradient U'_ϕ. The modal equation 2.81 is algebraically cumbersome, which masks some of the key physics. I proceed by splitting this modal equation into two analytically tractable equations which retain the key physical content of the full equation. The first reduced disc equation describes the disc behaviour in the near-ISCO 'strong field' regime, where relativistic dynamical effects dominate. The second describes the modal solutions to the Newtonian analogue of the evolution equation, relevant at larger radii. To distinguish between the modal solutions of these reduced equations and the full modal solution, I write the variable y as a proxy of ζ in the strong field regime, y solves the equation

$$-sy = \mathcal{W}(r \to r_I)\,\frac{\mathrm{d}}{\mathrm{d}r}\left(\frac{1}{U'_\phi(r \to r_I)}\frac{\mathrm{d}}{\mathrm{d}r}y\right), \tag{2.84}$$

and the modal solutions in the large radius limit, denoted y_N, satisfy

$$-sy_N = \frac{2\mathcal{W}}{\sqrt{GM}}\frac{\mathrm{d}}{\mathrm{d}r}\left(r^{1/2}\frac{\mathrm{d}}{\mathrm{d}r}y_N\right). \tag{2.85}$$

The vast majority of the disc is well described by the solutions of this Newtonian modal equation. The analytical procedure works as follows, equation (2.84) is solved and the inner modal solutions are found, these inner solutions depend on the properties of the stress $W^r{}_\phi$ at the ISCO, which sets the inner disc boundary condition. The outer modal equation (2.85) is then solved, the particular modal superposition in the outer regions is determined by a set of 'smooth matching conditions'. The smooth matching conditions state that at some intermediate radius r_m the inner disc and outer disc modes must have the same amplitude $y(r_m) = y_N(r_m)$ and the same gradient $y'(r_m) = y'_N(r_m)$. I will demonstrate that it is properties of the modal superposition in the outer Newtonian regions which characterise the global properties of the accretion disc. I begin below with an illustrative example.

2.5.2 The linear problem

Here, for the sake of simplicity, I shall assume a constant $W^r{}_\phi$, denoted in the model as w, (i.e., $\eta = \mu = 0$). This model is physically rather natural: it would emerge, for example, if the turbulent velocity fluctuations followed a Keplerian scaling of the form $\delta v^r \sim \delta v^\phi \sim r^{-1/2}$. A second simplification I shall make in this section is that I will assume that the black hole is non-rotating ($a = 0$) and is therefore described by the Schwarzschild metric. Neither of these simplifications effect the gross properties of the disc solutions.

Angular momentum profile

The Schwarzschild metric angular momentum gradient is

$$U'_\phi = \frac{\Omega}{2}\frac{r-6r_g}{(1-3r_g/r)^{3/2}} = \frac{\sqrt{r_g}}{2}\frac{r-6r_g}{(r-3r_g)^{3/2}}, \qquad \Omega = \sqrt{\frac{r_g}{r^3}}\,. \tag{2.86}$$

The angular momentum gradient U'_ϕ vanishes linearly at the ISCO radius $r_I = 6r_g$, and approaches $r\Omega/2$ in the Keplerian zone, $r \gg r_g$. I shall model U'_ϕ near the ISCO by its local linear form

$$U'_\phi = \sqrt{2}\Omega_I(r - r_I) \equiv \sqrt{2}\Omega_I x, \quad \text{(near ISCO)}, \tag{2.87}$$

where $\Omega_I = \sqrt{r_g/r_I^3}$ and $x = r - r_I$. In the outer disc, the usual Keplerian angular momentum gradient is recovered

$$U'_\phi = \frac{r\Omega}{2} = \frac{1}{2}\sqrt{\frac{GM}{r}}, \quad \text{(Keplerian)}. \tag{2.88}$$

The reduced model angular momentum gradient, denoted $\widetilde{U}'_\phi$, will be the piecewise continuous compilation of equations (2.87) and (2.88). Extrapolating (2.87) to the point where it matches (2.88) at the radius denoted r_m, defines $\widetilde{U}'_\phi$:

$$\widetilde{U}'_\phi = \sqrt{2}\Omega_I(r - r_I), \quad (r < r_m), \tag{2.89}$$

$$\widetilde{U}'_\phi = \frac{r\Omega}{2}, \quad (r \geq r_m). \tag{2.90}$$

Newtonian modes

For $r \geq r_m$ the modal equation is

$$-sy_N = \frac{2w}{\sqrt{GM}}\frac{\mathrm{d}}{\mathrm{d}r}\left[r^{1/2}\frac{\mathrm{d}y_N}{\mathrm{d}r}\right]. \tag{2.91}$$

Writing this equation in terms of $\xi = \sqrt{r}$ leads to

$$-\frac{s\sqrt{GM}}{2w}\xi y_N = \frac{\mathrm{d}^2 y_N}{\mathrm{d}\xi^2}, \qquad \xi \equiv r^{1/2}. \tag{2.92}$$

This equation has two linearly-independent solutions, y_+ and y_-, where[6]

$$y_\pm = \sqrt{\xi}J_{\pm 1/3}\left(\frac{2p}{3}\xi^{3/2}\right), \quad p^2 = \frac{s\sqrt{GM}}{2w}, \tag{2.93}$$

and the two functions $J_{1/3}$ and $J_{-1/3}$ are standard Bessel functions of order $1/3$ and $-1/3$ respectively. The derivation of this solution is presented in Appendix A. In general, the outer Keplerian solution will take the form of a linear superposition

$$y_N = C_1 y_- + C_2 y_+, \tag{2.94}$$

where C_1 and C_2 are constants determined by joining this outer Keplerian solution and its first derivative smoothly to the inner solution (2.97) at the matching radius r_m. The

[6]I suppress dimensional, but s-independent, multiplicative amplitudes from all of the y modal solutions in this Chapter. These factors do not affect the modal matching conditions but clutter the equations appearance. The full solution is $y_\pm = y_0 r_m^{-1/4}\sqrt{\xi}J_{\pm 1/3}\left(2p\xi^{3/2}/3\right)$ with constant y_0 which carries the dimensions of y (mass $\times$ length^2 $\times$ time^{-2}).

amplitude of the y_+ function vanishes at the origin, while the gradient of y_- vanishes at $r = 0$. I shall always write the outer Laplace mode solution in this form: the 'C_1' solution is understood to have a vanishing first derivative at the origin, while the 'C_2' solution vanishes itself at the origin. With y_N given by equations (2.93) and (2.94), standard Bessel function identities allow the important first derivative $\mathrm{d}y_N/\mathrm{d}r$ to be written as

$$\frac{\mathrm{d}y_N}{\mathrm{d}r} = \frac{p}{2}\left[-C_1 J_{2/3}\left(\frac{2p}{3}r^{3/4}\right) + C_2 J_{-2/3}\left(\frac{2p}{3}r^{3/4}\right)\right]. \tag{2.95}$$

In a strictly Newtonian system, equation (2.91) has only one solution that leaves Σ finite as $r \to 0$, the solution y_+ which vanishes linearly in ξ in this limit. In reality, an inner Kerr disc is cut-off at the ISCO, the $r = 0$ singularity is irrelevant to a relativistic calculation. In fact, the two matching constraints can only be satisfied by a superposition of both y_+ and y_-, and *it is this admixture that determines the late time behaviour of the general solution.*

Modal admixture — Finite ISCO stress

In this and the following section I calculate the coefficients C_1 and C_2 for different ISCO stresses, physical implications of these results are then discussed in section 2.5.3. For a finite ISCO stress the reduced ISCO equation reads

$$-\frac{s\sqrt{2}\Omega_I}{w}y = \frac{\mathrm{d}}{\mathrm{d}x}\left[\frac{1}{x}\frac{\mathrm{d}y}{\mathrm{d}x}\right]. \tag{2.96}$$

By making the substitution $z = x^2$, I can reduce this equation to the modified Bessel form studied in Appendix A (cf. equation 2.92), with solution $y \propto xJ_{\pm 2/3}(s^{1/2}x^{3/2})$. However, as noted in Balbus (2017) for this same problem, the solution of this equation can be equivalently written as a superposition of the first derivatives of the Airy and Bairy functions[7], which simplifies the algebra somewhat. The desired stable mode that decays exponentially inside the ISCO ($x < 0$) and is oscillatory for $x > 0$ is:

$$y = \mathrm{Ai}'(-kx), \qquad k^3 = \frac{s\sqrt{2}\Omega_I}{w}, \tag{2.97}$$

where Ai is the Airy function (Abramowitz and Stegun 1965) and Ai′ the derivative of this function with respect to its argument $\mathrm{Ai}'(\chi) \equiv \partial_\chi \mathrm{Ai}(\chi)$ where $\chi = -kx$. The Bairy

[7]The Airy and Bairy functions satisfies the differential equation $y'' - xy = 0$, and are explicitly equal (for $x < 0$) to particular superpositions of the $J_{1/3}$ and $J_{-1/3}$ Bessel functions.

function on the other hand grows exponentially for $x < 0$, and is neglected. I note that

$$\frac{\mathrm{dAi}'(-kx)}{\mathrm{d}r} = \frac{\mathrm{dAi}'(-kx)}{\mathrm{d}x} = -k\mathrm{Ai}''(-kx) = k^2 x\,\mathrm{Ai}(-kx), \tag{2.98}$$

where the prime $'$ denotes differentiation with respect to the displayed functional argument and the definition of the Airy function has been used in the final equality. I now have sufficient information to find the matching coefficients C_1 and C_2 of the outer Keplerian solution. I demand continuity of y and its first derivative $\mathrm{d}y/\mathrm{d}r$ at the matching radius r_m:

$$\frac{\mathrm{Ai}'(-kx_m)}{r_m^{3/4}} = C_1 J_{-1/3}(\tilde{p}) + C_2 J_{1/3}(\tilde{p}) \qquad \text{(continuity of y)}, \tag{2.99}$$

and

$$\frac{2k^2 x_m}{p}\mathrm{Ai}(-kx_m) = -C_1 J_{2/3}(\tilde{p}) + C_2 J_{-2/3}(\tilde{p}) \qquad \text{(continuity of dy/dr)}, \tag{2.100}$$

where to avoid a cluttered appearance in the equations I have defined $\tilde{p} \equiv 2r_m^{3/4}p/3$. I solve for C_1 and C_2:

$$C_1 = \frac{\mathrm{Ai}'(-kx_m)\ J_{-2/3}(\tilde{p})}{r_m^{3/4}\ \mathrm{Wr}} - \frac{2x_m k^2 \mathrm{Ai}(-kx_m)\ J_{1/3}(\tilde{p})}{p\ \mathrm{Wr}} \tag{2.101}$$

and

$$C_2 = \frac{\mathrm{Ai}'(-kx_m)\ J_{2/3}(\tilde{p})}{r_m^{3/4}\ \mathrm{Wr}} + \frac{2x_m k^2 \mathrm{Ai}(-kx_m)\ J_{-1/3}(\tilde{p})}{p\ \mathrm{Wr}} \tag{2.102}$$

where Wr is the Wronskian (Abramowitz and Stegun 1965) of the fractional Bessel functions:

$$\mathrm{Wr} \equiv J_{1/3}(\tilde{p})J_{2/3}(\tilde{p}) + J_{-1/3}(\tilde{p})J_{-2/3}(\tilde{p}) = \frac{3\sqrt{3}}{2\pi p r_m^{3/4}}. \tag{2.103}$$

Modal admixture — Vanishing ISCO stress

I locally modify the stress profile so that the stress tensor vanishes at the ISCO. This is done with a simple piecewise continuous parameterisation where the stress vanishes quadratically at the ICSO ($x = 0$)

$$w(r) = wx^2/x_m^2 \quad (r < r_m), \tag{2.104}$$

and then returns to its simple parameterisation in the rest of the disc

$$w(r) = w \qquad (r \geq r_m). \tag{2.105}$$

The governing modal equation is now

$$-\frac{s\sqrt{2}\Omega_I x_m^2}{w}y = x^2\frac{\mathrm{d}}{\mathrm{d}x}\left[\frac{1}{x}\frac{\mathrm{d}y}{\mathrm{d}x}\right]. \tag{2.106}$$

Making the substitution $z = x^2$, this becomes

$$-\frac{s\sqrt{2}\Omega_I x_m^2}{4w}y = z^{3/2}\frac{\mathrm{d}^2y}{\mathrm{d}z^2}. \tag{2.107}$$

The local solution near $x = 0$ is therefore a superposition of J_2 and Y_2 Bessel modes (Appendix A). The Y_2 modes however diverge at $x = 0$, rather than vanish, and so the near-ISCO solution is

$$y = xJ_2(2\sqrt{qx}), \quad q = 2\sqrt{2}\,s\Omega_I x_m^2/w, \tag{2.108}$$

where J_2 is the Bessel function of order 2. Using (Abramowitz and Stegun 1965):

$$\frac{\mathrm{d}y}{\mathrm{d}r} = \sqrt{qx}J_1(2\sqrt{qx}), \tag{2.109}$$

the system of equations to be solved is now:

$$\frac{x_m J_2(2\sqrt{qx_m})}{r_m^{3/4}} = C_1 J_{-1/3}(\tilde{p}) + C_2 J_{1/3}(\tilde{p}) \qquad \text{(continuity of y)}, \tag{2.110}$$

and

$$\frac{2\sqrt{qx_m}J_1(2\sqrt{qx_m})}{p} = -C_1 J_{2/3}(\tilde{p}) + C_2 J_{-2/3}(\tilde{p}) \qquad \text{(continuity of dy/dr)}. \tag{2.111}$$

This is identical to the system (2.99) and (2.100) with $x_m J_2$ replacing Ai' and $\sqrt{qx_m}J_1$ replacing $k^2 x_m \mathrm{Ai}$. The solution of this system is

$$C_1 = \frac{x_m J_2(2\sqrt{qx_m})\ J_{-2/3}(\tilde{p})}{r_m^{3/4}\ \mathrm{Wr}} - \frac{2\sqrt{qx_m}J_1(2\sqrt{qx_m})\ J_{1/3}(\tilde{p})}{p\ \mathrm{Wr}} \tag{2.112}$$

and

$$C_2 = \frac{x_m J_2(2\sqrt{qx_m})\ J_{2/3}(\tilde{p})}{r_m^{3/4}\mathrm{Wr}} + \frac{2\sqrt{qx_m}J_1(2\sqrt{qx_m})\ J_{-1/3}(\tilde{p})}{p\mathrm{Wr}} \tag{2.113}$$

2.5.3 Physical implications

I am interested in the the late time modal superposition of the outer Newtonian disc regions. At large times ($t \to \infty$) a superposition of modes with time dependence e^{-st} will be dominated by contributions from small s. I am therefore interested in the behaviour of the ratio C_1/C_2 in the limit $s \to 0$. I make use of the following small argument expansions

$$\lim z \to 0: \quad \mathrm{Ai}'(-z) \sim \mathrm{cst},\ \mathrm{Ai}(-z) \sim z,\ J_v(z) \sim z^v \quad (\text{for all } v). \tag{2.114}$$

The s scalings of the relevant parameters are

$$p \sim s^{1/2},\ q \sim s,\ k \sim s^{1/3}, \tag{2.115}$$

meaning

$$\lim s \to 0: \quad \mathrm{Ai}'(-kx_m) \sim \mathrm{cst},\ \mathrm{Ai}(-kx_m) \sim s^{1/3},\ J_v \sim s^{v/2}\ (\text{for all } v)\ . \tag{2.116}$$

The finite ISCO stress modal admixture, in the small s limit is

$$\frac{C_1}{C_2} = \frac{p\ \mathrm{Ai}'(-kx_m)\ J_{-2/3}(\tilde{p}) - 2r_m^{3/4}x_m k^2 \mathrm{Ai}(-kx_m)\ J_{1/3}(\tilde{p})}{p\ \mathrm{Ai}'(-kx_m)\ J_{2/3}(\tilde{p}) + 2r_m^{3/4}x_m k^2 \mathrm{Ai}(-kx_m)\ J_{-1/3}(\tilde{p})}$$
$$\sim \frac{s^{1/2}s^{-1/3} + s^{2/3}s^{1/3}s^{1/6}}{s^{1/2}s^{1/3} + s^{2/3}s^{1/3}s^{-1/6}} \sim s^{-2/3}, \tag{2.117}$$

the $\mathrm{Ai}'\ J_{-2/3}$ grouping is the dominant term for small s, and so therefore is the C_1 mode. When the inner ISCO boundary hosts a non-vanishing stress, the late time behaviour of the outer Keplerian zone is therefore dominated by the *negative index* $J_{-1/3}$ modes. However, when the stress vanishes at the ISCO

$$\frac{C_1}{C_2} = \frac{px_m J_2(2\sqrt{qx_m})\ J_{-2/3}(\tilde{p}) - 2r_m^{3/4}\sqrt{qx_m}J_1(2\sqrt{qx_m})\ J_{1/3}(\tilde{p})}{px_m J_2(2\sqrt{qx_m})\ J_{2/3}(\tilde{p}) + 2r_m^{3/4}\sqrt{qx_m}J_1(2\sqrt{qx_m})\ J_{-1/3}(\tilde{p})}$$
$$\sim \frac{s^{1/2}s^{-1/3}s + s^{1/2}s^{1/2}s^{1/6}}{s^{1/2}s^{1/3}s + s^{1/2}s^{1/2}s^{-1/6}} \sim s^{1/3}. \tag{2.118}$$

Now the dominant term for small s is the $J_1 J_{-1/3}$ group in the C_2 coefficient. This in turn means that the dominant contributing modes in the Keplerian zone are *positive* indexed, $J_{1/3}$ modes.

This is a result with real physical significance . The dominant mode in the outer Keplerian regions of the disc is critically dependent on the properties of the stress at the ISCO. For a finite ISCO stress and large times

$$y_N \to y_- = \sqrt{\xi}\, J_{-1/3}\left(\frac{2p}{3}\xi^{3/2}\right), \tag{2.119}$$

whereas for a vanishing ISCO stress

$$y_N \to y_+ = \sqrt{\xi}\, J_{1/3}\left(\frac{2p}{3}\xi^{3/2}\right). \tag{2.120}$$

The superposition integral (Gradshteyn and Ryzhik 1980)

$$\int_0^\infty J_v(\sqrt{s}X)J_v(\sqrt{s}X_0)e^{-st}\,\mathrm{d}s = \frac{1}{t}\exp\left(\frac{-X^2-X_0^2}{4t}\right) I_v\left(\frac{XX_0}{2t}\right), \tag{2.121}$$

demonstrates how to construct a Green's function solution for the J_v modes. Here v is any complex number whose real part exceeds -1, and I_v is the standard modified Bessel function. The right side is proportional to a delta function $\delta(X - X_0)$ as $t \to 0$, a result that is independent of v. Note that while I can always multiply $y_\pm$ by an arbitrary function of s and retain a true mode (this amounts to changing the initial condition of the disc), the particular Green's function superposition (2.121) requires a Bessel function of the form shown above with no s-dependent coefficient. The late time $t \to \infty$ asymptotic behaviour of the I_v function

$$\lim z \to \infty : I_v(1/z) \sim 1/z^v, \tag{2.122}$$

leads to a time dependence in the surface density scaling as

$$\Sigma \sim \frac{1}{t^{1+v}}. \tag{2.123}$$

The luminosity emergent from a thin disc is proportional to the integral of the locally liberated flux $\mathcal{F}_\mathcal{E}$ over the entirety of the emitting disc surface (presented here in the Newtonian limit)

$$L_{\rm bol} \propto 2\pi \int_0^\infty R\,\mathcal{F}_\mathcal{E}\,\mathrm{d}R, \qquad \mathcal{F}_\mathcal{E} = -\Sigma W^r{}_\phi \Omega'. \tag{2.124}$$

As the surface density is the only quantity that varies with time in the emission integral, $t^{-(1+v)}$ is also the late time power law time dependence of the total luminosity $L_{\rm bol}$. But the dominant modes for different ISCO stresses have Bessel function indices

differing by a sign. This is then a direct observational prediction, the luminosity of transient relativistic discs will have a time dependence

$$L_{\rm bol}(t) \sim 1/t^{1\pm v}, \tag{2.125}$$

where, crucially, the solutions take a + for a vanishing ISCO stress, and a − for finite ISCO stress. For the specific model studied in this section, a finite ISCO stress disc would have an evolving luminosity following $L_{\rm bol} \sim t^{-2/3}$, whereas a vanishing ISCO stress disc would satisfy $L_{\rm bol} \sim t^{-4/3}$.

It is important to note from the start here that there is something peculiar about the finite ISCO stress solutions. This can be most easily seen by computing the total energy radiated from the finite ISCO stress disc solutions, and noting that it diverges

$$E_{\rm rad}(t) = \int_0^t L_{\rm bol}(t')\,{\rm d}t' \sim t^{+1/3} \to \infty \text{ as } t \to \infty. \tag{2.126}$$

Clearly, one would expect a finite amount of energy to be released from the accretion of a disc with finite mass (like the Green's function solutions considered here), and thus some approximation in the solution must ultimately be breaking down. I will return to this point after extending the analysis of the previous sections to the more general cases of bi-power law turbulent stress tensors, $W^r{}_\phi \propto r^\mu \Sigma^\eta$.

2.5.4 Extension to radial power-law turbulent stress $W^r{}_\phi \propto r^\mu$

The modal solutions in the large radius limit satisfy equation 2.85

$$-sy_N = \frac{2\mathcal{W}}{\sqrt{GM}}\frac{\rm d}{{\rm d}r}\left(r^{1/2}\frac{\rm d}{{\rm d}r}y_N\right). \tag{2.127}$$

which I now analyse with a generalised turbulent stress model: stresses which follow a power-law in radius:

$$\mathcal{W} = w\left(\frac{r}{r_m}\right)^\mu. \tag{2.128}$$

This model could, for example, be used to represent the stress resulting from a simple constant coefficient of kinematic viscosity ν model (with $\mu = -1/2$). Defining $\xi = \sqrt{r}$ once again leaves

$$\frac{{\rm d}^2 y_N}{{\rm d}\xi^2} + \frac{s}{\bar{w}}\xi^{1-2\mu}y_N = 0, \tag{2.129}$$

where $\bar{w} \equiv 2wr_m^{\mu}/\sqrt{GM}$. I show in Appendix A that the solution to the differential equation of the form

$$\frac{\mathrm{d}^2u}{\mathrm{d}z^2} + bz^m u = 0, \tag{2.130}$$

for $b > 0$, is given by

$$u = z^{\frac{1}{2}} J_{\pm\frac{1}{m+2}}\left(\frac{2\sqrt{b}}{m+2} z^{\frac{m+2}{2}}\right). \tag{2.131}$$

Thus the Newtonian equation has the following modal solution

$$y_N = \xi^{\frac{1}{2}} J_{\pm\frac{1}{3-2\mu}}\left(\frac{2}{3-2\mu}\left(\frac{s}{\bar{w}}\right)^{\frac{1}{2}} \xi^{\frac{3-2\mu}{2}}\right) \tag{2.132}$$

Finally, after re-substituting $\xi = \sqrt{r}$, the full solution is

$$y_N = r^{\frac{1}{4}}\left[C_2 J_{\frac{1}{4v}}\left(\frac{1}{2v}\left(\frac{s}{\bar{w}}\right)^{\frac{1}{2}} r^v\right) + C_1 J_{-\frac{1}{4v}}\left(\frac{1}{2v}\left(\frac{s}{\bar{w}}\right)^{\frac{1}{2}} r^v\right)\right] \tag{2.133}$$

with[8]

$$v = (3-2\mu)/4. \tag{2.134}$$

By following identical reasoning as in the above section I can determine the late time behaviour of the bolometric luminosity of these thin disc solutions. The C_2 Newtonian modes once again dominate in the presence of a vanishing ISCO stress, while the C_1 mode dominates in a finite ISCO stress disc. Once again, the evolving surface density is the only time dependent quantity in the disc luminosity integral, and so I find a late-time power-law dependence of the luminosity of

$$L_{\mathrm{bol}} \sim \frac{1}{t^{1\pm 1/4v}}, \tag{2.135}$$

or equivalently

$$L_{\mathrm{bol}} \sim t^{-\left(\frac{3-2\mu\pm 1}{3-2\mu}\right)}, \tag{2.136}$$

where it is understood that one should take '+' for a vanishing ISCO stress, and '−' for a finite ISCO stress.

[8]The special case of $\mu = 3/2$ (when $v \to \infty$) corresponds to the Euler-Cauchy differential equation: $y_N'' + (s/\bar{w})y_N/\xi^2 = 0$, with solutions which depend on the amplitude of s. Define $m_{\pm} \equiv \left(1 \pm \sqrt{1 - 4s/\bar{w}}\right)/2$, then $y_N = c_1\xi^{m_-} + c_2\xi^{m_+}$ for $s < \bar{w}/4$, $y_N = c_1\xi^{1/2} + c_2\ln(\xi)\xi^{1/2}$ for $s = \bar{w}/4$, and $y_N = c_1\xi^{1/2}\cos(\ln(\xi)\sqrt{s/\bar{w} - 1/4}) + c_2\xi^{1/2}\sin(\ln(\xi)\sqrt{s/\bar{w} - 1/4})$ for $s > \bar{w}/4$. For large times ($s \to 0$) I recover $y_N \to c_1 + c_2 r^{1/2}$, in common with all of the Bessel function solutions.

2.6 Extension to the non-linear problem

The disc evolution equation in the linear regime (with a turbulent stress independent of disc density) has fortunate analytical properties: I am able to write down exact Bessel function solutions of the inner and outer Laplace-mode equations. With the modal Bessel function solutions at hand, I am then able to solve exactly the modal matching conditions, and determine the late-time behaviour of the disc as a whole.

It is likely however that the turbulent stress in a real accretion disc will have some dependence on the mean thermodynamic properties of the disc itself. Thus, the solutions of the disc equations in the non-linear regime form an important addition to this study. As demonstrated in section 2.4, the simple α-model of disc turbulence results in a bi-power-law dependence of the turbulent stress

$$W^{r}_{\ \phi} \propto r^{\mu}\Sigma^{\eta}, \tag{2.137}$$

and therefore represents an interesting and physically motivated example of the non-linear regime. I remind the reader that the two stress indices η and μ are not, in a formal α model, free parameters, but are determined solely by the dominant source of pressure and opacity within the disc. I shall however solve the problem of general η and μ, to highlight the lack of sensitivity of the properties of the disc to the exact stress parameterisation.

The surface density dependence of the turbulent stress means that simple and exact Green's function solutions no longer exist for each of the inner and outer modal equations. However, self-similar solutions of the non-linear disc evolution equation in the Newtonian limit have been derived and discussed by a number of authors in the early days of thin disc theory (Lynden-Bell and Pringle 1974, Pringle 1991, Cannizzo et al. 1990). I therefore approach the non-linear problem differently to the linear problem: I examine the properties of these existing Newtonian self-similar solutions, of which there are two (analogous to the C_1 and C_2 solutions). By identifying these non-linear solutions with their appropriate Linear Green's function cousins, I can infer the ISCO-stress dependence of the outer disc solutions in the non-linear regime.

2.6.1 General properties of the Newtonian self-similar solutions

The self-similar solutions of the non-linear *Newtonian* limit of the disc evolution equation exist if the turbulent stress is parameterised in the bi-power law form $W^r_{\ \phi} \propto r^\mu \Sigma^\eta$. The solutions are conveniently expressed in terms of a dimensionless radius x and time τ:

$$x = r/r_0, \quad \tau = wt/\left(2\sqrt{GMr_0^3}\right). \tag{2.138}$$

(For the present r_0 is fiducial, but will be defined as part of the initial disc condition in section 2.7.) The mathematical solutions then have the general form (Pringle 1991)

$$\Sigma = \Sigma_0 \, f(\xi) \, x^{-3/2} \, \tau^{-\chi}, \tag{2.139}$$

$$f(\xi) = \xi^\omega (1 - k\xi^\theta)^{1/\eta}, \tag{2.140}$$

$$\xi = \sqrt{x} \, \tau^{-\lambda}. \tag{2.141}$$

The five parameterisation constants $(\theta, \omega, k, \chi, \lambda)$ all depend upon η and μ, Σ_0 is a constant scaling factor, and there are two different self-similar solutions of this form, analogous to the C_1 and C_2 solutions, that pertain to different inner boundary conditions.

These self-similar solutions are *exact* solutions of the non-linear Newtonian evolution equation in their own right, but they are not the most general, and they may be expected to be a good description of an evolving physical disc only at later times. In effect, they govern the behaviour of the disc once the memory of the initial conditions has been lost. The singular behaviour of these solutions at early times ($t \to 0$) is therefore not a concern.

2.6.2 ISCO feedback: C_1 solutions

The self-similar solutions analogous to the C_1 Green's function solutions are those with vanishing inner radial derivative, and are generally discarded in studies of Newtonian discs. These self-similar solutions are associated (in a Newtonian setting) with a hard inner torque, and have a radial velocity which falls to zero at the inner disc edge. The disc is then completely stalled, and is outflowing at all radii.

The five parameters which describe the self-similar solution (equation 2.139) satisfying the finite stress boundary condition are given explicitly by:

$$\theta = (5\eta + 3 - 2\mu)/(\eta + 1), \tag{2.142}$$

$$\omega = (3\eta + 1 - 2\mu)/(\eta + 1), \tag{2.143}$$

$$k = \eta/[(4\eta + 3 - 2\mu)(5\eta + 3 - 2\mu)], \tag{2.144}$$

$$\lambda = 1/(4\eta + 3 - 2\mu), \tag{2.145}$$

$$\chi = 1/(4\eta + 3 - 2\mu). \tag{2.146}$$

This is mathematically equivalent to the Pringle (1991) solutions, rewritten in the notation of this thesis. At late times, the time dependence of the luminosity follows the leading order behaviour of the only time dependent terms in the disc luminosity integral: the combination $\Sigma W^r{}_\phi \propto \Sigma^{1+\eta}$. Noting that for physical models of the turbulent stress $\lambda B > 0$, at large times ($\xi = \sqrt{x}\tau^{-\lambda} \ll 1$) the self-similar function $f(\xi) = \xi^\omega(1 - k\xi^\theta)^{1/\eta} \to \xi^\omega$ over the regions of the disc responsible for the bulk of the luminosity. Thus the leading order behaviour at large times is

$$L(t) \propto \tau^{-(1+\eta)(\omega\lambda+\chi)} \sim t^{-(4\eta+2-2\mu)/(4\eta+3-2\mu)}. \tag{2.147}$$

In terms of the opacity indices A and B, this is

$$L(t) \sim t^{-(22+14A)/(28+15A+2B)}. \tag{2.148}$$

For example, an electron scattering opacity ($A = B = 0$) leads to a power law index of $-11/14 \approx -0.79$. Similarly, a disc dominated by Kramers opacity ($A = 1,\ B = 7/2$) leads to a power law index of $-18/25 = -0.72$. The index is not highly sensitive to the scattering physics, and is robustly less than unity.

2.6.3 Standard accretion: C_2 solutions

If the turbulent stress vanishes at the ISCO, then so must the local surface density and luminosity. In an early study of disc models for the late time luminosity arising from tidal disruption events, this class of self-similar solution was analysed by Cannizzo et al. (1990). This self-similar solution corresponds to the C_2, positive index, Bessel

function of the linear analysis. The self-similar parameters of this class of solutions are:

$$\theta = (4\eta + 3 - 2\mu)/(\eta + 1), \tag{2.149}$$

$$\omega = (3\eta + 2 - 2\mu)/(\eta + 1), \tag{2.150}$$

$$k = \eta/[(4\eta + 3 - 2\mu)(5\eta + 3 - 2\mu)], \tag{2.151}$$

$$\lambda = 1/(5\eta + 3 - 2\mu), \tag{2.152}$$

$$\chi = 2/(5\eta + 3 - 2\mu). \tag{2.153}$$

Identical analysis as above shows that at late times the luminosity follows a power law decline:

$$L(t) \propto \tau^{-(1+\eta)(\omega\lambda+\chi)} \sim t^{-(5\eta+4-2\mu)/(5\eta+3-2\mu)}, \tag{2.154}$$

or equivalently

$$L(t) \sim t^{-(38+18A+4B)/(32+17A+2B)}. \tag{2.155}$$

For the fiducial cases of electron scattering or Kramers opacity, the indices are $-19/16 \approx -1.19$ and $-5/4 = -1.25$ respectively.

It is interesting to note that Cannizzo et al. set the emitted luminosity proportional to the rate of change of disc mass $\dot{M}$, whereas I have performed a direct calculation of the locally emitted energy. There is an exact agreement between our two methods for the vanishing stress case. The case of a finite ISCO stress however, essentially a model with feedback, requires an explicit calculation of the luminosity.

2.6.4 Recovery of linear theory from non-linear theory

The large-time results of my linear analysis are recovered from these self-similar solutions in the formal $\eta \to 0$ limit. In this limit some care is required with handling the self-similar function

$$f(\xi) = \xi^{\omega}(1 - k\xi^{\theta})^{1/\eta}. \tag{2.156}$$

In both the finite and vanishing stress cases as $\eta \to 0$ the coefficient $k \to 0$. Simultaneously the exponent of $f(\xi)$ diverges, so that some additional attention is required. This involves making use of the well-known definition of the exponential function

$$\lim_{l\to\infty} (1 + X/l)^{l} = e^{X}. \tag{2.157}$$

Using this, I rewrite the function $f(\xi)$ in equation (2.139) in a form appropriate for the linear case

$$f(\xi) = \xi^{\omega}(1 - k\xi^{\theta})^{1/\eta} \to \xi^{\omega} \exp\left[-\frac{\xi^{\theta}}{(3-2\mu)^2}\right]. \tag{2.158}$$

Using the above result, equation (2.139) becomes:

$$\Sigma \propto \frac{r^{-(\mu+3/4)}}{\tau} \exp\left[-\frac{(r/r_0)^{2v}}{(3-2\mu)^2\ \tau}\right] \frac{r^{\pm 1/4}}{\tau^{\pm 1/4v}}, \tag{2.159}$$

where the $+/-$ sign is taken for the C_2/C_1 solutions respectively, and $v \equiv (3-2\mu)/4$ as defined in equation 2.133. Apart from a trivial difference in definition of τ, this is exactly the expression for the late time expansion of the Green's function solutions of the linear evolution equation in the linear regime, which I now prove. The dominant Bessel mode at late times in the Newtonian disc regions is always of the form

$$y_N = r^{\frac{1}{4}} J_{\pm\frac{1}{4v}}\left(\frac{1}{2v}\left(\frac{s}{\bar{w}}\right)^{\frac{1}{2}} r^{v}\right), \tag{2.160}$$

superimposing modes using equation 2.121, leaves:

$$\begin{aligned}\zeta(r,t) = C\int_0^{\infty} r^{\frac{1}{4}} J_{\pm\frac{1}{4v}}\left(\frac{1}{2v}\left(\frac{s}{\bar{w}}\right)^{\frac{1}{2}} r^{v}\right) J_{\pm\frac{1}{4v}}\left(\frac{1}{2v}\left(\frac{s}{\bar{w}}\right)^{\frac{1}{2}} r_0^{v}\right) \exp(-st)\,\mathrm{d}s \\ = C'\frac{r^{1/4}}{t}\exp\left(\frac{-(r/r_0)^{2v}-1}{\tau}\right) I_{\pm\frac{1}{4v}}\left(\frac{2r}{r_0\tau}\right),\end{aligned} \tag{2.161}$$

where C and C' are dimensional constants, and $\tau = (3-2\mu)^2 wt/\left(2\sqrt{GMr_0^3}\right)$. Thus at large times

$$\Sigma(r, t\to\infty) \propto \zeta(r, t\to\infty) r^{-(1+\mu)} \propto \frac{r^{-(\mu+3/4)}}{\tau}\exp\left[-\frac{(r/r_0)^{2v}}{\tau}\right]\frac{r^{\pm 1/4}}{\tau^{\pm 1/4v}}. \tag{2.162}$$

Where I have made use of the result $\lim z \to \infty : I_b(1/z) \sim 1/z^b$. Even though no information of the initial condition is explicitly present in these self-similar solutions, the exact late time behaviour of an initially narrow disc centred at a distance r_0 from the black hole is recovered.

2.7 Numerical verification of analytical results

The purpose of this section is to verify the key results of the proceeding analytical analysis, namely: 1. That there exists a dichotomy in the late-time behaviour of thin Kerr discs, controlled by the properties of the turbulent stress at the ISCO, and 2. that the precise late-time luminosity decay index n relates to the stress parameters η and μ (or equivalently the opacity variables A and B) through equations 2.148 & 2.155. Thirdly, and more generally, these solutions represent the first comprehensive numerical analysis of the global time-dependent properties of thin discs evolving in the full Kerr metric, extending previous simpler analysis (Garofalo and Reynolds 2005).

The mathematical problem I solve is that of the evolution of a very compact Gaussian ring, in effect the Green's function solution. While the short term evolution depends upon the initial radius chosen, the long term evolution of the extended disc does not.

2.7.1 Numerical formulation

I begin with a summary of the algorithm used to find the numerical solutions of the disc evolution equation. The interested reader will find technical details discussed in Appendix B. Some care is needed in handling the numerically singular behaviour near the ISCO, where U'_ϕ vanishes. The governing equation to be solved is

$$\frac{\partial \zeta}{\partial t} = \mathcal{W} \frac{\partial}{\partial r} \left(\frac{U^0}{U'_\phi} \frac{\partial \zeta}{\partial r} \right), \tag{2.163}$$

where

$$\zeta \equiv \frac{\sqrt{g} \Sigma W^r{}_\phi}{U^0}, \tag{2.164}$$

and

$$\mathcal{W} \equiv \left(\frac{1}{U^0} \right)^2 \left[W^r{}_\phi + \Sigma \frac{\partial W^r{}_\phi}{\partial \Sigma} \right] = (1+\eta) \left(\frac{1}{U^0} \right)^2 W^r{}_\phi, \tag{2.165}$$

where the final equality holds for the choice of $W^r{}_\phi \propto r^\mu \Sigma^\eta$. Numerically, I solve this equation using finite difference techniques, discretising the radial and temporal grids $\zeta(r,t) = \zeta(n \times \delta r, j \times \delta t) \equiv \zeta^n_j$, before approximating the radial and temporal gradients using the implicit-centred-finite-difference and forward-finite-difference approximations respectively. I use the (unconditionally stable) implicit finite difference method, and thus the resulting numerical equations require a tri-diagonal matrix to be inverted at each time-step. This was performed using the standard Thomas algorithm. For

the linear $\eta = 0$ stress parameterisation, the 'simple' implicit method can be used. However, for α-disc models, account needs to be taken of the non-linear character of the equation, and a 'predictor-corrector' implicit method must be used. Each algorithm is presented explicitly in Appendix B.

2.7.2 Initial condition

Each run presented in this section has as an initial condition a Gaussian ring. Explicitly, the initial condition is:

$$\Sigma(r, t = 0) = \Sigma_0 \exp\left[-\frac{(r - r_0)^2}{d^2}\right]. \tag{2.166}$$

The central radius r_0 is set to $15r_g$, roughly the tidal radius of a solar mass star around a 4×10^6 solar mass black hole. With r_0 set, Σ_0 and d are related, in a real disc, by the initial disc mass. I set the initial spread to $d = 3.165$ gravitational radii. The solutions of the equation are trivially scaleable, the amplitude Σ_0 cancels simply from both sides of equation 2.163, and was set to 1 in code units. While the short-term evolution depends upon the initial radius and dispersion of debris, I have verified numerically that the long-term evolution of the extended disc does not. The solutions in this section should be considered representative of more general Kerr thin disc solutions.

2.7.3 ISCO boundary conditions

At the inner edge of the evolving disc, corresponding to the ISCO, a boundary condition must be enforced, the precise nature of which depends upon the behaviour of the ISCO turbulent stress. It is straightforward to show that equation (2.163) may be rearranged to give:

$$U'_\phi \left[U'_\phi \dot{\zeta} - \mathcal{W} U^0 \zeta'' + \mathcal{W}\left(U^0\right)' \zeta'\right] + \mathcal{W} U^0 U''_\phi \zeta' = 0. \tag{2.167}$$

(Here, a prime denotes a radial r derivative and a dot a coordinate time t derivative.) As $U'_\phi(r_I) = 0$, if $\mathcal{W}(r_I) \neq 0$ this equality can be satisfied at the ISCO if and only if $\zeta'(r_I) = 0$. Thus, under the usual circular orbit assumption, the requirement that the first derivative of ζ vanishes at the ISCO is a generic requirement for any finite ISCO stress. Numerically, the value of ζ at the innermost (ISCO) grid point is set equal to its value at the adjacent external grid point. In the case of vanishing stress, $\mathcal{W}(r_I) = 0$, the appropriate boundary condition is $\zeta(r_I) = 0$.

2.7.4 Stress parameterisation

I solve equation 2.163 numerically for various different parameterisations of the turbulent stress behaviour: an α-model with electron scattering and Kramer's opacity, with either vanishing or finite ISCO stress, and more general phenomenological linear model $W^r{}_\phi \propto r^\mu$. In the "standard model", the disc is dominated by electron scattering opacity and gas pressure. In this case, the opacity is a constant κ_0, with $A = B = 0$ in equation (2.78), which implies

$$W^r{}_\phi = w \left(\frac{\Sigma}{\Sigma_0}\right)^{2/3} \left(\frac{r}{r_0}\right)^{1/2}. \tag{2.168}$$

On the other hand, the Kramer's opacity model assumes free-free or bound-free scattering throughout the disc. The functional dependence of the opacity on temperature and density is $A = 1,\ B = 7/2$ (equation 2.78). This implies

$$W^r{}_\phi = w \left(\frac{\Sigma}{\Sigma_0}\right)^{3/7} \left(\frac{r}{r_0}\right)^{4/7}. \tag{2.169}$$

In both of these expressions w is a scaling parameter which determines the length of the viscous timescale (equation 2.138), and was also set to $w = 1$ in code units (this merely sets the length of the codes δt). As both stress parameterisations depend on a positive power of the surface density, it is sufficient to set the surface density to zero at the ISCO to enforce a vanishing stress boundary condition.

2.7.5 Numerical results: summary and discussion

I have solved numerically for the time-dependent solutions of equation (2.163), the relativistic thin disc equation. Two different inner boundary conditions were explored, that of vanishing stress at the ISCO and that of non-zero ISCO stress. For the former ζ vanishes at the ISCO, whereas for the latter the radial gradient of ζ vanishes.

A representative evolving disc density profile is shown in Figure 2.1, for a turbulent stress parameterisation $W^r{}_\phi = w = \text{cst}$, and a finite ISCO stress. At early times, the disc spreads both radially inward and outward, until the disc surface density reaches a maximum at $t \simeq t_{\text{visc}}$. After this point the surface density at the ISCO gradually declines, and the angular momentum of the accreted material is slowly passed out to the outer disc regions, which gradually spread to larger and larger radii.

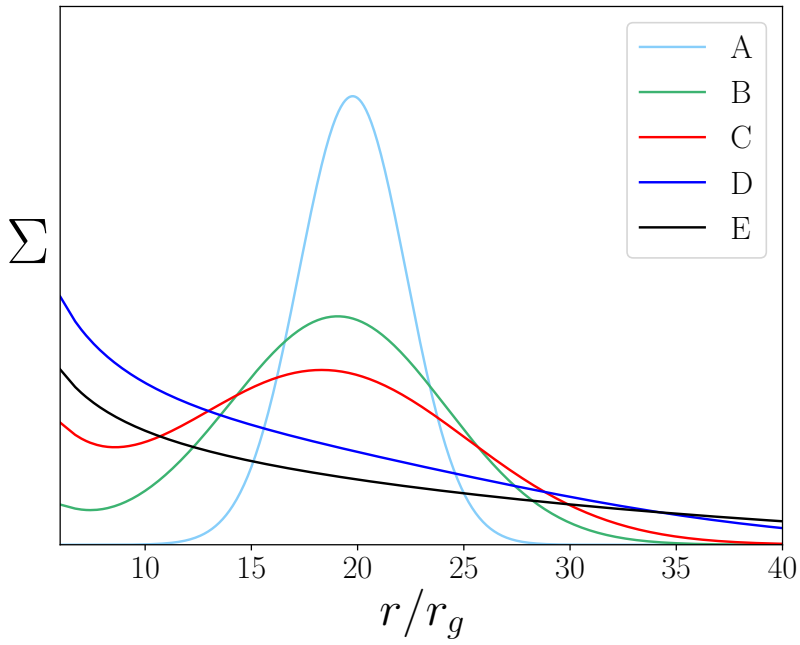

Figure 2.1: Evolution of the disc surface density (arbitrary units) in the Schwarszchild metric. The lines A to E are at progressively later times, showing the initial inwards drift of debris before the ISCO surface density decreases with time. The dimensionless times (equation 2.138) for the different stages of evolution are: $\tau = 0.06(\mathrm{A}), 0.24(\mathrm{B}), 0.43(\mathrm{C}), 1.84(\mathrm{D}), 6.06(\mathrm{E})$.

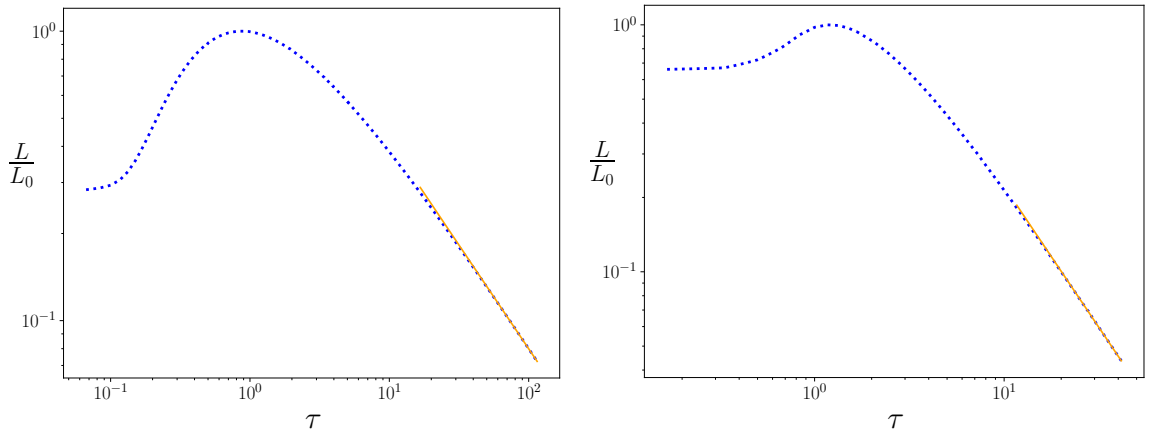

Figure 2.2: The Luminosity $L(t)$ for the 'standard model' of disc turbulence (a gas pressure dominated α model with electron scattering opacity, equation 2.168), based on solving the full Kerr equation (2.163). Left: Finite ISCO stress, Right: Vanishing ISCO stress. Both profiles are well fit by a (straight line) power law at late times, $L \sim t^n$. The fitted late time index for a finite ISCO stress is $n = -0.72$, while an index of $n = -1.14$ was found for the case of a vanishing ISCO stress. The dimensionless viscous time (2.138) is plotted on the horizontal axis. Numerical solutions were found for black hole angular momentum $a/r_g = 0.9$.

	Finite ISCO Stress		Vanishing ISCO Stress	
	n (num)	n (eq. 2.148)	n (num)	n (eq. 2.155)
Standard Model	-0.72	-0.79	-1.14	-1.19
Kramers Opacity	-0.66	-0.72	-1.25	-1.25

Table 2.1: Comparison between late time numerically determined luminosity decay indices n (num) and the analytical n values from equations (2.148) and (2.155). $W^r{}_\phi$ is given either by electron scattering "Standard Model" (equation 2.168), or by Kramer's opacity (equation 2.169). Numerical solutions were found for blackhole angular momentum $a/r_g = 0.9$.

Figure 2.2 show two example light curves for the case of electron-scattering opacity with the stress remaining finite (left panel) or vanishing (right panel) at the ISCO. Both light curves are normalised by their respective peak values. Note however that both solutions have identical initial conditions (and luminosities at $t \ll t_{\rm visc}$), and so the finite ISCO stress solutions are a factor $\sim 2-3$ times more luminous at peak.

I find two very distinct late time behaviours for the integrated luminosity $L(t)$: the finite stress solutions fall off less rapidly than t^{-1}; the vanishing stress solutions fall off more rapidly than t^{-1}. This is insensitive to how the stress is modelled exterior to the ISCO. Examination of equations (2.147) and (2.154) shows that this bimodal behaviour in late time luminosity decay indices can be explained purely in terms of which set of self-similar solutions are present in the late time Newtonian disc regime. This is a direct consequence of the properties of the turbulent stress at the ISCO.

Table 2.1 presents a comparison between analytical predictions and numerical solutions for the four different turbulent stress parameterisations considered in this section. Excellent general agreement between prediction and simulations is found. An exact match would not be expected, as I have neglected any luminosity emitted from the inner strong field zone in the analytic modelling. Note, however, that regardless of the exact behaviour of the inner disc, it must always join smoothly onto the self-similar solutions out at larger radius, and so it cannot have a significantly different time dependence.

Finally, one of the interesting uses of the relativistic disc equation is to ask what effect the black hole spin has on the evolution of Kerr thin discs. One of the principal effects of the black hole spin is demonstrated in Figure 2.3: thin discs around rapidly rotating Kerr black holes are significantly brighter than their counterparts around more

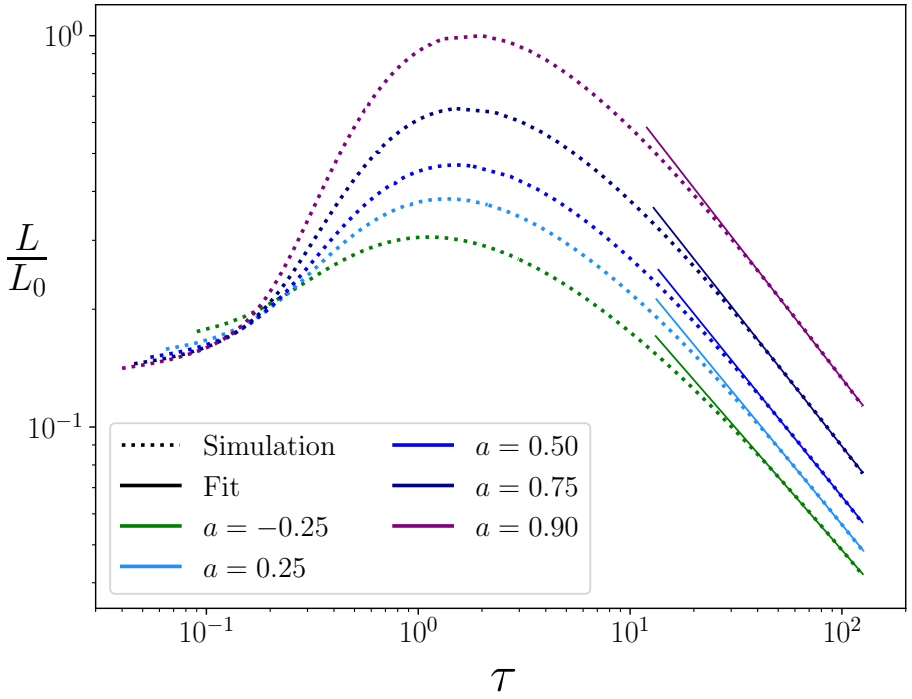

Figure 2.3: Luminosity profiles for a selection of different black hole angular momenta. L_0 is the $a/r_g = 0.9$ peak luminosity. The dimensionless time τ as defined in equation 2.138 is plotted on the x-axis. Each profile is well fit by a (straight-line) power law at late times, with index which varies from $n \simeq -0.6$ for $a/r_g = -0.5$ to $n \simeq -0.7$ for $a/r_g = 0.9$.

moderately spinning black holes. The physical mechanism for this is identical to that of a steady-state accretion system: the disc penetrates deeper into the gravitational well of a rapidly spinning Kerr black hole (which has a smaller ISCO radius in units of r_g), and the available free energy of the disc sheer is correspondingly larger. As can also be seen in Figure 2.3, the gross late time-evolution of the bolometric disc luminosity is only weakly dependent on black hole spin.

In conclusion, the numerical solutions of the Kerr evolution equation demonstrate the key characteristic expected from the analytical analysis of the proceeding sections: there exists a pronounced light curve dichotomy in the simplest Kerr modelling, with the luminosity of finite ISCO stress solutions falling off less rapidly than t^{-1}; while the vanishing stress solutions fall off more rapidly than t^{-1}. This work promises therefore an interesting observational diagnostic of a long-contentious theoretical question: does the stress vanish at the ISCO of a black hole accretion disc? Before I model observational datasets however, I must further examine the finite ISCO stress Kerr disc solutions.

2.8 Problems with first order solutions

In the sense that they give a very good approximate description of the disc behaviour at large times, the self-similar solutions presented in section 2.6.2, and the Green's function solutions of the linear regime, are the proper mathematical solutions of the relativistic evolution equation for the problem posed — the evolution of a disc where the stress is allowed to be non-zero at the ISCO, and Kerr circular motion is assumed. The question is, are these solutions physically sustainable in a real thin disc? By examining the radial fluid motion within the evolving finite stress discs I will demonstrate that these "zeroth order" solutions are not indefinitely sustainable, and that a more sophisticated orbital model must be developed. I examine first the underlying model assumptions in the presence of a finite ISCO stress, and suggest how a more accurate, quasi-circular orbit model could in principle resolve the difficulties. This more sophisticated model is then solved fully.

2.8.1 Radial fluid motion in a finite stress disc

The notion that magnetic stresses could exert sizeable torques on the inner regions of accretion discs has a long history (Page and Thorne 1974, Krolik 1999 and Gammie 1999). Numerical studies over the past twenty years have generally shown that the magnetic fields that drive the MRI lead to non-zero stresses at the ISCO (e.g. Noble et al. 2010).

In a disc with a non-zero ISCO stress, angular momentum is transported from the unstable disc region ($r < r_I$), back into the stable disc region ($r > r_I$). By the time they reach the event horizon, fluid elements (in numerical simulations) typically have angular momenta of order 5–15% less than what is required of a circular orbit at the ISCO (Noble et al. 2010). This liberated angular momentum results in the presence of an angular momentum flux from the ISCO neighbourhood. As time progresses, this effective torquing of the inner disc edge leads to the dominance of the C_1 solution.

In this picture, a continuous flow of disc material over the ISCO is required to produce the inner disc stress. It is theoretically possible for a disc with no net accretion to have a non-zero torque at the ISCO, e.g. by field lines attached to a spinning blackhole threading the inner disc edge (Agol and Krolik 2000). While such torques are potentially quite interesting, in this thesis my focus is upon the internal turbulent stress self-consistently produced by the disc material itself.

Is this type of finite ISCO stress model physically sustainable? To answer this question, consider the motion of the fluid elements within the disc. As discussed in section 2.2.3, the fluid outside of the ISCO is assumed to move to leading order on circular orbits, at first order to fluctuate therefrom, and only at second order to exhibit a radial 'drift' velocity. The latter is caused by the turbulent stress of the product of correlated first order fluctuations. This determines the radial disc evolution. This velocity hierarchy is encapsulated in the following scaling argument:

$$\delta U_\phi \ll U_\phi, \quad U^r \ll \delta U^r \sim \delta U_\phi / r \ll r U^\phi. \tag{2.170}$$

To calculate the radial drift velocity, use equation (2.24), which follows from a combination of mass and angular momentum conservation:

$$\Sigma U'_\phi U^r + \frac{1}{r}\frac{\partial}{\partial r}\left(r \Sigma W^r{}_\phi\right) - \Sigma W^r{}_\phi U_\phi U^\phi \left(\ln \Omega\right)' = 0. \tag{2.171}$$

Re-writing this expression in terms of ζ, after a simple manipulation I find

$$U^r = -\frac{W^r{}_\phi}{U'_\phi}\frac{\zeta'}{\zeta}. \tag{2.172}$$

If I assume Kerr metric circular orbits, then the ISCO values of both U'_ϕ and ζ' vanish, leaving – by l'Hopital's rule

$$U^r(r \to r_I) = -\frac{W^r{}_\phi}{U''_\phi}\frac{\zeta''}{\zeta}, \tag{2.173}$$

where I note that

$$U''_\phi(r_I) > 0. \tag{2.174}$$

This result ensures that in a finite ISCO stress disc, unlike a vanishing ISCO stress disc, the radial velocity is formally non-infinite at the ISCO.

Inspection of equation (2.172) demonstrates that the disc fluid flows in the direction of decreasing ζ. Accretion is therefore cut off if ζ ever reaches a maximum at the ISCO, since this would produce a positive radial velocity at all points in the disc. In the numerical finite ISCO stress solutions, this ISCO maximum is indeed seen (Figure 2.4). A systemic radial outflow at all points within the disc is an unsustainable result, as a real disc would be unable to maintain a non-zero ISCO stress indefinitely—not without continued accretion. In a real disc, the lack of accreting gas flowing inward

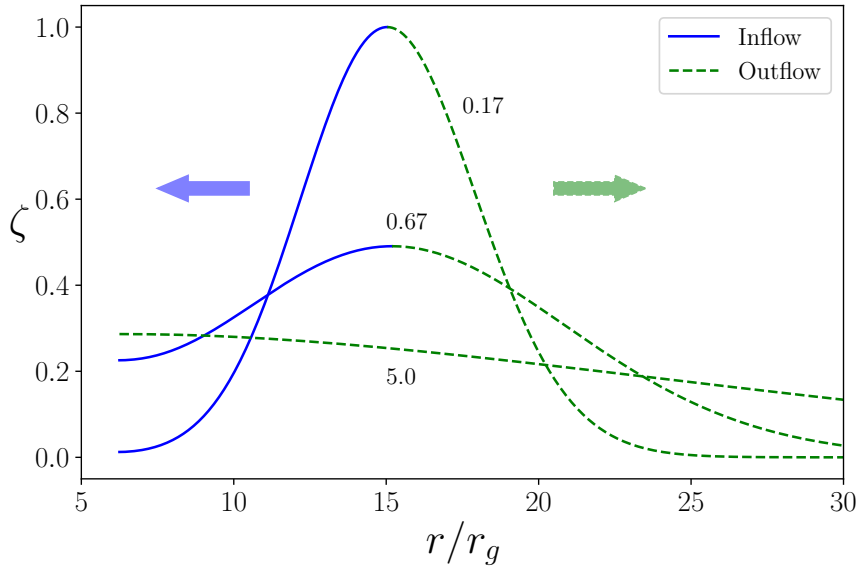

Figure 2.4: Plots of the (normalised) dynamical variable ζ at three different times. Each curve is labeled by its dimensionless time τ. The blue solid curves and green dashed curves represent regions in which the disc is inflowing and outflowing respectively. Eventually, $\zeta(r_I)$ becomes a global maxima, at which point the disc is outflowing at all external radii: the accretion stalls.

of the ISCO would almost certainly cause the ISCO stress to drop. This would in turn lower ζ, allowing accretion to pick up naturally once again.

Clearly, a more careful model of the late time disc dynamics is required when the stress at the ISCO is non-zero.

2.8.2 Energetics of finite ISCO stress solutions

The peculiar properties of the finite ISCO stress solutions was first noted in equation 2.126, where the total energy radiated from the finite ISCO stress solutions was computed for the simple $W^r{}_\phi = w = \text{cst}$ stress parameterisation:

$$E_{\text{rad}}(t) = \int_0^t L_{\text{bol}}(t')\,\mathrm{d}t' \sim t^{+1/3} \to \infty \text{ as } t \to \infty. \tag{2.175}$$

The total radiated energy diverges. A natural question is, what is the source for this energy? The disc has a finite total mass M_d, and the energy liberated is from the accretion of this material $\dot{M}_{\text{acc}}$, eventually this material must run out? The key conceptual point is that *only* a vanishing ISCO stress disc sources its radiated energy exclusively from the liberated gravitational potential energy of the accreting

material, for any non-zero ISCO stress there is an additional energy source: the angular momentum flux across the ISCO. In fact, at late times the finite ISCO stress solutions are sourcing their energy exclusively from this angular momentum flux, and are not accreting at all. Let us examine the total angular momentum J_d and mass M_d of the self-similar accretion solutions:

$$M_d(t) = \int 2\pi r \Sigma(r,t)\,\mathrm{d}r, \quad J_d(t) = \int 2\pi r\sqrt{GM_{\rm BH}r}\Sigma(r,t)\,\mathrm{d}r. \tag{2.176}$$

The radial extent of these integrals extends from $r = 0$ (in a Newtonian setting) to $r_{\rm out}(t)$ the time dependent location of the outer edge of the accretion disc. Re-writing these integrals over the self-similar variable $\xi = \sqrt{x}\tau^{-\lambda}$, I find

$$M_d(t) = 4\pi r_0^2\Sigma_0\tau^{\lambda-\chi}\int_0^{k^{-1/\theta}} \xi^{\omega}(1-k\xi^{\theta})^{1/\eta}\,\mathrm{d}\xi, \tag{2.177}$$

$$J_d(t) = 4\pi r_0^2\Sigma_0\sqrt{GM_{\rm BH}r_0}\tau^{2\lambda-\chi}\int_0^{k^{-1/\theta}} \xi^{1+\omega}(1-k\xi^{\theta})^{1/\eta}\,\mathrm{d}\xi, \tag{2.178}$$

where the integrals themselves are now simple constant factors[9]. The finite ISCO stress (C_1) solutions satisfy $\lambda = \chi$, while the vanishing ISCO stress (C_2) solutions satisfy $2\lambda = \chi$. Thus, the C_1 solutions (in a formal Newtonian setting) have constant mass, and increasing angular momentum, while the vanishing ISCO stress solutions have constant angular momentum and ever decreasing mass. (Note that the numerical Kerr solutions have, independent of disc stress, neither a constant mass nor angular momentum, as both are lost at early times through the inner disc edge, a property not captured by these Newtonian self-similar solutions).

The fact that the finite ISCO stress solutions are sourcing their energy from the inner disc torquing can be seen by noting that at late times:

$$L_{\rm bol} \sim \frac{\mathrm{d}J_d}{\mathrm{d}t} \sim t^{-n}, \quad (C_1 \text{ solution}), \tag{2.179}$$

with the same index n. The only manner in which the angular momentum of the disc can change is via the torque at its inner edge (the local turbulent interactions conserve angular momentum by construction in equation 2.163), thus $L_{\rm bol} \sim \mathcal{T}_I$, where $\mathcal{T}_I$ is the ISCO torque.

[9]The mass integral is: $k^{-(1+\omega)/\theta}\theta^{-1}\Gamma(\frac{1+\eta}{\eta})\Gamma(\frac{1+\omega}{\theta})/\Gamma\left(\frac{\theta+(1+\omega)(1+\eta)}{\theta(1+\eta)}\right)$, and the angular momentum integral is: $k^{-(2+\omega)/\theta}\theta^{-1}\Gamma(\frac{1+\eta}{\eta})\Gamma(\frac{2+\omega}{\theta})/\Gamma\left(\frac{\theta+(2+\omega)(1+\eta)}{\theta(1+\eta)}\right)$, where Γ is the usual gamma-function.

For completeness, note that the C_2 vanishing ISCO stress solutions satisfy

$$L_{\rm bol} \sim \frac{{\rm d}M_d}{{\rm d}t} \sim t^{-n}, \quad (C_2 \text{ solution}). \tag{2.180}$$

Again, the only manner in which the mass of the disc can change is through mass losses at the inner edge (the local turbulent interactions conserve mass by construction in equation 2.163), and thus $L_{\rm bol} \sim \dot{M}_I$, where $\dot{M}_I$ is the ISCO accretion rate.

2.8.3 Examining the canonical disc assumptions

The first term in this equation (2.171) describes an angular momentum deposition carried by the radial flow of the disc fluid. The second term is the angular momentum flux due to the various stresses present (turbulent, magnetic etc.), and the final term represents the angular momentum losses carried away by the emitted disc photons — itself a by-product of the stresses acting on the disc.

It is clear from inspection of equation (2.171) that the Kerr circular orbit's vanishing ISCO angular momentum gradient locally conserves the radial flux of angular momentum arising from any mass flow. If there is a finite total $W^r{}_\phi$ stress present, then this model has a non-zero *positive* radial flux of angular momentum at a disc location where the angular momentum flux from the bulk disc flow is strictly conserved. This outward $W^r{}_\phi$ flux is not conserved; its losses are a source for the photon angular momentum flux (Figure 2.5). But in the model solution, the disc can only supply the $W^r{}_\phi$ flux from the relatively small amount of material within the ISCO, because just outside the ISCO the disc velocity is outward: it is not accreting! This cannot go in indefinitely—unless the outward $W^r{}_\phi$ flux is somehow being fed externally. The fact, as noted above, that the integrated total luminosity of the solutions formally diverges as $t \to \infty$ is a clue: something external must be feeding this. This could in principle be a magnetic couple to the black hole itself (or a vertical accretion process), but how would a turbulent/viscous model resolve this issue? The C_1 solutions must not be the true $t \to \infty$ disc solutions; they represent instead an extended phase of disc evolution in which the accretion is stalled. While this may be very useful for understanding observations, it raises an important point of physics: how does a real disc "unstall" itself?

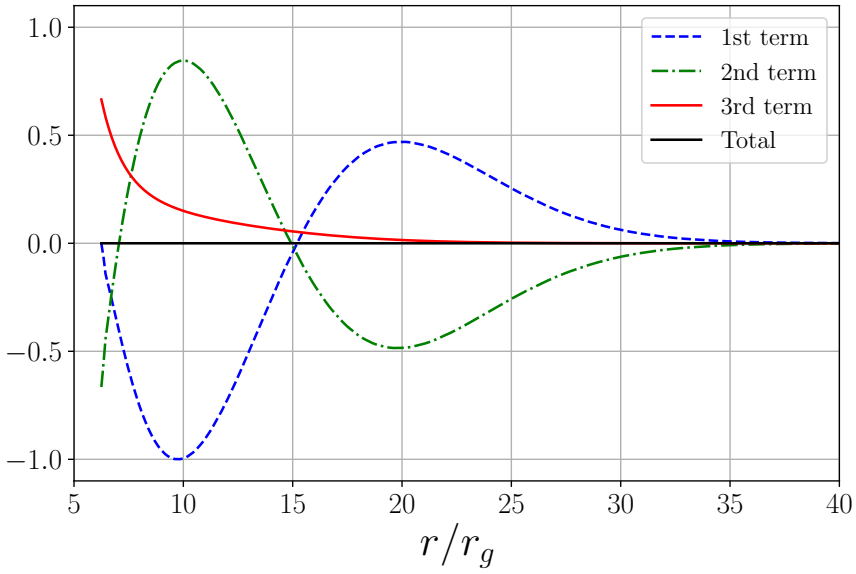

Figure 2.5: The normalised angular momentum flux-divergences, stemming from the three terms in equation (2.171), at a particular time ($\tau = 0.67$) in the disc evolution. Throughout the bulk of the disc, the angular momentum loss balance is predominantly between the radial flow (the first term) and the turbulent stresses (second term). In the region $r \lesssim 8r_g$, however, the photon losses (third term) dominate over the radial flow stress. This balance can be maintained as an extended phase, but not indefinitely.

2.9 An extended model

It is important to consider carefully what is meant by the 4-velocities U^μ which appear in the evolution equation (2.163). This equation is derived perturbatively, with the exact fluid 4-velocity u^μ split into a mean component U^μ and a perturbation δU^μ. The sole conditions placed upon the respective 4-velocity components are the following scaling relationships

$$\delta U_\phi \ll U_\phi, \quad U^r \ll \delta U^r \sim \delta U_\phi / r \ll r U^\phi. \tag{2.181}$$

The typical interpretation of these assumptions is that the fluid external to the ISCO moves, at leading order, on precisely circular geodesic orbits. This formalism implies, in particular, that the zeroth order mean fluid motion is independent of the properties of the disc stress.

But is this a reasonable assumption? A fluid element in an accretion disc is never on a precisely circular orbit – it is radially drifting either inwards or outwards. Finite inward radial velocities will generally reduce the angular momentum of a fluid element

below that required of a circular orbit. Ordinarily, this small change in the angular momentum is a second order effect and therefore negligible. But at the ISCO a small change in the vanishing angular momentum gradient denominator represents an important deviation – small and zero are qualitatively, and importantly, different, particularly when a quantity appears in the denominator of the governing equation. In fact, in general a finite ISCO stress *implies* that the ISCO angular momentum gradient of the fluid must not be precisely zero: by definition a finite $W^r{}_\phi$ stress means that the angular momentum of the flow is being redistributed radially. If this stress is produced internally in the disc flow, then the angular momentum of the fluid must vary as it crosses the ISCO: in other words, it must have an ISCO angular momentum gradient.

I shall accordingly investigate the simplest possible self-consistent thin disc model incorporating this: the evolution of an initially localised disc evolving with a finite ISCO stress and a non-zero angular momentum gradient at the ISCO.

2.9.1 Modified angular momentum profile

In the fundamental disc equation, only two mean flow quantities appear, U^0 and U'_ϕ. The gross properties of the disc are quite insensitive to small deviations in U^0. The key modification required is then in the gradient U'_ϕ. A generic change to the angular momentum gradient takes the form

$$U'_\phi = \left(V^c_\phi\right)' + \epsilon(r), \tag{2.182}$$

where I use the notation U_ϕ to indicate the mean fluid angular momentum entering equation (2.163), and V^c_ϕ is the corresponding angular momentum of an exact circular orbit. The function $\epsilon(r)$ is somewhat arbitrary. However, it is constrained by two simple properties: (i) it reaches a maximum at the ISCO, and (ii) it vanishes for $r \gg r_I$. (The idea is that ideal circular orbits are a good approximation to the mean fluid dynamics at large radii, and become progressively worse as the ISCO is approached.) It is convenient to adopt an exponential form

$$\epsilon(r) = \frac{\Delta j}{L} \exp\left(-x/L\right), \quad x \equiv r - r_I. \tag{2.183}$$

I will consider $x > 0$ only. For $x < 0$, the radial velocity of the disc material increases rapidly inwards and the disc density will see a correspondingly rapid decrease. The parameter L is the length scale over which the deviations from a circular orbit is

important. In this chapter, I adopt $L = 10r_g$, so that the change from circular orbits to in-spiralling orbits in the stable disc regime is a gradual one. The second parameter (Δj) is a measure of the magnitude of the deviation of the angular momentum of the material at the ISCO from that of the circular orbit angular momentum. This is seen by integration of equation (2.182)

$$U_\phi = V_\phi^c - \Delta j \exp\left(-x/L\right). \tag{2.184}$$

At the ISCO r_I itself,

$$U_\phi(r_I) = V_\phi^c(r_I) - \Delta j. \tag{2.185}$$

The quantities $\epsilon(r)$ and Δj are merely model parameters here. I adopt a simple and convenient functional form so as to understand the sensitivity of the disc solutions to a modified angular momentum gradient. A more precise form of the disc angular momentum profile is best determined by direct numerical simulation.

2.9.2 ISCO boundary condition

Earlier, I argued that the inner matching constraint is that the outer Newtonian y_N modes must match smoothly onto the local ISCO Ai′ function, selected for the property that it decays exponentially interior to the ISCO radius. In this section, with a finite $U'_\phi(r_I)$, the inner modal equation must be modified correspondingly. Following equation (2.172), there is only one possible boundary condition which conserves angular momentum within the disc:

$$\frac{\zeta'}{\zeta} = -\frac{U'_\phi U^r}{W^r_\phi} \qquad (\text{at } r = r_I). \tag{2.186}$$

The (density weighted) ratio $-(\rho W^r_\phi)/(\rho U^r)$ has dimensions of specific angular momentum, and may be readily extracted from numerical simulations (e.g., Noble et al. 2010). With the chosen functional form of the angular momentum gradient (equation 2.183), the boundary condition becomes

$$\frac{\zeta'}{\zeta} = -\frac{\Delta j}{L}\frac{U^r}{W^r_\phi} \equiv \frac{\gamma}{L} > 0. \tag{2.187}$$

(The term on the right hand side is positive as $U^r < 0$ for accretion). In specifying the dimensionless parameter γ (the ratio of the angular momentum circular orbit deficit to

$W^r{}_\phi/U^r$), the ISCO boundary condition for ζ is imposed. The exact circular orbit limit corresponds to $\gamma = 0$, while a vanishing ISCO stress corresponds to $\gamma \to \infty$. I will demonstrate that the size of γ profoundly influences the disc evolution in these models.

For the remainder of this chapter, I treat the parameter γ as a constant and examine its effect on an evolving Kerr thin disc. This is clearly a simplifying assumption: it may be that γ is sensitive to the disc stalling and changes its value accordingly. This may arise, for example, if there were a drop in the magnitude of the ISCO stress caused by the drainage of material interior to the ISCO, which is then not replenished by exterior material due to accretion stalling. Given that none of the parameters $W^r{}_\phi$, Δj and U^r can be determined from first principles, the actual behaviour of γ is best addressed by numerical simulations. Even restricted by this simplification, these constant γ models demonstrate a mathematically rich and astrophysically interesting pattern of behaviour.

2.9.3 Linear Laplace mode analysis

The dependence of the disc properties on γ can be once again understood with a normal mode Laplace decomposition. The calculations of section 2.5 may be recomputed here using the modified angular-momentum-gradient formalism, which of course changes only the form of the inner strong field solutions. As before, the inner solution matching conditions strongly modify the *global* behaviour of the disc as $t \to \infty$.

To make progress I treat the simplest analytic case in which the turbulent stress is a constant ($W^r{}_\phi = w = \text{cst}$) at all radii. With the near-ISCO form of the angular momentum gradient given by

$$U'_\phi \simeq \epsilon(r) = \frac{\Delta j}{L}\exp(-x/L), \tag{2.188}$$

the modified local form of this equation near the ISCO is

$$\frac{\partial y}{\partial t} = \frac{w}{L\Delta j}\frac{\partial}{\partial X}\left(e^X \frac{\partial y}{\partial X}\right), \tag{2.189}$$

where I have introduced $X \equiv (r - r_I)/L$, a dimensionless length. For stable Laplace modes ($y \sim e^{-st},\ s > 0$), this becomes

$$\frac{\mathrm{d}}{\mathrm{d}X}\left(e^X \frac{\mathrm{d}y}{\mathrm{d}X}\right) = -s\frac{L\Delta j}{w}y \equiv -b^2 y. \tag{2.190}$$

By changing variables to $Z = e^{-X}$ the equation reduces to

$$\frac{\mathrm{d}^2 y}{\mathrm{d}Z^2} + \frac{b^2}{Z} y = 0, \tag{2.191}$$

which is once again of the general form solved in Appendix A. This equation has exact solutions of the form

$$y = e^{-X/2}\left[C_3 J_1\left(2be^{-X/2}\right) + C_4 Y_1\left(2be^{-X/2}\right)\right], \tag{2.192}$$

where J_1 is the standard Bessel function of the first kind, and Y_1 the corresponding Bessel function of the second kind. Note that, unlike in the case of pure Kerr circular orbits, neither of these modal solutions are poorly behaved at $x = 0$, and I now have an additional undetermined ratio C_3/C_4 in the problem. This will turn out to be very consequential. Using standard Bessel function identities, the derivative of y with respect to radius is

$$\frac{\mathrm{d}y}{\mathrm{d}r} = -\frac{be^{-X}}{L}\left[C_3 J_0\left(2be^{-X/2}\right) + C_4 Y_0\left(2be^{-X/2}\right)\right]. \tag{2.193}$$

The outer Newtonian equation is completely unchanged. In this region, the (Newtonian) modal solutions of this equation, denoted y_N, are given by

$$y_N = r^{1/4}\left[C_1 J_{-1/3}\left(\frac{2p}{3} r^{3/4}\right) + C_2 J_{1/3}\left(\frac{2p}{3} r^{3/4}\right)\right], \quad p^2 = \frac{s\sqrt{GM}}{2w} \tag{2.194}$$

and $J_{\pm 1/3}$ are the usual Bessel functions of fractional order.The gradient of y_N is

$$\frac{\mathrm{d}y_N}{\mathrm{d}r} = \frac{p}{2}\left[C_2 J_{-2/3}\left(\frac{2p}{3} r^{3/4}\right) - C_1 J_{2/3}\left(\frac{2p}{3} r^{3/4}\right)\right]. \tag{2.195}$$

The smooth matching condition is that at some intermediate radius r_m the inner and outer modes have the same amplitude $y(r_m) = y_N(r_m)$ and the same gradient $y'(r_m) = y'_N(r_m)$. The key quantities to determine remain the coefficients C_1 and C_2. The matching conditions, presented with the respective Bessel function arguments suppressed (note that both p and b scale as $s^{1/2}$), are:

$$C_1 J_{-1/3} + C_2 J_{1/3} = A(s), \tag{2.196}$$

$$C_1 J_{2/3} - C_2 J_{-2/3} = B(s). \tag{2.197}$$

Here I have defined the boundary terms

$$A(s) = \frac{e^{-X_m/2}}{r_m^{1/4}} \left(C_3 J_1 + C_4 Y_1\right), \tag{2.198}$$

$$B(s) = \frac{2be^{-X_m}}{pL} \left(C_3 J_0 + C_4 Y_0\right). \tag{2.199}$$

The solutions of equations (2.196) and (2.197) are

$$C_1 = [A(s)J_{-2/3} + B(s)J_{1/3}]/\mathrm{Wr}, \tag{2.200}$$

$$C_2 = [A(s)J_{2/3} - B(s)J_{-1/3}]/\mathrm{Wr}, \tag{2.201}$$

where Wr is once again the Wronskian formed from the fractional Bessel functions:

$$\mathrm{Wr} \equiv J_{1/3}J_{2/3} + J_{-1/3}J_{-2/3} = \frac{3\sqrt{3}}{2\pi p r_m^{3/4}} \propto s^{-1/2}. \tag{2.202}$$

To determine the s-dependent properties of C_3/C_4, I next impose the ISCO boundary condition

$$\frac{y'}{y} = \frac{\gamma}{L}. \tag{2.203}$$

Substituting from equations (2.192) and (2.193) and rearranging, I find

$$\frac{C_3}{C_4} = -\left(\frac{bY_0 + \gamma Y_1}{bJ_0 + \gamma J_1}\right). \tag{2.204}$$

At late times, the $s \to 0$ behaviour of this solution is important. The Bessel functions have the following expansions for small z:

$$Y_1(z) \sim 1/z, \tag{2.205}$$

$$Y_0(z) \sim \ln(z), \tag{2.206}$$

$$J_1(z) \sim z, \tag{2.207}$$

$$J_0(z) \sim \text{constant}, \tag{2.208}$$

and more generally

$$J_\nu(z) \sim z^\nu. \tag{2.209}$$

Equation (2.204) shows that $C_3/C_4 \sim 1/b^2 \sim s^{-1}$ in the $s \to 0$ limit. This then implies $A(s)/B(s) \sim s^{1/2}$, and thus, in the $s \to 0$ limit,

$$C_2/C_1 \sim s^{-1/3}. \tag{2.210}$$

The coefficient C_2 therefore dominates at extremely late times. This is the late time behaviour that arises in standard vanishing ISCO stress models, but now it holds even in the presence of stress! *This is a very interesting result:* the reduction of the average disc angular momentum to a value below that of a circular orbit has lead to a qualitative change in the *outer* disc behaviour as $t \to \infty$.

How do I reconcile this finding with the conclusion of the proceeding sections, that C_1 behaviour, with its shallow light curve fall-off, follows from the presence of an ISCO stress? The answer comes down to a delicate asymptotically ordering of time scales, and the smooth matching conditions are once again key. The point is that equation (2.204) introduces another asymptotic scale into the set of equations: the relative size of b and γ. The coefficient b is an s-dependent quantity, and so the ratio γ/b will be different for each mode.

Consider the case $\gamma/b \to 0$, the opposite of a late time, small s, constant γ limit. The case I now consider will be appropriate for times restricted to be earlier than a characteristic time scale which is derived below. In this limit, $C_3/C_4 \to -Y_0/J_0$, implying that B vanishes while A remains finite. Finite s, vanishing B modes satisfy

$$C_1 \propto J_{-2/3}\left[\frac{2p(s)}{3}r_m^{3/4}\right],\ C_2 \propto J_{2/3}\left[\frac{2p(s)}{3}r_m^{3/4}\right]. \tag{2.211}$$

The large argument limit of a Bessel function is

$$J_\nu(z) = \sqrt{\frac{2}{\pi z}}\cos\left[z - \left(\frac{2\nu+1}{4}\right)\pi\right] + O(1/z^{3/2}), \tag{2.212}$$

meaning that in the $p(s)r_m^{3/4} \gg 1$ limit, C_1/C_2 is of order unity:

$$\frac{C_1}{C_2} \simeq \frac{\cos\left[2p(s)r_m^{3/4}/3 - 7\pi/12\right]}{\cos\left[2p(s)r_m^{3/4}/3 + \pi/12\right]} \sim O(1), \tag{2.213}$$

whereas when s is sufficiently small that $p(s)r_m^{3/4} \ll 1$,

$$C_1/C_2 \sim s^{-2/3} \gg 1. \tag{2.214}$$

Therefore, modes with $b \gg \gamma$ will have C_1 solutions at least comparable to, or potentially dominating, the C_2 modes. This inequality gives an effective time scale over which these modes will be important (all modes are of course ultimately suppressed by a

factor e^{-st}). These modes will be important up until a time $t_c \equiv 1/s_c$, where s_c is defined through the modal condition $\gamma/b(s_c) \simeq 1$:

$$b(s_c) = \sqrt{\frac{s_c L \Delta j}{w}} = \sqrt{\frac{s_c L \gamma}{|U^r|}} \simeq \gamma, \tag{2.215}$$

where I have used equation (2.187). Solving the above for $t_c = 1/s_c$ in terms of the viscous time scale appropriate for the inner disc regions, $t_v \equiv L/|U^r|$, I obtain an expression for the critical time scale:

$$t_c \simeq \frac{t_v}{\gamma}. \tag{2.216}$$

This means that for times $t \lesssim t_c$ the (shallow fall off) C_1 modes will be of at least comparable importance to the (steeper) C_2 modes; as time pass through $t = t_c$, the latter dominates. The key point is that if t_c is sufficiently large, there will be a extended period over which the C_1 solution dominates within the disc, and the accretion is stalled.

The results of section 2.5.2 — that for circular orbits the (steep-falling) C_2 solutions dominate when the ISCO stress is zero, and that the (shallow-falling) C_1 solutions dominate when the ISCO stress is finite — can be fully recovered by taking appropriate limits of the time parameter t_c. For vanishing ISCO stress $\gamma \to \infty$, $t_c \to 0$ and the period over which C_1 dominates is vanishingly brief. While for *any* non-zero γ the C_2 solution will eventually dominate, a finite ISCO stress with perfect circular orbits corresponds to the $\gamma \to 0$ limit, in this limit $t_c \to \infty$ and the C_1 solutions will dominate at late times.

From an observational standpoint, the most important prediction of the existence of the stalled accretion phase is that the luminosity from transient astronomical disc sources should be initially brighter, before following a more shallow decay profile, than they would in classical vanishing stress disc modelling. A key quantity of interest is the power law index, n—now perhaps best denoted as $n(t)$— a quantity that would be measured at each time in the light curve decay from a fit of the form $L \sim t^n$. Classical vanishing and finite ISCO stress models based on circular orbits make clean predictions of the power law index n at late times in the evolution of the disc. Here the behaviour is richer. During the stalled phase of accretion the power law index will be close to that of the C_1 solutions, $n \sim -0.7$, while at very late times the power law will be given by the C_2 solutions, typically $n \sim -1.2$ (section 2.6, Cannizzo et al. 1990). The power law

index evolves as time progresses, from smaller values less than unity in the stalled phase, to larger values greater than unity in the very-late time approach to the steady state.

To summarise: time-dependent accretion is generally a *three stage* process, controlled by what I have identified as the γ parameter. The early behaviour of a spreading accretion disc is insensitive to the stress and angular momentum modelling. Most of the disc material spreads rapidly inwards toward the ISCO, while the outermost regions move outward to take up the angular momentum of the inward bound material. This inward-moving material forces a density (and dynamical stress) build up in the inner disc regions, leading to a period of dominance of the C_1 solutions, characterised by stalled accretion and shallow light curves. These may be quite extended in time. Eventually, the ongoing slow depletion of the inner disc material lowers the disc density and dynamical (as opposed to kinematical) stress in this region, and a growing dominance of the (steep light curve) C_2 solutions at the latest times.

2.10 Numerical γ-disc solutions

As a verification of my analytical analysis, I have calculated numerical solutions of the evolution equation (2.163), with angular momentum profiles given by equation (2.182). The mathematical problem to be solved is the evolution of a very compact ring, in effect a Green's function solution. Consistent with the above analysis, I find that accretion in a finite ISCO stress thin disc follows the three stage pattern outlined above.

2.10.1 Fiducial γ-disc models: $W^r{}_\phi = w,\ a = 0,\ L = 10r_g$

The γ parameter may be estimated from numerical simulations. Noble et al. (2010) ran a series of disc simulations for a range of disc thicknesses and initial magnetic field geometries. Each of these simulations found *i)* a finite stress at the ISCO; *ii)* the near-ISCO local angular momentum less that of a circular orbit, and *iii)* an ISCO angular momentum flux also below that of a circular orbit. From their simulations it is possible to estimate the parameter γ that Noble et al. (2010) could have extracted from their simulations: Figures 14 and 15 of Noble et al. (2010) contain all of the required information. Typical values, normalised in units where $GM = c = 1$, were $\Delta j \sim 0.01$–0.1, and $W^r{}_\phi/|U^r| \sim 0.3$–$0.5$. For reference, in these units the ISCO circular angular momentum is $V^c_\phi(r_I) = 3.464$. There are, of course,

ample uncertainties in this estimation procedure: I have therefore examined a broad range of (dimensionless) $\gamma \sim 0.01 - 0.1$.

In my fiducial model, the simplest possible finite ISCO turbulent stress model is assumed: $W^r{}_\phi = w =$ constant everywhere. To implement a vanishing stress boundary condition at $r = r_I$ (which is only necessary for the $\gamma \to \infty$ limit), for $r \leq 10r_g$ the stress departs from its otherwise constant w value following the prescription

$$W^r{}_\phi = w\frac{(r - r_I)^2}{(10r_g - r_I)^2}. \tag{2.217}$$

I assume that the black hole is a Schwarzschild ($a = 0$) solution, and the initial condition is a tight gaussian ring, initially located at $r_0 = 15r_g$. This is a nominal tidal radius taken from Rees (1988), ~ 2.5 times the ISCO radius of a Schwarzschild hole. The natural dimensionless time for the viscous spreading of the disc is:

$$\tau \equiv \frac{9wt}{2\sqrt{GMr_0^3}}. \tag{2.218}$$

(Note that this differs from the τ used in section 2.6 equation 2.138, which was normalised for the ease of solving the non-linear Newtonian equation.) Finally, I use equation (2.187) to set the inner boundary condition.

In order to follow the rich behaviour of both the light curves and the power law indices themselves in this modified disc model, it is important to be able to convert the formal viscous timescale of these solutions to one that it is observationally convenient. I adopt the viscous timescale from α disc theory, noting that Ω has the same form in both Newtonian gravity and Schwarzschild geometry:

$$t_v = \alpha^{-1}(H/R)^{-2}\,\Omega^{-1}. \tag{2.219}$$

Using the following typical values appropriate for comparison to a generic tidal disruption event light-curves: $H/R = 0.02$, $\alpha = 0.1$, $M_{BH} = 4 \times 10^6 M_\odot$ and $r_0 = 15r_g$ (as above), leads to $t_v = 330$ days, which fixes the w parameter. The time axis of these plots is accordingly plotted from the numerical τ using the relationship $t = 330\tau$ days. It should be regarded as representative only.

The disc is truncated at its inner edge by the ISCO, at which point the gas flows rapidly inward, and the evolution equation (2.163) no longer accurately models the disc dynamics. Since the disc surface density will then fall off sharply, I shall assume that any interior emission will not significantly alter the integrated disc luminosity.

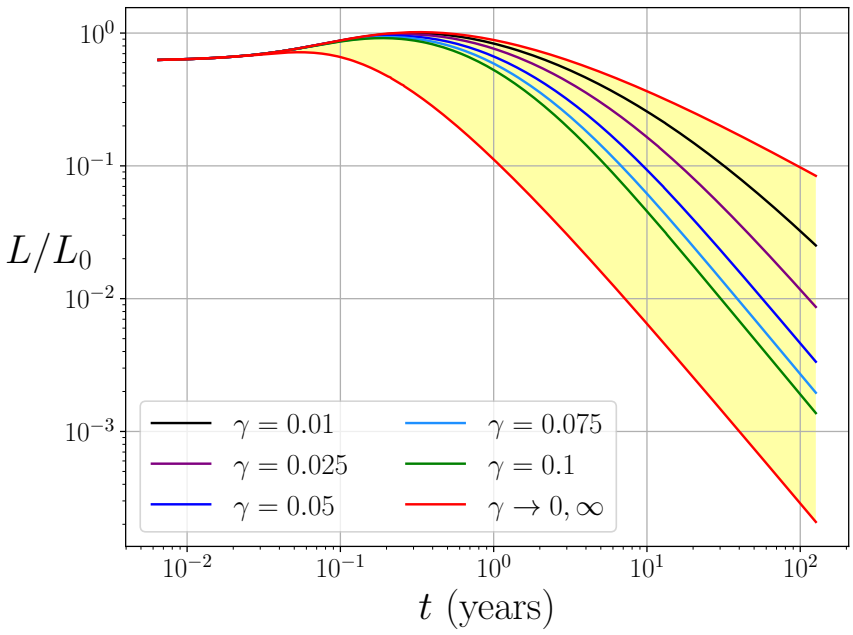

Figure 2.6: The evolving luminosity for a series of γ-discs in a Schwarzschild spacetime. The turbulent stress is given by $W^r{}_\phi = w$, a constant. The light curves are normalised by the peak luminosity of the brightest disc studied. As predicted, the light-curves of these modified γ-disc models are bounded by the simple vanishing stress (lower red) and finite stress (upper red) light curves.

2.10.2 Luminosity evolution

Figure 2.6 shows the evolving luminosity for a sequence of discs, differing only by their respective γ values, which were motivated by those inferred from GRMHD simulations. For reference, I also show the light-curves of the two simpler section 2.7 disc models, which together bound the finite γ runs from above and below. The lowest red curve corresponds to a vanishing ISCO stress disc ($\gamma \to \infty$), while the uppermost red curve corresponds to ideal circular motion in a finite ISCO stress disc ($\gamma = 0$). The light curves for a series of discs differing only by their γ value should lie in the yellow shaded region.

Figure 2.7 shows the effective local luminosity decay index $n = \mathrm{d}\ln L/\mathrm{d}\ln t$ as a function of time, starting from the time of light-curve peak. Note that the $\gamma \to \infty$ vanishing stress case evolves very rapidly over a matter of months, and quickly achieves $|n| > 1$. By contrast, the light curve emergent from any finite-γ disc has a much more extended period, characterised by a smaller luminosity decay index, of order $n \sim -0.7$ in the first several years. This is the hallmark of an extended period of stalled accretion,

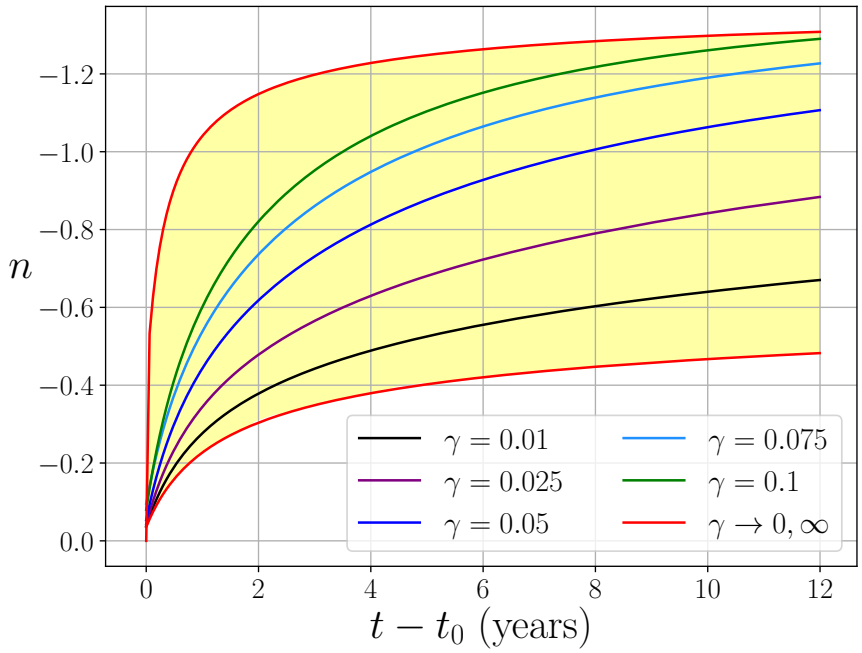

Figure 2.7: The evolving luminosity decay index n, a best fit to $L \sim t^n$ for each light curve in Figure 2.6, plotted as a function of time since the peak of the respective light-curves, t_0. The upper red curve now corresponds to a vanishing ISCO stress, whereas the lower red curve corresponds to the paper I finite stress model.

and when filtered by bandpass, an observational prediction. All of the non-zero-γ decay-index curves eventually approach that of the vanishing stress solution ($|n| > 1$) at the very latest times, which lie off scale to the right of the $t - t_0$ values plotted.

2.10.3 Radial fluid flow evolution

The nature of the radial flow in the inner disc determines which of the modal solutions dominates in the outer disc, and therefore much of the gross dynamical behaviour of the disc itself. To track the behaviour of the radial flow, the radius of zero radial velocity, R_T, is calculated at each time step as part of the solution. Inward of R_T the flow is accreting; outward of R_T it is expanding. The time dependence of this "turnover radius" determines the relative importance of the outer modal solutions, since these two solutions are linked to very different late time behaviours for R_T. For the stalled C_1 solutions, this is $R_T \to 0$; whereas for the C_2 solutions, $R_T \sim t^{2/3} \to \infty$ (for these constant turbulent stress models).

The evolution of R_T is plotted in Figure 2.8 for five different values of γ. Note

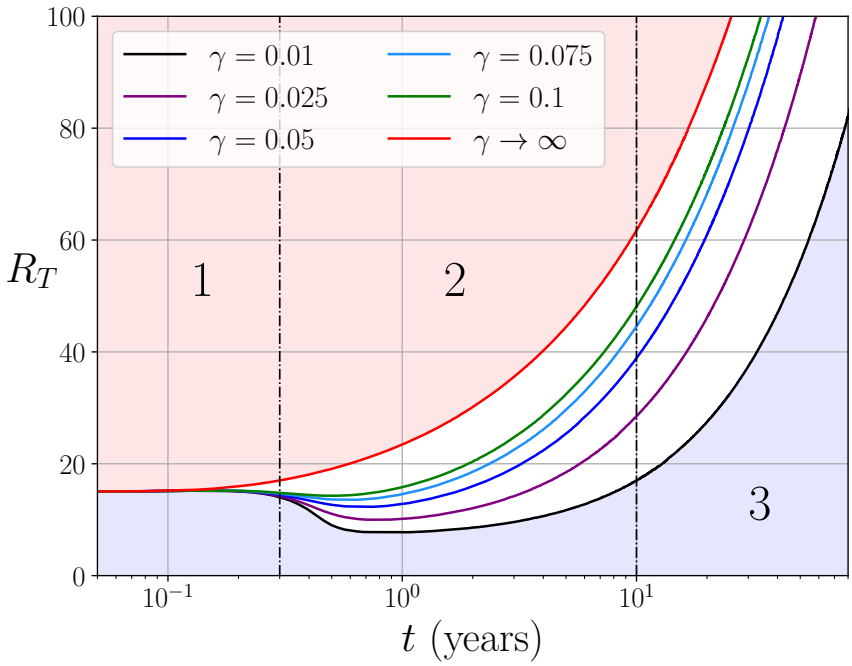

Figure 2.8: The long-term time evolution of R_T, the "turnover radius" at which the radial velocity of the disc is zero, for different values of γ. Radial outflow is present for $r > R_T$ and inflow for $r < R_T$. All discs studied are outflowing in the red shaded region and inflowing in the blue shaded region. The three stages of accretion are thus roughly separated by the vertical dashed lines: (1) rapid inflow; (2) stalled accretion; (3) approach to steady state.

the logarithmic timescale. The vertical black lines separate the figure into the three different disc accretion regimes: rapid inflow (1); stalled accretion (2); and the approach to the steady state (3). Inspection of Figure 2.8 demonstrates the stalling associated with a finite ISCO stress: while the eventual outward trajectory of R_T is similar for all values of γ, there is generally a significant time delay before this begins, particularly for the smaller values of γ.

A measure of the stalling time interval, t_c, is defined by the time at which R_T first becomes greater than r_0. The value of t_c is plotted in Figure 2.9 for the different R_T evolution profiles in Figure 2.8. I also plot a the best fit curve under the assumption that $t_c \propto 1/\gamma$. From the Laplace mode analysis of section 2.9, this scaling is how the time over which the C_1 solutions dominate the outer disc (the cause of the stalling phase) should indeed vary with γ. The zero-ISCO-stress disc has a vanishingly brief period of stalled accretion, as the disc passes directly from evolutionary stages 1 to 3 with R_T continuously increasing.

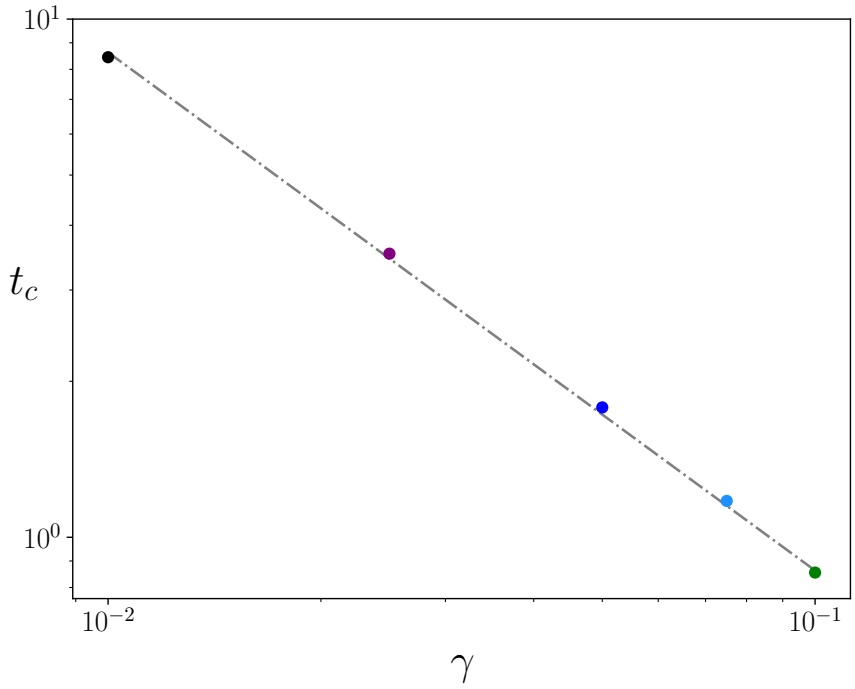

Figure 2.9: The time (in years) required for R_T to begin its upwards trajectory, defined as the time when R_T first becomes greater than r_0, plotted as a function of γ. This quantity is a proxy for the length of the stalled phase of accretion. The grey dashed line is a fit of $t_c \propto 1/\gamma$. This fit is in excellent agreement with the Laplace mode analysis result $t_c \sim 1/\gamma$ equation (2.216).

2.10.4 The evolution of ζ

In section 2.8, the finding that ζ evolved to a global maximum at the ISCO for the simplest ($\gamma = 0$) finite stress disc models implied large scale radial outflow, a behaviour now seen as an extended transient state that a slightly modified angular momentum profile can eventually resolve. Figure 2.10 shows explicitly the early to intermediate stages of the evolution of a set of discs, differing only in their respective γ parameters. Plots (a-d) in Figure 2.10 each show three dimensionless times: $\tau = 0.17$, 0.67 & 5.0. This corresponds to 56, 221 & 1650 days (respectively) in this fiducial model.

The very different behaviour of the finite and vanishing stress discs may be seen by comparison of plots (5a) & (5d), particularly at $\tau = 5$. This very different ζ evolution is responsible for the shallow versus steep light curve behaviour described in section 2.7. As has been noted in section 2.8, the $\tau = 5$ curve in plot (a) exhibits permanent stalling, with outflow at all points.

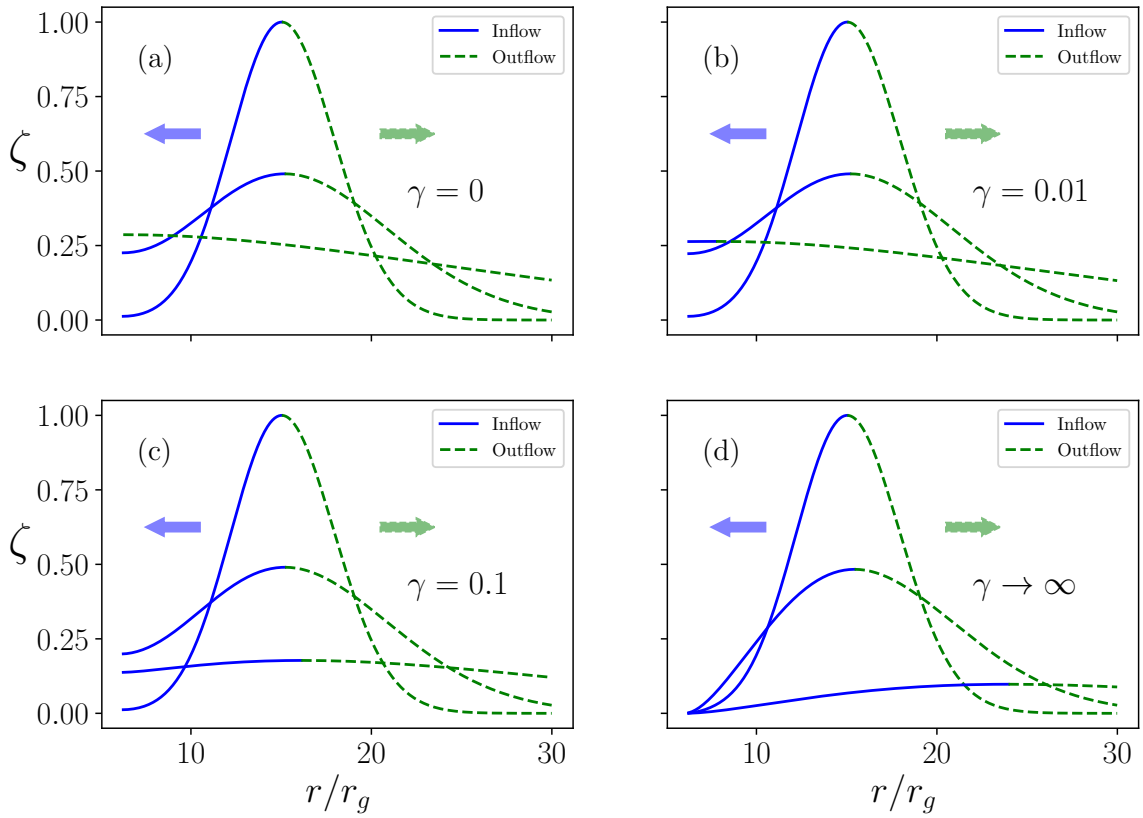

Figure 2.10: Plots of the normalised dynamical variable ζ at three different times in the disc evolution, with varying disc parameters γ, labelled on each plot. Each plot contains curves produced at three different dimensionless times, $\tau = 0.17, 0.67, 5$, the later times can be identified by the decreasing peak magnitude of ζ. The blue solid curves and green dashed curves represent regions in which the disc is inflowing and outflowing respectively.

The three finite stress curves (5a), (5b) & (5c) are indistinguishable at the earlier times $\tau = 0.17$ and 0.67, whilst they all differ from the vanishing stress plot (5d). The reason for this is that at early times all three finite stress solutions are in the stalled phase of accretion, a phase which is vanishingly brief for the vanishing ISCO stress disc. The stalled phase for the $\gamma = 0.01$ disc is extremely extended. Over the entire time examined, the (a) & (b) curves remain near indistinguishable, differing only in the innermost $\sim 2r_g$ exterior to the ISCO radius.

By $\tau = 5$, however, the $\gamma = 0.1$ disc in plot (c) shows an intermediate type behaviour, qualitatively different from the extremes seen in plot (a) and plot (d). The intermediate solution is transitioning from a completely stalled to a steady phase of accretion. This is also seen in Figure 2.11, which shows a comparison between the very-late time

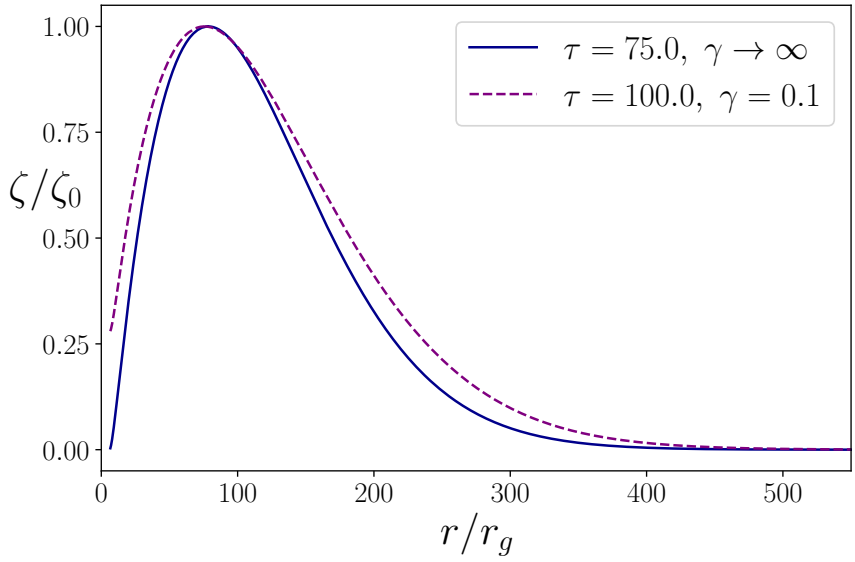

Figure 2.11: Comparisons between a $\gamma = 0.1$ disc and a vanishing ISCO stress disc at very large times, both normalised by their respective magnitudes. Note both the different times at which the two curves are plotted (see text), and also the much enlarged radial range compared to Figure 2.10.

behaviour of a $\gamma = 0.1$ disc and a vanishing ISCO stress disc. By this time, the $\gamma = 0.1$ disc solution is converging towards the profile of the vanishing ISCO stress solution, just as predicted by the analytical arguments of section 2.9.3. Note that the $\gamma = 0.1$ disc is plotted at a later time than the vanishing-ISCO-stress disc. The need for this time offset is in fact due to the presence of an extended, intermediate time, stalled phase.

2.10.5 Summary of numerical results

I have integrated the relativistic thin disc evolution equation (2.163), using a modified angular momentum profile of the form given by equation (2.184). Solutions were found for both a vanishing ISCO stress and a finite ISCO stress, where the inner boundary condition in the latter case was determined by equation (2.187), with a particular range of values of the γ parameter motivated by 3D GRMHD simulations of thin discs. I have shown that the inclusion of non-ideal deviations from circular orbits near the ISCO breaks the late time luminosity fall-off dichotomy of the “zeroth order" vanishing stress and finite ISCO stress solutions presented in section 2.7. The γ parameter in essence joins them in a continuous model parametrisation. These

new models demonstrate a richer behaviour with features of both the more idealised vanishing and finite stress ISCO stress solutions.

The key finding of these numerical studies is that, rather than acting to permanently stall accretion, a finite stress at the ISCO causes the evolution of a relativistic thin disc to follow three distinct stages. In common with vanishing stress discs, accretion with a finite ISCO stress begins with an initial phase of disc material flowing from the disc towards the ISCO, accompanied by an increase in the disc luminosity. This inrush of material leads to a build up of density in the inner regions. In a disc with non-zero ISCO stress this leads to an extended, but finite, period of stalled accretion. During this interval, the disc displays behaviour characteristic of the set of ideal finite stress solutions derived in section 2.7 – most notably, significantly shallower light-curves than vanishing stress discs. The gradual depletion of the inner disc from continued accretion then initiates the third stage of the accretion process, the approach to the steady state. In this final stage of accretion, all discs, independent of their non-zero parameter γ, evolve in a manner nearly identical to that of a traditional vanishing stress solution. Knowledge of γ is needed to determine the duration of the stalled accretion phase. Dedicated GRMHD simulations will be valuable in achieving this goal.

2.11 Simulation support for stalled accretion

I have shown that γ-disc evolution is comprised of three distinct stages. By contrast, the idealised zero ISCO stress disc evolution is a two stage process. The hallmark of a finite ISCO stress is the existence of an extended intermediate period of stalled accretion. It is natural to ask whether this clear prediction of my one-dimensional model has actually been seen in 3D GRMHD simulations of accretion discs, where the stress is self-determined.

The period of stalled accretion begins only after of order the viscous timescale, when the disc surface density has peaked in the inner near-ISCO regions. Running full 3D GRMHD simulations out to such long times is presently prohibitively expensive, and it seems unlikely that in the near future this will change dramatically. However, current 3D simulations do at least provide an arena to test the *early time* behaviour of these models – the initial spreading phase – where the behaviour of the relativistic γ-model should be compatible with what is seen in 3D simulations.

I begin with a comparison of the evolution of the accretion rate as a function of radius in my 1 dimensional disc model with a set of published 3D MHD simulations from Hawley and Krolik (2001). Figure 2.12, taken from the Hawley and Krolik (2001) study, shows the radial accretion rate of the disc at two different times, the accretion rate is plotted up until the ISCO at $r = 3r_S$. By comparison, Figure 2.13, shows the corresponding colour-coded profiles taken from a Schwarzschild γ-disc model. (Details are provided in the caption.) The accretion rate profiles from the 1D disc model are encouragingly similar to those of the full 3D simulations, at least at these early times.

Unlike 3D simulations, 2D axisymmetric simulations may be carried out to the much longer times required to enter the stalled phase of accretion. The catch is that the calculations require the input, "by hand", of a sub-grid mean field dynamo. (Recall that there is no true dynamo in 2D flow Moffatt 1978.) There is no obvious reason why this dynamically *ad hoc* procedure should alter the prediction of three stage accretion, however. A series of twelve 2D GRRMHD simulations were performed by Sądowski et al. (2015), five with initial near-Eddington accretion and seven with initial super-Eddington accretion. The seven super-Eddington simulations are thick disc simulations ($H/R \sim 1$), and are therefore not appropriate for comparison with thin disc models. However, the five starting with near-Eddington accretion rates have typical values of H/R of ~ 0.1, with a maximum value $H/R = 0.2$, and are therefore more amenable to comparison with the thin disc model predictions.

The findings by Sądowski et al. (2015) are very revealing. All five of their simulations followed an initial evolutionary pathway in which disc temperature and thickness evolved from their initial conditions towards values consistent with a turbulent accretion flow. However, in each of the simulations, the accretion flow transitioned to a state in which the disc density peaked in a narrow region near the ISCO. This build-up was then followed by an almost immediate pronounced drop in the accretion rate, despite the the vigorous presence of a fully resolved MRI. In other words, the accretion in these discs was *stalled* by a build-up of disc density in the inner disc regions, much as predicted by the one dimensional finite ISCO stress solutions. A dedicated study of "aided" 2D GRMHD disc simulations would be of great interest here to establish more definitively the existence of disc stalling and whether, at yet longer times, accretion is restored.

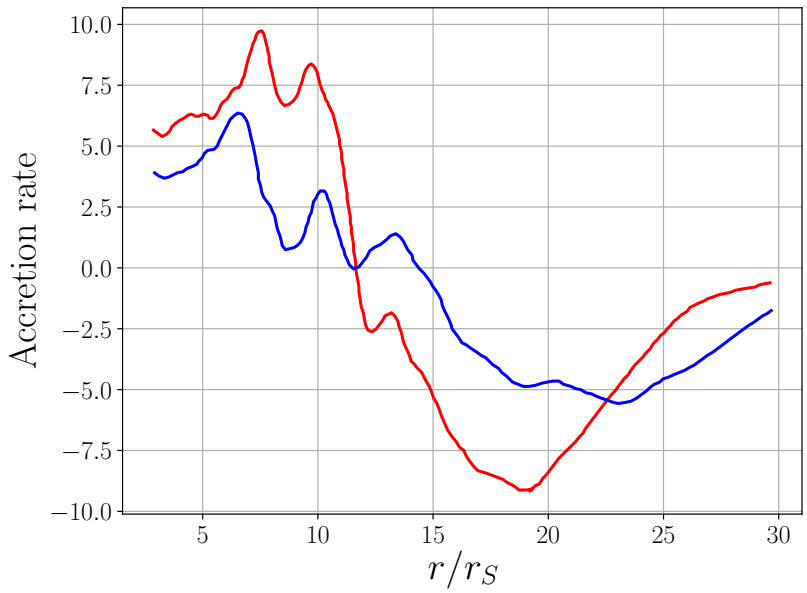

Figure 2.12: Accretion rate versus radius taken from the 3D MHD simulation of Hawley and Krolik (2001), which uses a Paczyński-Wiita potential, at two different times. The early time profile is coloured red and corresponds to $t = 1000\,GM/c^3$. The blue curve corresponds to the later time $t = 1500\,GM/c^3$.

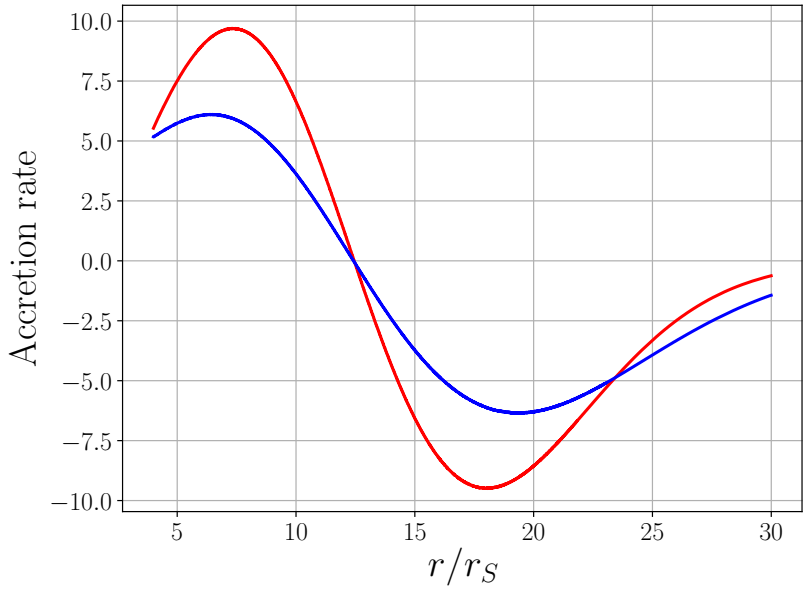

Figure 2.13: Accretion rate versus radius for a 1 dimensional Schwarzschild disc model with a constant turbulent stress ($W^r{}_\phi = w =$ constant; hence a finite stress at the ISCO) and $\gamma = 0.1$. The magnitude of the accretion rate is normalised so as to have the same peak value at $t = 1000\,GM/c^3$ as the Hawley and Krolik (2001) figure. The red curve corresponds to the earlier time, while the blue curve is the later time.

2.12 Discussion

In this Chapter I have derived and analysed the first explicit time-dependent solutions of the relativistic thin disc equations. These solutions display a mathematically rich and physically interesting set of behaviours, primarily controlled by the properties of the turbulent disc stress in the innermost near-ISCO regions. The global behaviour of the disc can be understood through both analytical Laplace modal-matching techniques, developed here, and through explicit numerical calculations.

Potentially the most important result of this Chapter is that the properties of the ISCO stress are far more important than being merely a choice of boundary condition which modifies the high energy portion of an X-ray spectrum. In fact, the ISCO stress has important consequences for the *global* evolution of a relativistic accretion disc. A sustained period with a substantial ISCO stress leads to a much slower evolution of the disc's inner region, and in particular a bolometric luminosity which is both initially brighter, and remains brighter for longer, than for a vanishing stress counterpart.

Furthermore, a key finding of this Chapter is that the classical modelling assumption of a perfect circular orbit description of the disc fluids mean flow must be modified in the near-ISCO region, as neither the vanishing ISCO stress solution (which has an infinite radial velocity) or the finite ISCO stress solution (which is permanently stalled) display sustainable behaviour in this limit. In this Chapter I have demonstrated that it is the reduction in the mean angular momentum of the fluid flow from that of a perfect circular orbit which resolves this issues, but detailed GRMHD simulations should be pursued to further clarify the behaviour of the disc fluid in this important regime.

On the observational front, this work has resulted in a clear prediction: the evolution of the luminosity of disc sources with a finite ISCO stress will be slower than an otherwise identical disc evolving with a vanishing ISCO stress. The calculations in this Chapter have involved computing the bolometric luminosity of the disc, but this must be filtered by observational bandpass (X-ray, optical, UV, etc.) before being confronted with observations, one never observes the total luminosity emitted from an accretion disc. Nevertheless, this is an extremely important finding: the nature of the ISCO stress has been a long controversial theoretical problem, and a new and clear observational discriminant of the ISCO stress value is therefore an exciting result. Compared with the direct interpretation of disc spectra, the late-time temporal behaviour of an evolving disc is a more powerful, less ambiguous, discriminator for the

presence or absence of finite stress at the ISCO. The disadvantage is of course that the best time for observing this is when the source is faintest.

Finally, I reiterate that real discs are much more complicated than my 1970's era thin disc model. Real discs need not be thin; they have outflows, jets, coronae, and as yet poorly understood major state transitions. The main point, however, is that four decades after its inception, even the ordinary thin disc model has not been understood in all of its temporal manifestations. We cannot hope to understand with any depth, or assess the need for, more complex calculations without a better understanding of our baseline modelling.

3

The evolving light curves of tidal disruption events: ASASSN-14li and ASASSN-15lh

The work in this chapter is based upon
Mummery and Balbus 2020a, MNRAS, 492, 5655
Mummery and Balbus 2020b, MNRAS, 497, L13

3.1 Introduction

The stellar concentration of galactic centres are high, and perturbations of the orbits of individual stars by the combined gravitational interactions of the galactic stellar population can occasionally set an unfortunate star onto a near-radial orbit about the central black hole. These stars, upon entering the so-called tidal radius of the central black hole, are destroyed *in their entirety* by the extreme gravitational tidal forces of the black hole's vicinity, an event known as a tidal disruption event (TDE). The debris from such an event are scattered onto different orbits: while some are unbounded and ejected to large radii, a significant fraction of the stellar debris remain bound to the black hole, and will subsequently accrete. The accretion of a sizeable fraction of a solar masses worth of material results in extremely bright flares, observable out to cosmological distances, which originate from previously quiescent galactic centres. These systems, which are inherently relativistic and time dependent, comprise a particularly interesting application of the relativistic disc theory developed in Chapter 2.

It is the purpose of this Chapter to extend the analytical and numerical results of Chapter 2, with the express purpose of developing a model with which tidal disruption event data can be understood and interpreted. Perhaps the most important development is in the treatment of the luminosity, the theoretical luminosity calculations described in Chapter 2 are bolometric, whereas observations are always taken over a well-defined instrumental bandpass. It is of interest therefore to investigate the time dependent emission from the simple 1D relativistic disc models of Chapter 2 over prescribed wavelength intervals. In this work I both use and generalise asymptotic expansion techniques applied to the disc spectral integral to derive rather simple, but fully time-dependent, analytic expressions appropriate to UV and X-ray bandpasses. These are very general results with wide applicability. In principle, such calculations, when fitted to observations, can reveal important properties of both the disc and the host black hole.

As an application, and test, of this asymptotic analysis I develop methods for the fitting and interpretation of observed TDE data. I first present direct data fits to perhaps the best observed and well known TDE ASASSN-14li, so named after the All Sky Automated Survey for Supernova which discovered it. ASASSN-14li was first discovered on 22 November 2014 (Holoien et al. 2016a), with a well identified host galaxy. At a distance of 90 Mpc ASASSN-14li was, at the time of writing, the closest observed TDE in more than a decade. There are high quality UV (Brown et al. 2017, van Velzen et al. 2019b) and X-ray (Bright et al. 2018) observations of ASASSN-14li spanning 1300 and 900 days respectively. Spectrally ASASSN-14li belongs to a so-called 'super-soft' class of TDEs, which are characterised by X-ray spectra that have been well modelled by a blackbody profile (Miller et al. 2015, Brown et al. 2017). The well-sampled light curves and likely thermal origin of the emitted flux makes ASASSN-14li an ideal candidate for our analysis.

The layout of this Chapter is as follows. In section 3.2, I describe the formal problem to be solved, which is to calculate the evolving spectrum from a relativistic thin disc. In section 3.3, I present an asymptotic analysis of the disc spectral integral in a number of physically meaningful limits. The direct fits to the ASASSN-14li light curves are presented in sections 3.4, 3.5 and 3.6. In section 3.4, I describe the underlying relativistic disc model and present fiducial fitted light curves. I find that this model not only provides a significantly improved fit to the observed X-ray light curve of ASASSN-14li when compared to other models in the literature, it also simultaneously fits the late time (final ~ 1200 days) UV emission. In section 3.5, I examine the effect

of varying black hole spin on the best fit light curves, and in section 3.6 I compare the best fit X-ray light curves of discs evolving with a finite and vanishing ISCO stress. In section 3.7 I perform a quantitive comparison of the asymptotic analysis, the best fit numerical light curves and the observed ASASSN-14li light curves.

The current population of TDE sources is notable for its observed variety. As such, in the final sections of this Chapter (sections 3.9–3.11), I model, analyse and discuss the light curves of another TDE candidate ASASSN-15lh. ASASSN-15lh was so chosen as it represents a markedly different 'type' of TDE to ASASSN-14li. ASASSN-15lh is X-ray dim, and its optical, infra red and UV emission have very different evolutionary properties to the more 'canonical' TDE ASASSN-14li. Nonetheless, I demonstrate that the evolving light curves of ASASSN-15lh are also well described as resulting from a relativistic thin disc, which is evolving in a more extreme (but physical) region of TDE parameter space. The results of this Chapter therefore demonstrate that the physical characteristics of relativistic discs can act as the basis for understanding the observed properties of a population of TDEs, a question I return to in later Chapters.

3.2 Relativistic disc spectrum

3.2.1 Dynamical equation

The underlying disc model comprises of the relativistic disc equations examined in Chapter 2, which describe the evolution of the azimuthally-averaged, height-integrated disc surface density $\Sigma(r,t)$. As in Chapter 2, it is convenient to introduce the quantity ζ

$$\zeta \equiv r\Sigma W^{r}{}_{\phi}/U^{0}. \tag{3.1}$$

The governing equation for the evolution of the disc in its most general form is:

$$\frac{\partial \zeta}{\partial t} = \mathcal{W}\frac{\partial}{\partial r}\left(\frac{U^{0}}{U^{0}_{\phi}}\frac{\partial \zeta}{\partial r}\right), \tag{3.2}$$

where the primed notation denotes a radial gradient, and I have defined the stress-like quantity

$$\mathcal{W} \equiv \frac{1}{(U^{0})^{2}}\left(W^{r}{}_{\phi} + \Sigma\frac{\partial W^{r}{}_{\phi}}{\partial \Sigma}\right). \tag{3.3}$$

Once $W^{r}{}_{\phi}$ and $\Sigma(r, t = 0)$ are specified, the evolution of $\zeta(r,t)$ is found with the numerical algorithm described in Chapter 2 and Appendix B.

3.2.2 Spectral integral

The dominant $r\phi$ component of the turbulent stress tensor $W^r{}_\phi$ serves to transport angular momentum outward as well as to extract the free energy of the disc shear, which is then thermalised and radiated from the disc surface. In standard α-disc modelling, which I follow here, both the the extraction and the dissipation are assumed to be local processes. With these assumptions, the profile of the disc surface temperature T is given by (Chapter 2, equation 2.45)

$$\sigma T^4 = -\frac{U^0 U^\phi}{2r}\,(\ln\Omega)'\,\zeta(r,t), \tag{3.4}$$

where σ is the Stefan-Boltzmann constant and

$$\Omega \equiv \frac{\mathrm{d}\phi}{\mathrm{d}t} = \frac{U^\phi}{U^0}. \tag{3.5}$$

By definition, the specific flux density F_ν of the disc radiation, as observed by a distant observer at rest (subscript o), is given by

$$F_\nu(\nu_\mathrm{o}) = \int I_\nu(\nu_\mathrm{o})\,\mathrm{d}\Theta_\mathrm{o}. \tag{3.6}$$

Here, ν_o is the photon frequency and $I_\nu(\nu_\mathrm{o})$ the specific intensity, both measured at the location of the distant observer O. The differential element of solid angle subtended on the observer's sky by a disc element is $\mathrm{d}\Theta_\mathrm{o}$. Since I_ν/ν^3 is a relativistic invariant (Misner et al. 1973), this integral can be related to quantities measured in the disc frame (subscript e) via

$$F_\nu(\nu_\mathrm{o}) = \int f^3 I_\nu(\nu_e)\,\mathrm{d}\Theta_\mathrm{o}, \tag{3.7}$$

where the frequency-shift factor f relates ν_o to the emitted disc frame frequency ν_e:

$$f(r,\phi) \equiv \frac{\nu_\mathrm{o}}{\nu_e} = \frac{p_\mu U^\mu\ (\mathrm{Ob})}{p_\lambda U^\lambda\ (\mathrm{Em})} = \frac{1}{U^0}\left[1 + \frac{p_\phi}{p_0}\Omega\right]^{-1}, \tag{3.8}$$

where (Ob) and (Em) refer to observer and emitter, respectively. The covariant quantities p_ϕ and $-p_0$ (on the far right) correspond to the angular momentum and energy of the *emitted photon* in the local rest frame. These may be conveniently regarded as constants of the motion for a photon propagating through the Kerr metric. Except for special viewing geometries, these quantities must in general be found by numerical ray tracing calculations (see Appendix C).

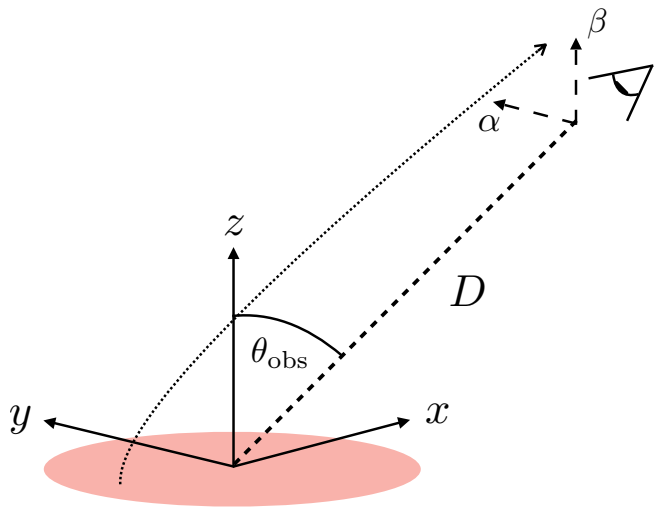

Figure 3.1: Ray tracing geometry. The coordinates α and β lie in the observer plane; x and y lie in the disc plane. A schematic photon trajectory from the inner disc is shown. The observer-disc inclination angle is denoted $\theta_{\rm obs}$.

The disc is assumed to be a multi-temperature black body, with surface temperature $T = T(r, t)$ given by equation (3.4). The specific intensity of the locally emitted radiation is then given by the Planck function B_ν

$$I_\nu(\nu_e) = B_\nu(\nu_e, T) = \frac{2h\nu_e^3}{c^2}\left[\exp\left(\frac{h\nu_e}{k_B T}\right) - 1\right]^{-1}. \tag{3.9}$$

For an observer at a large distance D from the source, the differential solid angle into which the radiation is emitted is

$$\mathrm{d}\Theta_{\rm o} = \frac{\mathrm{d}\alpha\,\mathrm{d}\beta}{D^2}, \tag{3.10}$$

where α and β are the impact parameters at infinity (Li et al. 2005). See Figure 3.1 for further details. The observed flux from the disc surface $\mathcal{S}$ is therefore formally given by

$$F_\nu(\nu_{\rm o}, t) = \int_{\mathcal{S}} f^3 B_\nu(\nu_{\rm o}/f, T)\,\mathrm{d}\Theta_{\rm o}. \tag{3.11}$$

To compare our results with *Swift* X-ray observations the total flux observed across the telescope's bandpass of 0.3 to 10 keV must be computed (F_X). This is easily calculated by integrating (3.11) over the corresponding (observer) frequency range:

$$F_X(t) = \int_{\nu_l}^{\nu_u}\int_{\mathcal{S}} f^3 B_\nu(\nu_{\rm o}/f, T)\;\mathrm{d}\Theta_{\rm o}\;\mathrm{d}\nu_{\rm o}. \tag{3.12}$$

Where ν_l and ν_u correspond to the lower (0.3 keV) and upper (10 keV) frequencies of the *Swift* telescope X-ray band. Note that f will generally depend upon α and β. With T given by equations 3.2 and 3.4, and ray tracing calculations determining $f(\alpha, \beta)$, the observed spectrum may be obtained with relativistic effects (kinematic and gravitational Doppler shifts, and gravitational lensing) included. These are needed for detailed comparison with observations at X-ray wavelengths. Finally, I note that radiative transfer physics such as absorption and Compton scattering of photons as they pass through the disc atmosphere has been ignored, a simplification that is often made. For spectrally 'super-soft' TDEs like ASASSN-14li these corrections are likely to be modest, as any large effects would result in noticeable deviations from simple integrated blackbody spectra. A more detailed radiative treatment is of interest, and will be returned to in Chapter 4.

3.3 Asymptotic analysis

3.3.1 Effective temperature

The canonical thermal accretion disc spectrum is by now well known: a low frequency Rayleigh-Jeans tail, an intermediate frequency power law section (arising from a superposition of blackbody emission peaks), and a high frequency, quasi-Wien tail. The relativistic case considered here is broadly similar, but with important distinctions in detail.

Begin by recasting the equations 3.11 and 3.12 into a somewhat more classical form by defining an "effective temperature" $\widetilde{T}$ by

$$\widetilde{T}(\alpha, \beta, t) = f(\alpha, \beta)\, T\Big(r(\alpha, \beta), t\Big). \tag{3.13}$$

This leads to

$$F_\nu(\nu_\mathrm{o}, t) = \frac{2h\nu_o^3}{c^2} \int_\mathcal{S} \left[\exp\left(h\nu_\mathrm{o}/k_B\widetilde{T}\right) - 1\right]^{-1} \mathrm{d}\Theta_\mathrm{o}, \tag{3.14}$$

and

$$F_X(t) = \int_{\nu_l}^{\nu_u} \int_\mathcal{S} \frac{2h\nu_\mathrm{o}^3}{c^2} \frac{\mathrm{d}\Theta_\mathrm{o}\, \mathrm{d}\nu_\mathrm{o}}{\exp(h\nu_\mathrm{o}/k_B\widetilde{T}) - 1}. \tag{3.15}$$

The high photon energy behaviour ($h\nu_\mathrm{o} \gg k_B\widetilde{T}$) of equation 3.14 may be found analytically by an asymptotic expansion of these integrals, without any detailed knowledge of the underlying disc model (Balbus 2014). By contrast, at intermediate

photon energies, knowledge of the spatial and temporal behaviour of T is required, as are solutions of the relativistic evolution equation 3.2. Approximate analytic solutions of the latter are discussed below.

3.3.2 Self-similar disc solutions

As a second order differential equation, equation 3.2 has two independent solutions. In Chapter 2 I showed that the gross properties of relativistic discs can be understood by self-similar solutions of the simpler, large r, Newtonian evolution equation. The key point is that the inner boundary condition, which is determined by the ISCO stress, directly affects the behaviour of the disc in the outer zone.

Self-similar solutions exist when the turbulent stress is of the form

$$W^r{}_\phi = w \left(\frac{\Sigma}{\Sigma_0}\right)^\eta \left(\frac{r}{r_0}\right)^\mu, \tag{3.16}$$

which is applicable to a rather wide range of turbulent disc models, including classical α-discs (Shakura and Sunyaev 1973). (The length r_0 and density Σ_0 are set by the initial conditions.) In terms of the dimensionless space and time variables $x = r/r_0, \tau = t/t_{\rm visc}$, the solutions have the general form (Pringle 1991, Chapter 2):

$$\Sigma = \Sigma_0\, \xi^\omega (1 - k\xi^\theta)^{1/\eta}\, x^{-3/2}\, \tau^{-\chi}, \quad \xi = x^{1/2}\, \tau^{-\lambda}. \tag{3.17}$$

The coefficients may be expressed in terms of η and μ (Pringle 1991, Chapter 2). Substituting the Newtonian self-similar solutions into the temperature equation 3.4 leads, after algebraic simplification, to a disc temperature profile of the form

$$T(x,\tau) = T_0\; x^{-m}\, \tau^{-n/4}\, \psi(x,\tau), \tag{3.18}$$

where

$$T_0 = \left(\frac{3w\Sigma_0}{4\sigma}\sqrt{\frac{GM}{r_0^5}}\right)^{1/4}, \tag{3.19}$$

and

$$\psi(x,\tau) = \left(1 - k\, x^{\theta/2}\tau^{-\lambda\theta}\right)^{(1+\eta)/4\eta}. \tag{3.20}$$

The power law indices m and n are given by, for a finite ISCO stress

$$m = 7/8, \tag{3.21}$$

$$n = \frac{4\eta + 2 - 2\mu}{4\eta + 3 - 2\mu}, \tag{3.22}$$

and for a vanishing stress

$$m = 3/4, \tag{3.23}$$

$$n = \frac{5\eta + 4 - 2\mu}{5\eta + 3 - 2\mu}. \tag{3.24}$$

The index n is the same index that appears in the bolometric luminosity $L \sim t^{-n}$. I remind the reader that while n depends only rather weakly on η and μ, it depends more sensitively upon the ISCO stress: $n \approx 0.8$ for finite ISCO stress modes versus $n \approx 1.2$ for vanishing ISCO stress modes. When confusion may arise from the different values of 'n', I shall denote the finite ISCO stress decay index (equation 3.22) by n_f, and the vanishing ISCO stress decay index by n_v (equation 3.24).

3.3.3 Rayleigh-Jeans limit

The Rayleigh-Jeans limit describes the lowest frequency part of the spectrum, where $h\nu_{\rm o} \ll k_B\widetilde{T}$ for all effective temperatures within the disc. At these frequencies the exponential may be expanded:

$$\exp\left(h\nu_{\rm o}/k_B\widetilde{T}\right) - 1 = h\nu_{\rm o}/k_B\widetilde{T} + \ldots, \tag{3.25}$$

and thus the time dependence of the Rayleigh-Jeans flux follows that of the disc temperature. At late times, equations 3.14 and 3.18 result in

$$F_\nu(\nu_{\rm o}, t) \sim \nu_{\rm o}^2\, t^{-n/4}. \tag{3.26}$$

3.3.4 Mid-range frequencies

Each disc radius has both a characteristic temperature (equation 3.18) and characteristic emission frequency $\nu \sim k_B T/h$. At intermediate frequencies where $T_{\rm out} \ll h\nu/k_B \ll T_0$ (here $T_{\rm out}$ is a typical temperature of the outer disc) the flux originates primarily from (Newtonian) regions where the self-similar solutions (equation 3.17) are a good approximation. In this regime, relativistic Doppler shifts are negligible ($f \simeq 1$) and gravitational optics unimportant: photons travel in nearly straight lines. This allows a further simplification of the integrals by using the standard Newtonian form for the differential solid angle of emission

$$\mathrm{d}\Theta_o = \frac{\mathrm{d}\alpha\,\mathrm{d}\beta}{D^2} = \frac{2\pi r}{D^2}\cos\theta_{\rm obs}\,\mathrm{d}r\,. \tag{3.27}$$

In this limit, the flux can be written as an integral over the dimensionless disc radius $x = r/r_0$ from a suitable inner radius $x_{\rm in}$ to the outer radius $x_{\rm out}$:

$$F_\nu(\nu_o, t) = A \int_{x_{\rm in}}^{x_{\rm out}} x \left[\exp\left(\frac{\epsilon x^m \tau^{n/4}}{\psi(x,\tau)} \right) - 1 \right]^{-1} {\rm d}x \,, \tag{3.28}$$

where the constants A and ϵ are given by

$$A = 4\pi h r_0^2 \nu_o^3 \cos\theta_{\rm obs}/(c^2 D^2), \quad \epsilon = h\nu_o/k_B T_0. \tag{3.29}$$

At late times, the dominant contribution of the mid-frequency flux comes from radii where $x^{1/2}\,\tau^{-\lambda}$ is small and $\psi \simeq 1$. With little contribution coming from either large or small radii, to leading order the limits of integration can be extended from 0 to ∞, and the integral becomes

$$F_\nu \simeq A \int_0^\infty x \left[e^{\epsilon x^m \tau^{n/4}} - 1 \right]^{-1} {\rm d}x. \tag{3.30}$$

This may be evaluated explicitly:

$$F_\nu = \frac{A}{m}\, \Gamma\left(\frac{2}{m}\right)\, \zeta_{\mathcal{R}}\left(\frac{2}{m}\right)\, \epsilon^{-2/m} \tau^{-n/2m} \sim \nu_o^{3-2/m}\, t^{-n/2m}, \tag{3.31}$$

where Γ and $\zeta_{\mathcal{R}}$ are the standard Gamma and Riemann zeta functions respectively (cf. Lynden-Bell 1969). For the finite ISCO stress mode $m = 7/8$, and the observed flux is

$$F_\nu(\nu_o, t) = 1.9039\, A \epsilon^{-16/7} \tau^{-4n_f/7} \sim \nu_o^{5/7} t^{-4n_f/7}, \tag{3.32}$$

whereas for the case of vanishing ISCO stress:

$$F_\nu(\nu_o, t) = 2.5762\, A \epsilon^{-8/3} \tau^{-2n_v/3} \sim \nu_o^{1/3} t^{-2n_v/3}. \tag{3.33}$$

The frequency dependence $F_\nu \sim \nu^{5/7}$ that is characteristic of a finite ISCO stress arises directly from the modified $T \sim r^{-7/8}$ temperature profile (cf. Agol and Krolik 2000). For a vanishing stress disc $T \sim r^{-3/4}$ and I recover the classic Lynden-Bell (1969) $F_\nu \sim \nu^{1/3}$ scaling. Thus, the mid-frequency spectral slope of a black hole disc contains information regarding the properties of the disc's ISCO stress. In Chapter 5, I discuss recent observations providing strong evidence for a finite ISCO stress from quasar disc observations (Weaver and Horne 2022).

3.3.5 Evolution of the mid-frequency spectral shape

These results suggest that when observed at frequencies below the thermal spectrum peak, some care is required when extracting the exact time dependence of the observed flux in a narrow observational band. As the disc cools and expands, the spectrum peaks at lower frequencies and decreases in overall magnitude. The peak frequency ν_p is related to the peak effective temperature by

$$\nu_p \sim \frac{k_B \widetilde{T}_p}{h} \sim t^{-n/4}. \tag{3.34}$$

(I have used equation 3.18 for the time dependence of $\widetilde{T}_p$; see section 3.3.6 below for further discussion.) Below the peak of the spectrum, the flux increases as a power law with ν (equations 3.32 and 3.33). The shifting of the peak of the spectrum to lower frequencies combined with a decreasing overall magnitude of the spectrum means that the observed flux at a particular frequency (or in a surrounding narrow band) will tend to remain nearly constant—or even increase—with time. Only at much later times will the observed flux follow the power-law declines derived earlier (equations 3.32 and 3.33). As I shall demonstrate, this subtle behaviour appears to present in the observed narrow band light curves of ASASSN-14li.

3.3.6 Quasi-Wien limit

The quasi-Wien limit of the disc spectrum is characterised by the largest photon energies,

$$h\nu_o \gg k_B \widetilde{T}_p. \tag{3.35}$$

In this limit, all of the emission is strongly concentrated near the temperature maximum, and the denominator of equation 3.14 may be simplified by neglecting the -1, since this introduces only exponentially small corrections. The flux is then formally given by

$$F_\nu(\nu_o, t) = \frac{2h\nu_o^3}{D^2 c^2} \iint_{\mathcal{S}} \exp\left(-h\nu_o / k_B \widetilde{T}\right) \, \mathrm{d}\alpha \, \mathrm{d}\beta. \tag{3.36}$$

Since only the hottest parts of the disc very near the temperature maximum contribute to the observed flux, the integral may be evaluated using Laplace's method (e.g. Bender and Orszag 1978). I follow Balbus (2014) by Taylor expanding the inverse of the effective temperature about the effective temperature maximum.

The finer details of this expansion will depend both on the properties of the ISCO stress (which affect the location of the disc temperature maximum), and the disc viewing angle (which affects the projected geometry of the hot inner disc). Current models of TDE evolution suggest that there should be a rather strong viewing angle dependence of the observed flux, with observable X-ray emission only when the disc is orientated near face-on (Dai et al. 2018). I shall therefore assume here that the disc is oriented nearly face-on. Asymptotic solutions of equation 3.36 may be straightforwardly obtained for different disc orientations and ISCO stress assumptions; these are presented in section 3.6 (vanishing ISCO stress), and Appendix E (different orientation angles).

For a face-on disc, there is little kinematic Doppler shifting of the observed radiation, and the effective temperature profile is therefore azimuthally symmetric in the image plane. The effective temperature may therefore be expanded in the radial image plane coordinate R:

$$R \equiv \sqrt{\alpha^2 + \beta^2}. \tag{3.37}$$

The leading order expansion of the effective temperature is then

$$\frac{1}{k_B \widetilde{T}} = \frac{1}{k_B \widetilde{T}_p} + \frac{1}{k_B \widetilde{T}_p^2} \left| \frac{\partial \widetilde{T}}{\partial R} \right|_{R_p} (R - R_p) + ... \tag{3.38}$$

where I have used the fact that for a disc with a finite ISCO stress the peak temperature $\widetilde{T}_p$ lies on the inner disc boundary at radial coordinate R_p in the image plane. For clarity, the (negative) temperature gradient appears here as an absolute value. It is possible to expand the observed flux to arbitrarily high powers of the small parameter

$$\delta \equiv \frac{k_B \widetilde{T}_p}{h\nu_o} \ll 1, \tag{3.39}$$

by keeping higher order terms in the Taylor expansion (equation 3.38). I will demonstrate, however, that for present purposes the leading order behaviour is sufficient, before returning to this expansion in Chapter 4. While all of the spatial dependence of the effective temperature is explicit in equation (3.38), it is important to remember that the peak effective temperature and effective temperature gradient are time-dependent quantities. Substitution of (3.38) into (3.36) leaves

$$F_\nu(\nu_o, t) = \frac{4\pi h \nu_o^3}{D^2 c^2} \exp\left(-\frac{h\nu_o}{k_B \widetilde{T}_p}\right) \int_{R_p}^{\infty} R \exp\left(-\frac{h\nu_o}{k_B \widetilde{T}_p^2} \left| \frac{\partial \widetilde{T}}{\partial R} \right|_{R_p} (R - R_p)\right) \mathrm{d}R. \tag{3.40}$$

The integral is now elementary. I define the order unity numerical constant ξ by

$$\xi \equiv \frac{R_p}{\widetilde{T}_p}\left|\frac{\partial \widetilde{T}}{\partial R}\right|_{R_p}, \tag{3.41}$$

which enters the expression for the flux as a normalisation factor. (For a finite ISCO stress Newtonian disc, $\xi = 7/8$, independent of time.) The resulting high frequency spectrum is

$$F_\nu(\nu_o, t) = \frac{4\pi}{\xi c^2}\left(\frac{R_p}{D}\right)^2 \left(\frac{k_B \widetilde{T}_p}{h\nu_o}\right) h\nu_o^3 \exp\left(-\frac{h\nu_o}{k_B \widetilde{T}_p}\right), \tag{3.42}$$

where the implicit time dependence of the flux enters via the disc temperature. The integral over the X-ray frequency band then follows straightforwardly:

$$F_X(t) = \int_{\nu_l}^{\infty} F_\nu(\nu_o, t)\, \mathrm{d}\nu_o, \tag{3.43}$$

where the lower limit ν_l corresponds to 0.3 keV for the *Swift* ASASSN-14li observations, and the upper integration limit is set to infinity (introducing only exponentially small corrections). This gives to lowest order

$$F_X(t) = \frac{4\pi}{\xi c^2}\left(\frac{R_p}{D}\right)^2 \left(\frac{k_B \widetilde{T}_p}{h\nu_l}\right)^2 h\nu_l^4 \exp\left(-\frac{h\nu_l}{k_B \widetilde{T}_p}\right), \tag{3.44}$$

which is quadratic in the small parameter δ.

Next I revisit the question raised in section 3.5, namely what form does the time dependence of the peak disc temperature take? With x_p fixed, in a Newtonian disc the peak temperature follows a simple power law in time $T_p \sim t^{-n/4}$ (equation 3.18). In a relativistic disc, the temperature in the innermost regions is not in general given by equation 3.18. However, the temporal behaviour of the disc temperature in the innermost regions is unlikely to be systematically different from that of the outer disc, since the Newtonian and relativistic regimes of the disc must join smoothly at all times. I therefore assume a peak temperature functional form of

$$\widetilde{T}_p(t) \equiv \mathcal{T}_p\, \tau^{-n/4}, \tag{3.45}$$

where $\mathcal{T}_p$ is a constant with dimensions of temperature and τ is the time in units of the viscous time scale. The viscous timescale τ for a Green's function solution is defined in terms of the initial radius r_0 (e.g., equation 2.138), and could in principal include

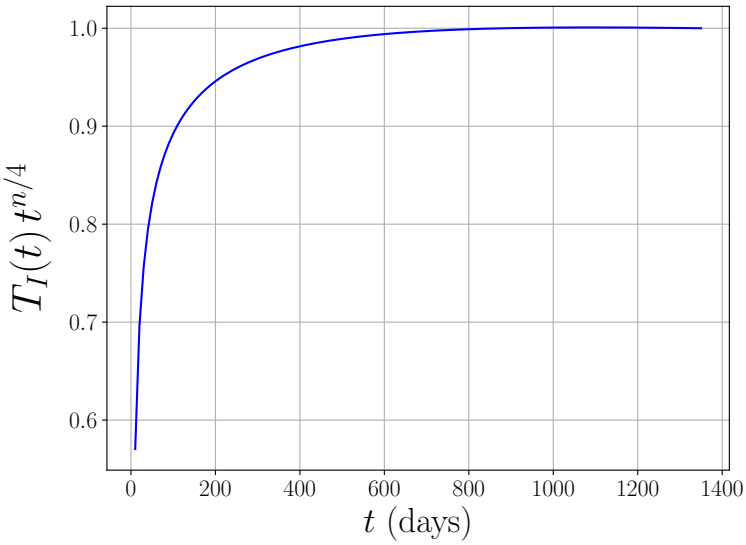

Figure 3.2: ISCO temperature versus time. The approximation of equation 3.45 is valid to within a few percent after 200 days. The y-axis is normalised so as to equal 1 at a time corresponding to the end of the available observations of ASASSN-14li. This plot was produced with $n = 0.86$.

a time offset t_0 to provide a finite X-ray luminosity as $t \to 0$. This assumption has been checked and explicitly verified by exact numerical calculation (Figure 3.2). This result now allows the explicit time dependence of F_ν and F_X to be calculated:

$$F_\nu(\nu_o, t) = \frac{4\pi}{\xi c^2}\left(\frac{R_p}{D}\right)^2 \left(\frac{k_B \mathcal{T}_p}{h\nu_o}\right) h\nu_o^3\, \tau^{-n/4} \exp\left(-\frac{h\nu_o}{k_B \mathcal{T}_p}\tau^{n/4}\right), \tag{3.46}$$

and

$$F_X(t) = \frac{4\pi}{\xi c^2}\left(\frac{R_p}{D}\right)^2 \left(\frac{k_B \mathcal{T}_p}{h\nu_l}\right)^2 h\nu_l^4\, \tau^{-n/2} \exp\left(-\frac{h\nu_l}{k_B \mathcal{T}_p}\tau^{n/4}\right), \tag{3.47}$$

with $n \approx 0.8$. The underlying assumptions of equation (3.47) are:

1. The emission is well approximated as thermal (eq. 3.11).
2. The emission is in the quasi-Wien limit, $h\nu_l \gg k_B \mathcal{T}_p$.
3. The peak disc temperature follows $T_p \sim t^{-n/4}$.
4. The peak temperature occurs at the innermost disc edge.
5. The disc is viewed close to face-on.

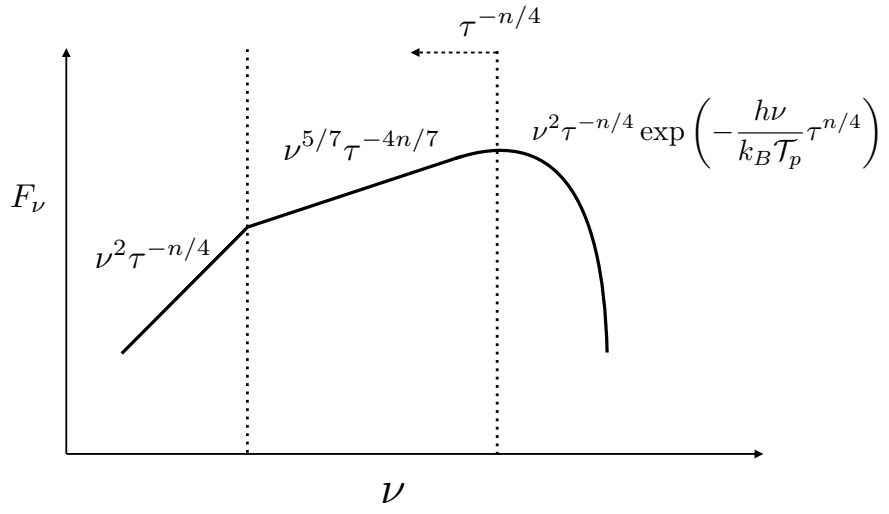

Figure 3.3: A schematic finite ISCO stress disc spectrum. The low, mid, and high frequency asymptotic regimes are delineated. (The effects of the evolving boundaries between the frequency domains may be seen in the numerical solutions displayed in Figure 3.12.)

Note that, for the solutions under consideration, the assumption that the peak temperature lies at the inner disc edge is, in effect, equivalent to assuming a finite ISCO stress. These results are likely to be valid under conditions rather more general than the thin disc model *per se*. In Appendix E I present analytic expressions for the time dependent X-ray emission, relaxing the final approximation. The functional form of the X-ray flux (equation 3.47) turns out to be rather insensitive to the precise viewing angle.

3.3.7 Summary

The observed flux in several diffrent limits of physical interest may be obtained by taking appropriate expansions of the disc flux integral (Figure 3.3). I find that even if the bolometric luminosity follows a simple power law decline $L \sim t^{-n}$, the observed finite bandpass flux will always have a different temporal behaviour. For example, if X-ray observations probe the quasi-Wien tail of the evolving disc spectrum, then rather than a power law decay, the X-ray light curves of transient disc sources is described by a function of the form

$$F_X(t) = F_0 \left(\frac{t+t_0}{t_X}\right)^{-n/2} \exp\left[-\left(\frac{t+t_0}{t_X}\right)^{n/4}\right], \tag{3.48}$$

with $n \approx 0.8$, and F_0, t_0 and t_X time-independent constants. At the very largest times the X-ray light curve becomes dominated by an exponential of a power law in time, with power law index less than 1 in magnitude. I therefore quite generally expect the X-ray luminosity of a TDE source to follow a decline that is steeper than a power-law, but more shallow than a pure exponential. Furthermore, if the UV luminosity is dominated by disc emission, this bandpass should be characterised by a nearly constant luminosity. This (perhaps) counterintuitive results stems from the combination of a decreasing temperature coupled with an increasing radial extent that places the peak of emission at smaller frequencies. At frequencies below but near the peak frequency of the disc spectrum, the observed flux remains near constant. These results will be discussed in detail in section 3.7.

3.4 ASASSN-14li numerical disc model

3.4.1 Observations

How well can a thin disc model explain the spectral observations of the confirmed TDE, ASASSN-14li (Holoien et al. 2016a), at both UV and X-ray wavelengths? The X-ray observations used here are taken from Bright et al. (2018), and are publicly available. The UV observations, predominantly taken from Brown et al. (2017), also use late time observations from van Velzen et al. (2019b). The UV observations span ~ 1300 days, the X-rays ~ 900 days. The observations are host-subtracted: I shall assume that all of the remaining flux is intrinsic flux from the TDE source.

The numerical technique is straightforward. One specifies a set of black hole properties (M, a) and disc parameters [$\Sigma(t = 0)$, W^r_ϕ], and solves the evolution equation (3.2) for the time-dependent disc temperature (3.4). For a given disc inclination angle $\mu = \cos(\theta_{\rm obs})$, ray tracing calculations allow the observed redshift (3.8) to be calculated. I calculate spectra at (narrow band) UV and (broad band) X-ray wavelengths. Such simultaneous fits at frequencies which differ by two orders of magnitude tightly constrain the model parameters (Appendix D).

The X-ray flux is given by (equation 3.12). For the narrower UV bands, I simply compute the evolving flux at the central wavelength of each UV band. For the three *Swift* bands of interest (UVW1, UVW2 and UVM2) these are[1] :

$$\bar{\lambda}_{W1} = 260.0\,\mathrm{nm}, \quad \bar{\lambda}_{M2} = 224.6\,\mathrm{nm}, \quad \bar{\lambda}_{W2} = 192.8\,\mathrm{nm}. \tag{3.49}$$

The UV results are presented as evolving AB magnitudes, where

$$m_{AB}(\bar{\lambda}, t) \equiv -2.5 \log_{10}\left[F_\nu\left(c/\bar{\lambda}, t\right)\right] - 48.60. \tag{3.50}$$

Here, F_ν is calculated from equation (3.11), and has units of erg/s/cm^2/Hz. This approach ignores any effects from the actual finite width of the UV bands, which are likely to be unimportant for present purposes. The UV bands are displayed as vertical lines in Figure 3.5 along with a disc spectrum, computed 200 days after disc formation using the best fit parameters.

3.4.2 Model parameters

In general, there are nine parameters which completely specify an evolving disc model. These parameters, which are described below, describe the observer orientation, the initial disc conditions, the turbulent stress, and the mass and angular momentum of the central black hole.

Observer parameters

This distance to the source serves as an overall normalisation of the observed flux, one that often is not necessarily accurately known. The distance to ASASSN-14li is however, it is tightly constrained by its well identified host galaxy: PGC 043234 (Holoien et al. 2016a), at a distance $D = 90$ Mpc. The disc-observer inclination angle is unknown for ASASSN-14li. As earlier noted, current TDE models suggest that sources observed at X-ray wavelengths are expected to be orientated near face-on, $\theta_{\rm obs} \lesssim 20^\circ$ (Dai et al. 2018). Given the lack of observational constraints and the expectation of a near face-on orientation, I shall assume for simplicity that $\cos(\theta_{\rm obs}) = 1$. In principle, this approach could be readily extended to model the observed X-ray and UV fluxes for a variety of different viewing angles.

[1] http://www.swift.ac.uk/analysis/uvot/filters.php

Central black hole parameters

A stationary black hole is completely described by exactly two parameters: its mass and spin. The mass of the central black hole is somewhat constrained by previous observations. Using measurements of the host galaxy's bulge mass and standard SMBH-host galaxy scaling relationships, Mendel et al. (2014) derived a black hole mass of $M \sim 10^{6.7\pm0.6} M_{\odot}$. Somewhat tighter constraints were found by Wevers et al. (2017), who performed velocity dispersion measurements and found a black hole mass of $M = 10^{6.23\pm0.4} M_{\odot}$. On the other hand, using Eddington-limit arguments Miller et al. (2015) inferred a mass of $M \sim 2 \times 10^6 M_{\odot}$. As these relationships are broadly uncertain, in the model fitting I have allowed the black hole mass to vary within the range $10^5 M_{\odot} < M < 10^7 M_{\odot}$.

The angular momentum of the central black hole is even less tightly constrained by observations. Pasham et al. (2019) reported a recent measurement of quasi-periodic oscillations (QPOs) in the observed ASASSN-14li X-ray spectrum. This was used to set upper and lower bounds on the black hole parameters: a high prograde spin ($a/r_g > 0.7$), and a mass less than $M = 2 \times 10^6 M_{\odot}$. However, the exact black hole mass and spin parameters inferred from QPO measurements are heavily dependent upon the underlying model for the origin of the QPO, something that is at present uncertain. (Pasham et al. (2019) assume an orbiting test particle model.) Here, I shall present my own analysis of the angular momentum of the ASASSN-14li black hole. In the following section I model the spectral fits for a somewhat more slowly rotating Kerr black hole, $a/r_g = 0.5$. In section 3.5 I examine the effect of varying the black hole's spin on the evolving disc light curves.

Turbulent stress modelling

As in Chapter 2, I will use a turbulent stress of the general form

$$W^r{}_{\phi} = w \left(\frac{\Sigma}{\Sigma_0} \right)^{\eta} \left(\frac{r}{r_0} \right)^{\mu}. \tag{3.51}$$

The precise parameterisation of $W^r{}_{\phi}$ affects the time dependent properties of the disc in two ways. The first is through its effects on the bolometric decay index n. This enters several expressions for the time dependent flux at a number of different wavelengths (e.g., equations 3.32 & 3.47). The value of n depends only weakly on the exact parameterisation of the stress (the indices $\eta \,\&\, \mu$), while it is strongly dependent

on the nature of the stress at the ISCO. Because of the limited effect of the exact turbulent stress parameterisation on the decay index n, I employ a simple self-similar turbulent stress model $W^r{}_\phi = w = \text{constant}$ (i.e, $\eta = \mu = 0$) in this Chapter. This model is also physically rather natural: it would emerge, for example, if the turbulent velocity fluctuations follow a Keplerian scaling of the form $\delta v^r \sim \delta v^\phi \sim r^{-1/2}$.

I shall assume that the stress is *finite* at the ISCO. To avoid unsustainable behaviour at lates times, I follow the 'quasi-circular' orbit approach developed in Chapter 2. This allows for deviations in the mean fluid motion of the disc from that of exact Kerr-circular orbits. These deviations must of course be present at some level, as a consequence of non-zero radial velocities in the innermost disc regions. The degree to which the mean fluid motion deviates from perfect circular orbits may be parameterised by a dimensionless number, denoted as γ. The γ parameter is defined by

$$\gamma \equiv \frac{\Delta j \, u^r}{W^r{}_\phi}, \tag{3.52}$$

where u^r and $W^r{}_\phi$ are the radial velocity and turbulent stress measured at the ISCO, and Δj is the difference in the disc fluids ISCO angular momentum from that of a circular orbit. A finite ISCO stress disc model with precisely circular orbits would therefore have $\gamma = 0$, whereas a vanishing ISCO stress disc must have $\gamma \to \infty$. The properties of γ cannot as yet be calculated from first principles. I therefore must rely on simulations to determine its value and variability. Current estimates based upon GRMHD simulations (Noble et al. 2010) place γ within the range $0.01 < \gamma < 0.1$. I adopt the midpoint of this range, $\gamma = 0.05$. The dimensionless parameter γ sets the time scale over which the finite ISCO stress modes (equation 3.17) dominate the behaviour of the disc. For small γ, the disc evolution is dominated by these modes for the entire ASASSN-14li observational period.

The next important parameter is the magnitude of the turbulent stress, w. For an evolving disc, w sets the duration of the "viscous" timescale t_v. For this choice of η and μ, t_v is given by

$$t_v = 2\sqrt{GMr_0^3}\Big/9w, \tag{3.53}$$

where r_0 is a radius of the the initial disc ring. The stress amplitude w is determined from a best fit to the viscous evolution timescale, calculated using the above.

Disc initial condition

The actual event which produced ASASSN-14li was not observed. The source was first observed on 22 November 2014. Prior to this date, its host galaxy PGC 043234 had not been observed since the 13th of July 2014, when no TDE was present, as the sun was obscuring this galaxy. This leaves a 132 day window between observations within which the initial disruption could have occurred. I therefore leave the 'disc formation time' t_D (the time at which I begin the disc evolution), as an additional free parameter:

$$-132 < t_D - 56983.6\,(\mathrm{MJD}) < 0, \tag{3.54}$$

where 56983.6 MJD corresponds to the Julian Date of the first recorded observation.

I take the initial density distribution of the disc to be a numerical delta function at a fixed radius of $r_0 = 15r_g$. This radius is equal to the tidal radius of a main sequence star with the mean stellar mass $M_\star = 0.36M_\odot$ (Kroupa 2001) around a $2 \times 10^6 M_\odot$ black hole, the best estimate of the black hole mass prior to fitting.

The process of disc formation post-TDE is dynamically complex. In reality, the initial matter distribution will depend upon the structure and orbit of the pre-disruption star and the mass and spin of the central black hole. This initial condition is thus an idealisation. However, the behaviour of disc light curves post-peak are in fact well-described by sets of self-similar solutions (equation 3.17), and these have lost memory of the initial conditions. Comparisons to the post-peak observations of ASASSN-14li are thus likely to be insensitive to the precise spatial form of the initial density distribution.

The final fitting parameter is the initial mass of the disc, calculated by

$$M_d = 2\pi \int_{r_I}^{\infty} (g_{rr} g_{\phi\phi})^{1/2}\, \gamma^{\phi}(r, a)\, \Sigma(r, t = 0)\, \mathrm{d}r. \tag{3.55}$$

Here γ^ϕ is a relativistic factor relating the disc area element in the rotating disc frame to that of the Boyer-Lindquist co-ordinate system (see Bardeen et al. (1972) for a discussion).

$M/M_\odot$	$1.85^{+0.03}_{-0.04} \times 10^6$
$M_d/M_\odot$	$1.63^{+0.07}_{-0.02} \times 10^{-2}$
$t_D - 56983.6$ (MJD)	-43.6^{+5}_{-7}
t_v (days)	$44.3^{+2.0}_{-2.4}$
$\bar{\chi}^2_{\rm min}$	6.19

Table 3.1: The best fit parameters for the fiducial disc model, and the reduced chi-squared of the best fit X-ray light curve. For comparison, the reduced chi-squared of the best fit power-law fit is $\bar{\chi}^2_{\rm pl} = 13.99$, and $\bar{\chi}^2_{\rm exp} = 8.54$ for an exponential fit. The formally large reduced chi-squared values are discussed further in section 3.4.6.

a/r_g	0.5
r_0/r_g	15
γ	0.05
D/Mpc	90
$\cos(\theta_{\rm obs})$	1

Table 3.2: Parameters fixed during fitting.

3.4.3 Best fit parameters

Table 3.1 summarises the best fit disc parameters for the recorded observations of ASASSN-14li. Table 3.2 summarises the parameters that remained fixed for the fitting procedure. The four fitted parameters may be divided into two categories: those that predominantly affect the evolutionary time scale of the system, and those that set the overarching scale of the emission.

The viscous time scale of the evolving disc t_v and the disc formation time t_D are well constrained by the X-ray observations, which are strongly time varying. The best fit time offset t_D is also consistent with an independent estimate of the TDE start time from radio observations (Alexander et al. 2016), which must pre-date the disc formation time.

The remaining two parameters, the disc mass M_d and the black hole mass M, are then constrained by the simultaneous fitting of the observed magnitudes of the UV flux and X-ray luminosity. Fitting either band independently is relatively easy, but this leaves large degeneracies in the fitted parameters. This degeneracy is broken only when the light curves are fitted *simultaneously.* See Appendix D for further detail and discussion.

It is extremely encouraging that the best fit black hole mass $M = 1.85 \times 10^6 M_\odot$ is consistent with a number of existing estimates ($M \sim 2 \times 10^6 M_\odot$ Miller et al. (2015), $M \lesssim 2 \times 10^6 M_\odot$ Pasham et al. (2019), $M = 10^{6.23 \pm 0.4} M_\odot$ Wevers et al. (2017) and $M = 10^{6.7 \pm 0.6} M_\odot$ Mendel et al. (2014)). These estimates comprise a wide range of very distinct methods of evaluating the black hole mass.

The best fit disc mass, at $M_d = 1.63 \times 10^{-2} M_\odot$, appears at first to be rather small. Rees (1988) suggests $M_d \sim M_\star/2$, where $M_\star$ is the mass of the star prior to disruption. However, it is important to distinguish the inferred disc mass of this model with the total mass fraction of the debris which remains gravitationally bound in the aftermath of the TDE. The model disc mass is in reality a *lower bound* of the total debris mass, as it represents only the total evolving mass required to reproduce the 900 days of observed X-ray emission and the late time UV emission.

The observed UV and X-ray light curves are by no means the only emission stemming from ASASSN-14li. For example, ASASSN-14li is also a source of significant radio emission (van Velzen et al. 2016, Bright et al. 2018), which presumably stems from the presence of a jet or an outflow launched at early times. An additional, rapidly decaying, light curve component is also required at early times to match the observations of ASASSN-14li at UV wavelengths (this will be discussed further in section 3.4.7). Neither the mass content of the jet/outflow or this additional UV component contribute to the best fit model disc mass. Hence, the actual debris mass is likely to be significantly larger than this mass value.

The small disc-to-debris mass ratio could be naturally explained if, preceding its first observation, ASASSN-14li was accreting at super-Eddington rates. The likely outflow launched by these high luminosities would then produce a large and transient early time UV flux, whilst removing much of the debris mass, leaving a more tightly bound, lower mass disc behind. In this case, the bolometric luminosity of the disc would be expected to be near the Eddington limit at times close to the first observation. This prediction will be examined further in section 3.4.9.

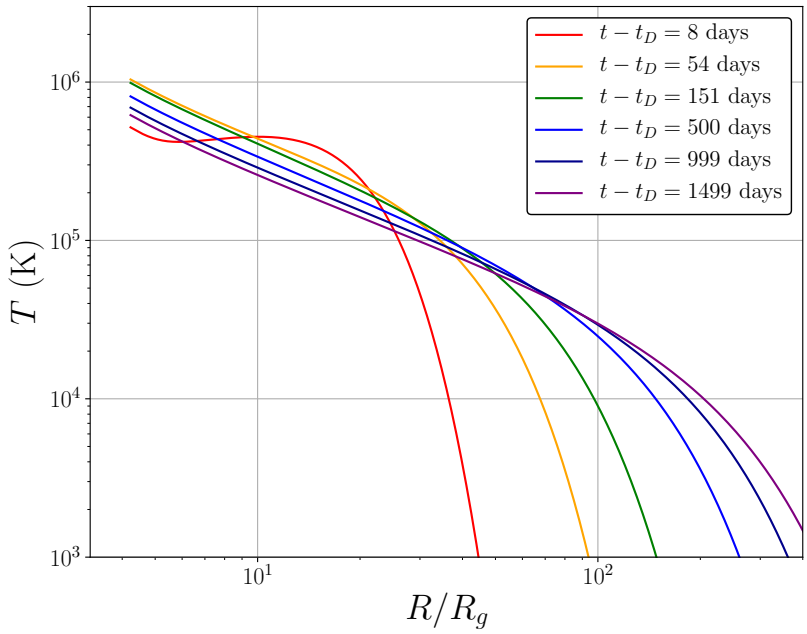

Figure 3.4: Snapshots of the disc temperature profile at a number of different times (denoted on plot) for the best fit model.

Finally, it is difficult to determine or constrain properties of the initial disc distribution, absent early time observations. The temporal peak of the best fit X-ray light curve coincides with the peak of the observed X-ray light curve (Figure 3.6). There is additional uncertainty here: if the X-ray flare were significantly more luminous at times preceding the first observation, the best fit mass could be significantly larger (so as to increase the inner disc temperatures and emitted X-ray flux).

The dynamical physics of post TDE disc formation are still poorly understood. The results of this section suggests that only a small fraction of the stellar material settles into an evolving disc at radii close to the black hole. The fate of the majority of the stellar mass thus remains an interesting and open question.

3.4.4 Disc evolution

The evolution of the disc is qualitatively rather simple, as seen in Figure 3.4. The temperature in the innermost regions reaches its evolutionary maximum on a simple viscous timescale. This is due to disc material rapidly spreading inwards towards the ISCO. Once the disc density reaches a maxima in the inner regions the disc enters the 'stalled-phase' of accretion (Chapter 2). This evolutionary phase is characterised

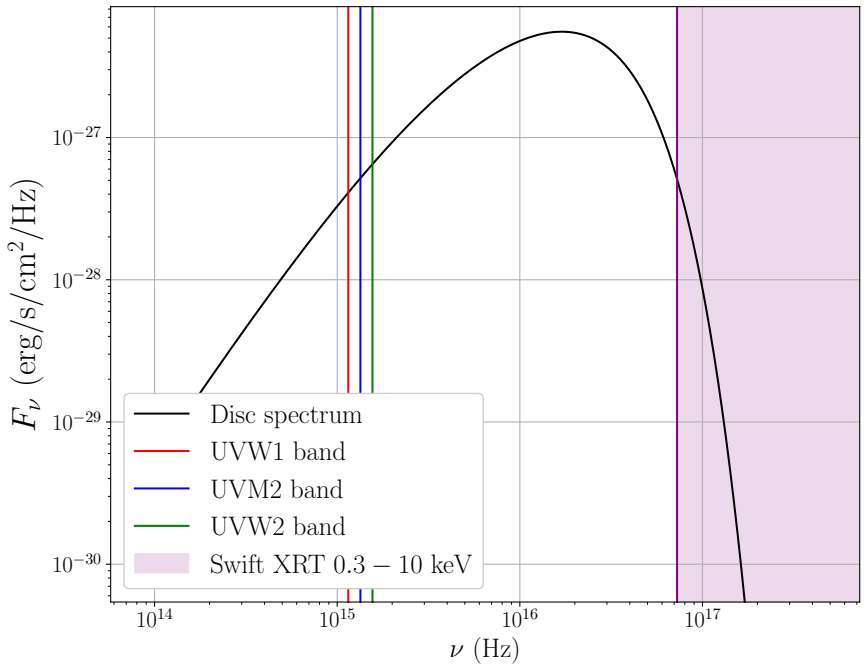

Figure 3.5: Best fit disc spectrum 200 days after disc formation, the location of the UV and X-ray bands is also shown.

by slow evolution of the inner disc (compare the temperature profile in the inner disc regions at 54 and 151 days), whilst the outer disc expands, taking up the angular momentum of the accreted material. At yet later times, the disc begins its approach to the steady state: the disc temperature gradually falls in the inner regions, and the outer region of the disc spreads to ever larger radii.

3.4.5 Continuum spectrum

Figure 3.5 is a fiducial continuum spectrum produced 200 days after disc formation. This was calculated using equation 3.11 and the best-fit parameters of Tables 3.1 and 3.2. The three central frequencies of the UV bands are shown as coloured lines, and the *Swift* X-ray telescope band is the dashed area on the right of the figure. This plot demonstrates that the observed UV flux is below the peak frequency, where the evolving flux would be expected to be near constant with time. The *Swift* X-ray bands probe the quasi-Wien tail of the spectrum, and should therefore be described by equation 3.47.

3.4.6 X-ray light curve

Figure 3.6 shows the observed ASASSN-14li $0.3 - 10$ keV X-ray flux (Bright et al. 2018), together with the best fit evolving X-ray flux of the fiducial disc model, and previous functional fits from the literature (Bright et al. 2018, their Table 1). These previous fits have the form

$$F_X(t) = F_0 \left[\frac{t + t_0}{t_0}\right]^{-5/3} \quad \text{(Power-law fit)} \tag{3.56}$$

and

$$F_X(t) = F_0 \exp\left[-\left(\frac{t + t_X}{t_X}\right)\right] \quad \text{(Exponential fit).} \tag{3.57}$$

In these models, the fitting parameters F_0, t_0 and t_X are unconstrained. Following Bright et al. (2018) I use the reduced chi-squared as a measure of goodness of fit:

$$\bar{\chi}^2 \equiv \frac{1}{N - d} \sum_{i=1}^{N} \frac{(O_i - M_i)^2}{\delta O_i^2}, \tag{3.58}$$

where the N observational quantities, denoted O_i, have associated uncertainty δO_i. A model with d free parameters produces N corresponding model predictions, denoted M_i. The X-ray light curve of ASASSN-14li has $N = 95$ data points, while $d = 2$ for both the power-law and exponential models, $d = 4$ for the disc model (Table 3.1). The reduced chi-squared of the three best-fitting models are

$$\bar{\chi}^2_{\rm power-law} = 1301.1/93 = 13.99, \tag{3.59}$$

$$\bar{\chi}^2_{\rm exponential} = 794.2/93 = 8.54, \tag{3.60}$$

$$\bar{\chi}^2_{\rm disc} = 562.8/91 = 6.19. \tag{3.61}$$

Given the wide parameter space available to the two fitted functions, it is noteworthy that the disc model provides a significantly better overall fit to the observed X-ray data than either of the previous fitting functions (Figure 3.6). Furthermore, of the two fitted functions the 5/3 power law is the more physically motivated (a 5/3 power law is a direct prediction of the Rees (1988) model). When compared to this pure power-law fit the current disc model gives a strikingly improved fit. In addition, the disc model provides the best fit at the late times, $t > 400$ days, where the three model predictions begin to strongly diverge. Further late time X-ray observations of ASASSN-14li would be of great interest, allowing a yet more precise testing of the three models.

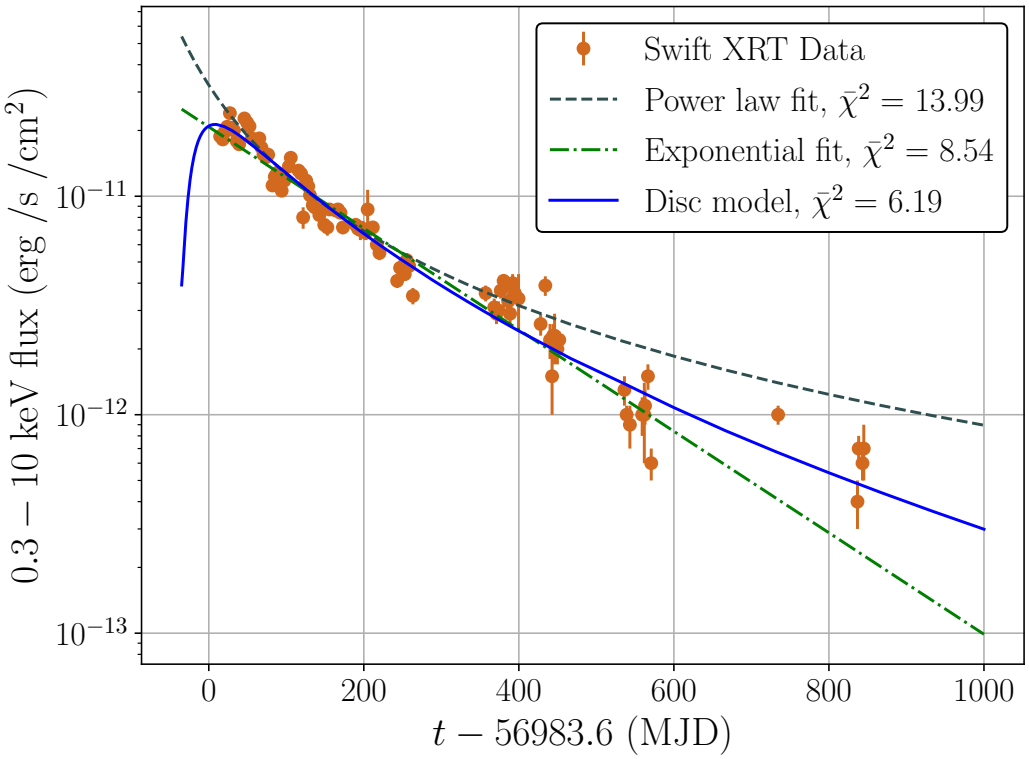

Figure 3.6: Fiducial disc model fit (solid blue curve) to *Swift* X-ray observations of ASASSN-14li (Bright et al. 2018). Also plotted are the two best fit models from the literature, a power-law (grey dashed curve) and exponential fit (green dot-dashed curve; see text). The disc model has the lowest reduced chi-squared statistic, providing the best fit to the observed ASASSN-14li light curve.

The qualitative properties of the evolving disc X-ray flux are nicely predicted by equation 3.47. After an initial phase of rising X-ray flux (whose properties are set entirely by the choice of initial disc conditions), there is a pronounced light curve decay. As may be clearly seen in Figure 3.6, the rate at which the disc X-ray flux falls off is faster than the 5/3 power law, but slower than the pure exponential exponential decay. This is in accord with an evolving flux with a time dependence given by equation 3.47. In section 3.7, I present a full quantitative comparison of the observed X-ray light curves with the analytical results of section 3.3.

Although the fit is good, the model still produces a relatively large formal reduced chi-squared statistic. This is due to the intrinsically short timescale variations of the X-ray flux, which cannot be accounted for in a simple decay model. These short time-scale fluctuations may be intrinsic to accretion (the bolometric luminosity of an

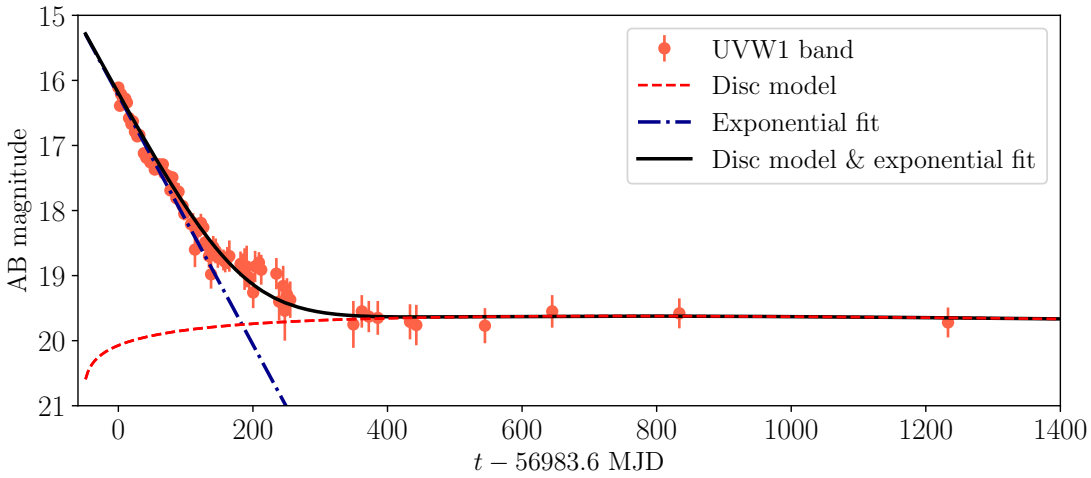

Figure 3.7: Fiducial disc model fit (dashed red curve) to the evolving UV light curve of ASASSN-14li in the UVW1 band (Brown et al. 2017, van Velzen et al. 2019b). The early time $t \lesssim 200$ days UV emission is not well fit by pure disc emission, but requires a secondary, exponentially decaying, component (blue dot dashed curve, see text). The disc and exponentially decaying components are assumed to sum independently. At times $t \gtrsim 200$ days the total UV emission (black solid curve) is completely dominated by disc emission, the properties of which are consistent with the analytical reasoning of section 3.3.5.

accretion disc is known to have log-normally distributed fluctuations, Lyubarskii 1997; Uttley et al. 2005; Hogg and Reynolds 2016; Turner and Reynolds 2021), or caused by matter returning to the disc from large radius orbits after the disruption (fallback). It is these short timescale fluctuations that are the dominant source of model discrepancy, so it is not possible to significantly improve on this reduced chi-squared statistic by further adjustment of other parameters in a smooth disc model.

3.4.7 UV light curve

Figure 3.7 shows the evolving flux of ASASSN-14li in the UVW1 band (Brown et al. 2017, van Velzen et al. 2019b). The UVW1 band has a central wavelength of $\bar{\lambda} = 260$ nm, and the light curve is expressed as an evolving AB magnitude. The best fit UVW1 light curve, calculated with equation 3.50, is plotted as a red dashed curve. Unlike the evolving X-ray luminosity, the observed UV emission of ASASSN-14li cannot be fit by pure disc emission at the earliest observed times. At early times a second, ad hoc, rapidly-decaying, component is required. To the first 100 days of observations, I fit an exponentially decaying component (blue dot-dashed curve)

taken from Holoien et al. (2016a):

$$F_\nu^{\rm exp} = F_0 \exp\left[-(t - t_D)/t_{UV}\right], \tag{3.62}$$

with a best fit of $t_{UV} = 54$ days. Assuming that the flux from these two components sum linearly, the total observed flux of the TDE is given by

$$F_\nu^{\rm total} = F_\nu^{\rm disc} + F_\nu^{\rm exp}. \tag{3.63}$$

This is plotted as the "total light curve" (black solid curve) in Figure 3.7. The fit is excellent. The dominance of an UV component during the early evolutionary stages ($t <$ 200 days post observation), not associated with thermal disc emission, has been noted previously (Pasham et al. 2017, van Velzen et al. 2019b) in accord with my findings.

After an initial phase dominated by this non-disc component, the evolving UV flux is strongly disc dominated. The final 1000 days of ASASSN-14li UV flux are almost completely unchanging with time. As argued in section 3.3.5, this is precisely what would be expected for bandpasses at frequencies below the thermal spectral peak, a condition satisfied here (Figure 3.5).

3.4.8 Characteristic observed temperatures

In fitting observations of tidal disruption events taken in a single band, modellers often infer a single characteristic temperature. For example, two distinct characteristic UV and X-ray temperatures of ASSASN-14li were reported in Brown et al. (2017). A single temperature is generally inferred by fitting a pure blackbody function to the observed spectrum i.e., a Planck function (equation 3.9), neglecting photon red-shifting ($f \simeq 1$) and assuming a constant temperature T. Figure 3.8 demonstrates that when observed with a single band pass, a *composite* disc spectrum of the form used in this work is practically indistinguishable from the spectrum of a single-temperature model. The best fit composite disc spectrum is consistent with both the X-ray and UV inferred temperatures of ASASSN-14li (Brown et al. 2017).

If one fits a sequence of standard Planckian profiles to an evolving narrow band TDE light curve, two time dependent quantities can be calculated: an evolving single temperature and emission radius. The latter is, in effect, an evolving overall normalisation. A time-dependent UV light curve (e.g., one with slowly decaying magnitude, $F_\nu \sim t^{-4n/7}$, equation 3.32) would then be interpreted by this procedure

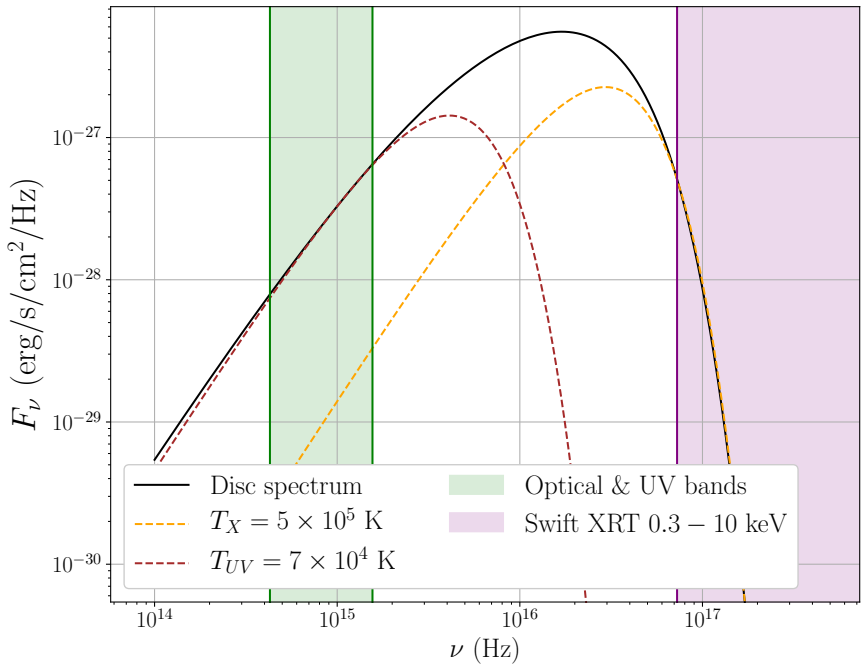

Figure 3.8: A comparison between a composite disc spectrum (black solid curve, Fig. 3.5) and two single colour blackbody spectrums (brown and yellow dashed curves), with 'characteristic' temperatures denoted on plot. When observed through either optical or X-ray bands a composite spectrum of the sort studied in this Chapter is largely indistinguishable from that of a single colour spectrum.

as a uniform temperature blackbody emission with a slowly shrinking radius. Very recently, a TDE-candidate ASASSN-18jd (Neustadt et al. 2020) was observed showing exactly this feature, and was analysed by the technique just described. In common with ASASSN-14li, ASASSN-18jd was discovered after a $\sim$ 120 day seasonal gap in observations, and appears to have already entered its UV plateau phase. The shallow decay of the UV light curve was interpreted by Neustadt et al. (2020) as a constant temperature blackbody which is slowly *contracting*. I suggest here a second possible interpretation: that ASASSN-18jd may be another example of a TDE exhibiting an extended disc-dominated phase, and that this disc is cooling and *expanding*.

Furthermore, van Velzen et al. (2019b) surveyed a population of 8 TDEs detected at optical and UV wavelengths. They found evidence for a late-time UV plateau in the 6 best-observed TDEs in their sample, suggesting that the majority of TDEs undergo a disc-dominated phase. This important point will be returned to in Chapter 5.

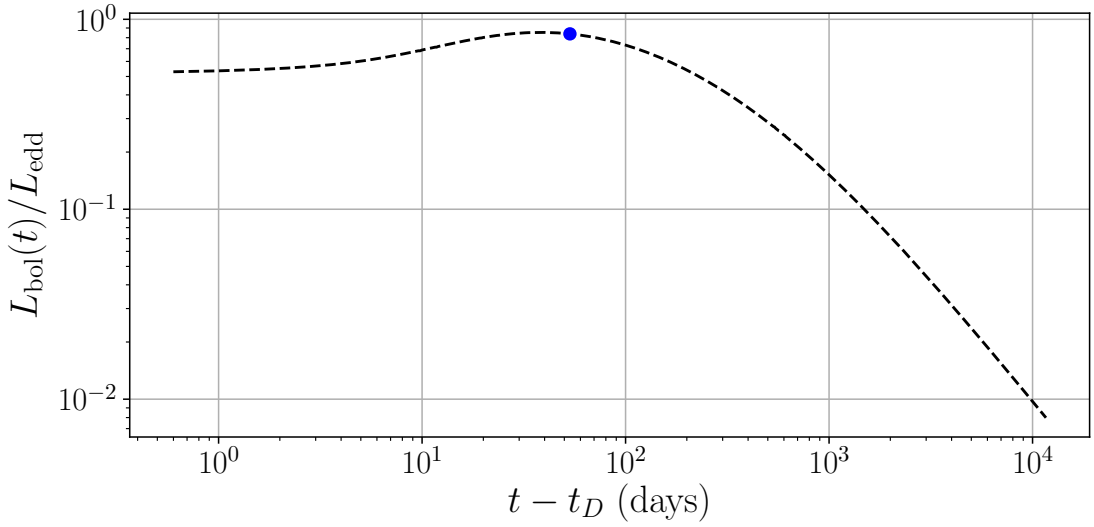

Figure 3.9: The bolometric luminosity of the best fit disc model, plotted in units of the Eddington luminosity of the best fit black hole mass. The blue dot coincides with the time of the first recorded observation of ASASSN-14li. The peak of this light curve corresponds to a bolometric luminosity of $L_{\rm peak} \simeq 0.85\, L_{\rm Edd}$.

3.4.9 Model limitations: a summary

In common with all analytic models of TDE evolution, the model presented here has necessarily been simplified in a number of ways. While I have included general relativistic effects, I have neglected radiative transfer in the disc atmosphere. These effects are likely to be small, but it is of course possible that the best fit model parameters would be affected by their inclusion. The general properties of relativistic thin disc light curves are likely to be insensitive to this level of detail: the UV plateau results from the spreading and cooling of the disc on large scales, whilst the X-ray light curve is described by equation 3.47. The peak effective temperature $\widetilde{T}_p$ could be somewhat modified to include a colour-correction factor to model disc opacity effects (Done et al. 2012), but the functional form itself will be unaltered: the explicit time dependence enters through the solution of the underlying disc equations.

Further potential sources of spectral modification could in principle arise from any irradiation of the disc by an external source (e.g., a jet), or even self-irradiation by disc photons which have been gravitationally deflected to such a degree that they illuminate the disc. (This final effect becomes important if the angular momentum parameter of the black hole approaches unity.)

A fundamental assumption of our model is that the disc is thin, and can therefore be described by the relativistic evolution equation 3.2. This assumption will breakdown if the ratio of the bolometric luminosity to the Eddington luminosity significantly exceeds unity. This may be checked numerically. The bolometric luminosity is found by integrating the locally emitted flux over the disc surface

$$L_{\rm bol}(t) = 2\pi \int_{r_I}^{\infty} (g_{rr} g_{\phi\phi})^{1/2} \gamma^{\phi}(r, a)\, 2\sigma \widetilde{T}^4(r, t)\, {\rm d}r. \tag{3.64}$$

For the best-fit black hole mass, $M = 1.85 \times 10^6 M_{\odot}$, the Eddington luminosity is

$$L_{\rm Edd} = 2.33 \times 10^{44}\, {\rm erg/s} \simeq 5.9 \times 10^{10} L_{\odot}. \tag{3.65}$$

The bolometric light curve of the best fit disc model is shown in Figure (3.9). Whilst at the earliest times the disc luminosity approaches the Eddington limit, peaking at $L_{\rm peak}/L_{\rm Edd} \simeq 0.85$ (the blue dot corresponds with the time of the first recorded ASASSN-14li observation), the disc is found to be sub-Eddington thereafter. With a peak luminosity of $L_{\rm peak} = 0.85 L_{\rm Edd}$, corrections to the thin disc model need not be negligible, as the "slim disc" regime is entered (Abramowicz et al. 1988). However, it is unlikely that such modifications will result in transformative changes in the observed light curves, as opposed to slightly altering the thin disc model fits. Along with the effects of radiative transfer and radiatively coupled outflows, slim disc modelling represents a promising avenue for refining the present treatment.

As was earlier suggested, both the small disc mass and the early time UV flux could result from a super-Eddington outflow, initiated at times predating the first observation. If so, it is not a surprise that the disc luminosity at the earliest times is close to the Eddington luminosity. If representative of the wider TDE population, these results suggest that a relatively small fraction of the stellar debris eventually settles into a disc at radii close to the central black hole. This will be particularly true of discs formed from TDEs around lower mass black holes, which have both a lower Eddington luminosities and larger bolometric luminosities for a given disc mass (note that the scaling relations for time dependent discs differ from classical steady state models, as in the former $\dot{M}$ is a dynamical variable). This idea will be returned to in Chapter 4.

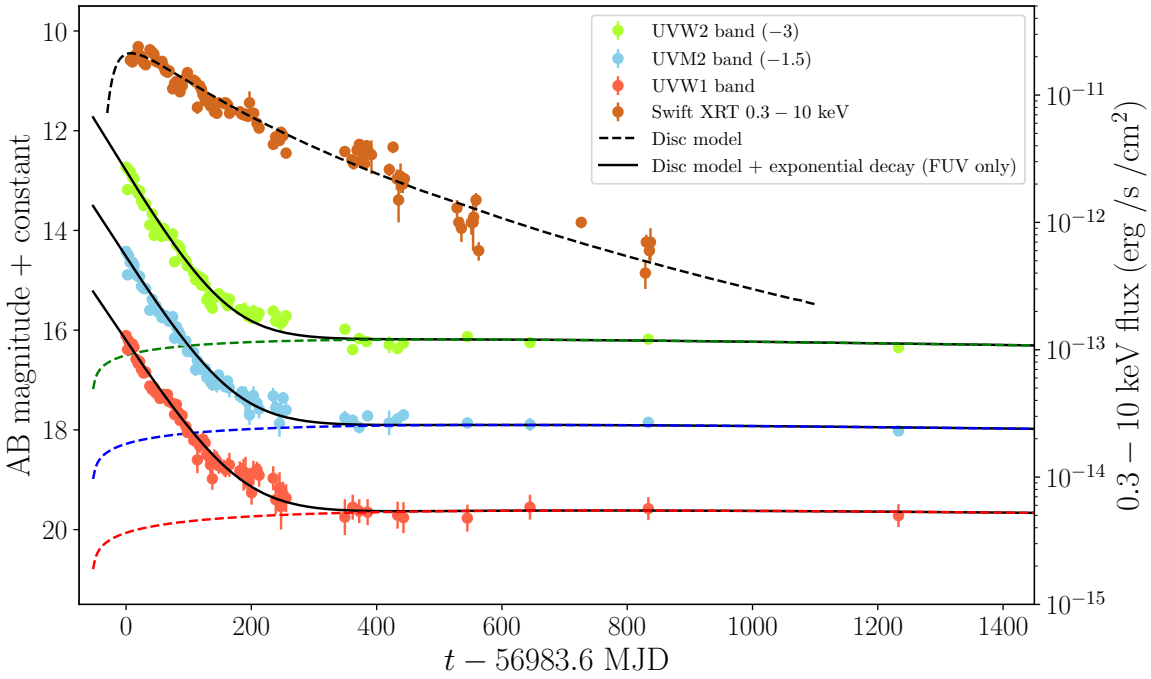

Figure 3.10: Comparison of the best fit disc light curves with the observed ASASSN-14li light curves at both X-ray (right scale) and UV (left scale) frequencies (UV data: Brown et al. 2017; van Velzen et al. 2019b; X-ray data: Bright et al. 2018). The disc model light curves are shown by the dashed curves, at UV wavelengths there is an additional exponentially declining component at early times. All four disc light curves result from the same disc model with only four fitted parameters.

3.4.10 Summary of numerical model

In this section, I have determined the best fit disc light curves at several different wavelengths for a relativistic thin disc evolving with a finite ISCO stress. These model light curves are fit to the observed light curves of the tidal disruption event ASASSN-14li. By solving the fully relativistic thin-disc equation 3.2 and performing ray tracing calculations, this model includes all relevant strong gravity effects. Figure 3.10 shows the evolving emission in 4 different observational bands, three at UV wavelengths and one corresponding to the *Swift* X-ray telescope 0.3 – 10 keV band. The dashed curves represent the contributions of the evolving disc to the emitted flux. The solid lines represent a combined disc and exponentially decaying component, only relevant at UV wavelengths.

The evolving X-ray flux is well described at all times by an evolving thin disc with a finite ISCO stress. The model requires no other spectral components and gives a

significantly better fit to the observations than either the canonical Rees (1988) power law model or an exponentially decaying model. The properties of this X-ray light curve are in good qualitative agreement with the analytical results of section 3.3: the X-ray flux of the disc model decays at a faster rate than that of a pure power law, but at a slower rate than a pure exponential decay.

The UV emission of ASASSN-14li at the earliest times appears not to be the result of thermal emission from a turbulently evolving thin disc. Instead, it is dominated by a much more rapidly decaying, secondary component. After $\sim$ 200 days however, the ASASSN-14li UV flux undergoes a 1000 day plateau, and is extremely well described by thin disc emission.

This means that for approximately 1000 days of observations, the entirety of the ASASSN-14li emission at both UV and X-ray wavelengths can be successfully reproduced by a relativistic thin disc model with nine total parameters, of which only four are inferred from the observations. These results demonstrate that while the behaviour of a TDE at its earliest times may be complex, the long term observed properties of a TDE can be very well described by a simple relativistic thin disc model. This opens up the exciting possibility that future modelling of well observed TDEs will be able to constrain the properties of a population of otherwise quiescent supermassive black holes.

3.5 Properties of the central black hole

To analyse the effects of varying the black hole spin on the best fit ASASSN-14li parameters, I solve the disc evolution equation 3.2, and perform ray-tracing calculations (equation 3.8), for a variety of black hole spins. For each black hole spin I fit the four free parameters t_v, t_D, M_d and M to the ASASSN-14li X-ray light curve and late time UV emission. Of these four parameters, the viscous timescale t_v, disc mass M_d and time offset t_D are the most poorly constrained by theory or observations. Thus, for each black hole spin, I present in Table 3.3 the best fit black hole mass M, and the minimum reduced chi-squared $\bar{\chi}^2_{\rm min}$ of the fitted X-ray light curve (equation 3.58).

The value of the minimum reduced chi-squared of the fitted X-ray light curves is relatively insensitive to the black hole spin (Table 3.3). This is due to the fact that residual short-timescale fluctuations in the ASASSN-14li X-ray light curve dominate the model-data discrepancy. This is further compounded by an intrinsic parameter

a/r_g	$M/M_\odot$	$\bar{\chi}^2_{\rm min}$
0.9	$2.00^{+0.05}_{-0.1} \times 10^6$	6.57
0.75	$1.93^{+0.03}_{-0.04} \times 10^6$	6.15
0.5	$1.85^{+0.03}_{-0.04} \times 10^6$	6.19
0	$1.66^{+0.06}_{-0.06} \times 10^6$	6.40
-0.5	$1.62^{+0.08}_{-0.07} \times 10^6$	6.49
-0.9	$1.55^{+0.1}_{-0.1} \times 10^6$	6.61

Table 3.3: Best fit black hole masses M and the minimum X-ray light curve reduced chi-squared $\bar{\chi}^2_{\rm min}$ for different black hole spin parameters. The non-fitted parameters of Table 3.2 are unchanged.

degeneracy between the black hole's mass and spin. The peak temperature of a relativistic disc, which is the physically relevant temperature for the X-ray flux (equation 3.47), depends strongly on the physical location of the ISCO. Increasing the (prograde) rotation of the black hole reduces the ISCO location in units of r_g, whereas increasing the black hole mass increases the magnitude of r_g in physical units. This is reflected in the positive correlation of the best fit black hole masses and spins (Table 3.3). With these caveats, a best-fit black hole spin lies in the range $0.5 < a/r_g < 0.75$. The black hole spin is much less well constrained than the other fitted parameters.

The physically allowed spin range of Kerr black holes is $|a/r_g| < 1$, which may be used to calculate bounds on the black hole mass. An important result of this analysis is that the central black hole mass of ASASSN-14li can be tightly constrained. Over the dimensionless spin range ($-0.9 < a/r_g < 0.9$) considered here, the best fit black hole mass varies by only a factor of 1.3, varying from $1.55 \times 10^6 M_\odot$ for rapid retrograde rotation $a/r_g = -0.9$, to $2 \times 10^6 M_\odot$ for rapid prograde rotation $a/r_g = 0.9$. This best fit mass range lies at the lower end of the range inferred from galactic bulge mass measurements ($10^{6.7\pm0.6} M_\odot$, Mendel et al. 2014), and is in tight agreement with the mass inferred from velocity dispersion measurements ($M = 10^{6.23\pm0.4} M_\odot$, Wevers et al. 2017).

Previous estimates based on the observed ASASSN-14li light curves are also in keeping with our findings, with Miller et al. (2015) inferring a black hole mass of $M \sim 2\times10^6 M_\odot$ based on Eddington limit arguments and the observed X-ray luminosity. Finally, our inferred mass range is also consistent with the QPO bound published by Pasham et al. (2019), $M \lesssim 2 \times 10^6 M_\odot$. It therefore appears that very distinct modelling techniques are converging onto a single black hole mass for the ASASSN-14li system, of order $M = 2 \times 10^6 M_\odot$.

3.6 Finite versus Vanishing ISCO stress

3.6.1 High photon energy expansion

If the stress vanishes at the ISCO, so too does the local disc temperature. This means that the hottest disc regions – those which contribute to the high energy Wien tail – take the geometric form of a ring at a disc radius exterior to the ISCO, within the body of the disc. To calculate the high frequency spectrum in this case, I follow section 3.3.6 and expand the effective temperature about its maximum, assuming a face-on disc orientation. Now, the maximum temperature is now longer at the integration limit, and the expansion takes the form

$$\frac{1}{k_B\widetilde{T}} = \frac{1}{k_B\widetilde{T}_p} + \frac{1}{2}\frac{\partial^2}{\partial R^2}\left[\frac{1}{k_B\widetilde{T}}\right]_{R_p}(R-R_p)^2 + ... \tag{3.66}$$

I define a dimensionless normalisation parameter

$$\xi \equiv R_p^2 k_B \widetilde{T}_p \frac{\partial^2}{\partial R^2}\left[\frac{1}{k_B\widetilde{T}}\right]_{R_p}, \tag{3.67}$$

and the leading order flux integral is (extending the lower integration limit to $-\infty$ introduces exponentially small corrections)

$$F_\nu = \frac{4\pi h\nu_o^3}{D^2c^2}\exp\left(-\frac{h\nu_o}{k_B\widetilde{T}_p}\right)\int_{-\infty}^{\infty} R\exp\left[-\frac{\xi h\nu_o}{2k_B\widetilde{T}_p}\frac{(R-R_p)^2}{R_p^2}\right]\mathrm{d}R. \tag{3.68}$$

This integral may be evaluated to give

$$F_\nu = \frac{4\pi h\nu_o^3}{c^2}\sqrt{\frac{2\pi}{\xi}}\left(\frac{R_p}{D}\right)^2\left(\frac{k_B\widetilde{T}_p}{h\nu_o}\right)^{1/2}\exp\left(-\frac{h\nu_o}{k_B\widetilde{T}_p}\right). \tag{3.69}$$

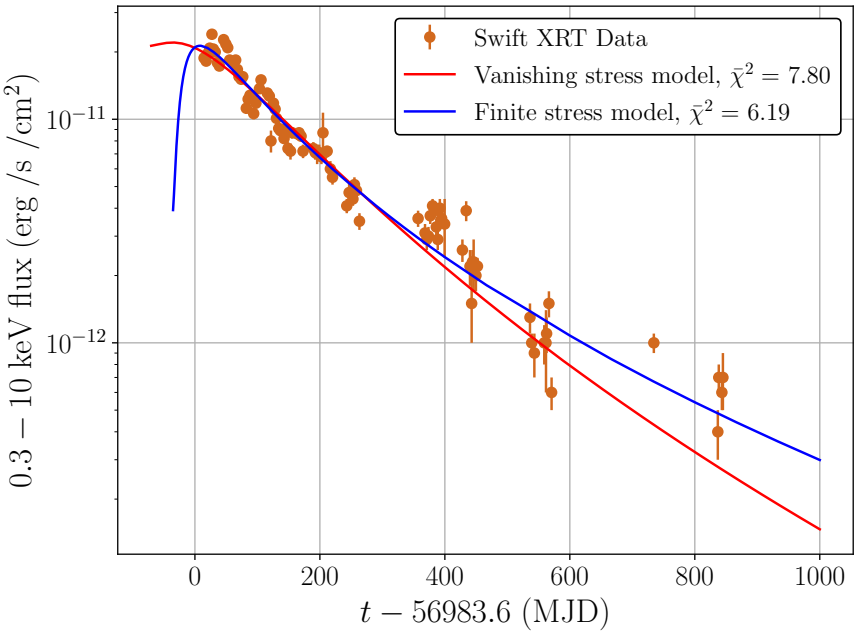

Figure 3.11: A comparison of the best fit X-ray light curves from discs evolving with finite (blue) and vanishing (red) ISCO stresses, with the observed X-ray light curve of ASASSN-14li (Bright et al. 2018). The steeper fall-off of the vanishing ISCO stress disc solution can be understood by its larger decay index n (see text). A disc with a finite ISCO stress produces a better fit to the observed ASASSN-14li light curve.

The X-ray luminosity is obtained by integrating this expression over the observer frequency band of interest. To leading order this is

$$F_X = \frac{4\pi h\nu_l^4}{c^2}\sqrt{\frac{2\pi}{\xi}}\left(\frac{R_p}{D}\right)^2\left(\frac{k_B\widetilde{T}_p}{h\nu_l}\right)^{3/2}\exp\left(-\frac{h\nu_l}{k_B\widetilde{T}_p}\right). \tag{3.70}$$

As in section 3.3.6, I assume a temperature time dependence of the form $\widetilde{T}_p \propto \tau^{-n/4}$. A disc with a vanishing ISCO stress therefore has an evolving X-ray light curve that takes the form

$$F_X(t) = F_0\left(\frac{t+t_0}{t_X}\right)^{-3n/8}\exp\left[-\left(\frac{t+t_0}{t_X}\right)^{n/4}\right]. \tag{3.71}$$

where t_0 and t_X are constants. I remind the reader that the vanishing ISCO stress solutions satisfy $n > 1$.

3.6.2 Best fit light curves

Figure 3.11 shows the best fit X-ray light curve of a vanishing ISCO stress disc. This light curve was found with the same non-fitted parameters of section 3.4 (Table 3.2), except for the ISCO stress parameter γ, which is in effect infinite for a vanishing ISCO stress (Chapter 2). Next, the free parameters (Table 3.1) were simultaneously fit to the ASASSN-14li X-ray and UV light curves.

The best fit parameters for the vanishing ISCO stress disc are: $M = 1.8 \pm 0.1 \times 10^6 M_\odot$, $M_d = 0.30 \pm 0.04 M_\odot$, $t_v = 400 \pm 20$ days and $t_D = 110 \pm 10$ days. The best-fit values for the vanishing ISCO stress disc are less certain than the finite ISCO stress disc as a result of the overall poorer fit, $\bar{\chi}^2_{\text{vanishing stress}} = 709.8/91$. As can be seen in Figure 3.11, the best fit vanishing and finite ISCO stress light curves are almost indistinguishable for the first ~ 300 days of observations, deviating only at later times. This late time deviation is entirely a result of the different luminosity power law exponents associated with vanishing and finite ISCO stress discs. With a power law index of $n \approx 1.2$, the late time vanishing ISCO stress X-ray light curve becomes dominated by a $F_X \sim t^{-0.45} \exp(-t^{0.3})$ time dependence. The correspondingly shallower decline of a finite ISCO stress X-ray light curve results from its $n \approx 0.8$ exponent, leading to a $F_X \sim t^{-0.4} \exp(-t^{0.2})$ late time profile. It is the different exponents within the exponentials which are responsible for the late time divergence of the two light curves.

Since ASASSN-14li has been observed for ~ 900 days, there are observations at sufficiently late times to differentiate between the two models. The X-ray light curve of ASASSN-14li is clearly better fit with a disc evolving with a finite ISCO stress than a disc with a vanishing ISCO stress (Figure 3.11), a distinction that can only be seen at times $t > 400$ days, where the two models cleanly diverge. An additional problem with the vanishing ISCO stress disc model is that to produce an acceptable X-ray flux, the disc must be super-Eddington. The vanishing ISCO stress disc's bolometric luminosity peaks at $L_{\text{peak}} = 1.31\, L_{\text{Edd}}$, and $L/L_{\text{Edd}} > 1$ for the first ~ 250 days. Interestingly, late time observations of evolving TDEs may be the best way to determine the nature of the ISCO boundary condition.

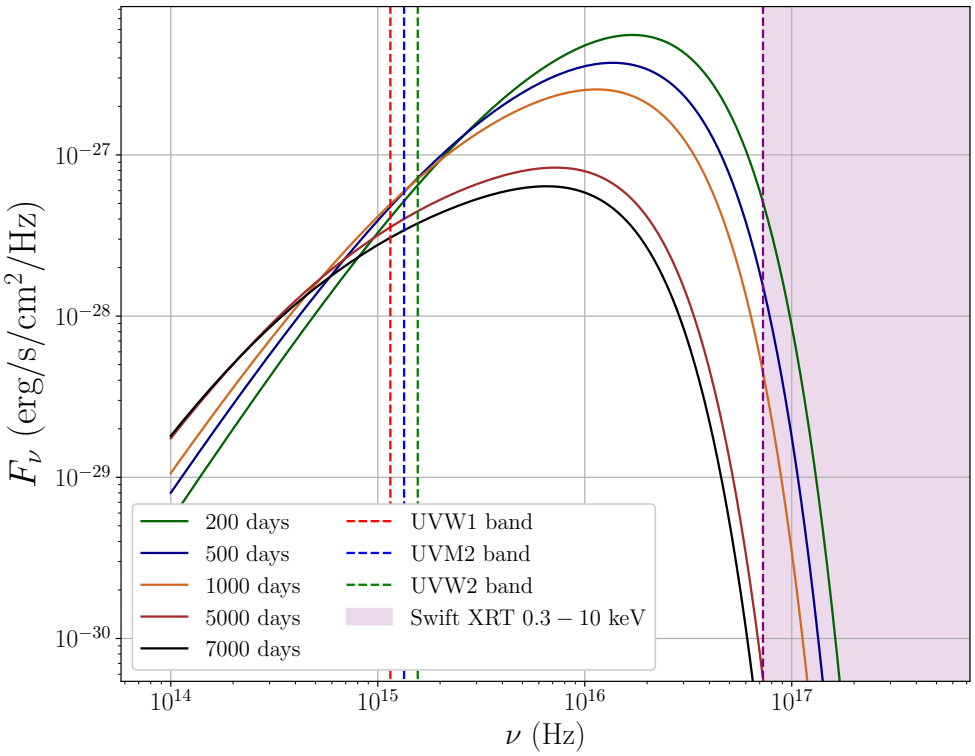

Figure 3.12: The disc continuum spectrum, calculated from equation 3.11, shown at several different times (denoted on plot). The simultaneous properties of both the (very shallow) UV and (rapidly declining) X-ray disc light curves can be simply understood from the evolution of the overall shape of the disc spectrum.

3.7 Comparison of numerical and analytical calculations

I have demonstrated that the results of the full numerical calculations of the evolving ASASSN-14li light curves are in good qualitative agreement with the analytical results of section 3.3. In this section I focus on a quantitive comparison between numerical and analytical calculations.

Not surprisingly, the behaviour of the ASASSN-14li light curves shows a strong dependence on observational band. The UV flux undergoes a prolonged plateau, whilst the X-ray flux declines both monotonically and rapidly. This behaviour can be understood by the relative location of the observational bands with respect to the frequency of the peak of the continuum accretion disc spectrum (Figure 3.12). As Figure 3.12 demonstrates, the UV bands probe frequencies smaller than peak of the

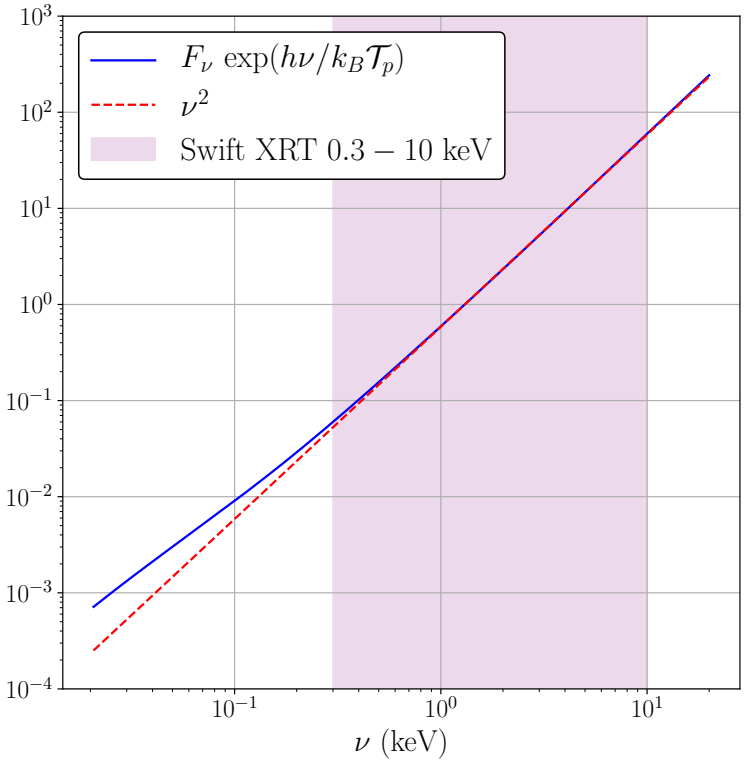

Figure 3.13: Comparison of $F_\nu \exp(h\nu/k\widetilde{T}_p)$ (renormalised for display) with the large ν asymptotic result for the case of a finite ISCO stress. The solid line is from a numerical evaluation (Figure 3.5); the dotted line is the large ν analytic result (equation 3.72).

disc spectrum. At these frequencies, the dual effects of a temporally decreasing peak intensity, coupled with the decline of the peak frequency itself leads to narrow band observations in which the disc flux plateaus for prolonged periods. This is particularly pronounced in the UV observations of ASASSN-14li (Figure 3.7).

I emphasise that this UV light curve plateau should be a signature feature of all tidal disruption events which undergo an evolutionary phase dominated by disc emission. Once a TDE system has settled down into an evolving thin disc (after an initial phase of UV emission dominated by some non-thermal component), values of the parameters t_v, M_d and M expected for typical TDE systems will result in the disc spectral peak lying at 'extreme' ultra-violet frequencies, which are much higher than the UV observational bands. The late time observations ($t \gtrsim 200$ days) of a wide range of TDEs should therefore display UV light curve plateaus (see Chapter 5).

As seen clearly in Figure 3.12, the observed ASASSN-14li X-ray flux stems from the quasi-Wien tail of the disc spectrum. This allows for a detailed comparison between

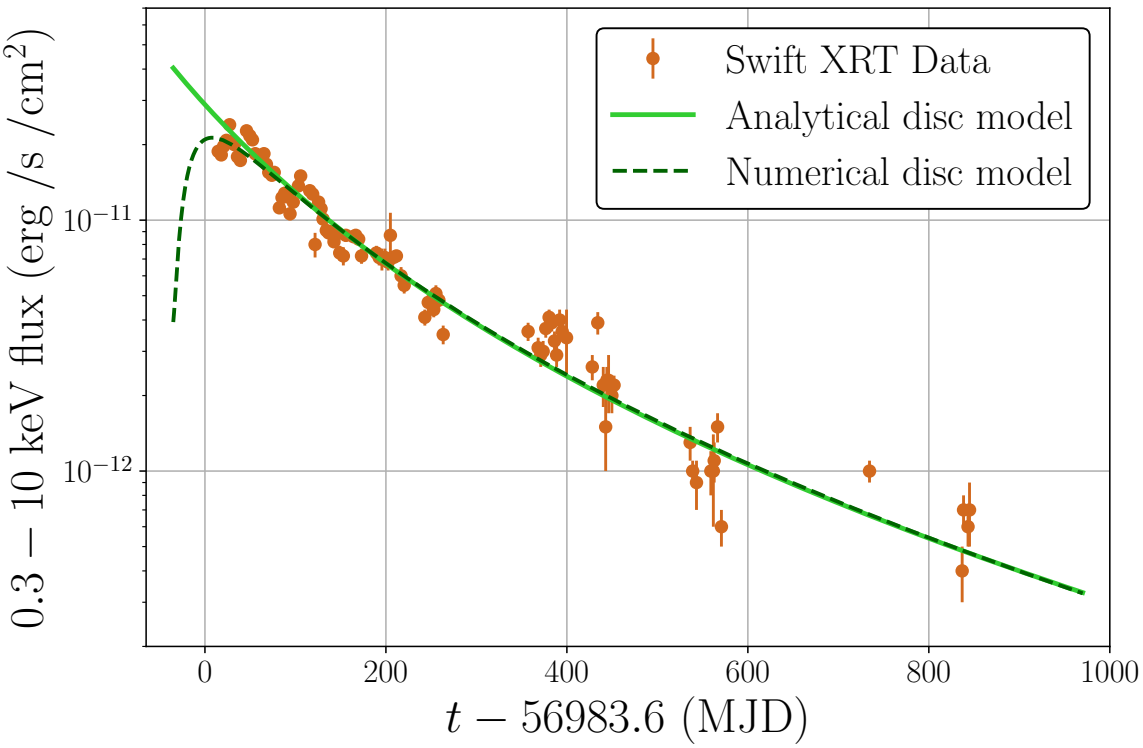

Figure 3.14: Comparison between the asymptotic X-ray light curve function (equation 3.73), the best fit numerical X-ray light curve (Figure 3.6), and observed X-ray light curve of ASASSN-14li (Bright et al. 2018). The numerical X-ray light curve is extremely well described by the asymptotic function (equation 3.73).

the high-photon-energy asymptotic expansions presented in section 3.3 (equations 3.36 & 3.47), and the best fit numerical spectrum, and evolving X-ray light curve, of section 3.4 (Figures 3.5 & 3.6). Figure 3.13 presents a comparison between the high-photon-energy spectrum of the fiducial disc model (best fit parameters from Table 3.1), and the functional form of the asymptotic expansion (equation 3.36). The observed flux has been renormalised for display purposes, but the frequency dependence is of course unaltered. The asymptotic flux expression

$$F_\nu \simeq \nu^2 \exp(-h\nu/k_B\mathcal{T}_p), \tag{3.72}$$

where $\mathcal{T}_p$ is the maximum effective temperature in the disc at the time of fitting, is clearly an excellent fit over the entire *Swift* XRT band.

Yet more striking is a quantitative comparison between the mathematical asymptotic expansion for the evolving X-ray light curve (equation 3.47) and both the observed

X-ray flux of ASASSN-14li, and the results of the full numerical disc model (Figure 3.14). It is only at the very earliest times that equation 3.47 and the full numerical disc model deviate at all! This is due to the assumption that the peak of the effective temperature distribution occurs at the inner disc edge, something which is manifestly not satisfied in the full numerical disc model at early times (see Figure 3.4). Once the evolving disc reaches the ISCO the two results very quickly converge, and are then in excellent agreement for the entire 900 days of observations. The value of the bolometric decay index was taken to be $n = 0.8$ during this fitting procedure, a value which is in agreement with time-dependent disc theory for a finite ISCO stress disc (Chapter 2). These results suggest that the observed X-ray light curves from disc-dominated TDE spectra should be well fit by the following function, which is a high energy asymptotic solution of the underlying disc emission integral assuming a finite ISCO stress:

$$F_X(t) = F_0 \left(\frac{t+t_0}{t_X}\right)^{-n/2} \exp\left[-\left(\frac{t+t_0}{t_X}\right)^{n/4}\right]. \tag{3.73}$$

with $n \simeq 0.8$.

3.8 Discussion

In this work, I have developed mathematical techniques, both numerical and analytical, to evaluate the emission profiles of a simple evolving relativistic thin discs. The effective temperature profiles are calculated using the disc evolution equation valid in the Kerr geometry (Chapter 2), and this modelling incorporates all relevant strong gravity optics. Thus this model represents a fully relativistic treatment of a TDE. At the ISCO, I have allowed for either a vanishing or finite value of the disc stress.

The results I have presented here are for the light curves of these solutions as observed at UV and X-ray frequencies. I have demonstrated that these light curves provide a significantly improved fit (when compared to previous models) to the spectral data of ASASSN-14li, a particularly well observed TDE. The calculated light curves of discs evolving with a finite ISCO stress provide a better fit than those of a vanishing ISCO stress. The analysis here is a much more stringent test of the nature of the ISCO stress than previous works which focussed on fitting power law indices.

The spectral modelling has been carried out in two complementary ways. First, I have integrated the evolution equation (for the effective temperature) and evaluated the disc emission integral by direct numerical methods. Second, I have used asymptotic

expansion techniques to obtain a simple analytic form for the X-ray flux (equation 3.73), and determine general properties of the evolving UV flux. A comparison between the observed light curves of ASASSN-14li, numerical calculation, and analytic formulae are all in good agreement. Over 1000 days of simultaneous UV and X-ray observations of ASASSN-14li are well fit by a relativistic thin disc model with a finite stress at the ISCO.

I believe that this work provides not only for a compelling fit to a disc model, but a deeper understanding of underlying TDE evolution. The results discussed here should be broadly applicable at late times to any TDE whose spectrum is dominated by a disc. In the remainder of this Chapter I examine one such disc-dominated TDE candidate: ASASSN-15lh, selected for the a-typical properties of its light curves.

3.9 ASASSN-15lh – modelling a novel transient

The source ASASSN-14li is in effect the canonical example of a super-soft thermal TDE: it is bright and has excellent observational coverage at both X-ray and UV photon frequencies. In common with most known TDEs, the emission of ASASSN-14li at X-ray, optical and UV frequencies declined rapidly at early times. While the physical properties of the X-ray and UV emission of TDEs are not necessarily fully understood, ASASSN-14li has characteristics similar to those TDEs discovered in the very early days of X-ray surveys (e.g., the handful of candidates discovered by the ROSAT survey Bade et al. 1996; Greiner et al. 2000; Esquej et al. 2008). These surveys had much poorer temporal sampling of their TDE-candidate light curves, but ASASSN-14li was none-the-less believed to be representative of a wide population of sources. It was natural therefore to start a study of accretion disc models of TDEs with ASASSN-14li. Given the success of this initial study, an obvious follow up question is: how well can this model describe the properties of some of the more atypical TDE candidates? Are atypical TDEs really distinct events which require different physical mechanisms to explain the observed emission, or are they merely disc-dominated sources in different regions of parameter space? In this section I examine the evolving light curves of ASASSN-15lh, potentially the TDE candidate with the most atypical optical and UV light curves.

ASASSN-15lh is an extremely luminous transient event with red-shift $z = 0.2326$ (Dong et al. 2016) whose physical origin is contested. Initially classified as a super-luminous supernova (Dong et al. 2016), it has since been argued that the properties of the host galaxy and the evolving spectrum of ASASSN-15lh are more consistent

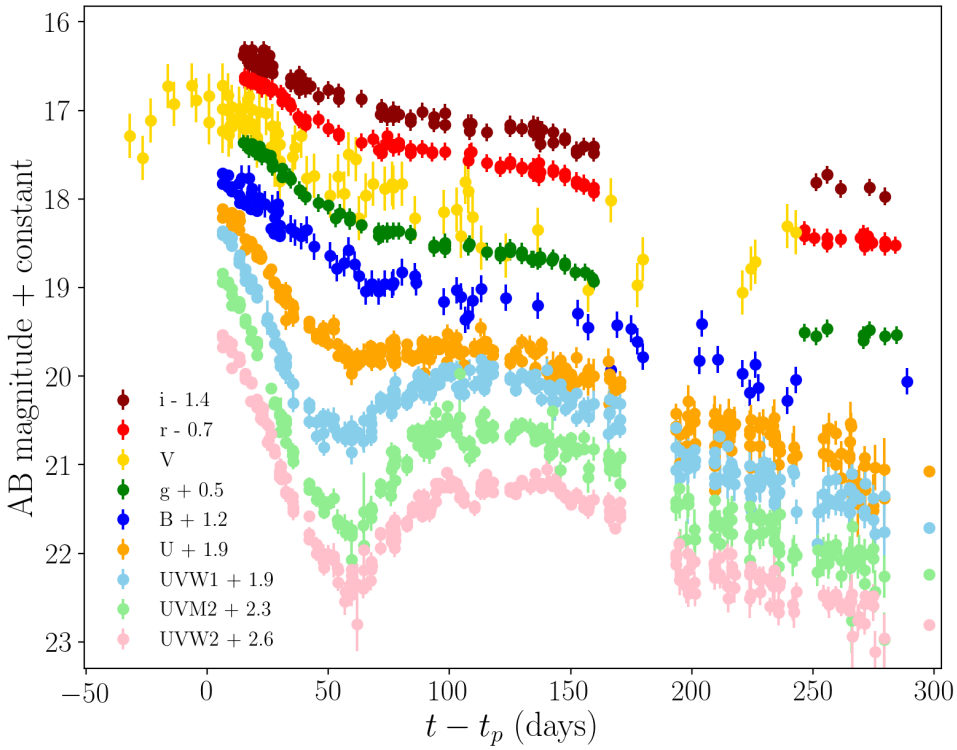

Figure 3.15: The observed light curves of ASASSN-15lh. The evolving flux (y-axis) is presented in AB magnitudes, with constant offsets between the light curves at different observing frequencies to aid readability (see legend).

with a tidal disruption event (Leloudas et al. 2016). The first 350 days of observations of ASASSN-15lh are shown in Figure 3.15. ASASSN-15lh is notable for its extreme brightness ($M_V = -23.5$ mag, $L_V \sim 10^{45}$ erg/s) and its double-humped UV light curves. It has been suggested that the properties of these UV light curves are supportive of a TDE origin for ASASSN-15lh, with the re-brightening corresponding to a transition to an accretion disc dominated state (Leloudas et al. 2016).

In the previous sections I developed a model for the evolution of TDE light curves in their disc-dominated phase. It is the purpose of this section to investigate whether a disc model can indeed, as suggested by Leloudas et al. (2016), reproduce the properties of the evolving ASASSN-15lh light curves. This will both serve as a test of the disc model in more novel accretion regimes, and as a test of the ASASSN-15lh TDE paradigm. I model all nine ASASSN-15lh light curves displayed in Figure 3.15, corresponding

to observed photon energies ranging from the infrared to ultra-violet energies. It is demonstrated that all 9 light curves transition to a disc-dominated state at $t \simeq t_{\rm peak}+65$ days. These light curves are all well-described by an evolving disc model for the next ~ 300 days (Figures 3.17, 3.18). Interestingly, the best fit black hole parameters are those of a maximally rotating black hole of mass $M \simeq 10^9 M_\odot$. This black hole mass is consistent with four independent estimates from galactic scaling relationships (Leloudas et al. 2016, Krühler et al. 2018, Wevers et al. 2017). For large black hole masses, rapid spins are strongly favoured, as only this regime allows for the tidal forces required to disrupt solar type stars outside of the black hole's event horizon. These results are strongly supportive of a TDE origin for ASASSN-15lh, which would thus become the first TDE to be observed in the disc dominated state at optical and infrared frequencies.

3.10 Light curve of a massive black hole

The host galaxy of ASASSN-15lh is a massive red galaxy with a small rate of ongoing star formation (Leloudas et al. 2016). Measurements of the galactic bulge mass, bulge luminosity and velocity dispersion (Leloudas et al. 2016, Krühler et al. 2018, Wevers et al. 2017) suggest that the central black hole in ASASSN-15lh must be extremely massive, $M \sim 10^9 M_\odot$. I show below that a detailed analysis of the ASASSN-15lh light curves reveals that they are indeed best fit by a $M \simeq 10^9 M_\odot$ black hole. For the present, however, I note that the ASASSN-15lh black hole properties may be inferred rather simply from qualitative features of the observed UV and optical light curves alone, without the need for any prior information about the host galaxy.

The light curves of many TDEs observed at ultraviolet energies show a transition to a disc dominated state at times $t \sim 100$–300 days after the initial disruption (van Velzen et al. 2019b, Figure 3.7). These same studies have likewise demonstrated that in this disc-dominated phase the light curves at ultra-violet energies are extremely flat with time, well approximated by $F_{UV} \sim$ const. ASASSN-15lh shows a different, strongly time varying behaviour after the light curves transition at $t - t_{\rm peak} \sim 65$ days.

This at first seems inconsistent with the results of the previous section. However, the "standard" flat UV light curves follow from a particular condition ordinarily satisfied by TDE discs (see Figure 3.12):

$$E_{UV} \ll k_B f_\gamma T_{\rm peak}. \tag{3.74}$$

Here, E_{UV} is the energy of the UV photons, and $f_\gamma T_{\rm peak}$ is the product of the maximum disc temperature $T_{\rm peak}$ and the red-shift factor f_γ of the disc photons emitted in that region which relates the observed energy of a photon to its emitted energy $f_\gamma \equiv E_{\rm obs}/E_{\rm emit}$. If, on the other hand,

$$E \gtrsim k_B f_\gamma T_{\rm peak}, \tag{3.75}$$

the observed light curves at these wavelengths will evolve more rapidly than the power-law fall off associated with the disc's bolometric luminosity (Figures 3.14, 3.12). If ASASSN-15lh truly is a disc-dominated TDE, then rapidly evolving UV light curves imply the condition:

$$f_\gamma T_{\rm peak} \lesssim E_{UV}/k_B \sim 5 \times 10^4 \,{\rm K}. \tag{3.76}$$

Typical TDE peak disc temperatures lie at $T_{\rm peak} \sim 10^6$ K (Figure 3.4, see also the X-ray 'temperatures' inferred by e.g. Brown et al. (2017)). A drop in peak temperatures of a factor $\gtrsim 20$ suggests atypical, rather extreme parameters associated with the disc.

In determining the magnitude of the physical peak disc temperature $T_{\rm peak}$, there are to leading order 3 degrees of freedom within a disc model: i) the disc mass M_d; ii) the turbulent stress (an 'α' type parameter); and iii) the black hole mass M. While one expects a spread of disc masses and α parameters, it is unlikely that either will vary by the orders of magnitude necessary to produce the ASASSN-15lh peak temperature change. Supermassive black hole masses, however, certainly span many orders of magnitude, and it is to the black hole parameters that I naturally turn for an explanation of the low peak disc temperature.

If the luminosity is a fixed fraction of the Eddington value, the disc temperature has a modest dependence on black hole mass $T \propto M^{-1/4}$. X-ray bright TDEs (those with the hottest observed disc temperatures) are typically associated with black hole masses of $M \sim 10^6$–$10^7 M_\odot$ (Wevers et al. 2017; Wevers et al. 2019b). To reduce the peak disc temperatures to UV energies, ASASSN-15lh must contain an unusually massive black hole.

While this argument is consistent with the large black hole mass inferred from host galaxy observations, it also implies a second condition: the black hole must be near maximally rotating. This is because the inferred black hole mass of ASASSN-15lh lies above the Hills mass (Dong et al. 2016, Leloudas et al. 2016), defined as the black hole mass at which a Schwarzschild black hole would first directly capture

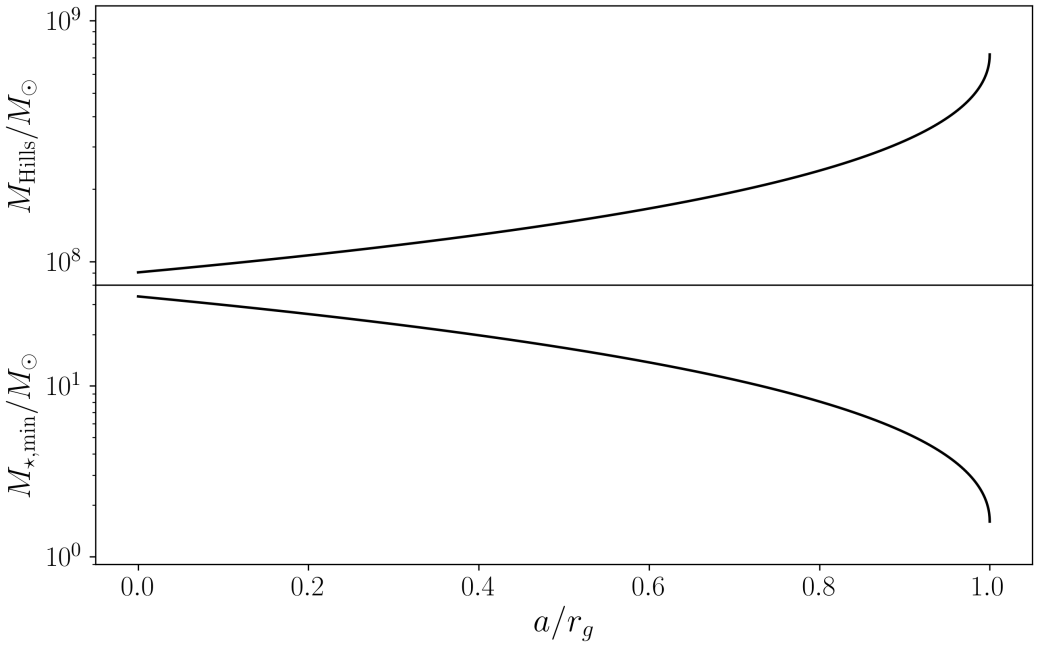

Figure 3.16: Upper: The Hills mass, defined as the maximum black hole mass which can disrupt a solar ($M_\star = M_\odot, R_\star = R_\odot$) star, as a function of black hole spin a. Lower: the minimum stellar mass of a solar type star ($R_\star = R_\odot(M_\star/M_\odot)^\xi, \xi = 0.79$) which can be tidally disrupted by a $M = 10^9 M_\odot$ black hole as a function of black hole spin.

a solar type star without tidally disrupting it: $M_{\rm Hills} \simeq 9 \times 10^7 M_\odot$ (Hills 1975). The Hills mass increases by roughly an order of magnitude for extreme Kerr spins (Kesden 2012), since a maximally rotating Kerr black hole has both a stronger tidal potential as well as a smaller event horizon. Figure 3.16 shows the analytical model of Kesden (2012), which predicts that a maximally rotating $10^9 M_\odot$ black hole can disrupt a $M_\star \gtrsim 1.5 M_\odot$ solar type star. This is probably a conservative estimate, as it neglects stellar rotation and the bulge distortion of the star's surface on its approach. Indeed, both hydrodynamical (Ivanov and Chernyakova 2006) and SPH (Sponholz 1994) simulations show the disruption of a $1 M_\odot$ by a maximally rotating $10^9 M_\odot$ black hole. The lower half of Figure 3.16 shows the minimum mass of a solar-type star (assumed to satisfy $R_\star \propto M_\star^{0.79}$, Kippenhahn and Weigert 1990), as a function of black hole spin, that can be tidally disrupted by a $10^9 M_\odot$ black hole.

The tidal disruption cross section increases slightly for more massive stars. A simple estimate (Magorrian and Tremaine 1999) implies $\sigma_{\rm TDE} \propto R_\star M_\star^{-1/3} \propto M_\star^{0.46}$. The enlarged cross section is countered by the sparsity of high mass stars ($\mathrm{d}N_\star/\mathrm{d}M_\star \propto$

$M_\star^{-2.35}$ for a Salpeter (1955) mass function). Thus, TDEs involving large stellar masses are expected to be rare $\mathrm{d}N_{\mathrm{TDE}}/\mathrm{d}M_\star \propto M_\star^{-1.89}$ (Stone and Metzger 2016), particularly for early type galaxies like the host of ASASSN-15lh (Leloudas et al. 2016). This suggests that ASASSN-15lh contains a massive black hole with a large prograde spin.

While large prograde black hole spins increase the physical peak disc temperature T_{peak}, the innermost regions of a highly spinning black hole will be strongly gravitationally red-shifted. For a black hole with spin parameter $a/r_g = 0.99$ (these quantities relate to the physical mass M and angular momentum J of the black hole by $r_g = GM/c^2$ and $a = J/Mc$) the red-shift factor for favourable (near face-on) orientations is $f_\gamma \approx 0.16$ at the ISCO. This means that for favourable orientations the large gravitational redshift counteracts the intrinsic disc temperature rise, significantly reducing the observed peak energy. A black hole with large mass and near maximal spin is the only combination of parameters that can reduce the observed peak disc energies to the UV scale, producing rapidly evolving UV light curves in the disc dominated phase, while still being able to tidally disrupt a typical low mass star. The question then is whether this combination of parameters can reproduce the light curves of ASASSN-15lh in quantitative detail.

3.11 Modelling ASASSN-15lh light curves

I follow the light curves fitting methods developed and described above. The one difference between this analysis and section 3.4 is that, rather than introducing the disc material as a delta-function ring at a single time t_D, here I gradually feed matter into a ring using a source term $\mathcal{S}_M$ in the governing disc equation:

$$\frac{\partial \zeta}{\partial t} = \mathcal{W}\frac{\partial}{\partial r}\left(\frac{U^0}{U'_\phi}\frac{\partial \zeta}{\partial r}\right) + \mathcal{S}_M. \tag{3.77}$$

I use the following prescription for the mass source term:

$$\mathcal{S}_M \propto \delta\left(r - 6r_g\right) \exp\left[-\left(\frac{t - t_1}{t_2}\right)^2\right]. \tag{3.78}$$

Here t_1 is an effective 'disc formation' time, which I expect to coincide roughly with the time of UV re-brightening, and t_2 controls the abruptness of disc formation (Table 3.4). This choice of injection function was chosen for the following simple reason: the purpose of this work is to determine whether the difference between the observed properties

t_1 (days)	$t_{\rm peak} + 92^{+5}_{-15}$
t_2 (days)	50^{+15}_{-20}
t_v (days)	$16.3^{+1.7}_{-1.5}$
$M_{\rm acc}/M_\odot$	$7.3^{+0.5}_{-0.3} \times 10^{-2}$
$M/M_\odot$	$1.4^{+0.2}_{-0.35} \times 10^9$
a/r_g †	0.99
$\bar{\chi}^2_{\rm min}$ *	2.49

Table 3.4: Best fit model parameters. † The black hole spin was fixed. * The formally large reduced chi-squared is discussed below.

of ASASSN-14li and ASASSN-15lh can be determined solely in terms of the mass of the central black hole in both sources. Ideally therefore I would have used an identical initial condition in both cases (that of a numeric delta function). However, injecting matter instantaneously into a ring introduces discontinuous jumps in the UV/optical light curves of discs around particularly massive black holes. This effects the formal quality of fit of the early time UV emission, which is only being modelled with a phenomenological profile, which then artificially affects the fitting procedure. The above form of the injection function allows the TDE light curves to transition smoothly from the early-time to disc-dominated phases, avoiding discontinuous behaviour that would be present from introducing matter instantaneously. I have verified numerically that by neglecting the early time emission entirely and only fitting to the emission at times $t > t_p + 65$ days, good fits to a numerical delta function initial condition are found, with best fit parameters consistent with the more smoothed profile described here.

Anticipating a large black hole mass, matter is fed into the innermost disc regions, with a feeding radius $r = 6r_g$. I have verified numerically that the choice of $6r_g$ does not noticeably effect the quality of fit or the inferred model parameters. The typical radius at which a TDE disc forms is strongly influenced by the tidal radius of the disrupted star, $r_T/r_g \sim M^{-2/3}$, thus discs around larger mass black holes will typically form at smaller radii.

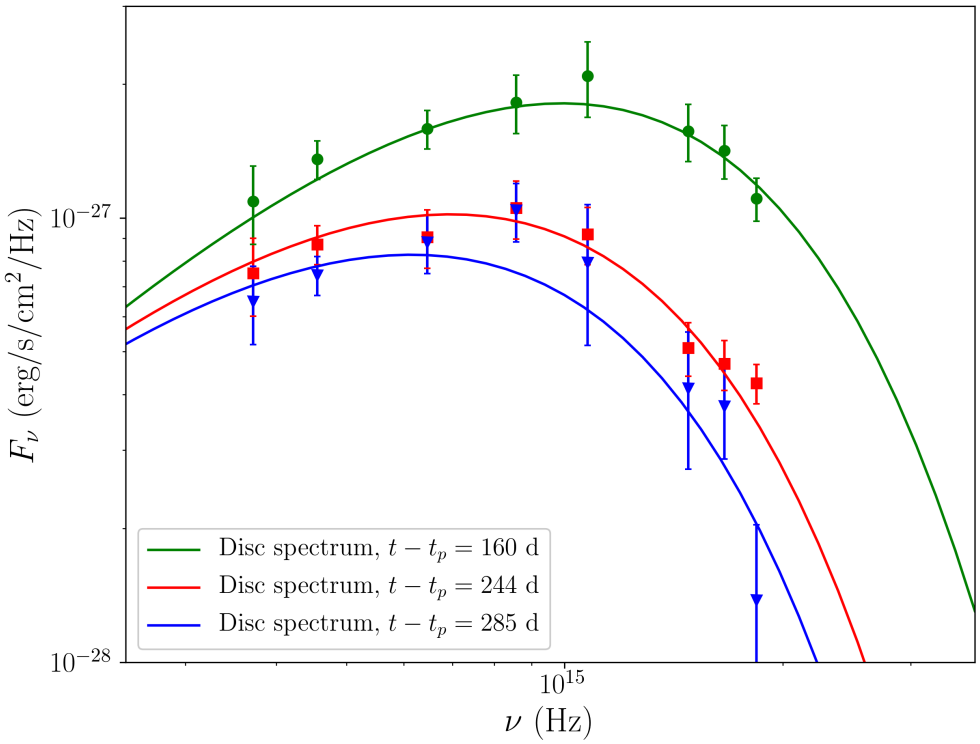

Figure 3.17: The best fit disc spectrum and nearly-simultaneous observations at three different times, denoted on plot.

I simultaneously fit the evolving flux in nine different observing bands, across infrared (i), optical (r, V, g, B), and ultra-violet (U, UVW1, UVM2, UVW2) frequencies. As above, the evolving disc flux is computed at each band's effective frequency. I fix the black hole spin to that of a rapid prograde spin $a/r_g = 0.99$, and orientate the disc face-on. Solutions for different spins and orientation angles are discussed in section 3.11.1. The remaining parameters are the black hole mass M, the accreted mass $M_{\rm acc}$ (in effect a normalisation on the source term $\mathcal{S}_M$), the viscous evolution timescale of the disc t_v, and the time constants t_1 and t_2 in the matter source term (equation 3.78). I fit the disc model with a small but finite ISCO stress, $\gamma = 5$ in the notation of Chapter 2. The presence of a large ISCO stress may be ruled out, which produces UV light curves that evolve too slowly. Acceptable fits were also found for a vanishing ISCO stress. The possible relationship between the ISCO stress and spin are relatively unexplored, especially near the near maximal prograde spin limit. But a small stress is to be expected: the distance between the event horizon, where the stress must vanish, and the ISCO is very small near maximal a/r_g.

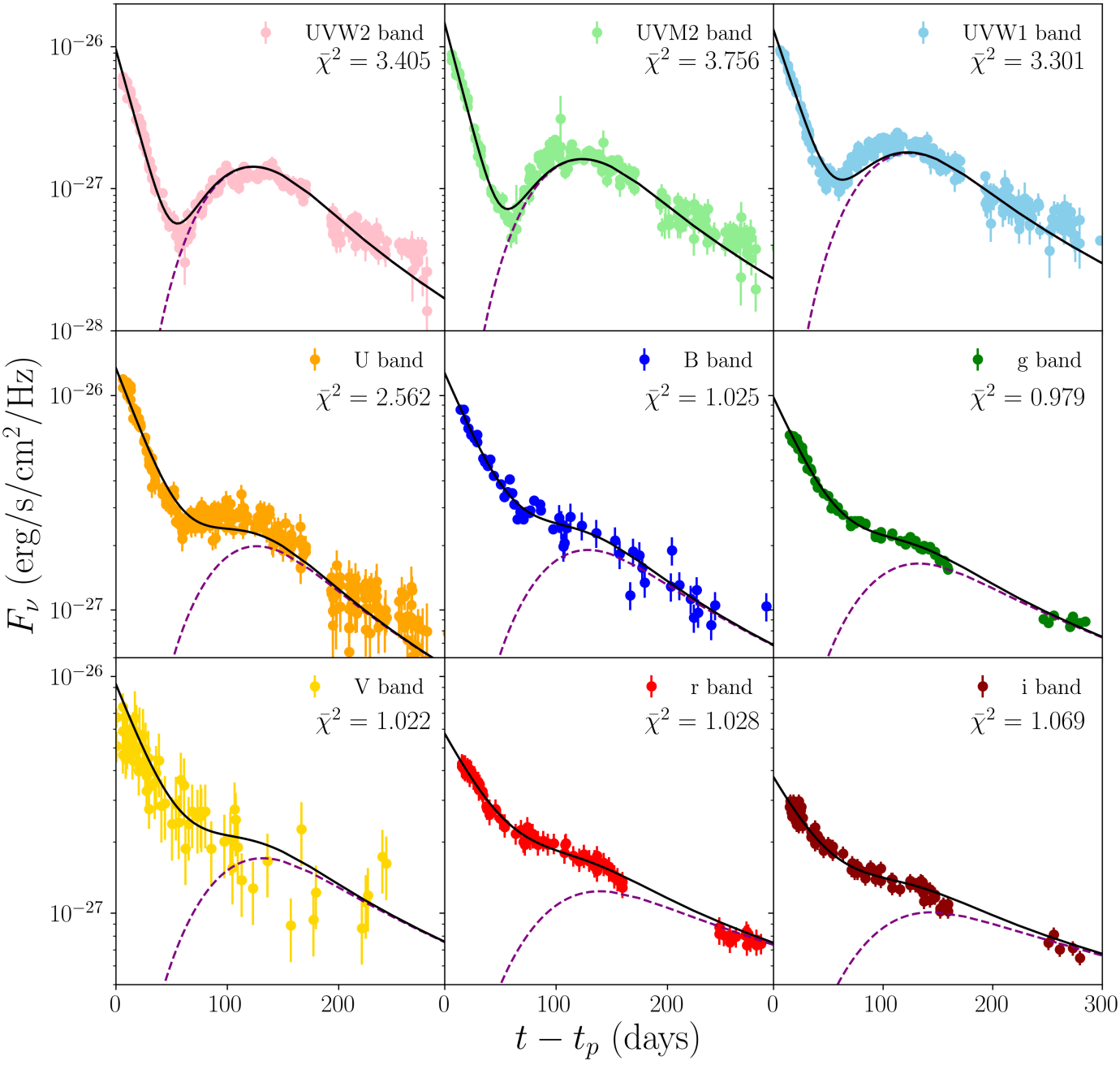

Figure 3.18: The disc model and observed ASASSN-15lh light curves. In each figure the contribution from the evolving accretion disc is displayed by a purple dashed curve. The sum of this disc flux and an exponentially declining flux, relevant at early times, is displayed by black solid curves. While the curves are fit simultaneously, the reduced χ^2 of each band is also displayed; the main source of model-data discrepancy results from correlated short-timescale fluctuations in the four UV light curves.

The fitting procedure minimised the combined χ^2 statistic of the nine observed light curves, with a best fit reduced value of $\bar{\chi}^2_{\rm min} = 3414.7/1370 = 2.49$ (Table 3.4). This formally large reduced χ^2 statistic is a clear consequence of short-timescale fluctuations present in the four well-sampled UV light curves, and is to be expected in any theoretical model using a smooth functional form for the turbulent stress tensor W^r_ϕ. This very standard approach implicitly averages over rapid turbulent variations. Short timescale fluctuations are likely to be highly correlated so that accurately assessing the statistical significance of the fit is not straightforward. I have therefore used χ^2 minimisation as a sensible guide towards finding a best fit, but as χ^2 does not have a gaussian normal distribution, I have not attempted a quantitative assessment of fit, leaving the plots to speak for themselves. The principal constraint on the black hole mass comes from the simultaneous fitting of the highest and lowest photon energy light curves (as is also the case for ASASSN-14li, Appendix D): If the black hole mass is too large, the solution is too bright in the infrared; too low a mass and the solution is too bright in the UVW2 band.

Figure 3.17 depicts the disc spectrum at three different times during the disc dominated phase (denoted on plot). Over-plotted are (nearly) simultaneous observations in a number of different observing bands. These are well fit by the disc model. As was argued in section 3.10, to reproduce the rapidly evolving ultra-violet light curves it is crucial that the observed peak frequency of the disc spectrum lies at $\nu_p \sim \nu_{UV} \sim 10^{15}$ Hz.

Figure 3.18 shows the fitted light curve in the nine different observing bands. The contribution from the disc at each frequency is shown by a purple dashed curve. As with ASASSN-14li, the disc component is separate from the observed flux at the earliest times: the 'total light curve' is found by adding an exponentially decaying early time component to the disc. The early time behaviour is modelled by:

$$F_\nu = A \exp\left(-t/\tau\right), \qquad \text{(early time)}, \tag{3.79}$$

each band with its own A and τ. The physical origin of the early time UV emission is beyond the scope of this model; it could result, e.g., from outflows present in the early stages of the TDE, or from material shocking in the disc formation process. In Figure 3.18 the combined disc and exponential flux is shown by a solid black curve. Exponential profiles are required to accurately model the rapid early time evolution of the UV bands. I find three distinct timescales for the early time emission: the highest

photon energy light curves evolve quickest, with $\tau_{\rm w1,m2,w2} \simeq 15$ d, whereas the emission at lower photon energies decay more slowly: $\tau_{\rm u,b,g,v} \simeq 35$ d, and $\tau_{r,i} \simeq 51$ d.

After ~ 100 days all light curves are dominated by the disc. The subsequent evolution is then dependent upon the explicit observing frequency, with higher energy light curves evolving more rapidly. The (highest photon energy) UVW2 light curve decays by an order of magnitude over an interval where the infrared light curve decays by a factor of only ~ 1.4. This is in accord with the ASASSN-14li analysis. Clearly, an evolving relativistic disc model describes the properties of all nine observed light curves very well.

The bolometric luminosity of the disc solution peaks at $\simeq 3.5 \times 10^{45}$ erg/s, making this disc sub-Eddington at peak ($0.02 L_{\rm Edd}$). The time-integrated radiated energy equals $E_{\rm rad} \simeq 6 \times 10^{52}$ erg.

3.11.1 Black hole properties

The source ASASSN-15lh is located at the centre of a massive red galaxy with limited star formation (Leloudas et al. 2016). There are four existing estimates of the mass of the black hole in ASASSN-15lh, which are based upon distinct, well-established galactic scaling relations. Two estimates are derived from properties of the galactic bulge (Leloudas et al. 2016), while two follow from velocity dispersion measurements (Krühler et al. 2018, Wevers et al. 2017). The estimates for the black hole's mass are: $\log_{10}(M) = 8.88 \pm 0.60$, (bulge mass scaling relationship, Leloudas et al. 2016), $\log_{10}(M) = 8.50 \pm 0.52$, (bulge luminosity scaling relationship, Leloudas et al. 2016), $\log_{10}(M) = 8.32 \pm 0.31$, ($M - \sigma$ relationship, measurement from Wevers et al. 2017) and $\log_{10}(M) = 8.70 \pm 0.41$, ($M - \sigma$ relationship, measurement from Krühler et al. 2018). My best fitting black hole mass $\log_{10}(M) = 9.15^{+0.05}_{-0.13}$ (Table 1) is consistent (at one sigma) with three of these four estimates of the black hole's mass, and is of course obtained by independent means. This good agreement strengthens the argument for a TDE origin of the source.

I have also fit the ASASSN-15lh light curves for a full range of black hole spins, including an $a = 0$ Schwarzschild spacetime, independently of any other considerations. The best fit central masses associated with smaller spins were systematically lower, but always found $M > 9 \times 10^8 M_\odot$. In general, smaller black hole spins produced poorer fits to the observed light curves. A Schwarzschild black hole (best fit mass $M = 9 \times 10^8 M_\odot$)

produced the worst fit $\bar{\chi}^2_{\rm min} = 4284.2/1370 = 3.13$, and would require a $28.3M_\odot$ solar-type star for disruption (Kesden 2012, Figure 3.16). This makes a low spin value very unlikely. For larger spins, the quality of fit is similar to the near-maximal $a/r_g = 0.99$ case. When $a/r_g = 0.9$, the best fitting light curve has: $\bar{\chi}^2_{\rm min} = 3383.1/1370 = 2.47$, with a very similar best fit black hole mass $M = 1.35 \times 10^9 M_\odot$. However even this slight reduction from maximal spin would require a $8.3M_\odot$ star for a disruption, compared to $M_\star = 2.6M_\odot$ for $a/r_g = 0.99$. From the light curves alone I cannot rule out the possibility of an extremely massive star being disrupted by a more moderately rotating black hole. The strong dependence of TDE rate on stellar mass ($\propto M_\star^{-1.89}$ as noted above) however clearly favours a near maximal spin.

The light curves of section 3.11 were produced assuming a face-on inclination. The best fit parameters are, in fact, only weakly sensitive to the disc-observer inclination, with only minor changes to the fitted parameters for $\theta < 20^o$. For higher inclination angles, larger black hole masses were required. Taking the uppermost black hole mass allowed from the galactic bulge range as a hard upper limit, the inclination may be constrained to be $\theta < 60^o$.

The implied large black hole mass points to a star with a mass in excess of $1M_\odot$ being disrupted. The analytical model of Kesden (2012) requires a main sequence star with mass $M_\star \simeq 2.6^{+0.6}_{-0.9} M_\odot$ for a full disruption. (The error range here corresponds to the error range on the fitted black hole mass). Other models give somewhat lower stellar masses for a full disruption (Ivanov and Chernyakova 2006, Sponholz 1994), but current estimates point to a stellar mass of at least $M_\star \sim 2M_\odot$ for full disruption.

Given that a relatively massive ($\sim 2M_\odot$) star has been disrupted, it is somewhat surprising that the disc component of the evolving light curves is powered by only a relatively small accreted mass $M_{\rm acc} \simeq 0.07M_\odot$. It is important to note that this accreted mass value, as in the case of ASASSN-14li, does not include the matter required to power the (extremely bright) early time emission (observed in all bands). Rather, the disc mass represents only a lower bound on the debris mass. Given the likely highly relativistic orbit of the disrupted star, it may well be that a significant portion of the stellar mass was directly accreted in the earliest stages. It has also been argued (Guillochon and Ramirez-Ruiz 2015) that relativistic orbital precession of the tidal disruption streams (induced by a large black hole spin) can lead to inefficient disc formation.

3.11.2 Radio and X-ray observations

No radio emission has been detected from ASASSN-15lh, with upper limits of order $\nu L_\nu \lesssim 10^{38}$ erg/s (Leloudas et al. 2016, Kool et al. 2015). Given the likely near maximal spin of its central black hole, it is perhaps surprising that a jet is not observed. (The observed radio emission is at least 2 to 3 orders of magnitude lower than the bright jetted TDE Swift J1644+57 Levan et al. 2011.) Moreover, unlike other jetted TDEs, ASASSN-15lh is X-ray dim. Initially undetected at X-ray energies (Leloudas et al. 2016), X-ray emission has been more recently detected by Margutti et al. (2017) at the level $L_X \sim 10^{41}$–10^{42} erg/s. A pure disc model is not able to produce even this level of X-ray flux, as the spectrum peaks in the UV and falls off sharply. With only a handful of detected photons, it is difficult to infer spectral properties, but the emission appears to be soft (Margutti et al. 2017). Krühler et al. (2018) note that spectral features of the ASASSN-15lh host galaxy indicate the presence of a weak AGN, which they argue might be the source of the observed X-rays, but at present the origin of the X-rays is poorly understood. It is interesting to note that the majority of TDEs do not appear to be associated with jets. It is not yet clear whether the absence of jet emission is an intrinsic or a misalignment effect.

3.12 Discussion and conclusions

I have modelled the extremely luminous transient ASASSN-15lh at nine separate frequencies (simultaneously), and have shown that a relativistic thin disc model reproduces the data well. The best fit is obtained for a central hole mass of $M \simeq 10^9 M_\odot$ and a near maximal spin parameter $a/r_g = 0.99$, both strikingly large and presumably the result of significant accretion across the black hole's lifetime. The deduced mass is consistent with independent observations based on galactic bulge properties and velocity dispersions. The overall quality of the fit is compelling evidence for a TDE interpretation for ASASSN-15lh. This would be the first TDE to be observed in the disc dominated state at optical and infrared wavelengths.

Most importantly, I have demonstrated that the disc model which well described the X-ray bright 'canonical' TDE ASASSN-14li, when placed into an unusual region of parameter space, was able to reproduce the observed light curves of a TDE source at the very edges of the known TDE parameter space. This provides compelling evidence for the central importance of accretion disc physics in providing a complete

understanding of TDE observables. With the exception of the bright early-time TDE emission observed across optical and UV bands, the dominant emission components of all other evolutionary TDE stages (the X-ray emission at all times, and the late time optical/UV emission) corresponds to direct emission from an evolving accretion disc.

The relativistic disc model of tidal disruption events developed in this Chapter is an extremely powerful probe of the underlying physics of these remarkable events. Numerical modelling of observed TDE data sets provide both excellent model fits to multi-band light curves (Figures 3.6, 3.10, 3.17 and 3.18), as well as strong constraints on the physical parameters of the system (Tables 3.1, 3.4). Complimenting this numerical analysis, detailed analytical modelling of the light curves of relativistic thin disc solutions elucidate *why* TDE light curves have such varied properties. It is chiefly the relative locations of the disc's peak emission frequency, and the frequencies of the observing bands which determines the properties of an individual TDE light curve (Figures 3.12, 3.17). In certain mathematically convenient and physically relevant limits, the full time dependence of TDE light curves can be determined analytically. The X-ray light curves of TDEs represent a particularly important example of this result, being described by what is ultimately an extremely simple analytical profile (equation 3.73, Figure 3.14).

Tidal disruption event systems are likely to span a large physical parameter space. As highlighted in this Chapter, a population of TDEs may contain black hole masses which span $\sim$ 3 orders of magnitude. Similarly, the masses of the population of stellar progenitors may themselves span an order of magnitude, as may the strength of the underlying disc turbulence (the 'effective disc α' values). Clearly, the observed properties of any one TDE system can depend rather sensitively on the precise values taken by its central black hole mass, disc turbulence, and disc mass. In the following Chapter I examine in detail the effect of varying these system parameters on the observed X-ray luminosity of a given TDE source. The goal here, ultimately, is to determine whether the observed variance of TDE populations can be described entirely in terms of the physics of relativistic discs.

4

An analysis of the X-ray luminosity of tidal disruption event discs

The work in this chapter is based upon the following peer-reviewed journal articles
Mummery and Balbus 2021a, MNRAS, 505, 1629
Mummery and Balbus 2021b, MNRAS, 504, 4730
Mummery 2021a, MNRAS, 504, 5144
Mummery 2021b, MNRAS, 507, L24.
Mummery 2022, submitted.

4.1 Introduction

There is now good observational and theoretical evidence that the dominant emission components of many tidal disruption event light curves come from evolving thin discs (Chapter 3). Late time UV observations of six well-observed TDEs show transitions to disc-dominated states after ~ 100 days (van Velzen et al. 2019b), and the spectra of a large sample of X-ray TDEs show properties which are analogous to the high-luminosity spectrally-soft accretion state of X-ray binaries (e.g., Saxton et al. 2012; Miller et al. 2015; Lin et al. 2015; Holoien et al. 2016a; Gezari et al. 2017; Wevers et al. 2019a; Jonker et al. 2020; Wen et al. 2020).

In the previous Chapter I studied in detail the light curves of one such TDE ASASSN-14li. While at early times the UV emission of ASASSN-14li was dominated

by non-disc processes, the full ~ 900 days of X-ray observations are well described by a disc model. Importantly, the X-ray properties of ASASSN-14li are simple to describe analytically, as they depend only on a single disc parameter: the temperature of the disc's hottest point. This result, which stems from the relatively cool ($kT_p \ll 300$ eV) peak disc temperatures of typical TDE systems, means that the observed X-ray properties of TDEs promise to be powerful probes of their underlying physical properties. This promise will only be realised if the key parameters describing a TDE (e.g., the black hole mass and spin, and the stellar mass) can be related to the peak temperature of the disc which forms in the TDE's aftermath. It is the purpose of this Chapter to develop these connections.

The observational evidence suggests that ASASSN-14li is a member of a relatively common spectral class of X-ray bright TDEs, those with extremely soft X-ray spectra. The number of known TDEs, of all spectral classes, now stands at ~ 40, and is set to grow rapidly in the coming years. The total TDE population can be broadly split into three distinct X-ray classes: X-ray dim TDEs, with no observed X-ray emission; X-ray bright TDEs with thermal spectra; and X-ray bright TDEs with nonthermal power-law-with-energy spectra. Two natural questions arise from this spectral information: why are some TDEs X-ray bright, and others not? Why do some TDEs, like ASASSN-14li, exhibit extremely soft X-ray spectra, while others display harder, more AGN-like, spectra? If, as the early evidence hints, all TDEs result in the formation of a relativistic disc, can this observed variety in TDE X-ray properties be explained simply in terms of accretion physics? I will argue in this Chapter that, like the two sources ASASSN-14li and ASASSN-15lh examined in the previous Chapter, the observed variety of the TDE X-ray population can be understood as resulting from the breadth of the underlying physical parameter space spanned by TDE sources. Unlike Galactic X-ray binaries, the central black hole mass of TDE sources may vary by up to three orders of magnitude, and profoundly affect the observed properties of a given source.

In this Chapter I will examine and analyse the properties of TDE systems, as observed at X-ray energies, from across the entire physical parameter space from which they can occur. This Chapter is split into three broad sections. The first, which begins with an extension of the thermal X-ray luminosity modelling of Chapter 3, focusses on those TDEs with spectrally soft X-ray emission. The second, starting in section 4.10, focusses on those TDE sources with harder, AGN-like, spectra. Finally, (starting

in section 4.17) I examine those TDEs which have the largest, potentially super-Eddington, luminosities at early times in their evolution. Each section is complimented by numerical solutions of the underlying disc equations, and comparisons to the current observed TDE populations.

4.2 Extension of the analytical X-ray analysis

In this section, I present a technical derivation of the analytical results used throughout this chapter. The derivation extends the results of Chapter 3 by applying Laplace expansion techniques (Bender and Orszag 1978) to the large photon energy disc spectrum. This extension involves computing explicit higher-order correction terms to the earlier leading-order results. The ultimate goal here is to model the X-ray luminosity emergent from TDE disc systems across the entire TDE parameter space. This parameter space is broad, and these correction terms are important for very luminous, or in particular very hot, X-ray sources.

4.2.1 Spectral integral

The frequency-specific flux density F_ν of the disc radiation, as observed by a distant observer (subscript o), is given by

$$F_\nu(\nu_o) = \int I_\nu(\nu_o)\,\mathrm{d}\Theta_o. \tag{4.1}$$

Following identical reasoning to the previous chapter, this can be expressed as

$$F_\nu(\nu_o) = \int f_\gamma^3 I_\nu(\nu_e)\,\mathrm{d}\Theta_o, \tag{4.2}$$

where the frequency ratio factor f_γ is the ratio of ν_o to the emitted local rest frame frequency ν_e of a photon originating from a disc coordinate (r, ϕ).

Extending the analysis of Chapter 3, I shall assume that the intrinsic disc emission is that of a *colour-corrected* multi-temperature black body, each disc annulus having a temperature T which is found by solving the underlying disc equations. As I intend to model disc solutions which are accreting in a wide range of physical regimes (and Eddington ratios), I incorporate radiative transfer effects via a simple spectral hardening factor f_{col} (Shimura and Takahara 1995), which I shall allow to vary dependent on the disc's properties (Done et al. 2012).

The physics of the "colour correction factor" is qualitatively relatively simple. While I may be modelling "thin" discs, these solutions still have important vertical structure, and in particular the path of photons through the disc atmosphere is a non-trivial radiative transfer problem. The central temperature of an accretion disc is hotter than the radiative temperature found from balancing the locally liberated energy of the disc shear with the local radiative flux, by roughly a factor of the optical depth to the one quarter power $T \sim T_c/\tau^{1/4}$. This radiative temperature T is the one which typically appears in the equations governing the disc's locally emitted spectrum. However, the energy of the disc photons produced in the disc midplane is higher than this, taking a value roughly $\sim k_B T_c$. Only if the liberated disc energy can be fully thermalised do the photons emerge with temperature T. On their path through the disc atmosphere, photons can either be absorbed and re-emitted (thus totally thermalising their energy), or they can undergo elastic scattering. Elastic scattering however, by definition, does not change the energy of the photon, and so if this process dominates in the disc atmosphere, photons will be observed to have the "hotter" temperatures associated with the altitudes closer to the disc midplane, not the disc's $\tau = 1$ surface. The colour-correction factor can therefore be thought of as quantifying the relative dominance of these two different opacities in the disc atmosphere.

The relative importance of different opacities cannot of course modify the constraints of total energy conservation, and so the specific intensity of the locally emitted radiation is typically modelled with a modified Planck function

$$I_\nu(\nu_e) = f_{\rm col}^{-4} B_\nu(\nu_e, f_{\rm col}T) \equiv \frac{2h\nu_e^3}{f_{\rm col}^4 c^2}\left[\exp\left(\frac{h\nu_e}{k_B f_{\rm col} T}\right) - 1\right]^{-1}. \tag{4.3}$$

Note that the normalising factor $f_{\rm col}^{-4}$ here ensures that, despite the temperature of the emission being increased, the total emitted luminosity remains σT^4 (and therefore energy is conserved). While scattering in the disc atmosphere generally acts to increase the observed temperature of the disc emission, at high enough temperatures there is a counteracting effect: photons are also Compton down-scattered by the atoms in the disc atmosphere, and this prevents the colour-correction factor reaching values which are too large. This 'saturation' typically leads to values $f_{\rm col} \sim 2$ for supermassive black hole discs (Done et al. 2012). The full radiative transfer equations in the disc atmosphere are far too complex to solve analytically, but simple (and relatively successful) models of $f_{\rm col}(T)$ have been developed, and will be used in this Chapter.

For an observer at a large distance D from the source, the differential solid angle into which the radiation is emitted is

$$\mathrm{d}\Theta_o = \frac{\mathrm{d}b_1 \mathrm{d}b_2}{D^2}, \tag{4.4}$$

where b_1 and b_2 are appropriate photon impact parameters at infinity (Li et al. 2005). (The impact parameters are usually denoted α and β. Here, however, I reserve α for the Shakura and Sunyaev (1973) viscosity parameter, and β for the inverse temperature.) The observed flux from the disc surface $\mathcal{S}$ is therefore

$$F_\nu(\nu_o) = \frac{1}{D^2} \iint_{\mathcal{S}} f_\gamma^3 f_{\mathrm{col}}^{-4} B_\nu(\nu_o/f_\gamma, f_{\mathrm{col}}T)\ \mathrm{d}b_1 \mathrm{d}b_2. \tag{4.5}$$

I am interested here in the high energy limit of this expression ($h\nu \gg k_B T$). An appropriate observational probe of this spectral region is F_X, the total X-ray flux observed across a satellite's passband (for the *Swift* telescope for example, this corresponds to photon energies in the range 0.3 to 10 keV). This is straightforwardly calculated by integrating equation 4.5 over the corresponding (observer) frequency range:

$$F_X = \frac{1}{D^2} \int_{\nu_l}^{\nu_u} \iint_{\mathcal{S}} f_\gamma^3 f_{\mathrm{col}}^{-4} B_\nu(\nu_o/f_\gamma, f_{\mathrm{col}}T)\ \mathrm{d}b_1 \mathrm{d}b_2\, \mathrm{d}\nu_o, \tag{4.6}$$

where ν_l and ν_u correspond to the formal lower and upper frequencies of the satellite's pass-band respectively.

4.2.2 High energy spectrum

I begin, as in Chapter 3, by recasting equations 4.5 and 4.6 into a more familiar form, defining an "effective temperature" $\widetilde{T}$ by

$$\widetilde{T}(b_1, b_2, t) = f_\gamma(b_1, b_2) f_{\mathrm{col}}(b_1, b_2, t)\, T\Big(b_1, b_2, t\Big), \tag{4.7}$$

where the disc temperature depends implicitly on b_1 and b_2 through its radial r-dependence, and the colour-correction factor will generally depend on the local disc temperature T. (Note that for an evolving disc, the effective temperature is a time-dependent quantity.) I define the dimensionless parameter Λ_o by

$$\Lambda_o \equiv \frac{h\nu_o}{k_B \widetilde{T}_p}, \tag{4.8}$$

where $\widetilde{T}_p$ is the maximum effective disc temperature $\widetilde{T}$. For the remainder of this chapter I shall work in the high energy limit, which corresponds to

$$\Lambda_o \gg 1. \tag{4.9}$$

In this regime, the observed flux is well-approximated by a modified Wien-tail form

$$F_\nu(\nu_o) = \frac{2h\nu_o^3}{D^2c^2} \iint_{\mathcal{S}} f_{\rm col}^{-4} \exp\left(-\frac{h\nu_o}{k_B\widetilde{T}}\right) \, \mathrm{d}b_1 \mathrm{d}b_2 \, . \tag{4.10}$$

To make analytic progress, I shall further assume that the disc is observed nearly face-on, and that the colour-correction factor $f_{\rm col}$ in the innermost disc regions is independent of radius. Generally, the colour correction factor increases with increasing disc temperature, as, for a given disc density, a disc's absorption opacity is lower at a higher temperatures[1] (Davis et al. 2006; Done et al. 2012). However, the maximum amplitude $f_{\rm col}$ can reach in an accretion disc is capped, with its value saturating at high temperatures. This saturation value is set physically by Compton downscattering in the disc, and approximately limits the colour correction factor to the following value

$$f_{\rm col} \sim \left(\frac{72\,\mathrm{keV}}{k_B T}\right)^{1/9}, \quad T > 10^5\,\mathrm{K}. \tag{4.11}$$

For the purposes of computing the integral in equation 4.10 only the colour correction factor of the very hottest disc regions is of interest, as these are the only disc regions which contribute to the Wien tail flux. As these disc regions are likely to have saturated the colour correction factor (for typical disc parameters they reach temperatures $T > 10^5$K), $f_{\rm col}$ will only depend very weakly on disc temperature, and even more weakly on disc radius, and so it is a reasonable assumption to treat it as a constant in integral 4.10. Complementing this analysis, at later points in this chapter I shall numerically model the colour correction factor within the disc using the full model of Done et al. (2012). It will be shown that a complex model of $f_{\rm col}$ has only a small effect on the *X-ray* flux of these disc models (although this is not true for all observing frequencies).

While numerical results for general inclination angles will also be computed below, face-on analytical solutions are extremely useful for understanding important gross properties of more general solutions. In the face-on limit, the observed radiation undergoes no relativistic Doppler-boosting, meaning that the frequency ratio factor

[1]Recall that the free-free Kramers opacity scales as $\kappa \propto \rho T_c^{-7/2}$.

f_γ is symmetric in the image plane. The above integrals can therefore be expressed in terms of a radial image coordinate R

$$R \equiv \sqrt{b_1^2 + b_2^2}\,, \tag{4.12}$$

and therefore the flux integral is given by

$$F_\nu(\nu_o) = \frac{4\pi h \nu_o^3}{D^2 c^2 f_{\rm col}^4} \int_{R_p}^{\infty} R \exp\left(-\frac{h\nu_o}{k_B \widetilde{T}}\right) \mathrm{d}R\,, \tag{4.13}$$

where R_p is the image plane coordinate of the inner disc edge. Note that, due to gravitational lensing of the emitted photons, this image plane inner disc coordinate is not equal to the ISCO radius $R_p \neq R_I$. Only the hottest parts of the disc very near the temperature maximum will contribute to the observed flux, and this integral may therefore be asymptotically expanded via Laplace's method. I start by Taylor expanding the inverse of the effective temperature about the effective temperature maximum:

$$\beta \equiv (k_B \widetilde{T})^{-1} = \beta_p + \frac{\partial \beta}{\partial R}(R - R_p) + \sum_{n=2}^{\infty} \beta^{(n)} \frac{(R - R_p)^n}{n!}, \tag{4.14}$$

where each derivative is evaluated at $R = R_p$, $\beta_p \equiv (k_B \widetilde{T}_p)^{-1}$, and

$$\beta^{(n)} \equiv \left(\frac{\partial}{\partial R}\right)^n \beta. \tag{4.15}$$

In this section, I shall assume that the temperature maximum occurs at the inner disc edge, which is appropriate for a disc with a finite ISCO stress. (Vanishing stress solutions will be presented in section 4.6.) Introducing the dimensionless variables

$$k_n \equiv \beta^{(n)} R_p^n / \beta_p, \quad y \equiv (R - R_p)/R_p, \tag{4.16}$$

leaves

$$F_\nu = \frac{4\pi h \nu_o^3}{c^2 f_{\rm col}^4} \left(\frac{R_p}{D}\right)^2 I(\Lambda_o), \tag{4.17}$$

where the function $I(\Lambda_o)$ is given by

$$I(\Lambda_o) = e^{-\Lambda_o} \int_0^{\infty} (1 + y)\, F(y, \Lambda_o)\, \exp\left(-k_1 \Lambda_o y\right) \mathrm{d}y\,, \tag{4.18}$$

and

$$F(y, \Lambda_o) = \exp\left(-\Lambda_o \sum_{n=2}^{\infty} k_n \frac{y^n}{n!}\right). \tag{4.19}$$

The large Λ_o solution of $I(\Lambda_o)$ is

$$I(\Lambda_o) = e^{-\Lambda_o} \sum_{m=0}^{\infty} \frac{F^{(m)}(0, \Lambda_o)}{(k_1 \Lambda_o)^{m+1}} \left(1 + \frac{m+1}{k_1 \Lambda_o}\right). \tag{4.20}$$

where $F^{(m)}(0, \Lambda_o)$ is the m^{th} y-derivative of $F(y, \Lambda_o)$, evaluated at $y = 0$[2]. I find that over the entire parameter space of interest, truncating this sum at order Λ_o^{-3} accurately reproduces the properties of the exactly calculated numerical X-ray light curves. I shall therefore neglect terms of order Λ_o^{-4}, and higher. To truncate this sum at order Λ_o^{-3}, the derivatives $F^{(m)}(y, \Lambda_o)$ up to and including $m = 4$ are required. These derivatives follow from the definition 4.19

$$F^{(0)}(0, \Lambda_o) = 1, \tag{4.21}$$
$$F^{(1)}(0, \Lambda_o) = 0, \tag{4.22}$$
$$F^{(2)}(0, \Lambda_o) = -k_2 \Lambda_o, \tag{4.23}$$
$$F^{(3)}(0, \Lambda_o) = -k_3 \Lambda_o, \tag{4.24}$$
$$F^{(4)}(0, \Lambda_o) = -k_4 \Lambda_o + 3k_3^2 \Lambda_o^2. \tag{4.25}$$

The flux integral is therefore given by

$$I(\Lambda_o) = e^{-\Lambda_o} \left[\frac{c_1}{\Lambda_o} + \frac{c_2}{\Lambda_o^2} + \frac{c_3}{\Lambda_o^3} + O\left(\Lambda_o^{-4}\right) + ...\right], \tag{4.26}$$

where

$$c_1 = 1/k_1, \quad c_2 = (k_1 - k_2)/k_1^3, \quad c_3 = (3k_3^2 - 3k_1 k_2 - k_1 k_3)/k_1^5. \tag{4.27}$$

To gain a sense of the scale of the numerical values of the c-coefficients, consider a simple disc temperature profile

$$T \propto R^{-q}, \quad q > 0, \tag{4.28}$$

and neglect the effects of gravitational red-shift. In this limit

$$k_n = \prod_{j=1}^{n} (q - j + 1), \tag{4.29}$$

and

$$c_1 = 1/q, \quad c_2 = (2 - q)/q^2, \quad c_3 = (3q^4 - 18q^3 + 38q^2 - 36q + 13)/q^3. \tag{4.30}$$

[2]This as an application of Watson's lemma (Bender and Orszag 1978).

These coefficients are all positive, and order unity, for $0 < q < 1$. For reference, classical disc models are well approximated by equation 4.28 in their inner regions, with $q = 3/4$ (vanishing ISCO stress, Chapter 3 equation 3.23) or $q = 7/8$ (finite ISCO stress; equation 3.21). For the case of finite ISCO stress:

$$c_1 = 8/7 \approx 1.14, \quad c_2 = 72/49 \approx 1.47, \quad c_3 = 1203/2744 \approx 0.44. \tag{4.31}$$

4.2.3 The X-ray flux

With a functional form for the spectrum in place, the observed X-ray flux may be simply calculated:

$$F_X = \int_{\nu_l}^{\infty} F_\nu(\nu_o)\,\mathrm{d}\nu_o = (h\beta_p)^{-1} \int_{\Lambda}^{\infty} F_\nu(\Lambda_o)\,\mathrm{d}\Lambda_o, \tag{4.32}$$

where

$$\Lambda \equiv \frac{h\nu_l}{k_B \widetilde{T}_p} \gg 1, \tag{4.33}$$

and the upper integration limit has been extended to infinity, which introduces only exponentially small corrections. The X-ray luminosity is then of the form

$$F_X = \frac{4\pi h \nu_l^4}{c^2 f_{\mathrm{col}}^4} \left(\frac{R_p}{D}\right)^2 K(\Lambda), \tag{4.34}$$

where $K(\Lambda)$ is the expansion:

$$K(\Lambda) = \frac{1}{\Lambda^4} \int_{\Lambda}^{\infty} e^{-\Lambda_o} \left[c_1 \Lambda_o^2 + c_2 \Lambda_o + c_3\right] \mathrm{d}\Lambda_o. \tag{4.35}$$

This becomes

$$K(\Lambda) = \frac{e^{-\Lambda}}{\Lambda^4} \left[(2 + 2\Lambda + \Lambda^2)c_1 + (1 + \Lambda)c_2 + c_3\right]. \tag{4.36}$$

The X-ray luminosity is then given by

$$F_X = F_0 \left(\frac{R_p}{D}\right)^2 \left[\frac{1}{\Lambda^2} + \frac{\psi_1}{\Lambda^3} + \frac{\psi_2}{\Lambda^4}\right] e^{-\Lambda}, \tag{4.37}$$

with amplitude

$$F_0 = \frac{4\pi}{c^2 f_{\mathrm{col}}^4} h \nu_l^4 c_1. \tag{4.38}$$

The factor $(R_p/D)^2$, is related to the angular size of the disc on the sky, and the coefficients are:

$$\psi_1 = 2 + c_2/c_1, \quad \psi_2 = 2 + (c_2 + c_3)/c_1. \tag{4.39}$$

For a disc with a temperature $T \propto R^{-7/8}$, these have numerical values

$$\psi_1 \simeq 3.29, \quad \psi_2 \simeq 3.67. \tag{4.40}$$

Equation 4.37 is very general, and holds for thermal emission from a finite ISCO stress disc whenever $h\nu_l > k_B T_p$. Note that *only* the temperature of the hottest part of the disc enters this equation. In this regard, the X-ray properties of these disc solutions are extremely simple to describe: one only needs to understand the properties of the hottest regions, not the global disc properties. The dependence of this important peak disc temperature scale on system parameters may be determined analytically, once a turbulent stress parameterisation and initial condition are specified.

4.3 Temperature, X-ray flux, and bolometric luminosity scalings

4.3.1 Disc temperature

The dominant r-ϕ component of the turbulent stress tensor $W^r{}_\phi$ serves to transport angular momentum throughout the disc as well as to extract the free energy of the disc shear. This free energy is then thermalised and radiated from the disc surface. Both the extraction and the dissipation are assumed to be local processes. These standard assumptions lead to a disc temperature profile given, in relativistic theory, by (Chapter 2)

$$\sigma T^4 = -\frac{U^0 U^\phi}{2r} \, (\ln \Omega)' \, \zeta(r,t), \tag{4.41}$$

where

$$\zeta \equiv r \Sigma W^r{}_\phi / U^0, \tag{4.42}$$

and σ is the standard Stefan-Boltzmann constant. In terms of more practical physical variables, equation 4.41 reads

$$\sigma T^4 = \frac{3\sqrt{GM}}{4\, r^{7/2}} \frac{\zeta(r,t)}{1 - 3r_g/r + 2a\sqrt{r_g/r^3}}. \tag{4.43}$$

where the gravitation radius r_g is defined by $r_g = GM/c^2$.

There are five physical variables which completely describe the characteristic peak temperature scale of the disc: the initial disc mass M_d; the initial disc radius r_0; the black hole mass M; the black hole spin a; and the magnitude of the turbulent stress, which is expressed in terms of the Shakura and Sunyaev (1973) parameter α. The peak disc temperature is particularly sensitive to the three parameters M_d, M and α. When expressed in terms of these three variables, radial scales (such as the ISCO) vary linearly with the black hole mass

$$r \propto M, \tag{4.44}$$

and by modelling the disc as an initial ring of material laid down at some radius r_0, the surface density scales as

$$\Sigma \propto M_d/r_0^2 \propto M_d M^{-2}. \tag{4.45}$$

The form of the turbulent stress cannot be found from first principles of course; some prescription is needed. As in Chapters 2 and 3, I compute the turbulent stress using a gas pressure dominated version of the standard α-disc model of Shakura and Sunyaev (1973). As demonstrated in Appendix F, the precise details of modelling are not critical, as long as the evolution is stable. This α prescription is just a special case with rather simple physics. Of course, the degree to which a particular stress parameterisation accurately models the properties of a true turbulent stress is in any case very difficult to quantify. The principal conclusions of this study are not sensitive to the precise functional form of the turbulent stress, and thus this approach should capture the essential disc dynamics and energetics, provided only that *some* well-defined, local enhanced stress tensor exists, even if it is not of the precise mathematical form used here.

The turbulent stress $W^r{}_\phi$ in this simplified α-disc model is defined by:

$$W^r{}_\phi \equiv \alpha r c_s^2, \tag{4.46}$$

where c_s is the isothermal gas sound speed, which is related to the gas pressure P_g and density ρ through the standard ideal gas equation of state

$$c_s^2 = \frac{P_g}{\rho} = \frac{k_B T_c}{\mu m_p}. \tag{4.47}$$

In this expression, T_c is the disc mid-plane temperature, and μ is the mean molecular mass of a fluid element in units of the proton mass m_p. The extra factor of r in equation

4.46 is a consequence of its mixed tensorial form: with a covariant ϕ index, $W^r{}_\phi$ measures correlated fluctuations between the angular *momentum* and radial velocity of the fluid, rather than fluctuations in the ordinary circular and radial velocities of the fluid.

In the simplest radiative α models, the central mid-plane temperature of the disc T_c is related to the surface temperature T (equation 4.43) by

$$T_c^4 = \frac{3}{8}\kappa\Sigma T^4, \tag{4.48}$$

where κ is the disc opacity. In the Newtonian limit, the surface temperature is given by

$$\sigma T^4 = -\frac{1}{2}W^r{}_\phi \Sigma\Omega'. \tag{4.49}$$

The opacity within the disc is expected to be dominated by electron scattering, and therefor the total opacity is assumed constant and equal to

$$\kappa = \kappa_{\rm es} \simeq 0.034\,{\rm m^2 kg^{-1}}. \tag{4.50}$$

Results for different opacity laws are presented in Appendix F. The system of equations 4.46–4.50 is closed, with a resulting turbulent stress given by

$$W^r{}_\phi = C\,\Sigma^{2/3} r^{1/2}, \tag{4.51}$$

where C is the dimensional constant

$$C \equiv \alpha^{4/3}\left(\frac{k_B}{\mu m_p}\right)^{4/3}\left[\frac{9}{32\sigma}\kappa_{\rm es}\sqrt{GM}\right]^{1/3}. \tag{4.52}$$

Equation 4.49 then simplifies to

$$\sigma T^4 = \frac{3C}{4r^2}\Sigma^{5/3}\sqrt{GM}, \tag{4.53}$$

and the disc surface temperature T then satisfies the following scaling law:

$$T \propto \frac{\alpha^{1/3} M_d^{5/12}}{M^{7/6}}. \tag{4.54}$$

Note that these scalings are thus far not particular to my own modelling; rather, they follow from standard α theory. Nevertheless, I shall demonstrate that these dependencies have considerable observational significance.

4.3.2 Bolometric luminosity

Both the peak temperature and the bolometric luminosity of the thin disc equation solutions are strongly dependent on the model parameters, particularly the black hole mass (equation 4.54). The luminosity is found by integrating the locally radiated flux over the entirety of the disc. More explicitly,

$$L_{\rm bol}(t) = 2\pi \int_{r_I}^{\infty} (g_{rr} g_{\phi\phi})^{1/2} \gamma^{\phi}(r, a)\, 2\sigma T^4(r, t)\, {\rm d}r. \tag{4.55}$$

Here γ^{ϕ} is a relativistic factor relating the disc area element in the rotating disc frame to that of the Boyer-Lindquist coordinate system. (See Bardeen et al. 1972 for a detailed discussion.)

The peak bolometric luminosity scaling follows from equation 4.54:

$$L_{\rm bol,peak} \propto R^2 T_p^4 \propto \alpha^{4/3} M_d^{5/3} M^{-8/3}. \tag{4.56}$$

The Eddington luminosity $L_{\rm Edd} \propto M$, hence the luminosity ratio scales as:

$$l \equiv \frac{L_{\rm bol,peak}}{L_{\rm Edd}} \propto \frac{\alpha^{4/3} M_d^{5/3}}{M^{11/3}} \leq 1. \tag{4.57}$$

The final inequality is a self-consistency constraint, as l values in excess of unity are unlikely to be compatible with the assumptions of the thin disc model. It will transpire that the constraints imposed by the Eddington luminosity are important for understanding the X-ray light curves of TDEs.

4.3.3 X-ray flux

The X-ray flux is very sensitive to the parameter $\Lambda \equiv h\nu_l / k_B \widetilde{T}_p$. Explicitly displaying the key parameter scalings, whilst absorbing other collateral factors into an amplitude A_1, leaves

$$\Lambda = A_1 \frac{M^{7/6}}{\alpha^{1/3} M_d^{5/12}}. \tag{4.58}$$

By construction, A_1 then depends upon the non-displayed system parameters (notaby the black hole spin a), and will be determined numerically. Finally, the angular size of the disc on the sky is proportional to $(M/D)^2$, and thus the leading order X-ray flux scales as

$$F_X \propto \frac{1}{D^2} \frac{\alpha^{2/3} M_d^{5/6}}{M^{1/3}} \exp\left(-A_1 \frac{M^{7/6}}{\alpha^{1/3} M_d^{5/12}}. \right) \tag{4.59}$$

It is clear from this analysis that the X-ray flux of evolving relativistic disc solutions will be an extremely sensitive function of the system parameters M_d, α and M. The flux depends upon the disc parameters in a more-or-less intuitive manner: larger mass discs with a greater turbulent stress will be brighter in X-rays than lower mass discs with weaker turbulence. Similarly, since discs around more massive black holes penetrate less deeply into their central gravitational potential, they attain lower peak disc temperatures. For a given disc mass and α parameter, such cooler discs produce substantially dimmer X-ray light curves around more massive black holes: this is a more important effect than the M^2 scaling of the emitting disc area.

4.4 Numerical evaluation – fiducial case

In this section, so as to verify this analysis, I numerically compute the peak observed flux of the evolving X-ray light curves for a fiducial set of disc parameters.

4.4.1 Fiducial model light curve

I compute the 0.3–10 keV X-ray light curves of a simple disc model, with parameters summarised in Table 4.1. The initial disc is described by a numerical delta function ring located at a radius $R_0 = 30r_g$, with initial mass $M_d = 0.5M_\odot$. The disc is evolved forward in time using the evolution equation 3.2, with turbulent stress given by equations 4.51 and 4.52 with $\alpha = 0.1$. The numerical simulations in this section all assume a finite ISCO stress. To avoid unsustainable behaviour at large times in the form of a divergent luminosity, I implement the 'quasi-circular orbit' approach developed in Chapter 2, with a γ parameter of $\gamma = 0.1$. This allows a small but finite departure from strictly circular orbits. By way of comparison, results for a vanishing ISCO stress are presented in section 4.6.

The time-dependent disc temperature profile is calculated with equation 4.43, and photon ray tracing calculations, assuming a face-on disc orientation, are used to compute the disc's evolving X-ray light curve (see Appendix C). In this section I assume that the spectral hardening factor has saturated in the innermost disc regions, to a value of $f_{\rm col} = 2$. This value is in keeping with the analytic estimate of

$$f_{\rm col} \simeq \left(\frac{72\,{\rm keV}}{k_B T}\right)^{1/9} \tag{4.60}$$

Parameter	Value
a/r_g	0
R_0	$30r_g$
α	0.1
M_d	$0.5M_\odot$
$\theta_{\rm obs}$	0°
$f_{\rm col}$	2
D	100 Mpc

Table 4.1: The parameters used to calculate the fiducial X-ray light curves of Figure 4.1.

for the typical peak disc energies considered in this work (Davis et al. 2006; Done et al. 2012). In the much cooler disc regions at larger disc radii a constant $f_{\rm col}$ will be a poor assumption, however these regions will not contribute to the X-ray flux (in later sections I will relax this assumption and use the full colour correction model of Done et al. (2012), the effects of using a more complex model are minor).

The peak observed X-ray flux, assuming a source-observer distance of $D = 100\,\mathrm{Mpc}$, is recorded for each disc solution. I repeat this procedure for black hole masses varying between $M = 5 \times 10^5 M_\odot$ and $M = 1.5 \times 10^7 M_\odot$. The peak observed flux versus black hole mass is plotted as blue points in Figure 4.1. The black dashed line corresponds to the *Swift* XRTs minimum flux sensitivity[3], $F_{X,\rm lim} = 4 \times 10^{-14}\,\mathrm{erg\,s^{-1}cm^{-2}}$.

I also compute the evolving disc's bolometric luminosity using equation 4.55. For each black hole mass, the peak value of the disc bolometric light curve is compared with the black hole's Eddington luminosity. Discs for which this peak value exceeds the Eddington luminosity are plotted with green diamonds. The governing assumptions of the relativistic disc model will not be valid in this regime, and these values should thus be viewed as purely formal.

[3]http://swift.gsfc.nasa.gov/about_swift/xrt_desc.html

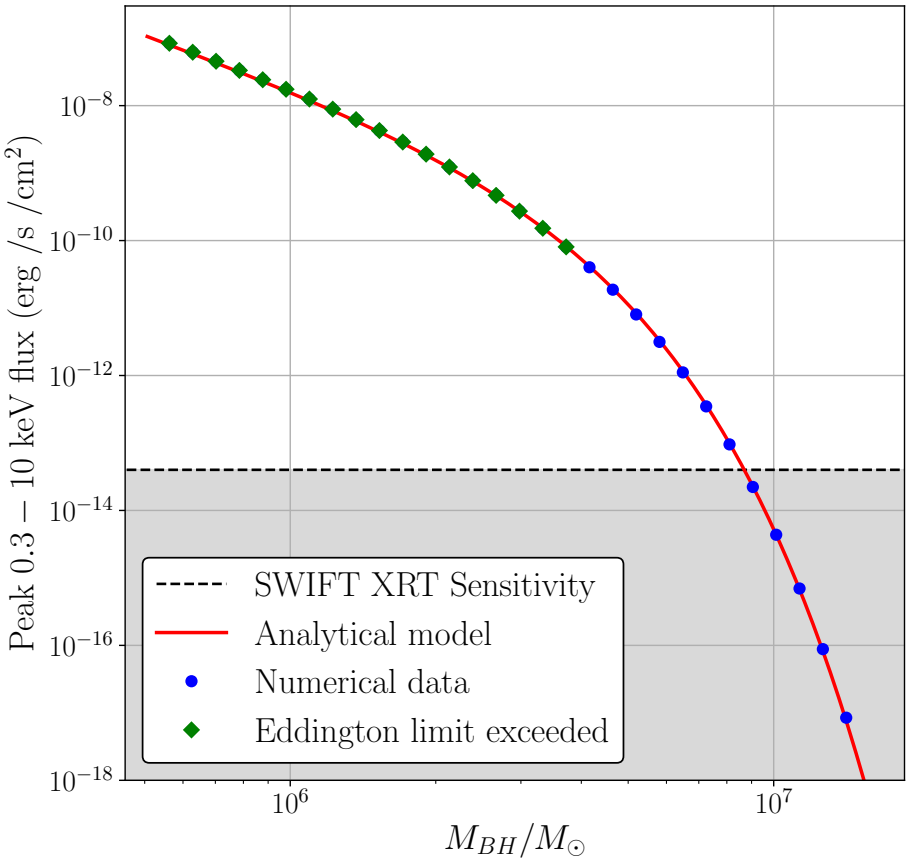

Figure 4.1: The peak 0.3–10 keV X-ray flux, assuming a distance of 100Mpc, for models with an initial disc mass $M_d = 0.5M_\odot$ and $\alpha = 0.1$, as a funtion of black hole mass. Blue dotted points correspond to discs with sub-Eddington peak bolometric luminosities, whereas green diamonds correspond to discs with super-Eddington bolometric luminosities, which are presented for completeness but do not represent a physically valid regime. The red solid curve is a comparison fit to the theoretical curve equation 4.59, indistinguishable from the numerical result. The grey zone lies below *Swift* detectability.

The parameters F_0, ψ_1, ψ_2 and the amplitude of the Λ parameter A_1 are fit to these numerically calculated values. The best fit analytic curve is plotted as the red solid curve. The analytic expression (equation 4.59) provides an excellent fit to the numerically calculated values. In Appendix G I present the fitting equations in full, in order to facilitate the reproduction of these results.

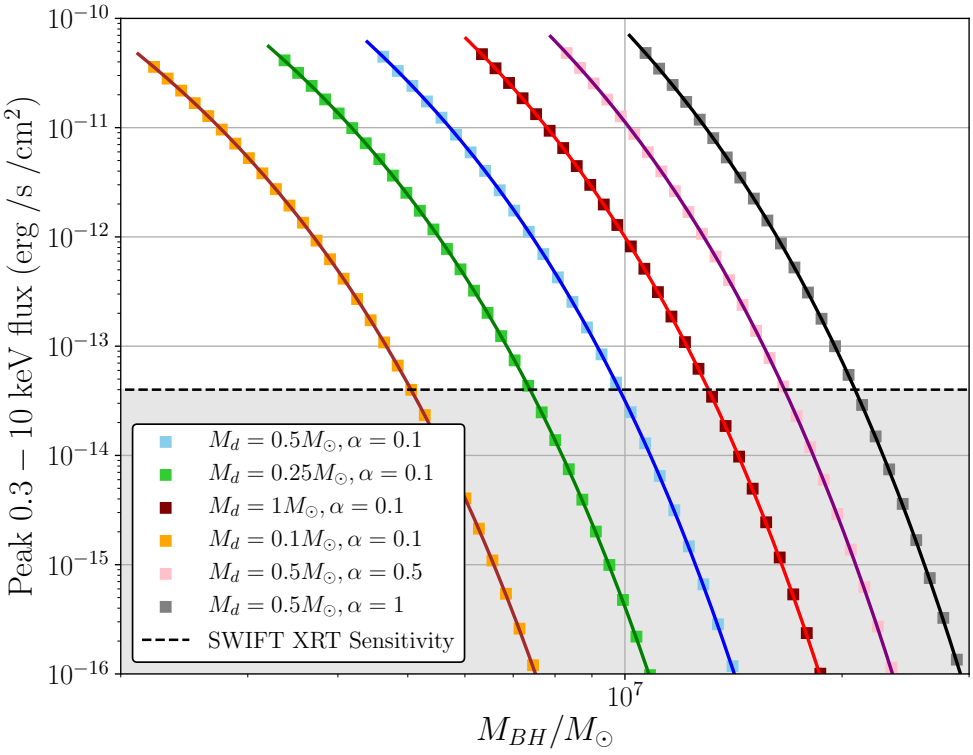

Figure 4.2: The peak X-ray flux, as observed at 100Mpc, for different initial disc masses M_d and α parameters as shown.

4.4.2 Varying α and M_d

Once F_0, ψ_1, ψ_2 and A_1 have been determined from a single set of numerically determined fluxes, the peak X-ray flux for different values of α, M_d and M follows simply. Figure 4.2 shows the peak observed X-ray fluxes as a function of black hole mass, for light curves produced with different disc parameters, as shown. Only the parameter regimes where $L_{\rm bol} < L_{\rm Edd}$ are displayed. Since $L_{\rm bol} \propto M^{-8/3}$ (equation 4.56), this corresponds to black hole masses in excess of a characteristic value I denote as $M_{\rm Edd}$. This "Eddington mass" is a function of the disc mass and α parameter (equation 4.57). The solid curves in Figure 4.2 are calculated using the analytical model (equation 4.37).

Figure 4.2 demonstrates that the analytical model reproduces the numerical results very well for a wide range of physically reasonable disc parameters. The exponential cut-off of the X-ray flux from large mass black holes means that TDE discs around black hole masses larger than a critical limiting value (denoted $M_{\rm lim}$), will be unobservable at X-ray energies.

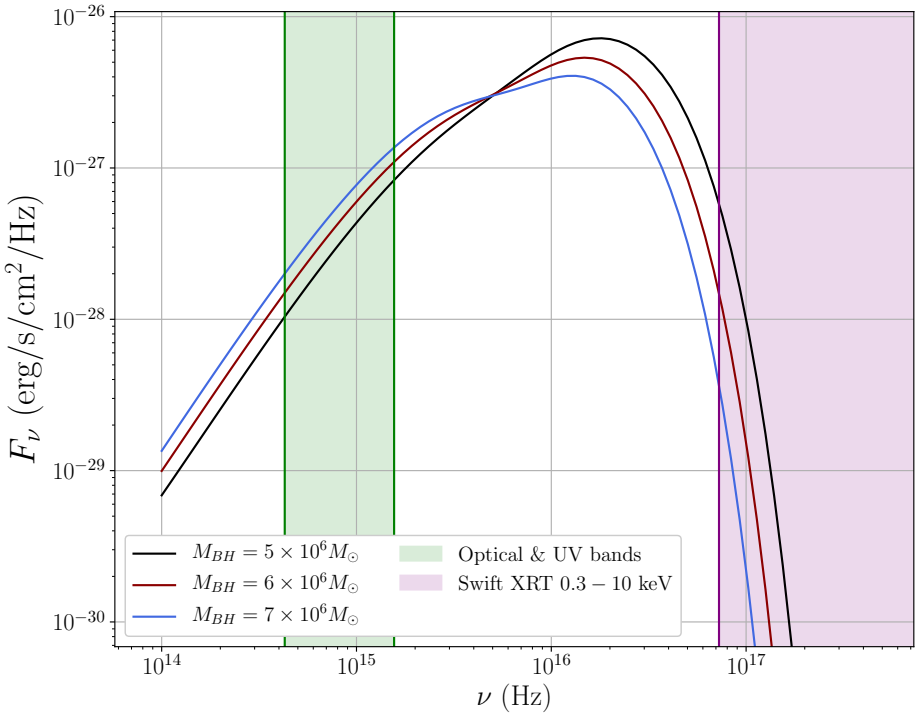

Figure 4.3: The disc spectrum at the time of peak bolometric luminosity for three different discs, all with initial mass $M_d = 0.5 M_\odot$ and $\alpha = 0.1$, for three different black hole masses. The disc spectra are calculated assuming $f_{\rm col} = 2$ when the disc temperature $T > T_\star = 7 \times 10^4$ K, and $f_{\rm col} = 1$ otherwise. The green and purple shaded regions correspond to optical and (part of the) X-ray observing bands respectively. Note that while the bolometric luminosities of these solutions are similar, the observable X-ray luminosity is strongly black hole mass-dependent.

4.4.3 Summary

The peak observed 0.3–10 keV fluxes of TDE discs evolving in a Schwarzschild spacetime for a wide variety of assumed disc parameters have been computed. The interest here is in sub-Eddington disc solutions, which for a given disc mass and α parameter, are those around black holes with masses larger than a characteristic scale $M > M_{\rm Edd}$. The X-ray flux of these solutions is exponentially cut-off as a function of black hole mass, leading to TDE discs becoming unobservable at X-ray energies for black hole masses larger than a value $M_{\rm lim}$, the X-ray limiting mass.

Note that while the X-ray luminosities of these disc solutions at the "Eddington" and "Limiting" masses differ by a large degree ($L_{X,\rm Edd}/L_{X,\rm lim} \sim 1000$), their *bolometric* luminosities differ by a much smaller factor ($L_{\rm bol,Edd}/L_{\rm bol,lim} = (M_{\rm lim}/M_{\rm Edd})^{8/3} \sim 6$). The total energetics of the bolometric light curves are therefore grossly similar; it

is only the respective spectral distributions which sharply differ. This is especially clear in Figure 4.3, which shows a snapshot of the disc spectrum at the time at which the disc bolometric luminosities peak, for different black hole masses (denoted on the plot). This demonstrates the heightened sensitivity of the observed X-ray flux to the peak disc temperature, in contrast to the much smaller variation of the bolometric disc luminosity for different black hole masses.

4.5 Limiting observable black hole mass

4.5.1 Simple physical picture

As is clear from Figure 4.2, thin disc models of X-ray TDEs naturally lead to a maximum black hole masses, for a given set of disc parameters, from which observable levels of X-ray emission are produced. While I have thus far analysed a somewhat restricted and simplified model, the sense of these results are robust and will hold more generally. The ISCO in higher mass black hole discs lies farther out in (physical) radius, where less energy is locally liberated from the disc shear. This naturally results in lower peak disc temperatures. The X-ray luminosity is extremely sensitive to the temperature of the hottest part of the disc (equation 4.37), and so the lower peak disc temperatures associated with larger mass black holes translates to significantly lower X-ray luminosities.

I present a more general and detailed numerical calculation of these effects in sections 4.6 & 4.7. Here however I focus on some important observational implications of the results at hand. Clearly, even if a massive accretion disc is able to form efficiently in the aftermath of a TDE, a high mass black hole will not result in observable levels of X-rays. By contrast, as is clear from Figure 4.3, the optical & UV luminosities of the relativistic disc solutions are significantly less sensitive to the black hole mass (although they are still functions of black hole mass, Chapter 5). These results therefore imply that extremely X-ray dim TDEs should still be observed to exhibit the characteristic UV-plateau at large times, which can be regarded as a test of the presence of a (cool) accretion disc in these systems.

4.5.2 Mathematical description

For the simplified numerical set-up of section 4.4, the functional form of the dependence of the "Limiting" black hole mass on disc parameters may be determined both analytically, as well as by direct numerical calculation. Numerically, I simply iterate computations of disc light curves until the black hole mass, for a given M_d and α, at which the observed flux equals a prescribed limiting cut-off $f_{\rm lim}$ is found. For the *Swift* X-ray telescope I use the value $f_{\rm lim} \equiv 4 \times 10^{-14}\,{\rm erg/s/cm^2}$.

To proceed analytically, equation 4.37 must be inverted for the black hole mass

$$F_X(M, M_d, \alpha, D) = f_{\rm lim} \rightarrow M_{\rm lim} = M_{\rm lim}(\alpha, M_d, D, f_{\rm lim}). \tag{4.61}$$

An explicit form for $M_{\rm lim}$ may be derived by retaining only the leading-order large black hole mass behaviour of the X-ray flux (equation 4.59). Keeping only the leading order terms here should provide a reasonable fit, as at the point of tenuous X-ray observability the discs will be relatively cool $\Lambda \ll 1$. I define dimensionless distance $d \equiv D/100$ Mpc, disc mass $m_d = M_d/0.5M_\odot$, and black hole mass $m = M/\widetilde{M}$, where $\widetilde{M}$ is defined so that $\Lambda = m^{7/6}/\alpha^{1/3}m_d^{5/12}$ in equation 4.58. With an amplitude f_0 carrying the dimensions of flux, the equation to be inverted has the form

$$F_X \simeq \frac{f_0}{d^2}\frac{\alpha^{2/3}m_d^{5/6}}{m^{1/3}}\exp\left(-\frac{m^{7/6}}{m_d^{5/12}\alpha^{1/3}}\right) = f_{\rm lim}. \tag{4.62}$$

Collecting terms and defining the variables x and y by

$$x \equiv \frac{m}{\alpha^{2/7}\,m_d^{5/14}}, \quad y \equiv \frac{f_{\rm lim}}{f_0}\frac{d^2}{\alpha^{4/7}\,m_d^{5/7}}, \tag{4.63}$$

the inversion simplifies to the compact equation

$$y = x^{-1/3}\exp\left(-x^{7/6}\right) \tag{4.64}$$

This may be solved easily when x is small ($x \simeq 1/y^3$) or when x is large ($x \simeq |\ln y|^{6/7}$). More generally, the inversion may be carried out by using the lambert W function[4], W_0 (Corless et al. 1996):

$$x = \left[\frac{2}{7}\,W_0\left(\frac{7}{2y^{7/2}}\right)\right]^{6/7}, \tag{4.65}$$

[4]The lambert W function is defined as the solution of the following, generally complex, equation: $w\exp(w) = z \rightarrow w = W_k(z)$, for some integer k. For real valued w and z only two values of k exist: $k = 0$ and -1. For (real) $z > 0, w = W_0(z)$ while for (real) $-1/e < z < 0, w = W_{-1}(z)$.

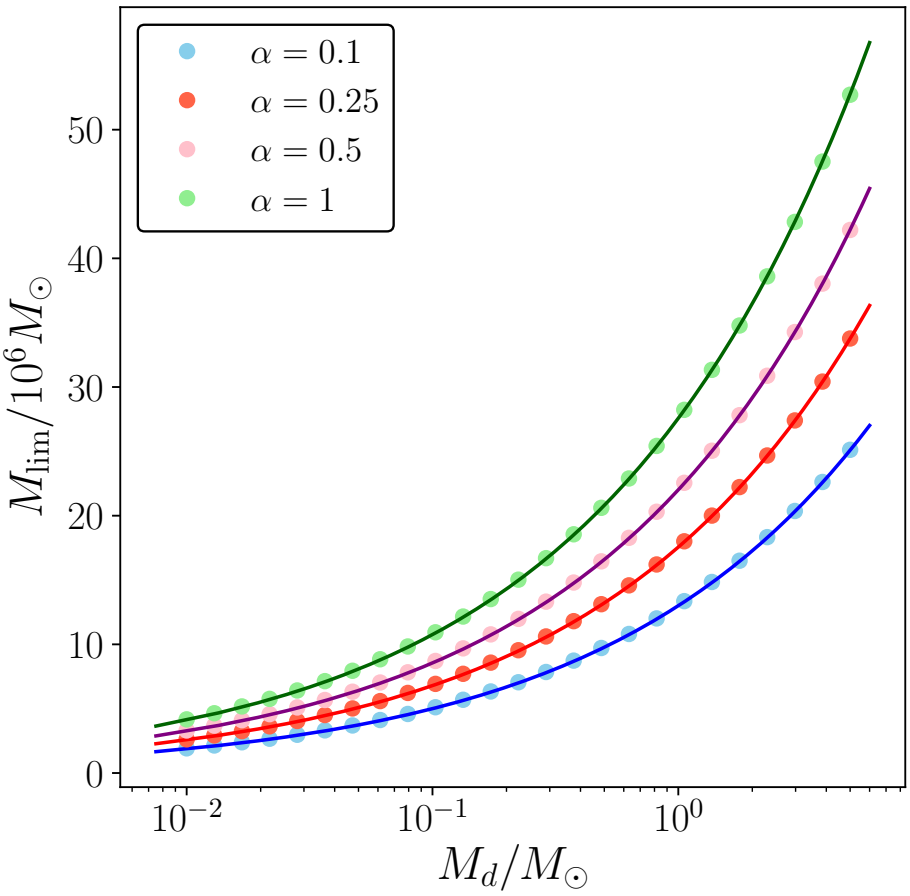

Figure 4.4: The maximum observable black hole mass, defined as the black hole mass at which the peak X-ray disc flux is $4 \times 10^{-14}\,\mathrm{erg/s/cm^2}$, as a function of initial disc mass, for four different α parameters at a distance of 100 Mpc. The solid curves are the theoretical predictions of equation 4.66, which reproduce the parameter dependence well.

and so

$$M_{\rm lim} = \widetilde{M}\,\alpha^{2/7} m_d^{5/14} \left[\frac{2}{7} W_0\left(\frac{7\alpha^2\, m_d^{5/2}}{2d^7}\left(\frac{f_0}{f_{\rm lim}}\right)^{7/2}\right)\right]^{6/7}. \tag{4.66}$$

Figure 4.4 shows the numerically computed limiting black hole masses, as a function of disc mass, for four different α parameters, with a numerical set-up identical to that of section 4.4. Also plotted is the analytical expression (equation 4.66; see Appendix G for numerical values of f_0 and $\widetilde{M}$). The analytical results reproduce the numerical results with great fidelity. "Standard" TDEs (those with disc masses $M_d < 1 M_\odot$, and $\alpha \simeq 0.1$), will only be observed at X-ray energies from Schwarzschild black holes with masses $M \lesssim 10^7 M_\odot$.

4.6 Vanishing ISCO stress

TDEs represent a promising observational path to probe a contentious theoretical issue: does the dynamical disc stress vanish at the inner edge of a relativistic accretion disc? In Chapter 2 I demonstrated that the properties of the ISCO stress directly control the disc's temporal evolution, the bolometric luminosity from finite (vanishing) ISCO stress discs decreases more slowly (rapidly). The effects of the ISCO stress are particularly pronounced at X-ray energies, which generally originates in the near-ISCO region. Detailed modelling of *individual* sources will always be the accurate probe of the properties of the ISCO stress. For example, in Chapter 3 I demonstrated that the TDE ASASSN-14li was best modelled as a disc with a finite ISCO stress, whereas ASASSN-15lh is better modelled with a maximal spin and much smaller ISCO stress. Nevertheless, consideration of more general properties of the population of X-ray TDEs may offer some valuable insight into the nature of the ISCO stress.

In this section I outline the required calculations, analogous to those of section 4.2, for the case in which the stress is assumed to vanish at the ISCO.

4.6.1 Analytical results

There is a key difference between the finite and vanishing ISCO stress disc models, which is particularly relevant when considering X-ray energies: in standard vanishing stress models, the disc temperature also vanishes at the ISCO. This means that the temperature maximum occurs within the disc, and at a location defined by (see equation 4.16),

$$k_1 \equiv \left(\frac{R_p}{T_p}\right) \left.\frac{\partial T}{\partial R}\right|_{R_p} = 0. \tag{4.67}$$

With k_1 vanishing, the leading order term relevant for the Laplace integral expansion is the quadratic k_2 term (equation 4.14, 4.16). This leads to a series of gaussian integrals for the disc spectrum and X-ray flux, rather than exponential integrals. Aside from this important detail, the procedure is identical to that performed in section 4.2. The gaussian form of the integrals change the leading power law exponent of the X-ray flux expression, which now has the form

$$F_X = F_0 \left(\frac{R_p}{D}\right)^2 \left[\Lambda^{-3/2} + \phi_1 \Lambda^{-5/2} + \phi_2 \Lambda^{-7/2}\right] e^{-\Lambda}. \tag{4.68}$$

In this expression, Λ is defined in the same way as in section 4.2 (equation 4.58). The flux amplitude F_0 and expansion coefficients ϕ_1 and ϕ_2 remain constants, but differ by order unity factors from the definitions used in section 4.2. The disc temperature has the same parameter dependence as in a finite ISCO stress disc, and so the leading order parameter dependence is given by

$$F_X \propto \frac{\alpha^{1/2} M_d^{5/8} M^{1/4}}{D^2} \exp\left(-A_1 \frac{M^{7/6}}{\alpha^{1/3} M_d^{5/12}}\right). \tag{4.69}$$

Similarly, a calculation of the upper observable mass limit for vanishing ISCO stress discs, analogous to that of section 4.5, can be performed. Using the same dimensionless variables as in section 4.5, equation 4.69 now has the form

$$F_X \simeq \frac{f_0}{d^2}\, \alpha^{1/2} m_d^{5/12} m^{1/4} \exp\left(-\frac{m^{7/6}}{m_d^{5/12} \alpha^{1/3}}\right) = f_{\rm lim}. \tag{4.70}$$

This leads to

$$M_{\rm lim} = \widetilde{M} \alpha^{2/7} m_d^{5/14} \left[-\frac{3}{14} W_{-1}\left(-\frac{14}{3} y^{14/3}\right)\right]^{6/7}, \tag{4.71}$$

where

$$y \equiv \frac{f_{\rm lim}}{f_0} \frac{d^2}{\alpha^{4/7} m_d^{5/7}}, \tag{4.72}$$

and W_{-1} is the negative branch of the Lambert W function. All numerical values of relevant parameters are presented in Appendix G.

4.6.2 Numerical results

In this section I perform a set of numerical experiments analogous to section 4.4, computing the peak value of the evolving X-ray light curves of accretion discs with various values of initial disc mass and α parameters. The same initial conditions are used, as is the same source-observer distance $D = 100$ Mpc; the only difference in the modelling is the ISCO stress value, which is set to zero throughout.

Figure 4.5 shows the peak observed X-ray fluxes as a function of black hole mass, for disc light curves produced using different disc parameters, as denoted on the plot. As before, only the parameter regime where $L_{\rm bol} < L_{\rm Edd}$ is shown, which corresponds to black holes more massive than $M_{\rm Edd}$. Figure 4.5 demonstrates that equation 4.68 reproduces the numerical results for a wide range of physically reasonable

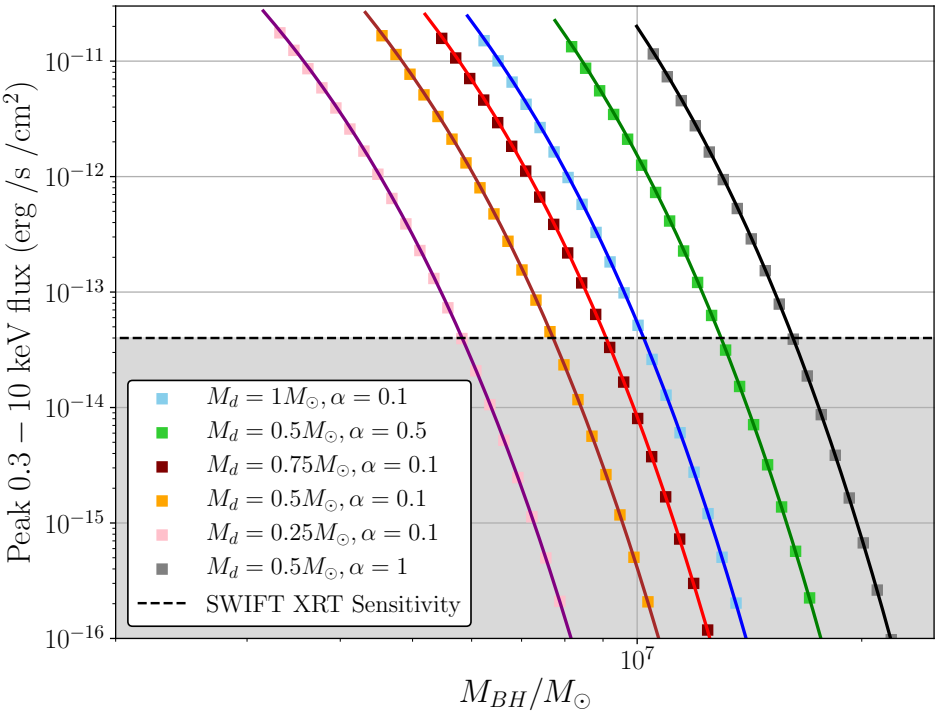

Figure 4.5: The peak X-ray flux, as observed at 100Mpc, for discs evolving with a number of different initial disc masses M_d and α parameters, denoted on plot. This plot was made with a vanishing ISCO stress.

disc parameters. Figure 4.6 shows the maximum observable black hole masses for vanishing ISCO stress discs, computed numerically with an identical set up as Figure 4.5, as a function of disc mass for four different α parameters. Also plotted is the analytical expression of the previous section (equation 4.71), which reproduces the numerical results with great fidelity.

Loosely, the properties of the X-ray luminosity are relatively insensitive to the properties of the ISCO stress in the $L_{\rm bol} < L_{\rm Edd}$ regime. The dominant behaviour in this regime for any ISCO stress is the diminution of the X-ray flux arising from cooling discs of fixed α and M_d about larger mass black holes, $T \propto M^{-7/6}$. In quantitive detail however, otherwise identical discs (same M, α, M_d, $f_{\rm col}$ etc.) with a finite ISCO stress produce larger X-ray luminosities when compared with their vanishing ISCO stress counterparts. This results in finite ISCO stress discs being observable around black holes with somewhat larger masses. It may well be the case that a population of X-ray bright, thermal TDEs around black holes of large masses ($M \gtrsim 2 \times 10^7 M_\odot$) is indicative of non-zero ISCO stresses present in TDE discs.

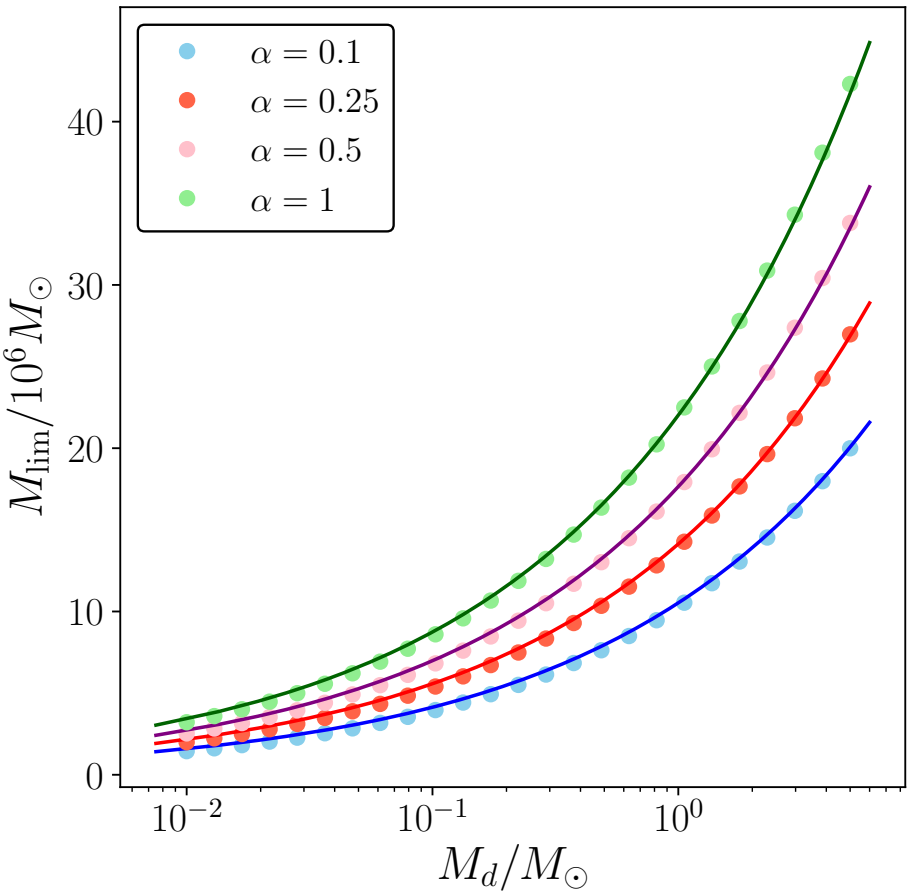

Figure 4.6: The maximum observable black hole mass, defined as the black hole mass at which the peak X-ray disc flux is $4 \times 10^{-14}\,\mathrm{erg/s/cm^2}$, as a function of initial disc mass for four different α parameters at a distance of 100 Mpc. This plot was made with a vanishing ISCO stress. The solid curves are the theoretical predictions of equation 4.71, which capture the parameter dependence well.

4.7 The effects of black hole spin and inclination angle

The previous calculations have all been carried out for discs around Schwarzschild blackholes observed face-on. Astrophysical black holes will generally have a non-zero angular momentum parameter, being described by the Kerr metric, and may of course be observed at a general angle $\theta_{\rm obs}$. In the following section I revisit the numerical results of sections 4.4 & 4.6.2 for a variety of different blackhole spins and disc-observer inclination angles.

In what follows, along with more general metrics and viewing angles, I shall also adopt the colour correction model of Done et al. (2012). This model is routinely used for the modelling of AGN disc spectra, and is likely therefore to reasonably accurately model TDE disc colour-correction effects. For the lowest disc temperatures, below a critical temperature $T = 3 \times 10^4$K, Hydrogen is neutral and the Hydrogen absorption opacity is extremely large. This results in the full thermalisation of the liberated disc energy, meaning that the emitted disc spectrum is well described by a pure blackbody function, with

$$f_{\rm col}(T) = 1, \quad T < 3 \times 10^4 {\rm K}. \tag{4.73}$$

As the temperature increases above 3×10^4 K, the colour correction factor begins to increase. This results from the growing ionisation fraction of Hydrogen and Helium, which reduces the total absorption opacity, and electron scattering opacity begins to dominate. Done et al. (2012) model the colour correction factor in this regime as

$$f_{\rm col}(T) = \left(\frac{T}{3 \times 10^4 {\rm K}}\right)^{0.83}, \quad 3 \times 10^4 {\rm K} < T < 1 \times 10^5 {\rm K}. \tag{4.74}$$

For the highest disc temperatures $T > 1 \times 10^5$K, electron scattering completely dominates the absorption opacity and the colour correction factor begins to saturate, a result of Compton down-scattering in the disc atmosphere, to

$$f_{\rm col}(T) = \left(\frac{72\,{\rm keV}}{k_B T}\right)^{1/9}, \quad T > 1 \times 10^5 {\rm K}. \tag{4.75}$$

Note that the magnitude of $f_{\rm col}$ is continuous between these final two regimes.

4.7.1 Schwarzschild black hole – varying inclination

When a relativistic accretion disc is observed at an inclined angle, substantial Doppler blue shifting of photons emitted from the inner disc material moving with large line-of-sight velocities can overcome the gravitational red-shift. This results in frequency ratio factors $f_\gamma > 1$, boosting the observed high-energy emission relative to a face-on orientation. Counteracting this effect is the fact that disc regions moving away from the observer have large Doppler red shifts, and so the observed area of the hottest disc regions (those regions with maximum $\widetilde{T} = f_{\rm col} f_\gamma T$) decreases with increasing inclination. The net result of these two competing effects cannot be determined analytically and detailed numerical calculations are required.

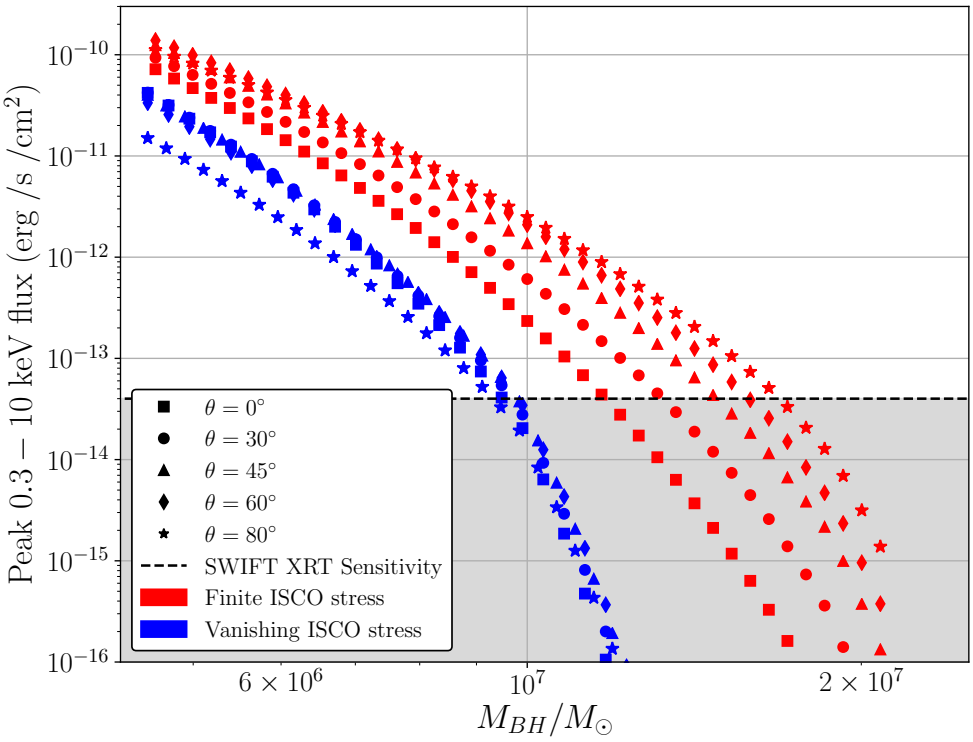

Figure 4.7: The peak X-ray flux, as observed at 100Mpc, for discs evolving with $M_d = 0.5M_\odot$, $\alpha = 0.1$ for a number of different observer inclination angles, denoted on plot. Discs with a vanishing ISCO stress are plotted in blue while discs with a finite ISCO stress are plotted in red.

For a Schwarzschild black hole the effects of inclination angle are modest, and the qualitative properties of the X-ray luminosity of the disc solutions at a general angle are quite similar to the face-on case. Indeed, for a vanishing ISCO stress disc around a Schwarzschild black hole the inclination has almost no effect on the peak X-ray luminosity. Finite ISCO stress discs are more sensitive to the inclination: their temperature profiles peak closer to the central black hole, where changes in the Doppler boosting are more pronounced. This is demonstrated in Figure 4.7. The enhanced Doppler boosting of the emitted radiation for more edge-on inclinations means that the maximum observable black hole mass is larger for larger observer inclinations. The asymmetry of the photon red-shift factor f_γ and the disc temperature dependence of the colour correction factor (equations 4.75, 4.74, 4.73) means that the analytical results derived in section 4.2 no longer describe the numerical results with great accuracy. Their physical content is, however, very revealing of more general models.

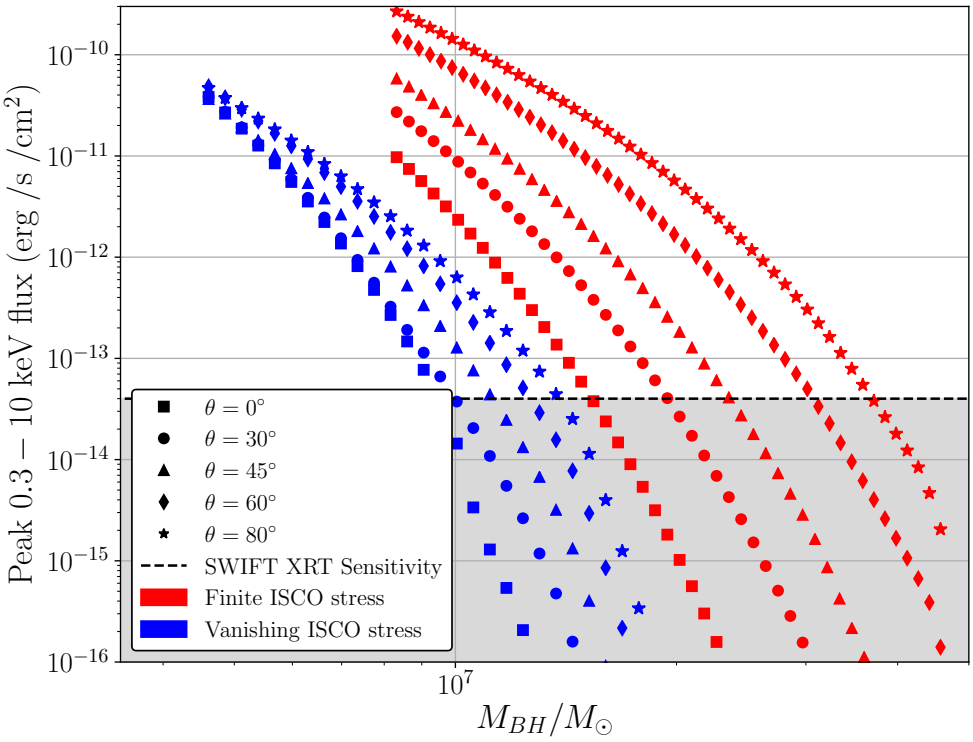

Figure 4.8: The peak X-ray flux, as observed at 100Mpc, for discs evolving with $M_d = 0.5M_\odot$, $\alpha = 0.1$ for a number of different observer inclination angles, denoted on plot. The black hole spin is $a/r_g = 0.9$. Discs with a vanishing ISCO stress are plotted in blue while discs with a finite ISCO stress are plotted in red.

4.7.2 Rapid black hole spin – varying orientation

The numerical calculations of Figure 4.8 are identical to those in Figure 4.7, except that the black hole spin now corresponds to that of a more rapidly rotating black hole $a/r_g = 0.9$. For higher spins, the differences between the different models of the ISCO stress are much more pronounced. Like their steady state analogues, time dependent finite ISCO stress discs have intrinsically harder spectra, and larger mass-to-light efficiencies than vanishing ISCO stress discs (Agol and Krolik 2000). For larger black hole spins, these differences are more pronounced, and finite ISCO stress discs are much brighter at X-ray energies. They can therefore be observed around black holes a factor of ~ 2 more massive than vanishing ISCO stress discs.

The finite ISCO stress solutions presented here were produced with a large ISCO stress (small γ). In Chapter 2 I argued that the general properties of numerical disc solutions should be thought of as part of a continuum between heavily stressed and

vanishing stress solutions, controlled by the γ parameter. These solutions should therefore be regarded somewhat as extremes: a disc with a smaller, but non-zero, ISCO stress will lie somewhere between the two sets of results.

Quantitively, the differences between the results of a rapidly spinning black hole and those of a Schwarzschild black hole are relatively modest, with only factor ~ 1.5 change in the maximum observable mass. It is therefore a robust prediction that TDEs with thermal X-ray spectra will not be observed around black holes more massive than $M_{\rm lim} \sim 3 \times 10^7 M_{\odot}$. Exceptions would only arise for TDEs involving extremely massive stars, or for discs with very large α parameters, $\alpha \simeq 1$.

4.8 The thermal X-ray TDE population

Finally, I compare the properties of the black hole masses of the observed thermal X-ray TDE population with the results of this Chapter. At the time of writing, the author is aware of 12 X-ray TDEs with X-ray spectra which are well-modelled by thermal disc emission, and which have published estimates of the central black hole mass. In view of the results presented here, I would expect the black hole mass distribution of these sources to peak below $M_p < 10^7 M_{\odot}$, and that sources with masses $M \gtrsim 3 \times 10^7 M_{\odot}$ should be rare. With a sufficiently large disc mass, thermal X-ray TDEs could be observed around black holes with extremely large masses, but the sparsity of high-mass stars ($\mathrm{d}N_{\star}/\mathrm{d}M_{\star} \propto M_{\star}^{-2.35}$) should make these events uncommon.

For this analysis I use well-established galactic scaling relationships between the black hole mass and (i) the galactic bulge mass $M : M_{\rm bulge}$, (ii) the galactic velocity dispersion $M : \sigma$, and (iii) the bulge V-band luminosity $M : L_V$. All of the scaling relationships are taken from McConnell and Ma (2013). Where available, values of $M_{\rm bulge}$, σ and L_V were taken from the literature for each TDE, and are presented in Table H.2 in Appendix H. The mean black hole mass for each TDE is then presented in Table 4.2. In an ideal world I would not combine black hole mass estimates found from distinct scaling relationships in this manner. However, unlike optically-discovered TDEs (which I shall discuss more later), TDEs discovered by X-ray surveys have not always been comprehensively followed up, and many are missing the galaxy spectra required to make measurements of e.g., the galaxies velocity dispersion σ. Coupled with the intrinsic scarcity of these sources, choosing any one scaling relationship would substantially

TDE name	$\langle M_{\rm BH} \rangle / 10^6 M_\odot$
ASASSN-14li	$2.9^{+2.9}_{-1.6}$
ASASSN-15oi	$8.1^{+7.1}_{-4.3}$
AT2018hyz	$4.3^{+6.9}_{-3.3}$
AT2019dsg	$20.4^{+28.3}_{-14.7}$
AT2019azh	$4.5^{+8.0}_{-3.5}$
AT2019ehz	$6.6^{+8.0}_{-3.8}$
AT2018zr	$11.0^{+14}_{-6.7}$
SDSS J1311	$5.2^{+8.9}_{-3.3}$
XMMSL1 J1404 [a]	$2.8^{+1.4}_{-1.0}$
OGLE 16aaa	26.0^{+35}_{-16}
3XMM J1521	$5.4^{+5.1}_{-3.0}$
3XMM J1500	$7.3^{+5.5}_{-3.2}$

Table 4.2: The mean black hole mass of the 12 Thermal X-ray TDEs from the literature. [a] The TDE XMMSL1 J1404 also has non-thermal X-ray components present, but the non-thermal component is subdominant (Saxton et al. in prep, Wevers 2020).

reduce the sample size, and statistical power, of the X-ray TDE populations. Future studies, which consistently use only one scaling relationship, are of interest.

In the upper section of Figure 4.9 I show the black hole masses of the twelve thermal X-ray TDEs obtained from each galactic scaling relationship, along with the mean black hole mass of each TDE (black diamond). I also display, as vertical dashed lines, three characteristic limiting black hole masses, corresponding to discs with masses $M_d = 0.05, 0.2$ and $0.5 M_\odot$, and an α-parameter of $\alpha = 0.1$ about black holes of spins $a/r_g = 0.9$ at an observed distance of $D = 100$ Mpc and inclination angle $\theta = 60°$. In the lower section of Figure 4.9 I show the distribution of these

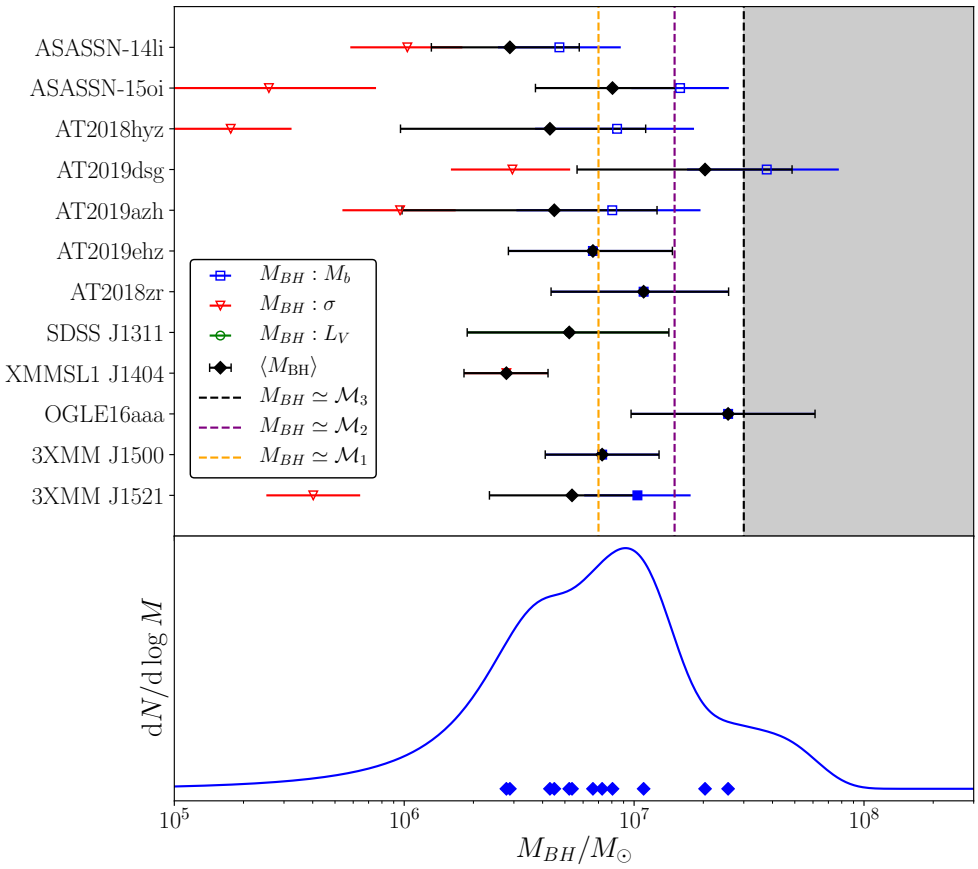

Figure 4.9: The black hole mass distribution of the 12 TDEs with bright quasi-thermal X-ray spectra. The upper panel shows the black hole mass values inferred for each individual TDE, calculated using correlations with (i) the galactic bulge mass $M : M_{\rm bulge}$ (blue squares), (ii) the galactic velocity dispersion $M : \sigma$ (red triangles), and (iii) the bulge V-band luminosity $M : L_V$ (green circles). The mean black hole mass for each TDE is plotted as a black diamond. The lower panel shows the black hole mass distribution of the quasi-thermal X-ray TDE population, obtained using kernel density estimation using a kernel width equal to the uncertainty in each TDE's black hole mass.

black hole masses, obtained using kernel density estimation using a kernel width equal to the uncertainty in each TDE's black hole mass[5].

It is clear that the current thermal X-ray TDE population is consistent with the expectations of this chapter: the distribution peaks at a black hole mass $M \simeq 9\times10^6 M_\odot$,

[5]Formally, each TDE data point is represented by a Gaussian probability distribution with mean μ given by the mean inferred black hole mass from scaling relationships, and standard deviation $\sigma = (\sigma_+ + \sigma_-)/2$, where $\sigma_\pm$ are the asymmetric uncertainties on the black hole's mass. The total black hole mass distribution is then found by integrating over the individual probability distributions and re-normalising.

and is strongly suppressed above $M \gtrsim 3 \times 10^7 M_\odot$. It is interesting that one of the TDEs with the largest inferred black hole mass, AT2019dsg, had jetted radio emission associated with it (Stein et al. 2021). In a disc model, bright thermal X-ray emission from black holes this large should result via the disruption of an unusually large star by a black hole with large black hole spin, precisely the sort of physical scenario in which a jet may be launched.

An important black hole mass scale with which to compare these results to is the Hills mass (Hills 1975). The Hills mass M_H is defined as the black hole mass at which a solar type star would be swallowed whole by the black hole before it reaches its tidal radius and undergoes tidal destruction. A simple estimate (using Newtonian gravity) gives $M_H \simeq 9 \times 10^7 M_\odot$, although this mass scale increases by an order of magnitude for extreme values of the black hole spin parameter (Chapter 3, Kesden 2012), and increases with stellar mass. Given that this mass scale will set an upper limit on the black hole mass distribution of *all* types of TDEs, it is important to demonstrate that the suppression of bright thermal X-ray TDEs above $M \sim 10^7 M_\odot$ is a result of the mechanism set out in this Chapter, and not merely this Hills mass effect.

A simple way to test that the observed suppression of high black hole mass TDEs observed with thermal X-ray spectra is a result of the mechanism set out in this Chapter is to ask how many TDEs of other spectral types have been observed with black hole mass $M > 3 \times 10^7 M_\odot$. In later sections of this chapter I examine TDEs from across the entire black hole mass range. I find twelve TDEs with inferred black hole masses greater than $10^7 M_\odot$, and six TDEs with inferred black hole masses $M > 3 \times 10^7 M_\odot$. None of these six highest black hole mass TDEs were observed to have thermal X-ray spectra.

I stress that the argument here is not that TDEs observed at X-ray energies around black holes of masses $M > 10^7 M_\odot$ are themselves intrinsically rare. There are almost as many of these sources (nine) as there are X-ray TDEs with masses less than $10^7 M_\odot$ (ten). The mass distribution of the total X-ray TDE population is approximately flat from $M \sim 10^6 - 10^8 M_\odot$ (Wevers et al. 2019b). The point is that the dominant emission components from these TDEs with larger masses are observed to be dominated by nonthermal components (Wevers 2020), not disc-like thermal components.

While TDEs evolving in harder accretion states can produce observable levels of nonthermal emission around the largest black hoe mass TDEs, it is important to recognise that, even in those TDEs with nonthermal/coronal emission components present, the thermal components of the X-ray flux of these sources will still be well

described by the scaling relationships developed in this Chapter. The upper black hole mass limit of $M \sim 3 \times 10^7 M_\odot$ for thermal-dominated X-ray TDEs is a robust prediction, and will not be modified by including small nonthermal components. In the coming years, wide-field X-ray surveys are expected to discover many more thermal X-ray TDEs, and will rigorously test these predictions. I would expect these newly discovered populations to follow the qualitative distribution predicted here, namely, that the majority of bright thermal X-ray TDEs will occur around black holes with $M \simeq 5 \times 10^6 M_\odot$, with very few occurring around high-mass ($M > 3 \times 10^7 M_\odot$) black holes.

4.9 Discussion

In this section I have modelled, analytically and numerically, the properties of the thermal X-ray emission emergent from relativistic time-dependent accretion discs, tailoring this analysis to parameter regimes most appropriate for comparison with TDEs. The key theoretical result of this section is the demonstration of the strong suppression of thermal X-ray emission from accretion discs around black holes with large masses (equation 4.59). This then results in a clear observational prediction: there will exist a maximum black hole mass at which thermal X-ray TDEs will be observed. Quantitatively, thermal emission will only be observable around black holes with masses $M < 3 \times 10^7 M_\odot$, for typical TDE disc parameters. Both the properties of the X-ray luminosity and the limiting black hole mass are a function of disc parameters, with a full dependence which can be described explicitly (equations 4.59 and 4.66).

Furthermore, I have demonstrated that the current (admittedly small) population of observed thermal X-ray TDEs is indeed consistent with the existence of an upper black hole mass limit of order $M \sim 10^7 M_\odot$ (Figure 4.9). These quantitative predictions about the mass-distribution of TDEs discovered by upcoming wide-field X-ray surveys will be directly tested in the coming years.

As mentioned above however, it is not just thermal processes which can produce bright X-ray emission from a TDE source: some TDEs are observed with a nonthermal power-law-with-energy X-ray spectrum. Additional physical processes must therefore be incorporated into the relativistic disc models of this thesis, so that TDEs from across the entire population of sources can be modelled.

4.10 Non-thermal X-ray emission from TDEs

The models put forward in this thesis to describe the evolving properties of TDE light curves have thus far focussed on the thermal emission emitted from the disc surface which then travels unimpeded to the observer. These models are theoretically simplest, and accurately describe the observed spectral properties of a large number of TDEs (e.g., five recently discovered sources in van Velzen et al. 2021). However, other TDEs (e.g., XMMSL1 J0619, Saxton et al. 2014) have X-ray spectra which are better modelled by nonthermal "hard-state" emission, characterised by a power-law with energy dependence.

This is not itself a surprising observational result[6], X-ray binary (XRB) and AGN discs routinely show this same hard state emission. The nonthermal emission itself originates from the Compton up-scattering of thermal disc photons by a "corona": a population of hot ($\sim 10'\text{s} - 100'\text{s}$ of keV) electrons which are located close to the black hole itself. The precise geometry, size and location of this 'corona' is not generally well understood, and remains a topic of debate. I do not aim to resolve any of these topics in this work, but instead put forward *a* model for hard state emission from TDE discs, with the intention of understanding the dependence of the observed nonthermal X-ray luminosity of TDE discs on the TDE's physical parameters.

TDE sources of the hard spectral type have been previously modelled in the literature. The typical approach involves applying a sequence of steady-state AGN models to each individual observation (e.g. Saxton et al. 2019), adjusting the fitting parameters of these steady-state models by allowing them to vary with each observation. However, sequential steady-state modelling does not allow for the true self-consistent dynamical evolution of system parameters with time. For example, in the sequential steady-state approach the mass accretion rate $\dot{M}$ can be chosen to take whichever value best fits each particular observation. In reality, these disc parameters are physically determined by the initial conditions and the constraints of mass, energy and angular momentum conservation.

In this work, I incorporate self-consistent dynamical time evolution by generalising the relativistic thin disc TDE model of Chapters 2 & 3 by incorporating nonthermal X-ray emission. The key physical assumption made is that this emission arises from

[6]Potentially a much more surprising result is that many TDEs are observed with no nonthermal X-ray spectral component at all.

Compton up-scattering of thermal disc photons by a compact electron corona in a region enveloping the innermost stable circular orbit. The disc parameters are thus free to evolve self-consistently with time without prescriptive fitting, and both nonthermal and thermal X-ray spectral components are produced.

4.11 The spectral state of TDEs around large mass black holes

4.11.1 Overview

It is well-established that black hole X-ray binaries (hereafter XRBs) undergo transitions from the 'high-soft' state, characterised by thermal X-ray spectra, to the 'low-hard' state, characterised by nonthermal (power-law) X-ray spectra, when the mass accretion rate in Eddington units is of order 1%, $\dot{m} \equiv \dot{M}/\dot{M}_{\rm edd} \sim 10^{-2}$ (e.g., Fender and Belloni 2004; Maccarone 2003). Although there is evidence that AGN discs undergo similar state transitions (Maccarone et al. 2003), the significantly extended evolutionary timescale of typical AGN discs generally prevents such transitions from being directly observed. While the central black hole masses of TDE discs are similar to those of AGN, the discs themselves are generally much more compact than their AGN counterparts: they span a radial range from $\sim$ the ISCO out to $\sim$ the tidal radius at early times. This leads to a much shorter evolution timescales. TDE discs may act as scaled-up analogues of XRB discs, and thus exhibit X-ray state transitions as well.

TDEs have been observed to form in both the low-hard state (e.g, XMMSL2 J1446, Saxton et al. 2019) and the high-soft state (e.g, ASASSN-14li, Brown et al. 2017). Compelling (albeit circumstantial) evidence for state transitions in TDE discs has recently been presented by Jonker et al. (2020). Jonker et al. observed four TDE sources at late times, all of which had been previously undetected at X-ray energies. Nonthermal X-ray emission was observed from three of these four sources. Although these sources were dim and detailed spectral information unavailable, one source was well-modelled by a hard power law $\Gamma \sim 2.5$, and another by a much softer power-law $\Gamma \sim 4$. (The third source was too dim for a reliable power-law index to be determined). The authors suggest that the early-time X-ray emission of each TDE in the high-soft state was below detectable levels, but that at later times the discs underwent a state transition into the low-hard state. Thereafter, detectable nonthermal X-ray emission emerged.

Furthermore, there is evidence that one TDE, AT2018fyk (Wevers et al. 2019a, Wevers et al. 2021), may have transitioned between these two states at early times in its evolution. AT2018fyk's X-ray emission was initially dominated ($\sim 70\%$ by flux) by its thermal component, but once its X-ray light curve peaked (some ~ 75 days after the source was first detected) it was found that the X-rays were dominated ($\sim 80\%$ by flux) by a power-law component. When viewed in combination with the results of Jonker et al. (2020), AT2018fyk may represent the first example of a TDE undergoing an accretion state transition in real time. These results are supportive of the idea that TDE discs behave like 'scaled up' XRB discs. This TDE-XRB connection will be central to the modelling in this Chapter.

Wevers (2020) presents evidence for an underlying trend between TDE spectral state and system parameters, demonstrating a correlation between the central black hole mass of seven X-ray bright TDEs and the degree to which the X-ray spectra is dominated by nonthermal power-law components. TDEs associated with the most massive black holes were observed in a harder state, and it was suggested that this may be evidence for TDE discs around more massive black holes evolving more rapidly.

I suggest that it is unlikely that TDE discs around more massive black holes evolve more rapidly than similar discs around smaller mass black holes. The viscous timescales of accretion discs around more massive black holes are expected to be larger than their less massive counterparts, owing to the enhanced radial distances which must be covered by their fluid elements. In this section, I present an alternative interpretation of Wevers (2020) findings: TDEs around more massive black holes are more likely to *form* in the hard state, a result stemming from the sensitive dependence of the disc's bolometric luminosity upon its black hole mass. This is not to say that TDE discs are unable to transition between accretion states. Indeed, I assume that TDE discs do undergo such state transitions, as may have already been observed. The point I stress here is that, given the strong dependence on black hole mass of a TDE discs bolometric luminosity (equation 4.96), an individual TDE system is statistically unlikely to form a disc with its critical Eddington ratio close to the transitional scale $\dot{m} \sim 0.01$, as opposed to either $\dot{m} \gg 0.01$, or $\dot{m} \ll 0.01$. Therefore the majority (but not necessarily all) of TDEs should be observed to be evolving in either one of the two (thermal or nonthermal) accretion states. A more detailed scaling analysis of this argument is presented below.

4.11.2 Scaling analysis

Earlier I demonstrated that the peak temperature in a time-dependent relativistic accretion disc depends sensitively upon the black hole mass (equation 4.54). This implies an Eddington ratio l which scales as:

$$l \equiv \frac{L_{\rm bol,peak}}{L_{\rm edd}} \propto \frac{\alpha^{4/3} M_d^{5/3}}{M^{11/3}}. \tag{4.76}$$

Note the strong black hole mass dependence of $l \propto M^{-11/3}$. Consider now a disc with mass M_d, a prescribed α-parameter, a central black hole mass of $M_{\rm edd}$ corresponding to a peak bolometric luminosity of $l = 1$ (i.e., at precisely the Eddington limit). With this definition for $M_{\rm edd}$, an otherwise identical disc with a central black hole of mass $M_{\rm HS}$ ("Hard State") forms at an Eddington ratio $l_{\rm HS}$, where

$$M_{\rm HS} = M_{\rm edd}\, l_{\rm HS}^{-3/11}, \tag{4.77}$$

where $M_{\rm edd}$ now embodies the α and M_d dependencies. Thus, if TDE discs with Eddington ratios $l_{\rm HS} \sim 10^{-2}$ form predominantly in the hard state and produce observable nonthermal X-ray emission, nonthermal X-ray TDEs would tend to be found around more massive black holes (i.e., in excess of $M_{\rm HS}$). This is in accord with the Wevers (2020) findings.

Because of the strong mass dependence of the Eddington ratio, the change in black hole mass required for this hard-state transition is generally rather small: e.g., $l_{\rm HS}^{-3/11} \simeq 3.5$ for $l_{\rm HS} = 0.01$. The black hole mass at which the peak bolometric disc luminosity exactly equals the Eddington luminosity can be determined numerically; for a Schwarzschild black hole with disc mass $M_d = 0.5 M_\odot$ and $\alpha = 0.1$, $M_{\rm edd} \simeq 5 \times 10^6 M_\odot$ (Figure 4.1). The simple argument presented above would then predict nonthermal emission to be observable from an otherwise identical disc around a black hole with mass $M > M_{\rm HS} \simeq 2 \times 10^7 M_\odot$. Given the upper limit for observable thermal X-ray emission, $M_{\rm lim} \sim 10^7 M_\odot$, this simple analysis suggests that the populations of thermal X-ray TDEs and nonthermal X-ray TDEs should be drawn from black hole populations with systematically different masses, being either distributed above (nonthermal) or below (thermal) a characteristic black hole mass of order $\sim 10^7 M_\odot$ (Figure 4.11).

4.12 Comptonized disc emission

I model the effects of a Comptonizing corona following the approach used in the "SIMPL" (Steiner et al. 2009) fitting module in XSPEC (Arnaud 1996). I assume, without modelling in detail, that a Comptonising corona forms and is active when the Eddington ratio of the disc reaches some critical value, $l_{\rm HS}$, introduced in section 4.11.2. The corona covers the innermost regions of the accretion disc, from the ISCO radius out to a radius $R_{\rm Cor}$. The geometry is shown in the upper half of Figure 4.10.

Thermal disc photons emitted from radii $r > R_{\rm Cor}$ pass directly to the observer, as a standard colour-corrected blackbody superposition (blue curve, Figure 4.10). For disc annuli $r \leq R_{\rm Cor}$ a fraction $1 - f_{SC}$ of the photons pass through the corona unscattered, contributing once again a colour-corrected black body component to the disc spectrum (green curve, Figure 4.10), while a fraction f_{SC} undergo multiple Compton scattering (orange curve, Figure 4.10). Photon number conservation in the scattering region then determines the observed properties of the scattered spectrum. For an input distribution of photons $n(E_0)\mathrm{d}E_0$, the outgoing photon distribution in an energy range dE around energy E, $n'(E)\mathrm{d}E$, is given via an integral transformation[7] (Steiner et al. 2009)

$$n'(E)\mathrm{d}E = (1 - f_{SC})n(E)\mathrm{d}E + f_{SC}\left[\int_0^\infty n(E_0)G(E;E_0)\mathrm{d}E_0\right]\mathrm{d}E. \tag{4.78}$$

In this model, the input distribution $n(E_0)$ is the photon occupation number at an energy E_0, obtained by summing the contribution from all of the disc annuli with $r < R_{\rm Cor}$, assuming that each disc annulus emits thermally following the disc evolution solutions of the previous section. The physics of the scattering events is then described by the Green's function $G(E;E_0)$, which accounts for the ensuing energy distribution of scattered photons for a δ-function input at energy E_0. I use the following prescription for $G(E;E_0)$, which has a single free parameter Γ (Sunyaev and Titarchuk 1980; Steiner et al. 2009):

$$G(E;E_0) = \frac{(\Gamma-1)(\Gamma+2)}{(1+2\Gamma)}\frac{1}{E_0}\begin{cases} (E/E_0)^{1+\Gamma}, & E < E_0, \\ (E/E_0)^{-\Gamma}, & E \geq E_0. \end{cases} \tag{4.79}$$

[7]Photon number conservation is ensured in this formalism provided $G(E;E_0)$ is any function satisfying $\int_0^\infty G(E;E_0)\mathrm{d}E = 1$. This can be proven via: $\int_0^\infty n'(E)\mathrm{d}E = (1-f_{SC})\int_0^\infty n(E)\mathrm{d}E + f_{SC}\int_0^\infty\int_0^\infty n(E_0)G(E;E_0)\mathrm{d}E_0\mathrm{d}E$. Swapping the order of integration on the final term gives $\int_0^\infty n'(E)\mathrm{d}E = \int_0^\infty\left[(1-f_{SC}) + f_{\rm SC}\int_0^\infty G(E;E_0)\mathrm{d}E\right]n(E_0)\mathrm{d}E_0 = \int_0^\infty n(E_0)\mathrm{d}E_0$.

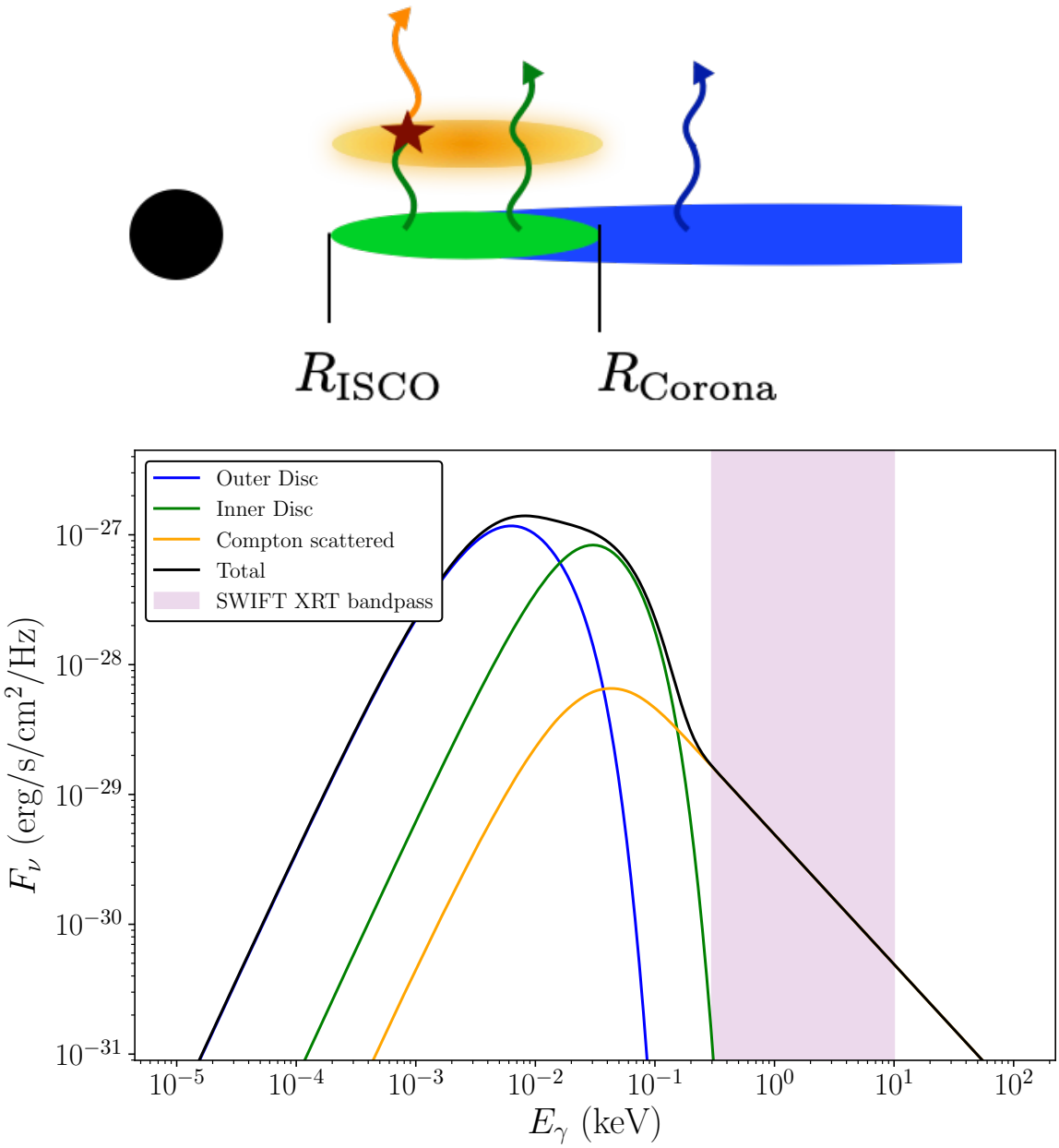

Figure 4.10: Upper: A schematic of the Comptonizing corona geometry. Lower: an example 'hard state' disc spectrum. This was produced at the time when the disc's bolometric luminosity peaks for a disc with initial mass $M_d = 0.5M_\odot$ and $\alpha = 0.1$, around a Schwarzschild black hole with mass $M = 2 \times 10^7 M_\odot$. The corona extended from the ISCO ($6r_g$) out to $R_{\rm Cor} = 12r_g$ and scattered a fraction $f_{SC} = 0.1$ of the soft disc photons with photon index $\Gamma = 2.0$. The blue, green and orange curves in the lower panel correspond to the contributions to the total disc spectrum (black) from each of the different emission regions of the disc-corona system.

The normalisation is determined by photon number conservation; the model is valid for any $\Gamma > 1$. This Green's function is a phenomenological model designed to recreate the properties of unsaturated repeated scattering of soft photons by non-relativistic thermal electrons. It can be shown that the full solutions of the Kompaneets equation (which properly describes photon diffusion through the corona) do indeed produce power-law distributions of photon energies with this functional form (Shapiro et al. 1976). Technically, for any complete model of Comptonization, the up-scattered power-law distribution is exponentially cut off for photon energies larger than the temperature of the coronal electrons $E > k_B T_e$. As I am considering relatively soft observed X-ray energies $E < 10$ keV, neglecting the cut-off in up-scattered photons above $k_B T_e$, which can be as high as $k_B T_e \sim 100'$s keV, should not significantly affect the results.

A final – and important – assumption of this model is that the electron corona affects only the observed distribution of photons via Compton scattering, and not the dynamical evolution of the accretion disc. Hard state models of XRBs often invoke truncations of the thin disc at large distances from the black hole (e.g. Narayan and Yi 1995; Esin et al. 1997) with the central region replaced by a so-called advection-dominated accretion flow (ADAF). AGN discs in quiescence ($L_{\rm bol} \sim 10^{-8} L_{\rm edd}$) are similarly expected to be truncated at very large radii from the central black hole. On the other hand, brighter AGN discs are often well-modelled by an accretion disc extending down to the ISCO, with innermost regions enshrounded by an electron scattering corona (e.g., the bright AGN Markarian 335, Wilkins and Gallo 2015). Measurements of the black hole spins of AGN (e.g., Reynolds 2013) are also consistent with the accretion disc extending down to the ISCO. In this Chapter I shall assume that the underlying TDE accretion disc is described by the relativistic thin disc evolution equation at all radii down to the ISCO. No claims are made here that the model of the disc-corona geometry and evolution presented in this Chapter are a *unique* description of a TDE disc in a hard accretion state, but it is one that is physically viable with testable predictions.

4.13 Analysis of the nonthermal emission

In this section I present representative numerical and analytical results of the X-ray properties of hard-state TDEs, assuming the disc-corona geometry of Figure 4.10. I demonstrate that physically reasonable parameters for the disc and corona produce observable levels of nonthermal X-ray flux for central black holes of large mass ($M > 2 \times 10^7 M_\odot$). I also present analytical results which describe the properties of the Comptonized X-ray flux well, both as a function of disc and black hole parameters, and as a function of time.

The results in this section require the calculation of numerical solutions of the relativistic disc equation: I use identical solutions to those considered earlier in this Chapter (section 4.4).

4.13.1 Observability

Can a compact Compton-scattering corona produce observable levels of X-ray flux from an accretion disc around a massive black hole which would otherwise be too cool to produce observable X-rays (equation 4.43)? Figure 4.11 shows the peak value of the evolving 0.3 – 10 keV light curves of accretion discs, with fixed disc mass $M_d = 0.5 M_\odot$ and $\alpha = 0.1$, about Schwarzschild black holes of different masses, viewed from a distance $D = 100$ Mpc. Points with blue squares are computed with pure thermal emission, as the Eddington ratio in these cases is $l > l_{\rm HS} = 10^{-2}$. For black hole masses larger than $M \simeq 2 \times 10^7 M_\odot$, the disc Eddington ratio is $l < l_{\rm HS}$, and I include a Compton scattering corona covering the disc from the ISCO ($r_I = 6 r_g$) out to $R_{\rm Cor} = 12 r_g$. The corona scatters a fraction $f_{SC} = 0.3$ of the soft disc photons. Light curves are computed for a number of different photon indices Γ.

It is clear from Figure 4.11 that the compact corona model used here can readily produce observable levels of X-ray flux for TDE discs around large mass black holes. The solid curves in the Compton scattering regime are the analytic scaling relationships derived in section 4.13.3 (equation 4.87). Note that coronae with harder indices (smaller Γ) produce *brighter* X-ray discs, observable at larger black hole masses. This model suggests that the populations of thermal X-ray TDEs and nonthermal X-ray TDEs should be drawn from black hole populations with systematically different masses, either above (nonthermal) or below (thermal) a characteristic black hole mass of order $\sim 10^7 M_\odot$.

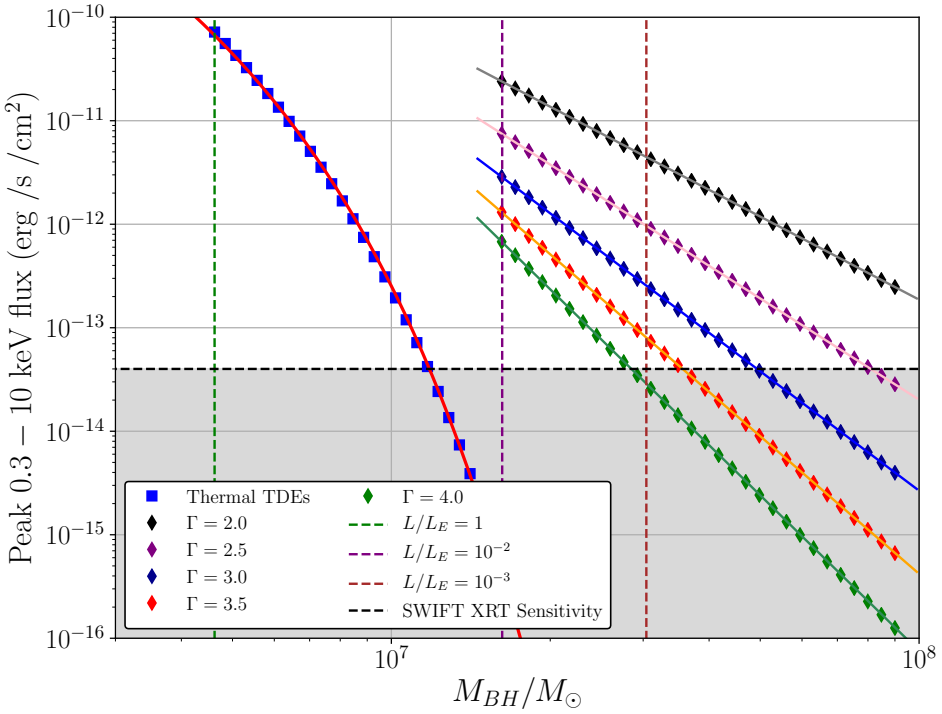

Figure 4.11: The peak X-ray flux from evolving disc light curves with initial disc mass $M_d = 0.5M_\odot$ and $\alpha = 0.1$ at a distance of $D = 100$ Mpc. Thermal X-ray emission is strongly suppressed around larger mass black holes, becoming unobservable at $M \simeq 10^7 M_\odot$. This model produces observable nonthermal X-ray fluxes from black holes of mass $M > 1.5{\times}10^7 M_\odot$, where the bolometric Eddington ratio $l < 0.01$. The corona was assumed to extend from the ISCO ($6r_g$) out to $R_{\rm Cor} = 12r_g$ and scatter a fraction $f_{SC} = 0.3$ of the soft disc photons for a number of photon indices Γ, denoted on plot. The solid lines are the analytical scaling relationships given by equation 4.87. The vertical dashed lines denote the Eddington ratio of the disc solutions.

4.13.2 The observed X-ray spectral composition of TDE discs

The properties of the X-ray spectra of X-ray bright TDEs can be roughly split into three classes: those with 'pure' thermal spectra (e.g., ASASSN-14li, Brown et al. 2017), those with pure nonthermal spectra (e.g., XMMSL2 J1446, Saxton et al. 2019), and a third class observed with nonthermal spectral components accompanied by a low energy 'thermal excess' (e.g., XMMSL1 J0740, Saxton et al. 2017).

The results of the modelling thus far seem to imply that TDE discs should be observed in *either* a thermal or nonthermal X-ray state (Figures 4.10, 4.11). In fact, there are at least five physical mechanisms by which a 'thermal excess' may be observed in addition to a nonthermal power-law component in a TDE X-ray spectrum.

The first mechanism lies beyond the scope of our simple model, and relates to the orientation angle of the TDE accretion disc with respect to the observers line of sight. The material in the innermost regions of a black hole accretion disc is moving at highly relativistic speeds, and discs at moderate inclination angles therefore have regions where emitted photons undergo a large Doppler blueshift en route to the observer. This blueshifted radiation will be observed at higher energies, which can result in an observed thermal excess. While this may seem like a minor effect, the thermal *Wien-portion of the X-ray flux* is exponentially sensitive to the redshift factor (defined by the ratio of the observed and emitted photon frequencies $f_\gamma = \nu_{\rm obs}/\nu_{\rm emit}$) of the hottest disc regions, which can vary by a factor ~ 3 with varying orientation angle. Modelling the spectral interaction between Doppler shifting, gravitational redshift, and Compton scattering of photons on their path to the observer is an extremely complex problem, which lies beyond the scope of the simple phenomenological model presented in section 4.12.

The remaining four mechanisms are more easily modelled and understood. The first result arises from uncertainty in the magnitude of the colour-correction factor ($f_{\rm col}$) of the hottest disc regions. In producing figures 4.10 and 4.11, I have taken a fairly standard value $f_{\rm col} = 2$; however, there is uncertainty associated with the exact value. Simple models (e.g., equations 4.73–4.75, taken from Done et al. 2012) can produce values up to $f_{\rm col} \sim 2.7$. A $\sim 30\%$ increase in the disc's colour-correction factor could lead to an observable thermal excess in some of the models discussed in this Chapter, which nevertheless appear to be nonthermal in the X-ray band.

TDE discs which transition into a harder accretion state at higher Eddington ratios $l_{\rm HS}$ can also show a prominent thermal excess. While it is well-known that XRBs undergo transitions when the Eddington ratio is of order 1%, and there is some evidence that AGN discs undergo similar state transitions (Maccarone et al. 2003), the extended viscous evolution timescale of typical AGN discs makes it much more difficult to precisely determine a typical luminosity scale at which state transitions occur in discs around more massive black holes. Initial findings specific to TDEs (Wevers 2020) suggest that these discs undergo a transition at $l_{\rm HS} \sim 0.03$, but with significant uncertainty. If some TDE discs undergo state transitions at higher luminosity scales (e.g. $l_{\rm HS} \sim 0.1$), these higher-luminosity sources could well display a prominent thermal excess in addition to their coronal emission. This is a direct result of the exponential sensitivity of the thermal X-ray luminosity on the disc transitional luminosity scale (e.g. Figure 4.11).

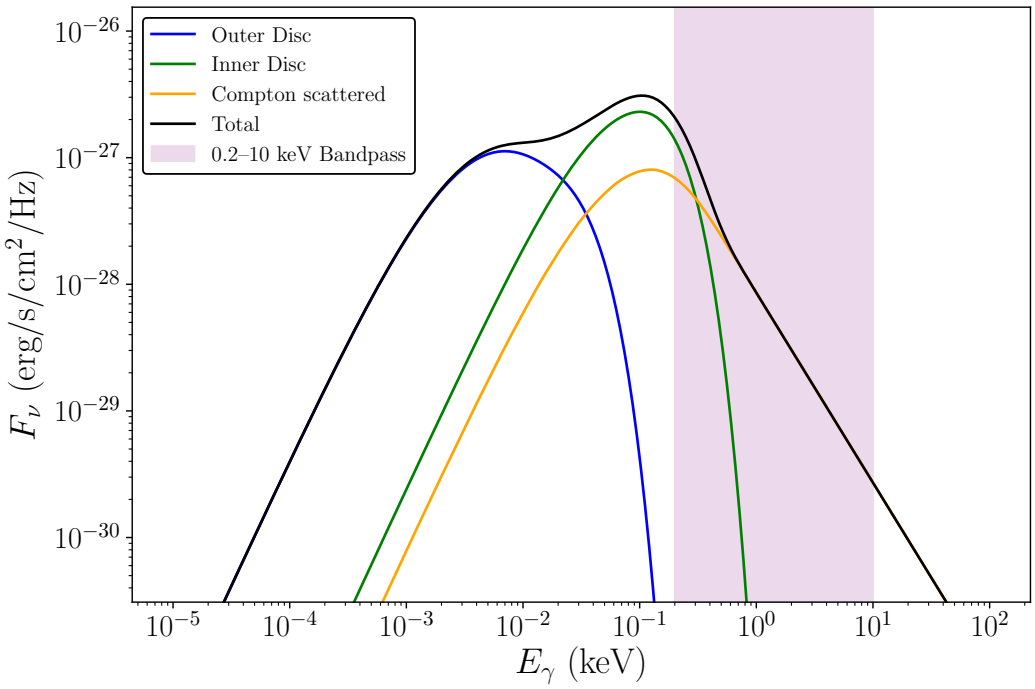

Figure 4.12: This model produces an observable low energy 'soft excess' above a dominant nonthermal X-ray spectral component. This disc was described by mass $M_d = 0.5 M_\odot$ and $\alpha = 0.1$, while the black hole had mass $M = 2 \times 10^7 M_\odot$ and spin $a/r_g = 0.9$. The corona covered the disc from the ISCO to $R_{\rm Cor} = 8 r_g$, and scattered a fraction $f_{SC} = 0.3$ of the soft disc photons with $\Gamma = 2.5$. The source-observer distance was $D = 100$ Mpc. A disc without a corona with these same parameters would have a bolometric luminosity $l = L_{\rm bol}/L_{\rm edd} = 0.03$. The X-ray band displayed here ($0.2 - 10$ keV) corresponds to the XMM observing range; XMM has discovered a number of TDEs with mixed component X-ray spectra (e.g. XMMSL1 J0740, Saxton et al. 2017).

In addition, the physical properties of the corona itself (in particular its geometry and scattering fraction) strongly influence the nature of the thermal excess. To see this most starkly, consider the (likely unphysical) limit $f_{SC} \to 1$. The disc thermal emission would then appear to peak at the temperature $T_{\rm Cor} \equiv T(r = R_{\rm Cor})$, rather than $T_p = T(r = R_{\rm ISCO})$. All photons emitted between $R_{\rm ISCO} < r < R_{\rm Cor}$ would Compton scatter. Typically, the disc temperature falls off with radius at least as quickly as $T \sim r^{-3/4}$, meaning that $T_{\rm Cor}$ can be substantially lower than the peak disc temperature $T_{\rm Cor} \simeq T_p \, (R_{\rm ISCO}/R_{\rm Cor})^{3/4}$, particularly if the corona is large. Conversely, lower scattering fractions and physically smaller corona will lead to a thermal disc profile much more similar to a 'bare' disc, and are therefore more likely to display a thermal excess.

Finally, and potentially most interestingly, black holes of higher spins will generally produce a more prominent thermal excess. Under otherwise similar physical conditions, a large-spin Kerr black hole emits more of its bolometric luminosity at higher energies, owing to the greater inward encroachment of the ISCO. This leads to increased maximum disc temperatures. Hence, discs around large-spin Kerr black holes with Eddington ratios $l \simeq 10^{-2}$ may still produce readily observable levels of thermal X-ray emission, in addition to their nonthermal power-law component.

This is explicitly demonstrated in Figure 4.12. If observed only in the X-ray band, the spectrum would appear to be well-modelled by a simple power-law with a 'soft-excess', which could be modelled as an additional black-body component with temperature $kT \sim 100$ eV. Note that, other than a change in the spin, Figure 4.12 retains the same black hole and disc parameters as seen in Figure 4.10. The properties of this thermal excess can be further quantified by calculating its 'temperature'. This temperature measurement is computed as follows. The observed 0.3–10 keV disc spectrum is modelled by two simple components, one thermal, the other nonthermal:

$$F(E) = A_0 E^{1-\Gamma} + A_1 B_\nu(E, T_{BB}), \quad 0.3 < E/\mathrm{keV} < 10, \tag{4.80}$$

where $B_\nu(E, T_{BB})$ is a Planck function, defined with a single temperature T_{BB}, and A_0 and A_1 are constant amplitudes. By fitting the above functional form to a full disc spectrum, observed across the X-ray bandpass, a best fitting temperature of the thermal excess T_{BB} is determined. Figure 4.13 shows the best-fitting blackbody temperatures of a series of discs around black holes of increasing spins. Each disc had coronal parameters $f_{SC} = 0.3$, $\Gamma = 2.0$, $R_{\rm Cor} = 12 r_g$, a disc mass $M_d = 0.5 M_\odot$ and $\alpha = 0.1$. Figure 4.13 clearly shows that the inferred temperature of TDE accretion discs increase monotonically with the central black hole's spin.

Clearly, there are many different mechanisms by which a hard-state TDE disc can produce a thermal excess. It is likely that future high-quality observations of mixed thermal & nonthermal X-ray TDEs (e.g., AT2018fyk Wevers et al. 2019a and XMMSL1 J0740 Saxton et al. 2017) will be able to constrain, or even measure, the spins of supermassive black holes, a goal of considerable astrophysical interest.

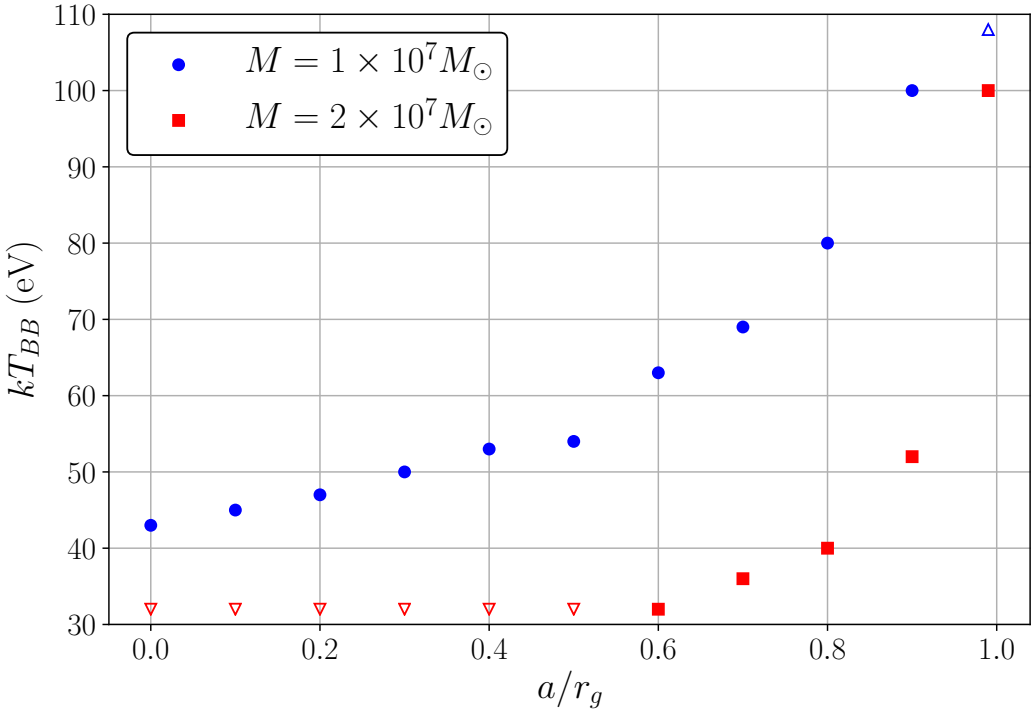

Figure 4.13: The 'temperature' of the thermal excess of accretion discs (defined in text) around black holes of different spins of masses $M = 2 \times 10^7 M_\odot$ (red squares), and $M = 1 \times 10^7 M_\odot$ (blue circles). There is a clear positive trend between black hole spin and the inferred temperature of the thermal excess. For the highest mass black hole no thermal excess is present for spins $a/r_g < 0.6$. The temperature of the largest spin value ($a/r_g = 0.99$) for the lower mass black hole is not displayed for aesthetic reasons, but equals $kT_{BB} = 205$ eV.

4.13.3 X-ray flux scalings

Under the simplifying assumption that all of the observed X-ray flux comes from the hard Compton scattered component, one may obtain expressions for this flux. The observed flux across a bandpass with upper and lower energy limits E_u and E_l is

$$F_X = \frac{1}{D^2} \int_{E_l}^{E_u} E\, n'(E)\, \mathrm{d}E, \tag{4.81}$$

where $n'(E)$ is the photon occupation number as a function of energy, after any Compton scattering has taken place (equation 4.78). The intrinsic disc spectrum will peak at some energy E_p before falling off sharply. If $E_l \gg E_p$, then only the Compton scattered photons will contribute to the observed X-ray flux (i.e., the second

term of equation 4.78), leading to

$$F_X \simeq \frac{f_{\rm SC}}{D^2} \int_{E_l}^{E_u} E \left[\int_0^\infty n(E_0)\, G(E; E_0) \mathrm{d}E_0 \right] \mathrm{d}E. \tag{4.82}$$

The photon occupation number from the intrinsic disc emission can be approximately described by the functional form

$$n(E_0) \simeq \frac{N_\gamma}{E_p} \left(\frac{E_0}{E_p} \right)^b \exp\left(-\frac{E_0}{E_p} \right), \tag{4.83}$$

where the cut-off energy is related to the peak disc temperature T_p by $E_p \simeq k_B T_p$. This approximation for the intrinsic disc emission holds provided that the disc colour-correction factor is a weak function of temperature. The normalisation N_γ is (up to a numerical factor) the total number of photons emitted per unit time, and depends upon the disc and black hole properties. Combining equations 4.83 and 4.79 leaves

$$F_X \simeq \frac{1}{D^2} \frac{(\Gamma-1)(\Gamma+2)}{(1+2\Gamma)} \frac{N_\gamma f_{\rm SC}}{E_p} \int_{E_l}^{E_u} E^{1-\Gamma} \mathrm{d}E \int_0^\infty \left(\frac{E_0}{E_p} \right)^b E_0^{\Gamma-1} \exp\left(-\frac{E_0}{E_p} \right) \mathrm{d}E_0, \tag{4.84}$$

which, after defining $x \equiv E_0/E_p$, becomes

$$F_X \simeq \frac{1}{D^2} \frac{(\Gamma-1)(\Gamma+2)}{(1+2\Gamma)} N_\gamma f_{\rm SC} E_p^{\Gamma-1} \int_{E_l}^{E_u} E^{1-\Gamma} \mathrm{d}E \int_0^\infty x^{b+\Gamma-1} \exp(-x)\, \mathrm{d}x. \tag{4.85}$$

The integrals are mere normalisation factors, and the numerical value of the index b does not affect the parameter dependence of the scattered X-ray flux. With the total number of photons emitted per unit time N_γ scaling as the bolometric disc luminosity divided by the characteristic disc energy,

$$N_\gamma \sim L_{\rm bol}/E_p \sim M^2 E_p^3, \tag{4.86}$$

the parameter dependence of the X-ray flux is

$$F_X \propto f_{\rm SC} N_\gamma E_p^{\Gamma-1} \propto f_{\rm SC} M^2 E_p^{\Gamma+2}. \tag{4.87}$$

Earlier I demonstrated that (equation 4.54)

$$E_p \propto T_p \propto \frac{M_d^{5/12} \alpha^{1/3}}{M^{7/6}}, \tag{4.88}$$

which gives the black hole mass dependence of the observed X-ray flux (cf. Figure 4.11):

$$F_X \propto M_d^{(5\Gamma+10)/12}\, \alpha^{(\Gamma+2)/3}\, M^{-(7\Gamma+2)/6} \tag{4.89}$$

Recall that after the disc temperature reaches its peak value it decays with a shallow power-law in time

$$E_p \propto t^{-n/4}, \tag{4.90}$$

where n is the bolometric luminosity decay index, $L \sim t^{-n}$. This means that nonthermal X-ray TDEs should be described by power-law decays at large times

$$F_X(t) \propto t^{-(\Gamma+2)n/4}. \tag{4.91}$$

The dependence of the X-ray decay index on Γ means that softer (larger Γ) X-ray TDEs will decay more quickly than their harder counterparts, and for all corona with $\Gamma > 2$ the X-ray flux will evolve quicker than the bolometric disc luminosity. It is interesting to note that this late-time decay law is much slower than the late-time decay of thermal X-ray TDE light curves: $F_X(t) \propto t^{-n/2} \exp\left(-At^{n/4}\right)$, where A is a constant (equation 3.73). A general prediction of this model therefore is that thermal X-ray TDEs (or the thermal components of mixed spectrum TDEs) will decay more rapidly than their nonthermal counterparts.

Detailed numerical calculations of the time dependence of a hard component light curves agree very well with the simple analytic predictions of equation 4.91. In Figure 4.14 I compute the evolving 0.3 – 10 keV flux for discs with initial mass $M_d = 0.5M_\odot$ and $\alpha = 0.1$ around a Schwarzschild black hole of mass $M = 2 \times 10^7 M_\odot$. The corona extends from the ISCO ($6r_g$) to $R_{\rm Cor} = 12r_g$, and scatters a fraction $f_{SC} = 0.3$ of the soft disc photons. Light curves are then produced for different photon indices Γ, using equation 4.78.

In Figure 4.14 each light curve is normalized by its peak flux value and the time axis is plotted in units of the time at which the light curve peaked. The solid curves show the large time scaling result $F_X(t) \propto t^{-(\Gamma+2)n/4}$, with $n = 1.19$. This n value is the theoretical value of the asymptotic decay index which is appropriate at large times (after the stalled accretion phase, Chapter 2). The analytical model describe the full numerical results at large times extremely well.

Finally, note that two of the free parameters describing the disc-corona model, $R_{\rm Cor}$ and f_{SC}, exhibit a formal degeneracy: a physically larger corona (larger $R_{\rm Cor}$) which scatters a smaller fraction f_{SC} of the thermal disc photons can produce qualitatively similar X-ray fluxes to those emerging from a smaller corona scattering a larger photon fraction. However, in practice this is only a weak degeneracy, since the X-ray flux is

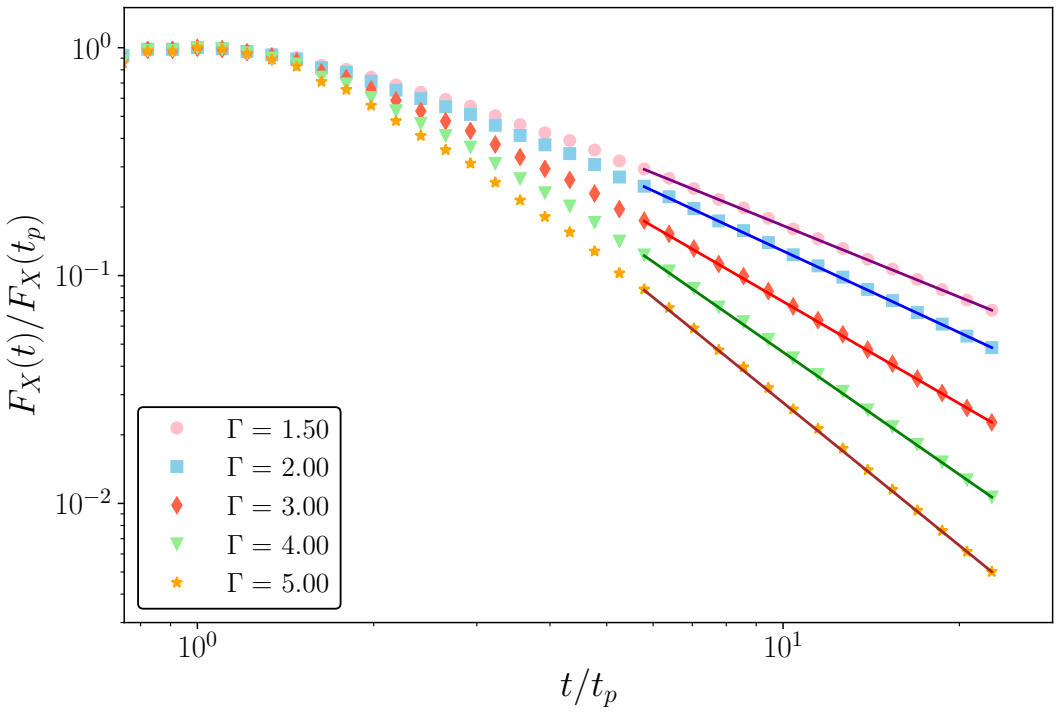

Figure 4.14: Simple nonthermal X-ray light curves from a black hole of mass $M = 2\times10^7 M_\odot$, for discs with $M_d = 0.5M_\odot$ and $\alpha = 0.1$, and a range of different corona photon indices Γ. The solid curves at large times show the predicted analytical behaviour (equation 4.91) $F_X(t) \propto t^{-(2+\Gamma)n/4}$, with $n = 1.19$.

rather insensitive to the physical size of the corona $R_{\rm Cor}$. As can be seen from equation 4.85, the properties of the X-ray flux primarily depend on the coronal scattering fraction f_{SC} and the power-law index Γ, a finding that has been numerically verified.

4.13.4 Evolving coronal properties

The above light curves were produced numerically assuming that the properties of the corona were time-independent. In reality, there is no powerful physical reason why this must be the case. TDEs have been observed with nonthermal X-ray spectral components which both soften (e.g., AT2019azh, Wevers 2020), and harden (e.g., AT2018fyk, Wevers et al. 2019a) at late times. Significant evolution of the Γ parameter can cause large deviations from the simple power-law light curves of Figure 4.14. This is demonstrated in Figures 4.15 & 4.16, which examine some simple ways in which the coronal properties may vary.

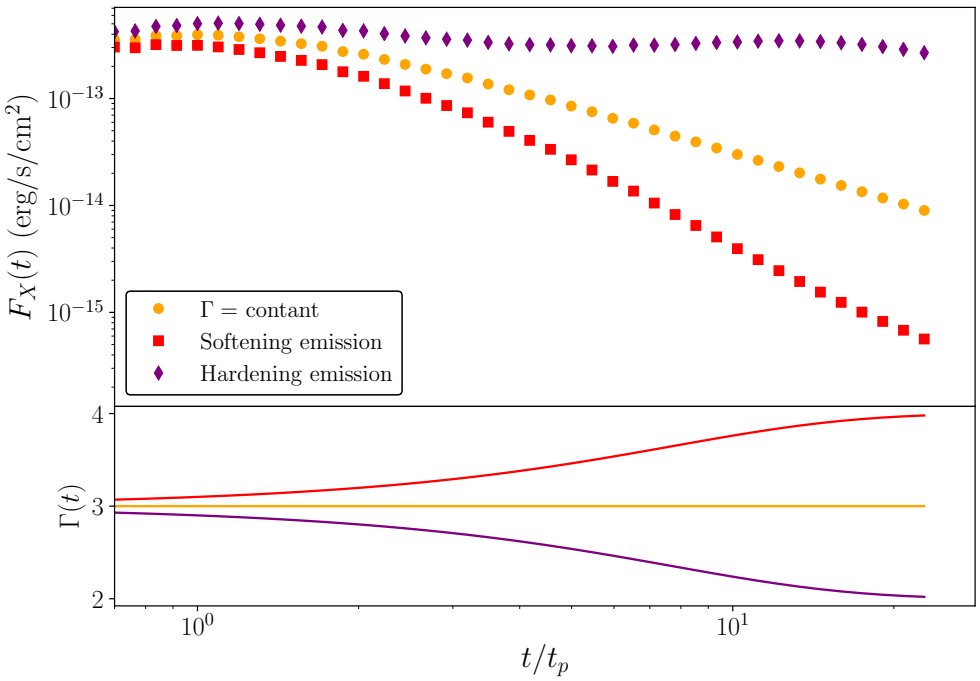

Figure 4.15: The effect of time-dependent photon indices $\Gamma(t)$ on the evolving nonthermal X-ray light curves of simple disc models. Corona with photon indices which harden (decreasing Γ, purple diamonds and curve) remain significantly brighter than constant Γ models, while softening (increasing Γ, red squares and curve) photon index light curves decay at a more rapid rate. All light curves were produced with $M_d = 0.5M_\odot$, $\alpha = 0.1$ and $M = 2 \times 10^7 M_\odot$.

Figure 4.15 shows three 0.3 – 10 keV light curves for accretion discs with an identical disc evolution profile. Each disc has initial mass $M_d = 0.5M_\odot$ and $\alpha = 0.1$, and surrounds a Schwarzschild black hole of mass $M = 2 \times 10^7 M_\odot$. The only difference between the light curves stems from the evolution of the coronal Γ parameter, which in this instance smoothly vary over the course of the disc evolution according to

$$\Gamma(t) = \Gamma_0 + \delta\Gamma_\pm \tanh\left(t/10t_p\right). \tag{4.92}$$

I take $\Gamma_0 = 3$, $\delta\Gamma_\pm = \pm 1$, and $+/-$ corresponds to softening/hardening emission[8]. The evolving Γ profiles are shown in the lower half of Figure 4.15. As well as determining the rate at which the X-ray flux decays, the Γ parameter also influences the amplitude of the X-ray flux itself (equation 4.85). This results in the softening (red) light curve falling off at a much more rapid rate, while the hardening (purple) light curve re-brightens at large times.

[8]No claim is made here that this is a physically reasonable evolution profile for the Γ parameter, it is chosen to be illustrative.

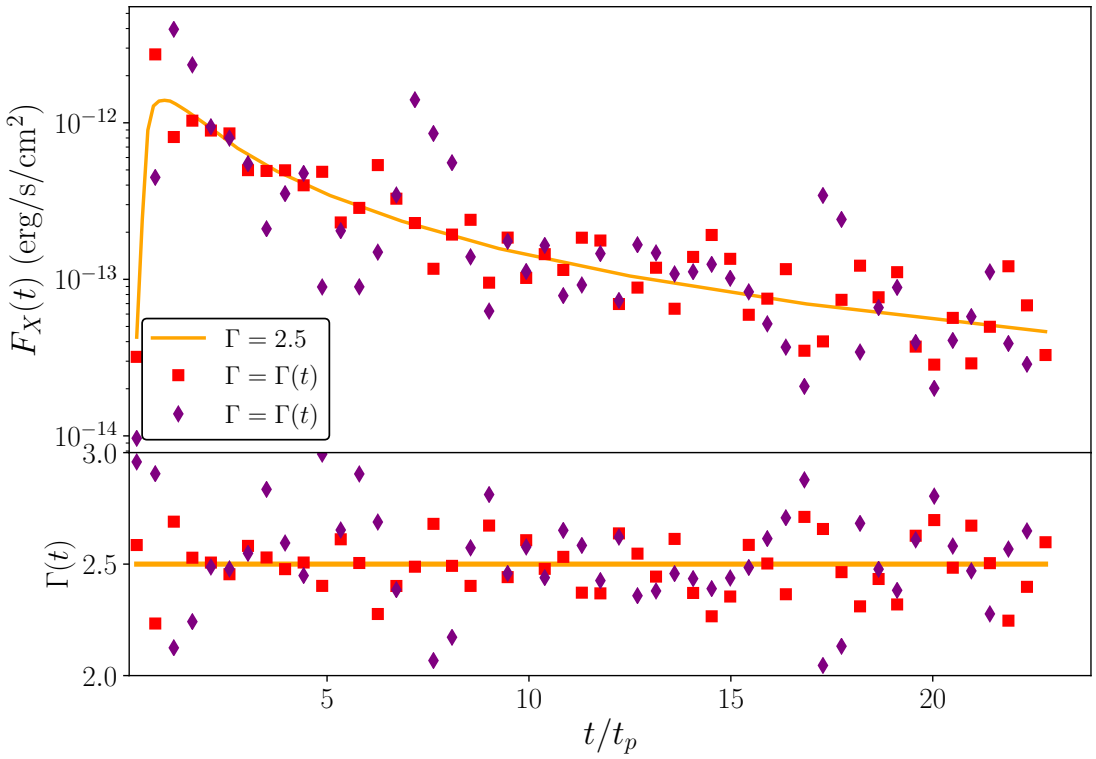

Figure 4.16: The effect of time-dependent photon indices $\Gamma(t)$ on the evolving nonthermal X-ray light curves of simple disc models. Note that small time-scale fluctuations in Γ of order $\sim 10\%$ cause much larger relative fluctuations in the observed X-ray flux (e.g., purple diamonds).

Furthermore, if the Γ parameter varies on short timescales, then much larger amplitude fluctuations in the observed X-ray light curves can be observed. Figure 4.16 shows the effect of random fluctuations in the Γ parameter on the observed X-ray light curves. The disc evolution is identical to the light curves of Figure 4.15, but now the Γ parameter is given by $\Gamma = 2.5$ (orange curve), or is normally distributed around $\Gamma = 2.5$ with standard deviation equal to 0.05Γ (red points) or 0.1Γ (purple points). While the time-dependent Γ profiles of Figures 4.15 & 4.16 need not be a central feature of real TDE systems, it is important to note the sensitivity to time-dependent coronal properties on the observed light curves of otherwise smoothly evolving disc systems.

4.14 X-ray TDE Population analysis

4.14.1 Overview

This analysis predicts that the populations of thermal X-ray TDEs and nonthermal X-ray TDEs should be drawn from black hole populations with systematically different masses, distributed either above (nonthermal) or below (thermal) a characteristic black hole mass scale of order $\sim 10^7 M_\odot$. In this section, I compare the currently known distribution of nonthermal X-ray TDE masses with the predictions of this Chapter; namely, that the black hole mass distribution should peak above $M_p > 10^7 M_\odot$ and decline at lower masses, with sources of mass $M \lesssim 5 \times 10^6 M_\odot$ being rare. The black hole mass $M = 5 \times 10^6 M_\odot$ corresponds to the hard state mass scale for a disc with small initial mass content $M_d = 0.05 M_\odot$, and $\alpha = 0.1$.

At the time of writing the author is aware of seven X-ray bright TDEs with X-ray spectra which are well-modelled by nonthermal emission, and which have formal estimates of the central black hole mass. As in section 4.8, for this analysis I use well-established galactic scaling relationships between the black hole mass and (i) the galactic bulge mass $M : M_{\rm bulge}$, (ii) the galactic velocity dispersion $M : \sigma$, and (iii) the bulge V-band luminosity $M : L_V$. All of the scaling relationships are taken from McConnell and Ma (2013). Where available, values of $M_{\rm bulge}$, σ and L_V were taken from the literature for each TDE, and are presented in Table H.1 in Appendix H. The mean black hole mass for each TDE is given in Table 4.3.

4.14.2 Source selection and hard state designation

Source selection

The sample selection criteria is very simple. For inclusion, the TDE must have two properties: an unambiguous early-time X-ray detection with a well-observed X-ray spectrum. In addition, there must at least one published estimate for the central black hole mass. Note that I include only those TDEs which are X-ray bright at early times, and neglect those that were initially X-ray dim but then observed as X-ray bright only at much later times. (There are three such sources reported in Jonker et al. 2020). The reason for this neglect is that the focus here is upon those TDEs which have formed around large mass black holes at low Eddington ratios, rather those which have *transitioned* into the hard state as a result of cumulative late-time cooling.

Hard and soft state designation

The decision of whether a TDE should be designated as a hard state TDE or a soft state TDE is based, of course, entirely upon the properties of the sources X-ray spectrum. For many sources this was unambiguous, as they were observed in either a 'pure' thermal or nonthermal state. However, other sources have both thermal and nonthermal components present in their X-ray spectrum, and some additional consideration is required. The X-ray spectra of all of these 'mixed sources' was quantitatively analysed as part of the initial data reduction, and the fraction of the total observed X-ray flux resulting from each spectral component determined (e.g. Table 1, Wevers 2020). In mixed cases, if the X-ray flux is more than 50% dominated by power-law emission, it is designated as 'hard state'; otherwise it is designated as 'soft state'. For sources where there were multiple observations with spectral information present I use the observation at which the source is at its maximum X-ray luminosity to designate its spectral classification.

This procedure sorts the 19 TDEs with both black hole mass estimates and a well-observed X-ray spectrum. I note that there are two potentially ambiguous sources of interest, AT2018fyk and XMMSL1 J0740, which could arguably be sorted into either category, which is discussed below.

Edge cases: AT2018fyk and XMMSL1 J0740

AT2018fyk was, in its very earliest detections, observed with a two-component X-ray spectrum with $\sim 25 \pm 13\%$ of its X-ray flux resulting from its power-law component, suggesting that it was a soft-state TDE. At peak brightness however, AT2018fyk had an X-ray spetrum which was significantly harder, with a power-law fraction of $\sim 80\%$ (Wevers et al. 2021). This hardening to a power-law dominated state occurred within 75 days (Wevers et al. 2019b), in total the X-ray luminosity increased by a factor 10. In this work I have designated AT2018fyk a hard-state TDE, for two primary reasons. First, there is hard nonthermal emission present at all times during its evolution, suggesting that a corona formed in the earliest stages of the disc evolution. Second, when AT2018fyk is at maximal X-ray brightest it has a power-law fraction of 80%.

Finally, the source XMMSL1 J0740 is also a potential borderline case, with an observed power-law fraction of $f_{PL} = 59 \pm 11\%$ (Wevers 2020), meaning that, within the quoted uncertainty, it could be deemed a soft state TDE. It is perhaps unsurprising, therefore, that XMMSL1 J0740 has the smallest inferred black hole mass of all of the hard-state TDEs in the literature. This small black hole mass is in keeping with what would be expected from the analysis performed in this Chapter.

Possible contamination of TDE sample from flaring AGN

Three of the sources included in the 'hard state' TDE sample (XMMSL1 J0619, Saxton et al. 2014; ASASSN-18jd, Neustadt et al. 2020; and PTF-10iya, Cenko et al. 2012), have also been flagged as potential flaring AGN by the discovering authors. The difficulty here is that, unlike the super-soft X-ray flares from soft-state TDEs which are easily distinguished from variable AGN behaviour, TDEs which form discs in the hard state produce X-ray spectra much more similar to those of AGN (see Zabludoff et al. 2021 for further discussion). It is therefore a challenge to distinguish between a TDE which forms a disc in a harder accretion state, and a flare which takes a previously unobservable (but nevertheless present!) AGN disc to a higher, and thereafter observable, luminosity.

Distinguishing between flaring AGN and TDEs which form in a hard accretion states will always be a difficult observational problem, one that will not be solved in this work. The reader should be aware, therefore, that not every classification in the samples is completely secure, and that the conclusions must be interpreted bearing in mind this caveat.

4.14.3 Population analysis and comparison

Noting the above uncertainties, I next analyse the two X-ray sub-populations of TDEs. In Table 4.3 I present the mean black hole masses of the 7 TDEs with dominant nonthermal (hard state) emission, the mean black hole masses of the 12 TDEs dominated by thermal (soft state) emission are presented in Table 4.2.

In the upper section of Figure 4.17 I show the black hole masses of the seven nonthermal X-ray TDEs obtained from each galactic scaling relationship, along with the mean black hole mass of each TDE (black diamond). I display as vertical dashed lines three characteristic hard state (Schwarzschild) black hole masses, corresponding to initial disc masses $M_d = 0.05, 0.2$ and $0.5 M_{\odot}$, with $\alpha = 0.1$, under the assumption that

TDE name	$\langle M_{\rm BH} \rangle / 10^6 M_\odot$
ASASSN-18jd	145^{+105}_{-116}
AT2018fyk	$37.7^{+53.4}_{-12.0}$
XMMSL1 J0740	$7.9^{+4.4}_{-2.9}$
XMMSL2 J1446	$41.2^{+47.1}_{-27.9}$
SDSS J1323	$14.7^{+20.7}_{-10.2}$
PTF-10iya	$34.9^{+46.7}_{-22.6}$
XMMSL1 J0619	$33.3^{+19.6}_{-19.6}$

Table 4.3: The mean black hole mass of the 7 nonthermal (hard state) X-ray TDEs from the literature. See Appendix H for further details.

discs form in the hard state when the Eddington ratio is $l < 0.01$. In the lower section of Figure 4.17 I show the current distribution of the black hole masses of the nonthermal X-ray TDE population obtained, as before (Figure 4.9), using kernel density estimation.

The nonthermal X-ray TDE population appears to be completely consistent with the expected results of this Chapter: the distribution peaks at a black hole mass $M \simeq 6 \times 10^7 M_\odot$, and is strongly suppressed below $M \lesssim 1 \times 10^7 M_\odot$.

In Figure 4.18 I compare the current distributions of the black hole masses of both the thermal and nonthermal X-ray TDE populations, obtained using kernel density estimation. Figure 4.18 is revealing, while the total (thermal & nonthermal) X-ray bright TDE population is approximately flat over a range of black hole mass between $M \sim 2 \times 10^6 - 8 \times 10^7 M_\odot$ (as was first reported by Wevers et al. 2019b), there is a clear systematic mass offset between the distributions of the thermal and nonthermal sub-populations, just as predicted. Quantitatively, a two-sample K-S test rejects the null-hypothesis that the two sub-populations result from the same black hole mass distribution (p-value = 0.01). A two-sample Anderson-Darling test (a test which is more sensitive to the wings of the distribution) also rejects this null-hypothesis, but at an even stronger level (p-value = 0.002).

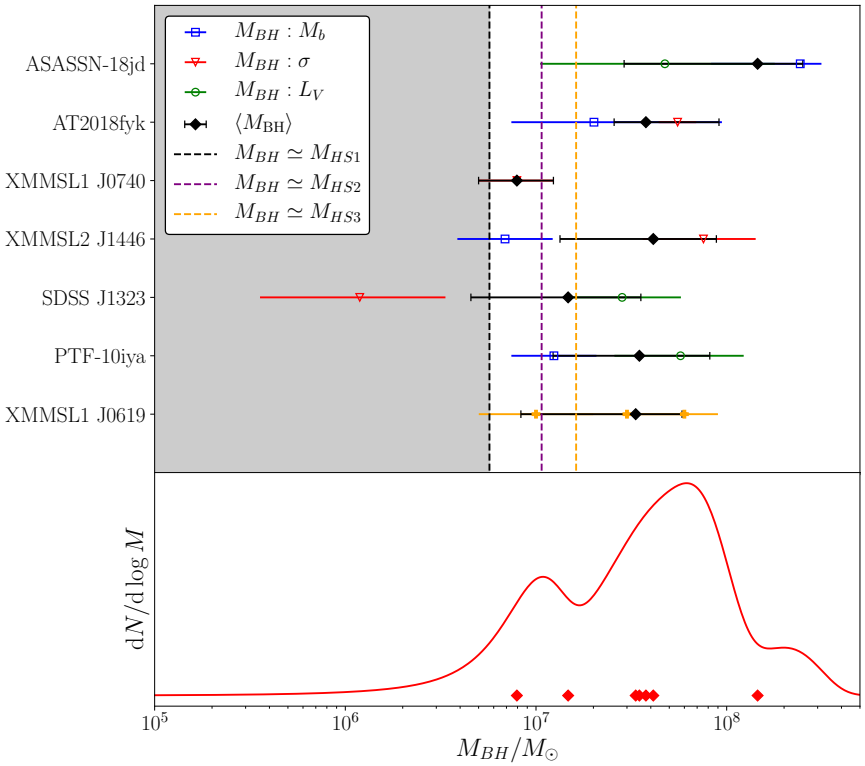

Figure 4.17: The black hole mass distribution of TDEs with bright nonthermal X-ray spectra. The upper panel shows the black hole mass values inferred for each individual TDE, calculated using correlations with (i) the galactic bulge mass $M : M_{\rm bulge}$ (blue squares), (ii) the galactic velocity dispersion $M : \sigma$ (red triangles), and (iii) the bulge V-band luminosity $M : L_V$ (green circles). The mean black hole mass for each TDE is plotted as a black diamond. The lower panel shows the black hole mass distribution of the nonthermal X-ray TDE population, obtained using kernel density estimation using a kernel width equal to the uncertainty in each TDE's black hole mass.

While the results of this analysis are clearly supportive of the model put forward in this Chapter, I note that by either changing the accretion state designation of the borderline TDE AT2018fyk, or by excluding it from the analysis entirely, a lower statistical significance is found for the difference between the two sub-populations of TDEs. Explicitly, excluding AT2018fyk results in p-values of $p = 0.03$ (K-S 2 test) and $p = 0.004$ (Anderson-Darling test). Changing AT2018fyk's accretion state designation results in $p = 0.11$ (K-S 2 test) and $p = 0.01$ (Anderson-Darling test). Additional complications may arise if the two TDE subpopulations are contaminated by flaring AGN. While the effect of misdiagnosing any particular subset of TDEs can be modelled and calculated, this is not particularly informative.

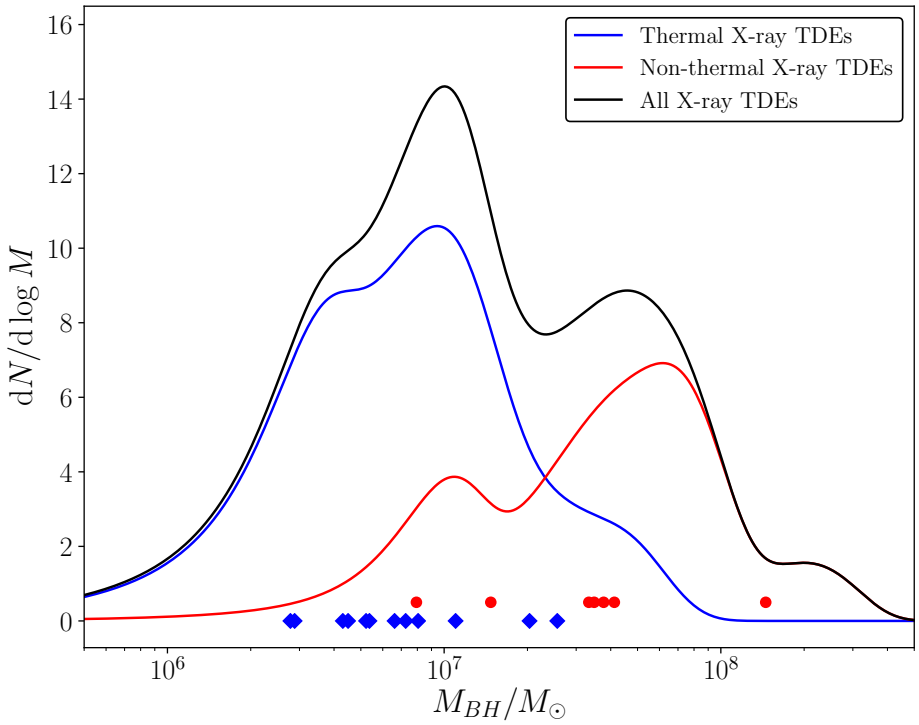

Figure 4.18: The black hole mass distribution of the quasi-thermal (blue; Table 4.2) & nonthermal (red; Table 4.3) X-ray TDE populations, obtained using kernel density estimation using a kernel width equal to the uncertainty in each TDE's black hole mass. The blue diamonds and red circles show the mean black hole mass values of the individual TDEs of the quasi-thermal and nonthermal populations respectively. There is a clear systematic mass offset between the two sub-populations of X-ray bright TDEs, as predicted in this work.

Perhaps the best way to view these results is as promising initial support for a prediction which will be much more rigorously tested over the coming years. The eRosita telescope, for example, is expected to find hundreds to thousands of X-ray bright TDEs over the next 5 years (Khabibullin et al. 2014). With this vastly increased sample size, it will be possible to perform a much more definitive analysis of the properties of the two TDE sub-populations.

In summary, the properties of the known TDE population are thus far supportive of two distinct sub-populations of X-ray bright TDEs with different spectral properties, separated by black hole mass. Explicitly, an analysis of the mean black hole masses of soft-state and hard-state TDEs with an Anderson Darling two-sample test shows statistically significant ($p < 0.01$) differences between their mass distributions.

4.15 A model of state transitions in TDE discs

The primary focus of this section has been on those TDE discs which form in *either* the soft or hard state. However, the behaviour of TDE sources which transition between accretion states is also of great astrophysical interest. Late-time transitions in TDE discs are to be expected, since the late-time bolometric luminosity of an accretion disc in standard models decays as a power law, $L \sim t^{-n}$. Discs which formed with Eddington ratios above the hard state transitional scale $l_{\rm peak} > l_{\rm HS}$, should transition when $l(t) < l_{\rm HS}$.

To better understand the behaviour of the X-ray light curves of TDE accretion discs which undergo a state transition, I model the state transition of the disc at some Eddington ratio l_u as a corona with an expanding coronal radius, in the following simple way:

$$R_{\rm Cor}(l) = \begin{cases} R_I \quad (\text{no scattering}), & l(t) > l_u, \\ R_I + (R_C - R_I) f(l), & l_u > l(t) > l_l, \\ R_C, & l_l > l(t), \end{cases} \tag{4.93}$$

where

$$f(l) = \frac{l_u - l(t)}{l_u - l_l}, \quad l_u > l(t) > l_l. \tag{4.94}$$

Representative light curves are shown in Figure 4.19, in which three accretion discs, all with $M_d = 0.5 M_\odot$ and $\alpha = 0.1$, form around Schwarzschild black holes of different masses. All have peak Eddington ratios $l_{\rm peak} > l_u = 0.01$. The corona in each disc "switches on" when the evolving Eddington ratio of the disc $l(t_u) = l_u$, and then expands out to $R_C = 12 r_g$ at $l(t_l) = l_l = 5 \times 10^{-3}$. The corona scatters a fraction $f_{SC} = 0.3$ of the soft disc photons with a photon index $\Gamma = 3$.

In the upper panel of Figure 4.19 I show the X-ray light curves of the three disc solutions, in the middle panel the evolving Eddington ratios, and in the lower panel the disc UV light curves, expressed as an evolving AB magnitude for the UVW1 band. The discs are at a fiducial source distance $D = 100$ Mpc. The orange (triangular points) light curve is of particular interest, corresponding to the most massive black hole ($M = 12 \times 10^6 M_\odot$). At early times ($t \lesssim 4$ years), the thermal disc emission is insufficient to produce observable levels of X-ray flux, due to the cool inner disc regions around such a large mass black hole.

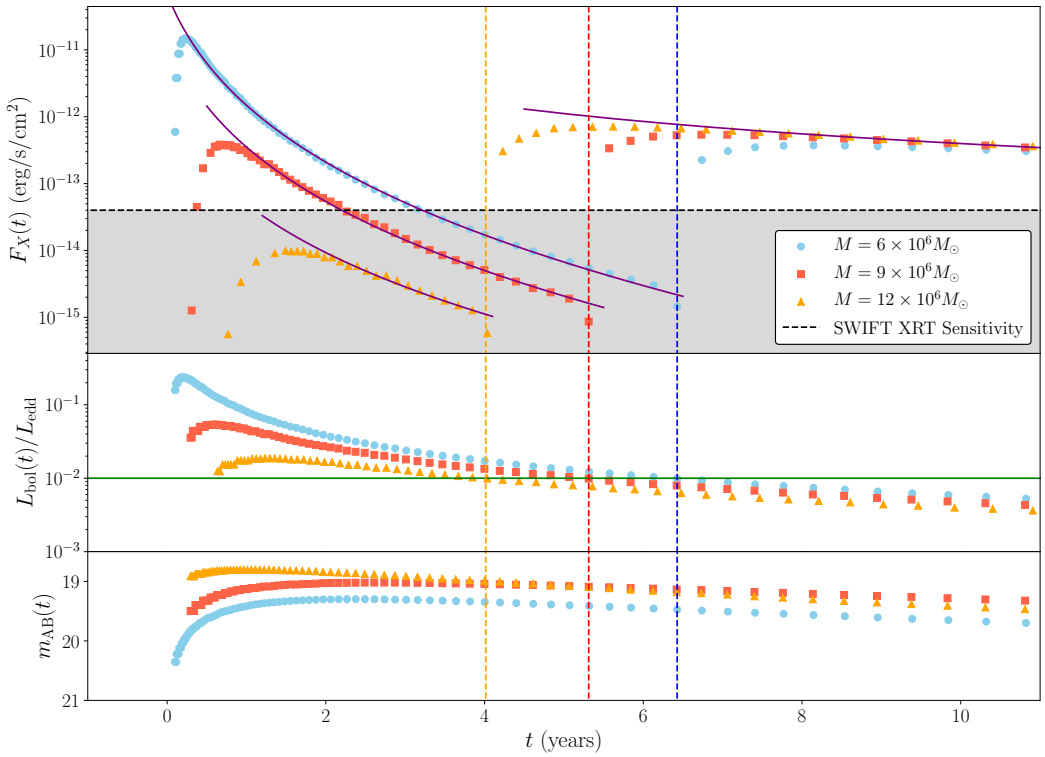

Figure 4.19: Example X-ray (upper), bolometric (middle) and UV (lower) light curves from Schwarzschild black holes of different masses, denoted on plot. In this model the corona 'switches on' (equation 4.93) when the disc's Eddington ratio becomes $l = 0.01$ (at times denoted by vertical dashed lines). The purple solid curves are the analytical models of equation 4.91 (late times, nonthermal emission) and equation 3.73 (early times, thermal emission). Of particular interest is the orange curve, which is unobservable at X-ray energies at early times but becomes X-ray bright after $t > 4$ years.

However, at yet later times ($t \gtrsim 4$ years) the up-scattered nonthermal X-ray emission is detectable. The properties of this light curve is therefore qualitatively similar to those observed by Jonker et al. (2020). I suggest that TDE sources which are initially X-ray dim and around black holes of large ($M \gtrsim 10^7 M_\odot$) inferred masses may be interesting sources to follow up at X-ray frequencies at large times, as they are likely to transition into a harder accretion state within reasonable observational timescales. The detection of hard X-ray emission from these sources at large times will provide further evidence for the TDEs-as-scaled-up-XRBs paradigm.

Finally, I note that the UV light curves, with their characteristic late-time plateau observed in many TDEs (van Velzen et al. 2019b; Chapter 3), are unaffected by the switching on of a compact corona (lower panel, Figure 4.19). This is because the UV

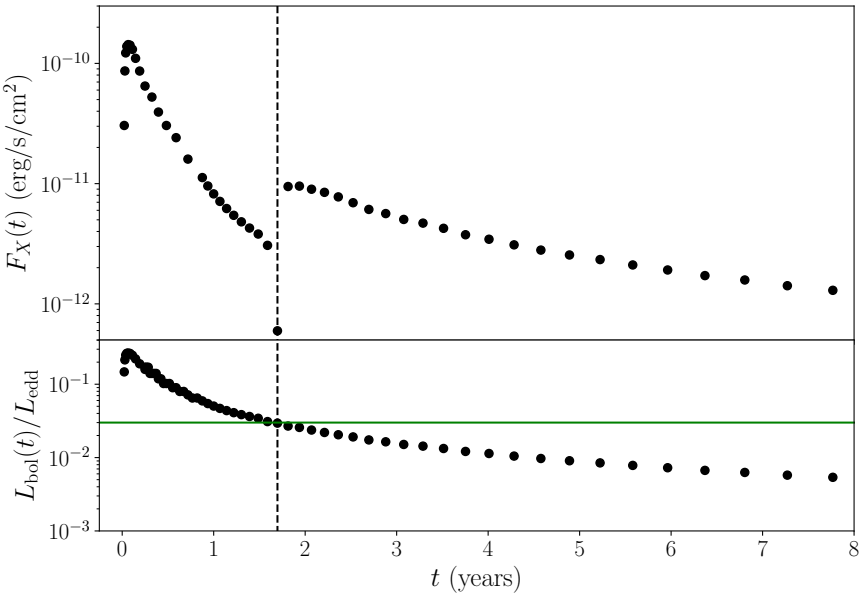

Figure 4.20: The X-ray light curve of a rapidly rotating ($a/r_g = 0.9$) black hole of mass $M = 10^7 M_\odot$. The disc parameters were $M_d = 0.1 M_\odot$ and $\alpha = 0.3$. The transition to harder emission occurred when the disc's Eddington ratio was $l = 0.03$, at which point thermal X-ray emission was still observable. TDEs around black holes with large rotation parameters may offer the best opportunity to see TDE accretion disc transitions in real time.

emission results primarily from radii much farther out than the ISCO, and is thus unaffected by the inclusion of a compact corona in the inner disc regions.

As highlighted in section 4.13, in contrast to the discs of Figure 4.19, where the actual accretion state transition occurs at times when unobservable levels of X-ray flux are produced, discs around more rapidly rotating Kerr black holes will be observed to behave differently. Figure 4.20 shows the X-ray and bolometric light-curves of a disc ($M_d = 0.1 M_\odot$, $\alpha = 0.3$), around a $M = 10^7 M_\odot$ black hole which is more rapidly rotating $a/r_g = 0.9$. These (physically reasonable) disc parameters were chosen so that the disc system underwent a state transition on the typical timescales of which TDE sources are observed. As can be seen in Figure 4.20, this disc system begins to transition at $l(t_u) = 0.03$, when bright X-ray emission is observable. It is interesting to note the very different rates of decay of the disc systems X-ray light curve in Figure 4.20, with the evolution much more rapid in the thermal-dominated state. The existence of distinct rapid/slow decay modes is a general prediction of our model. TDEs around more rapidly rotating Kerr black holes are the most promising systems to observe disc accretion state transitions in real time.

4.16 Discussion

In this section I have extended the relativistic time-dependent thin-disc TDE model to describe nonthermal X-ray emission produced by the Compton up-scattering of thermal disc photons by a compact electron corona.

I have shown from simple scaling arguments that, assuming that TDE discs undergo state transitions into harder accretion states at Eddington ratios of order $L_{\rm bol}/L_{\rm edd} = l_{\rm HS} \sim 10^{-2}$, nonthermal X-ray emission will be detected from TDEs around black holes with masses larger than a characteristic scale $M_{\rm HS}$, which is given approximately by

$$M_{\rm HS} \simeq 2 \times 10^7 \left(\frac{M_d}{0.5 M_\odot}\right)^{5/11} \left(\frac{\alpha}{0.1}\right)^{4/11} \left(\frac{l_{\rm HS}}{10^{-2}}\right)^{-3/11} M_\odot, \tag{4.95}$$

where M_d is the initial disc mass and α is the Shakura and Sunyaev (1973) α-parameter. A simple prediction of this analysis (in combination with the results of the proceeding section) is that nonthermal and thermal X-ray TDEs should be drawn from different populations of black holes characterised by different masses, either being distributed above (nonthermal), or below (thermal), a characteristic black hole mass scale $M \sim 10^7 M_\odot$. I have demonstrated that the current X-ray bright TDE population (19 sources: 12 thermal, 7 nonthermal) are consistent with this picture. The mean black hole mass (calculated from galactic scaling relationships) of thermal TDEs is $\langle M_{\rm TH} \rangle = 9 \times 10^6 M_\odot$ while the mean black hole mass of nonthermal X-ray TDEs is $\langle M_{\rm NT} \rangle = 45 \times 10^6 M_\odot$. A two-sample K-S test rejects the null-hypothesis that the two sub-populations result from the same black hole mass distribution (p-value = 0.01), while a two-sample Anderson-Darling test (a test which is more sensitive to the wings of the distribution) also rejects this null-hypothesis, but at an even stronger level (p-value = 0.002).

This work represents the first detailed modelling of evolving TDE light curves which includes both thermal and nonthermal X-ray components. By drawing connections between TDE discs and the better established properties of XRB discs, I have been able to make quantitative predictions for the properties of the population of hard state X-ray TDEs. These predictions can and will be tested rigorously in the near future, as considerably more observational data becomes available. If confirmed, this work will have established a connection between TDE and XRB discs, accreting onto black holes which span a range of 100 million in mass.

4.17 Tidal disruption events around low-mass supermassive black holes

The preceding two sections have focussed on those TDEs around relatively large supermassive black holes $M \gtrsim$ few $\times 10^6 M_\odot$. TDE black holes may of course have masses potentially an order of magnitude below this, if intermediate mass black holes do exist, approaching values $M \sim 10^5 M_\odot$. As I have demonstrated in this Chapter, the bolometric luminosity of a TDE disc is an extremely sensitive function of the central black hole mass, and these low-mass TDEs will have large initial bolometric luminosities, likely exceeding their Eddington values. Again, the better studied X-ray binary population can help here: when accreting at very high rates X-ray binaries launch outflows, where disc material is unbound from the disc-black hole system by large radiation pressures. These outflows have important effects on the observed properties of a the X-ray binary systems at X-ray energies (for example the remarkable Galactic source SS433, which is encased in a large mass disc outflow, has a very low X-ray luminosity $L_X \sim 10^{35}$ erg/s, for its mass feeding rate $\sim 10^{-4} M_\odot$/year, Fabrika 2004). It is extremely likely that these same physical processes will have important effects on the observed properties of some TDEs.

In fact, at lower observed photon energies, outflows have been repeatedly invoked as the physical mechanism which may explain observed TDE emission (Strubbe and Quataert 2009, Metzger and Stone 2016, Dai et al. 2018). These outflow models aim to reproduce the properties of some TDE radio outbursts (with other radio bright sources being associated with a jet), and the optical emission observed from TDEs at early times. The overarching idea of these models is that some fraction of the stellar debris produced in the aftermath of a TDE is expelled from the black hole-disc system, this material then reprocesses (absorbs and re-emits) disc photons to lower energies. The debris resulting from the tidal destruction of a star will be gravitationally bound to its central black hole to various different degrees, and so it is not surprising that some material may settle into a disc while other debris will be ejected from the system entirely. X-ray and UV emission stemming from the accretion disc passes through this outflowing material on the way to the observer, where it is absorbed and re-emitted at lower photon frequencies.

Models of outflows from TDEs therefore generally act to suppress observations of high energy (X-ray) TDE emission and to increase the amount of observed optical

TDE emission. In this section I aim to build upon and extended these outflow models in a number of ways. Firstly, I examine over which regions of TDE (black hole and disc) parameter space outflows are likely to be launched from a TDE disc. I do this by coupling the launching of a radiatively driven outflow to the amplitude of the disc's bolometric luminosity in Eddington units. This differs from previous treatments (Metzger and Stone 2016) which link the launching of an outflow to the rate at which stellar debris returns to the pericentre of the disrupted star's orbit. By coupling the radiatively driven outflow to the properties of the disc luminosity (as opposed to a proxy for the disc luminosity) I am able to quantitatively predict exactly which TDEs will be observationally affected by outflows suppressing their X-ray luminosity.

In addition, I examine whether there are any characteristic observable predictions that can be tied to this luminosity-coupled launching of outflows. In particular, I demonstrate that those discs which have bolometric luminosities equal to their Eddington luminosity will in fact have X-ray luminosities which take on a near black hole mass-independent value of order $L_X \sim 10^{43} - 10^{44}$ erg/s.

4.18 Disc Eddingtonization & Outflows

In this section I justify and then formally introduce the disc-outflow model for high-luminosity TDEs. I begin by outlining the evidence, obtained from X-ray spectral observations, which imply that no, or at most very few, TDE has yet been observed in a super-Eddington accretion state. I then recap arguments for why high-luminosity TDEs will likely produce a radiatively driven outflow. In the second half of this section I introduce the disc-outflow TDE model.

4.18.1 Observational justification

The strong system parameter dependence of the peak disc temperature in an out-of-equilibrium accretion disc leads to Eddington ratios with the following strong parameter dependence:

$$l \equiv \frac{L_{\rm bol,peak}}{L_{\rm edd}} \propto \frac{\alpha^{4/3} M_d^{5/3}}{M^{11/3}}. \tag{4.96}$$

Equation 4.96 demonstrates that the peak Eddington ratio of a time dependent accretion disc is an extremely sensitive function of the central black hole mass. For any given

disc mass and α parameter there will exist a limiting black hole mass (which I shall again denote $M_{\rm edd}$), where $L_{\rm bol,peak} = L_{\rm edd}$. It is then clear from equation 4.96 that all TDEs with identical disc parameters (M_d and α) around black holes with masses lower than this value would produce initially super-Eddington bolometric luminosities. As an important reference value $M_{\rm edd}$ may be determined numerically, and for a Schwarzschild black hole with disc mass $M_d = 0.5M_\odot$ and $\alpha = 0.1$, $M_{\rm edd} \simeq 5 \times 10^6 M_\odot$ (Figure 4.1).

If TDEs around black holes with masses $M < M_{\rm edd}$ did indeed form super-Eddington accretion flows at early times, then an abundance of low black hole mass TDEs with X-ray spectra similar to those observed in ultra-luminous X-ray sources (ULXs) would be observed. ULX spectra are characterised by a much higher comptonization optical depth ($\tau \sim 5 - 20$), compared to those seen in the X-ray binary (XRB) high-soft state ($\tau < 1$) (Gladstone et al. 2009). The XRB high-soft state is expected to be the spectral state most similar to TDE discs which form with Eddington ratios $0.01 \lesssim l \lesssim 1$.

However, there is as of yet no observational evidence for this super-Eddington 'ULX-like' accretion state in low black hole mass TDEs[9] (Jonker et al. 2020). On the contrary, early-time soft X-ray detections of TDE candidates generally find quasi-thermal spectra that are analogous to an XRBs high-luminosity, spectrally soft state (Komossa and Greiner 1999; Greiner et al. 2000), particularly in TDEs with good quality early time X-ray spectra (e.g. Saxton et al. 2012; Miller et al. 2015; Lin et al. 2015; Holoien et al. 2016a; Gezari et al. 2017; Wevers et al. 2019a; Jonker et al. 2020; Wen et al. 2020).

Taken at face value this is a rather surprising result. The not unreasonable set of disc parameters $M_d = 0.5M_\odot$, $\alpha = 0.1$ around a Schwarzschild black hole with mass $M = 2 \times 10^6 M_\odot$ would lead to an Eddington ratio at peak of[10] $l \simeq 30$ (or even higher for a rapidly spinning Kerr black hole). I suggest that this observational fact cannot be merely a coincidence of system parameters.

Rather, I suppose that these observations may be indicating a fundamental property of dynamical disc formation in the aftermath of a TDE. In this section I assume that X-ray TDEs with ULX-like spectra have not been observed because the amount of stellar debris that can form into an accretion disc at radii close to the central black hole, and are thus hot enough to produce thermal X-rays, is set dynamically by the Eddington limit.

[9] Although note that the jet in the jetted TDE Swift J1644 (Burrows et al. 2011) may have been launched by super-Eddington accretion.

[10] Formally, this assumes that the thin disc scaling relationship (equation 4.96) continues to hold in the super-Eddington regime. While these relationships may not hold precisely, the Eddington ratio of a source with these parameters will undoubtedly be $l \gg 1$.

There are a number of reasons to suspect that a large fraction of the stellar debris in a TDE may be unable to form into a disc when that disc is producing large bolometric luminosities. The matter within a TDE disc is gradually deposited, with debris returning to the pericentre of the disrupted star's orbit approximately according to $\dot{M}_{\rm fb} \sim t^{-5/3}$ (Rees 1988). This means that if disc luminosities reach large values at early times in the TDE evolution, a large fraction of the stellar debris will still not have yet returned to the disc. This remaining material is then susceptible to being expelled by the disc luminosities large radiation pressures. Moreover, much of the total returning matter is likely to be only tenuously gravitationally bound (Metzger and Stone 2016). In fact, it is known that not all of the debris mass forms into a disc: exponentially declining light curve components are observed across optical and UV bands at early times, prior to these light curves transitioning to a disc dominated state (van Velzen et al. 2019b; Chapter 3). I propose that the amount of matter that forms into a TDE accretion disc is set so that, at peak, $L_{\rm bol} \leq L_{\rm edd}$.

The physical mechanism by which this disc formation process is likely to be mediated is the launching of radiation driven outflows. Models of the effects of outflows on observed TDE properties already exist (e.g., Strubbe and Quataert 2009; Metzger and Stone 2016; Dai et al. 2018). However, the model described here differs in one important aspect: the launching of the radiative outflow will be linked to the disc's bolometric luminosity L, as opposed to the rate at which debris return to pericentre $\dot{M}_{\rm fb}$. In the following section I demonstrate that this coupling means that radiatively driven outflows will be dynamically and observationally important at systematically lower black hole mass scales when compared to the scales predicted by these previous works.

4.18.2 Analytical model

In this work I will assume that the amount of material which forms into a compact accretion disc near to the central black hole in the aftermath of a TDE is set so that the peak bolometric luminosity of the resulting accretion disc is equal to, or less than, the Eddington luminosity. I call this behaviour "disc Eddingtonization". The remainder of the stellar debris, if any, is assumed to be ejected from the accretion disc by a radiatively driven outflow.

I define $M_{\rm deb}$ as the amount of stellar material which remains gravitationally bound to the central black hole after disruption, and which could potentially form into a disc. I further define l_p as the peak Eddington ratio which would occur had *all* of $M_{\rm deb}$

formed into a disc (according to equation 4.96). With these definitions in place, it follows from equation 4.96 that if the surviving disc mass M_d is given by

$$M_d = \begin{cases} M_{\rm deb}, & l_p < 1, \\ \\ M_{\rm deb}\, l_p^{-3/5}, & l_p \geq 1, \end{cases} \tag{4.97}$$

then the peak Eddington ratio of a disc which forms with mass M_d is $l \leq 1$, with equality in the radiatively driven outflow regime. The remaining matter is assumed to be ejected as an outflow $M_{\rm out} = M_{\rm deb} - M_d$:

$$M_{\rm out} = M_{\rm deb} \left[1 - l_p^{-3/5}\right], \quad l_p \geq 1. \tag{4.98}$$

As the Eddington ratio is a function of black hole mass (equation 4.96), this can be equivalently written in terms of the ratio between the black hole mass M and the black hole mass at which all of the debris mass could form into a disc with Eddington ratio $l = 1$ ($M_{\rm edd}$),

$$M_{\rm out} = M_{\rm deb} \left[1 - \left(\frac{M}{M_{\rm edd}}\right)^{11/5}\right], \quad M \leq M_{\rm edd}. \tag{4.99}$$

The critical Eddington mass value $M_{\rm edd}$ is a function of disc parameters, with a scaling which can be found from equation 4.96, and an amplitude which can be determined numerically (Figure 4.1). The following result is approximately valid for a Schwarzschild black hole:

$$M_{\rm edd} \simeq 5 \times 10^6 M_\odot \left(\frac{M_d}{0.5 M_\odot}\right)^{5/11} \left(\frac{\alpha}{0.1}\right)^{4/11}. \tag{4.100}$$

The amplitude in this relationship remains a function of black hole spin, with higher black hole spins resulting in higher Eddington masses. The Schwarzschild value quoted above is a broadly representative figure of all systems.

An important implication of the surviving disc mass being determined dynamically by the Eddington limit is that the peak disc temperature in this regime now only depends on the black hole mass, in the following way

$$T_p \propto M^{-1/4}, \quad M \leq M_{\rm edd}. \tag{4.101}$$

This well known result can be verified by combining equations 4.43, 4.96 & 4.97. A change in parameter dependence of the peak temperature from an extremely sensitive

function of disc and black hole parameters (equation 4.43), to a weak dependence on only the black hole mass (equation 4.101), results in markedly different properties of the X-ray luminosity in the two regimes. The peak X-ray flux from a thermal TDE disc scales, to leading order, like

$$F_X \propto \left(\frac{M}{D}\right)^2 \left(\frac{k_B T_p}{E_l}\right)^A \exp\left(-\frac{E_l}{k_B T_p}\right), \tag{4.102}$$

where E_l is the lower energy of the X-ray telescopes band pass, D is the source-observer distance, and the index A depends on assumptions about the ISCO stress and observer orientation angle. For a face-on finite ISCO stress disc $A = 2$, whereas for a face-on vanishing ISCO stress disc $A = 3/2$. The different parameter dependences of the peak disc temperature filter through to extremely different X-ray flux dependences (here showing the result for a vanishing ISCO stress):

$$F_X \propto \begin{cases} M^{1/4} \exp\left(-C_1 M^{7/6}\right), & M > M_{\rm edd}, \\ \\ M^{13/8} \exp\left(-C_2 M^{1/4}\right), & M \leq M_{\rm edd}. \end{cases} \tag{4.103}$$

In this expression C_1 and C_2 are dimensional parameters which depend on the disc properties. These two expressions have qualitatively different properties. When sub-Eddington ($M > M_{\rm edd}$) the X-ray flux is given by the product of a polynomial which is a weak function of mass, and a negative exponential which is strongly mass dependent. However, when in the outflow regime ($M < M_{\rm edd}$), the X-ray flux is given by the product of a polynomial which is a strongly increasing function of mass, and an exponential which is only weakly mass dependent.

I shall demonstrate numerically that the dual effects of this growing power-law and weakly decaying exponential effectively cancel out, leading to near-constant (i.e., black hole mass independent) X-ray luminosities for TDEs in this regime.

4.19 Numerical results

In this section I examine the properties of the X-ray luminosity of TDE disc systems in the radiatively driven outflow regime. I assume that the amount of matter which forms into a compact accretion disc in the aftermath of a TDE is set such that the bolometric luminosity of the resulting disc is no brighter than the Eddington luminosity of the central black hole.

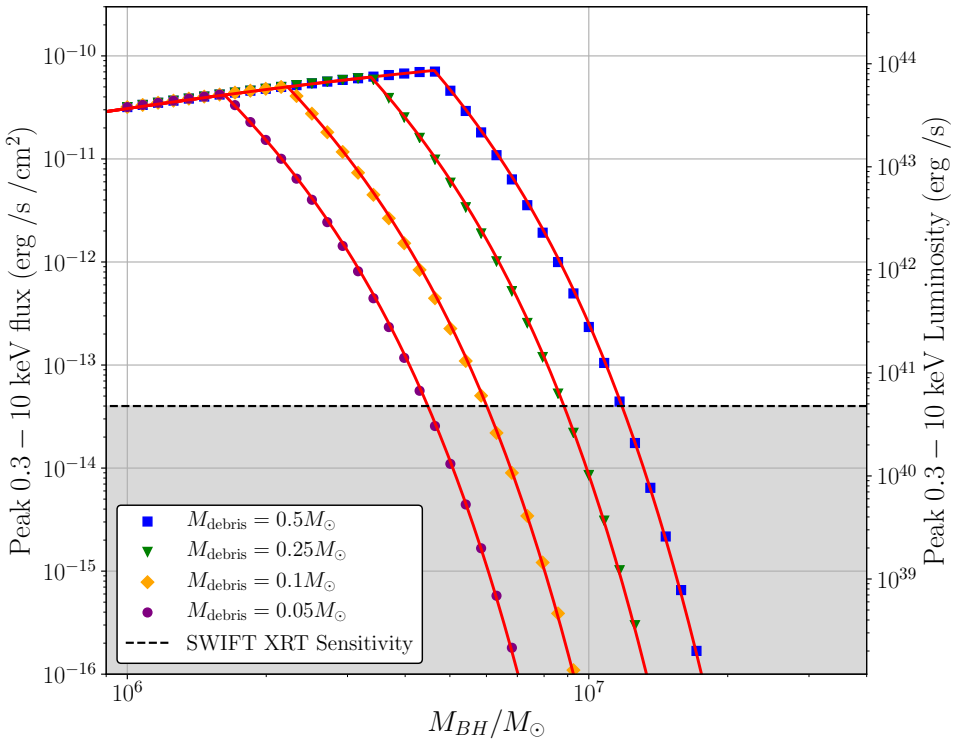

Figure 4.21: The peak 0.3–10 keV X-ray flux, as observed for a face-on disc orientation at 100Mpc, for discs evolving with $\alpha = 0.1$ and a number of different debris masses $M_{\rm deb}$ denoted on plot. The initial disc mass is equal to $M_{\rm deb}$ except for black hole masses where the bolometric luminosity is found to be super-Eddington. For these black holes the disc mass is reduced until the peak luminosity is equal to the Eddington luminosity. The solid curves are the analytical model of equation 4.37, with disc mass given by equation 4.97. The near constant X-ray luminosity in the $M < M_{\rm edd}$ regime is independent of the disc microphysics.

I shall examine the properties of the disc's X-ray luminosity for a wide range of both ISCO stress vales and disc-observer orientation angles, along with other disc parameters. In reality it is unlikely that TDE discs spanning the full range of both of these parameters will actually be observed. For example, at high luminosity values TDE accretion discs will likely have moderate aspect-ratios (becoming 'slim' discs), meaning that discs observed at large disc-observer orientation angles will have their inner-most regions obscured from view by their outer regions. This will act to suppress the observed X-ray emission from these sources. Furthermore, it may well be the case that high luminosity TDE discs do not span a large range of ISCO stress values. I examine the full range of parameter space for these parameters here so as to confirm that the maximum X-ray luminosity scale of TDE discs is robust to variations in all the system parameters.

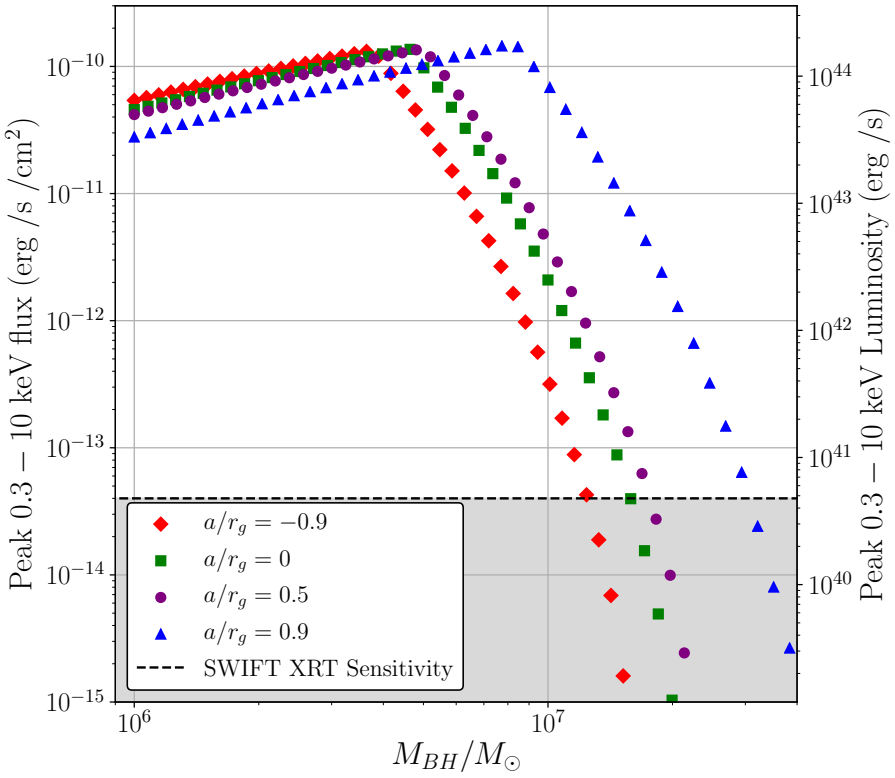

Figure 4.22: The peak 0.3–10 keV X-ray flux, as observed at 100Mpc, for discs evolving with $\alpha = 0.1$ and $M_{\rm deb} = 0.5 M_\odot$. The flux is computed as in Figure 4.21, but now with an inclination $\theta_{\rm obs} = 60^\circ$ and a number of different black hole spins, denoted on plot. This Figure was produced for discs with a finite ISCO stress. The upper X-ray luminosity scale is only weakly dependent on black hole spin.

To compute the evolving X-ray luminosity of the TDE disc system I numerically solve the general relativistic thin disc evolution equation (Chapter 3 equation 3.2), assuming an α model of the disc turbulence (see section 4.4 for full details). The disc is initially parameterised by a debris mass $M_{\rm deb}$, and α-parameter α. I compute the evolving bolometric and X-ray light curves of the resulting disc system. If for a given debris mass $M_{\rm deb}$ and black hole mass M the disc's bolometric luminosity exceeds the black hole's Eddington luminosity, the initial disc mass is reduced until the peak of the bolometric light curve equals the Eddington luminosity. For that new disc mass the peak X-ray flux (as observed at a distance of $D = 100$ Mpc) is computed. This method includes the temperature-dependent colour-correction factor $f_{\rm col}(T)$ of Done et al. (2012) (equations 4.73–4.75), and a fully general relativistic ray-tracing calculation (Appendix C).

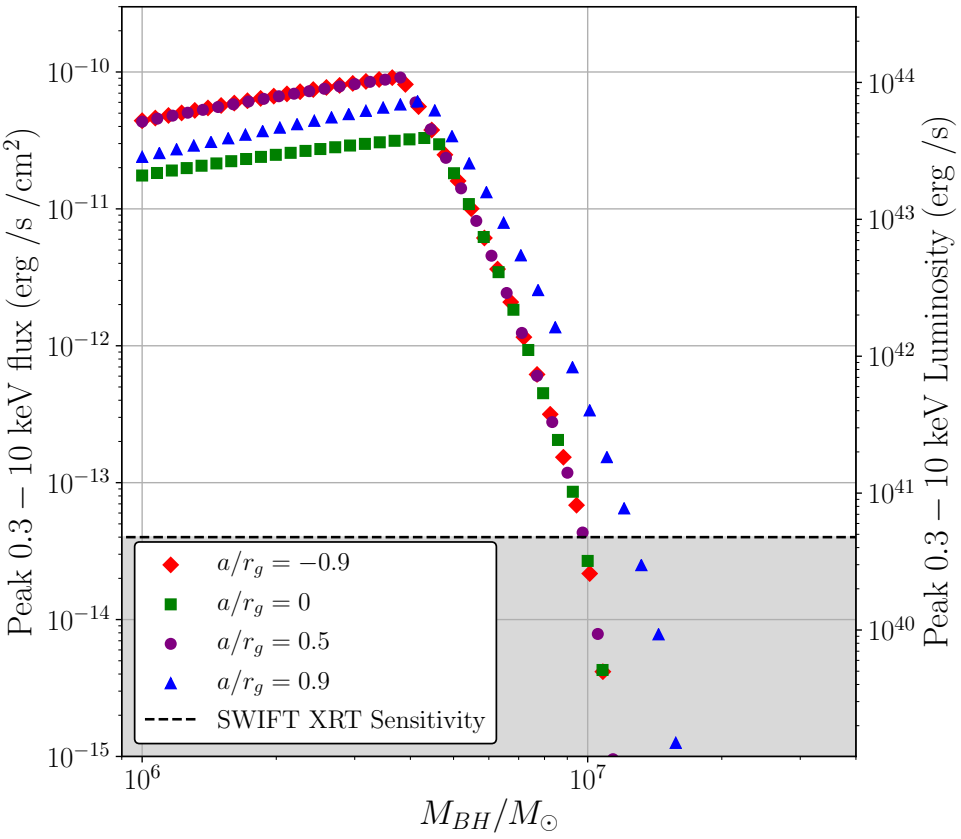

Figure 4.23: The peak 0.3–10 keV X-ray flux, as observed at 100Mpc, for discs evolving with $\alpha = 0.1$ and $M_{\rm deb} = 0.5M_\odot$. The flux is computed as in Figure 4.22, except for the ISCO stress which is now assumed to vanish. The upper X-ray luminosity scale is only weakly dependent on assumptions about the ISCO stress.

The peak observed $0.3 - 10$ keV flux calculated as described above, assuming a face-on orientation, a Schwarzschild black hole and a number of different initial debris masses, is displayed in Figure 4.21. The red solid curves are the analytical model of equation 4.37, with disc mass given by equation 4.97.

It is clear to see that the assumption of disc Eddingtonization leads to a maximum observed X-ray luminosity (which I shall denote L_M) of TDE disc systems. For the system parameters considered in Figure 4.21 this is of order $L_M \equiv 4\pi D^2 F_{X,\rm max} \simeq 5\times10^{43}$ erg/s. The X-ray luminosity scale is independent of the original disc parameters $M_{\rm deb}$ and α, as in this regime the peak disc temperature only depends on the black hole mass (equation 4.101), and the X-ray luminosity of TDE disc systems only depends on these disc parameters through the hottest temperature within the accretion disc (equation 4.102).

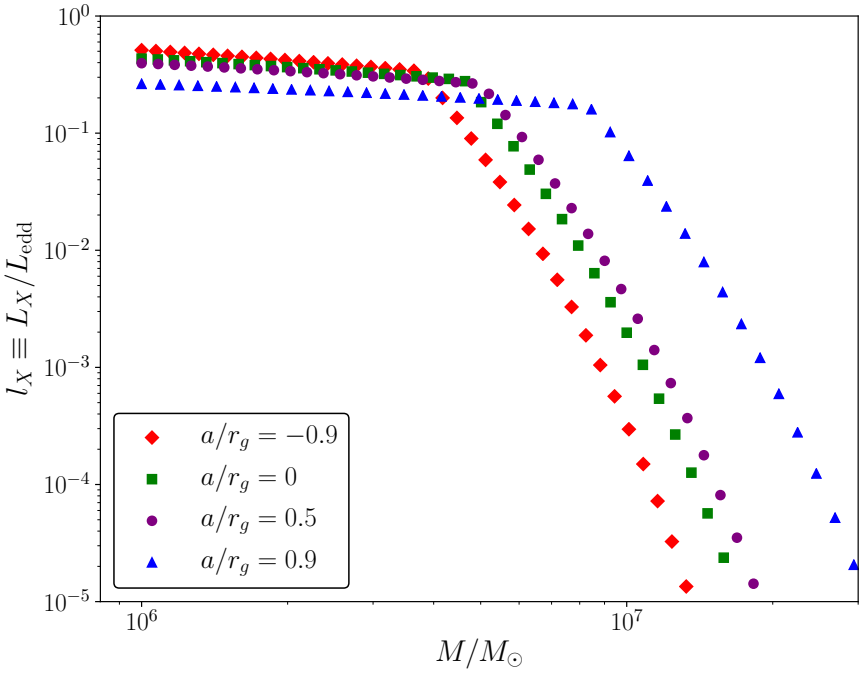

Figure 4.24: The peak observed X-ray Eddington ratios of the evolving disc solutions from Figure 4.22. Disc models of TDE X-ray evolution predict X-ray Eddington ratios at most $L_X/L_{\rm Edd} \sim$ few $\times 10^{-1}$, but which can vary by many orders of magnitude over a small range of black hole masses.

This X-ray luminosity scale is only weakly dependent on black hole spin (Figure 4.22), assumptions about the ISCO stress (Figure 4.23), and orientation angle. The peak X-ray luminosity varies from $L_M \sim 10^{43} - 10^{44}$ erg/s depending on the particular spin, ISCO stress and orientation angle chosen. I therefore expect to observe the imprint of this X-ray luminosity scale on the observed X-ray TDE population. If X-ray bright TDE discs typically form with Eddington ratios close to unity, then the majority of thermal X-ray TDEs should have peak luminosities of order $\sim 10^{43} - 10^{44}$ erg/s. The observational evidence for this behaviour will be explored further in section 4.22.

An X-ray luminosity upper limit means that observed X-ray Eddington ratios $l_X \equiv L_{X,\rm max}/L_{\rm edd}$ are always smaller than unity. Furthermore, the strong suppression of thermal X-ray emission for black hole masses $M > M_{\rm edd}$ can lead to potentially large ranges of observed l_X over small black hole mass ranges (Figure 4.24). This has been observed by Wevers (2020), who found X-ray Eddington ratios spanning 4 orders of magnitude in a small sample of 7 X-ray TDEs.

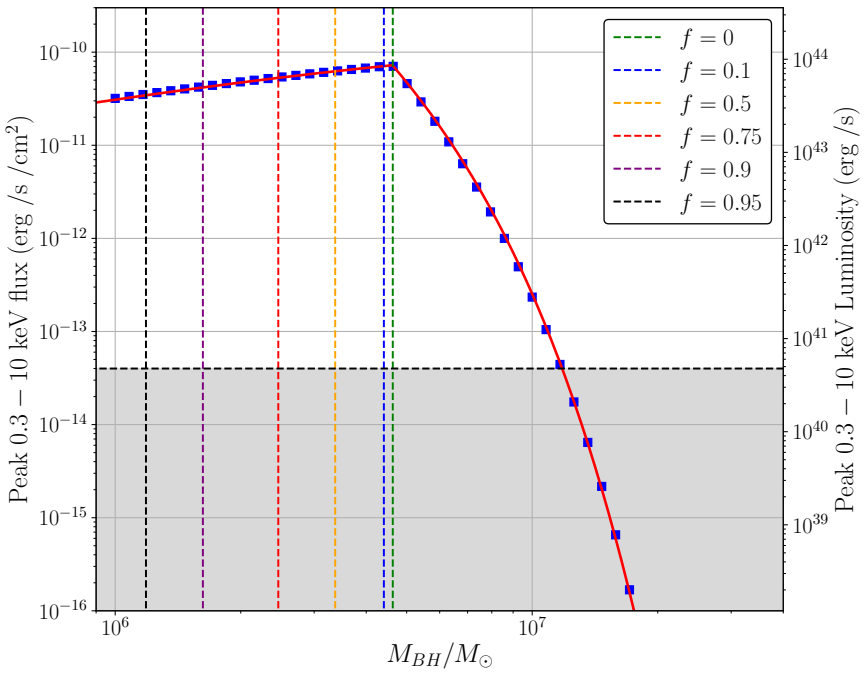

Figure 4.25: The peak observed $0.3 - 10$ keV flux, calculated as in Figure 4.21, for debris mass $M_{\rm deb} = 0.5 M_\odot$ and $\alpha = 0.1$. Over plotted as vertical dashed lines are the fraction f of the initial debris mass which has been expelled from the disc system. At low black hole masses ($M \simeq 10^6 M_\odot$) the vast majority $f > 0.95$ of the initial disc mass has been expelled. This material will likely obscure the X-ray emitting disc region from observations.

4.20 X-ray obscuration due to large mass outflows from low black hole mass TDEs

In addition to predicting an upper observed X-ray luminosity scale in disc-dominated TDEs, this TDE disc-ouflow model makes a second prediction: that large amounts of the stellar debris will be expelled from TDEs around low-mass ($M \lesssim 10^6 M_\odot$) black holes. Explicitly, the outflow mass is given by

$$M_{\rm out} = M_{\rm deb}\left[1 - \left(\frac{M}{M_{\rm edd}}\right)^{11/5}\right], \quad M \leq M_{\rm edd}, \tag{4.104}$$

meaning that the expelled mass very quickly becomes comparable to the surviving disc mass:

$$M_{\rm out} = M_d = 0.5 M_{\rm deb} \quad \text{for} \quad M = 0.73 M_{\rm edd}. \tag{4.105}$$

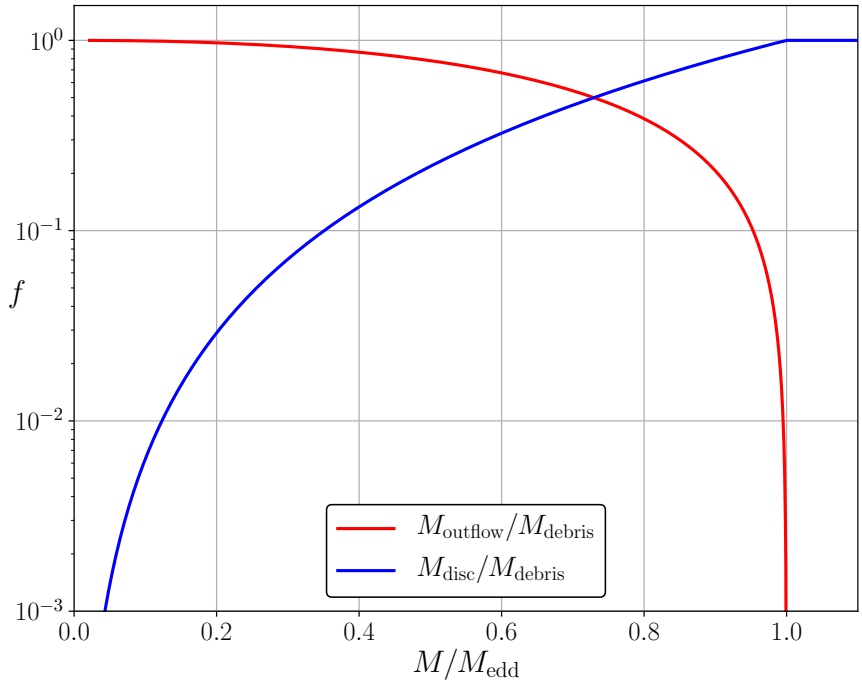

Figure 4.26: The fraction of the initial debris matter which is expelled from the system (red curve), and which forms into a disc (blue curve) as a function of the black hole mass in units of $M_{\rm edd}$, the black hole mass at which all of the debris mass can form into a disc with Eddington ratio $l = 1$.

In Figure 4.25 I denote by vertical dashed lines the fraction f of the initial debris mass expelled from the TDE system for the parameters used in Figure 4.21: a TDE system with an initial debris mass $M_{\rm deb} = 0.5M_\odot$ and $\alpha = 0.1$, around Schwarzschild black holes of varying masses. TDEs around black holes with masses much smaller than $M_{\rm edd}$ result in only a tiny fraction of the debris mass forming into an Eddington-limited disc. As an explicit example, the disc parameters $M_{\rm deb} = 0.5M_\odot$, $\alpha = 0.1$ around a Schwarzschild black hole of mass $M = 10^6 M_\odot$ lead to an outflow mass $M_{\rm out} = 0.484M_\odot = 0.968M_{\rm deb}$. The surviving and expelled mass fractions, as a function of black hole mass are explicitly displayed in in Figure 4.26.

It is likely that for low black hole masses this large outflow of material will obscure the innermost X-ray producing regions of the accretion disc. Metzger and Stone (2016) studied the observed properties of TDEs in the limit where the disc formation fraction $f_{\rm in} \equiv M_d/M_{\rm deb} \ll 1$. (Notation of Metzger and Stone 2016.) This corresponds to the $M \ll M_{\rm edd}$ limit of the TDE outflow model. Metzger and Stone demonstrated that in this limit the ejected material will remain sufficiently neutral to block hard EUV

and X-ray radiation from the hot inner disc, which becomes trapped in a radiation-dominated nebula. Ionising radiation from this nebula then heats the inner edge of the ejecta to temperatures of $T \sim$ few $\times 10^4$ K, converting the emission to optical/near-UV wavelengths. At these frequencies the photons more readily escape the nebula due to the lower opacity (see Metzger and Stone 2016 for full details). Metzger and Stone linked the launching of the radiative outflow to the rate at which the disrupted stellar material returns to the pericentre of the star's orbit ($\dot{M}_{\rm fb}$), which can be formally 'super-Eddington' (i.e., the matter can return to pericentre at a larger rate than the formal Eddington accretion rate $\dot{M}_{\rm edd}$), even when the disc's bolometric luminosity is sub-Eddington. In this model I link the launching of the radiative outflow directly to the disc's bolometric luminosity L, which means this obscuring outflow is important (for typical disc parameters) for black hole masses $M \sim 10^6 M_{\odot}$, which is a smaller mass scale than the Metzger and Stone (2016) model predicts.

The disc Eddingtonization model therefore makes a clear prediction: TDEs around low-mass black holes $M \lesssim$ few $\times 10^6 M_{\odot}$ will launch such massive outflows that the inner X-ray producing region of the disc will be obscured from observation, and these TDEs will be only observed at optical and UV frequencies. This prediction can be simply tested by inferring the black hole masses of different types of TDEs from galactic scaling relationships (e.g. Wevers et al. 2019b).

In Figure 4.27 I compare the inferred black hole masses of thermal X-ray TDEs (blue points & curve, taken from Table 4.2), non-thermal X-ray TDEs (red points & curve, taken from Table 4.3), and optical/UV-only TDEs (green points & curve, data in Table H.3, Appendix H). Unlike the X-ray bright TDEs, the optical/UV bright TDE population have been consistently followed and velocity dispersion (σ) measurements have been taken for a comprehensive sample (Wevers et al. 2019b, their table A1). As such, I am not required to include $M_{\rm bulge}$ and L_V measurements for these sources, as (unlike for X-ray bright TDEs) a comprehensive sample already exists. Indeed, while all of these optical TDEs have published σ measurements, they do not all have published measurements of either $M_{\rm bulge}$ or $L_{\rm bulge}$. I include 13 of the 15 optical TDEs catalogued by Wevers *et al.*, but do not include ASASSN-14li and ASASSN-15oi as they were also observed at X-ray energies at early times. I calculate the black hole masses of the optical/UV TDEs from the $M - \sigma$ relationship of McConnell and Ma (2013). The inferred distributions (solid curves) are calculated using kernel density estimation with a kernel width equal to the uncertainty in each TDE's black hole mass.

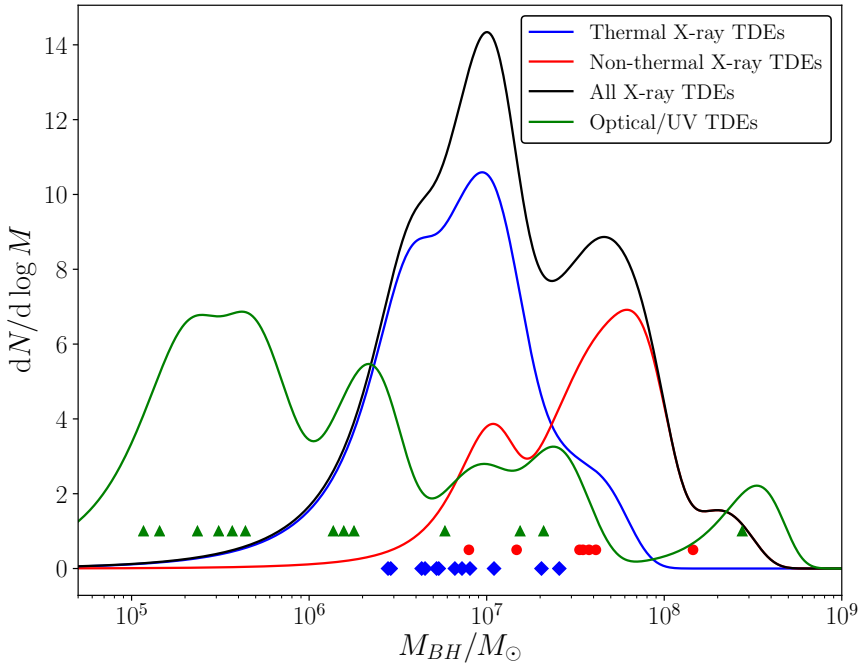

Figure 4.27: The black hole masses of thermal X-ray TDEs (blue points & curve, Table 4.2), non-thermal X-ray TDEs (red points & curve, Table 4.3) and optical/UV-only TDEs (green points & curve, Wevers et al. 2019b, their table A1). The inferred distributions (solid curves) are calculated using kernel density estimation using a kernel width equal to the uncertainty in each TDE's black hole mass. The population of optical/UV-only TDEs fit exactly as predicted by the disc Eddingtonization model. All TDEs with inferred masses $M < 2 \times 10^6 M_\odot$ are only observed in optical and UV bands (corresponding to the 9 TDEs with the lowest inferred masses). The larger mass $M \sim 10^7 M_\odot$ optical/UV-only TDEs likely lack X-ray radiation due to the suppression of X-ray emission from large mass black holes.

It is clear from Figure 4.27 that the population of optical/UV-only TDEs fit exactly as predicted by this Eddingtonization model. All TDEs with inferred masses $M < 2 \times 10^6 M_\odot$ were only observed in optical and UV bands (corresponding to the 9 TDEs with the lowest inferred masses). The larger mass $M \sim 10^7 M_\odot$ optical/UV-only TDEs likely lack X-ray radiation due to the suppression of X-ray emission from the cool discs of large black hole mass TDEs (as discussed in this Chapter). The extremely massive outlier is ASASSN-15lh (Chapter 3). Finally, I note that the $M-\sigma$ relationship of McConnell and Ma (2013) is not well calibrated for masses $M < 10^6 M_\odot$, and so while the lowest mass TDE hosts in Figure 4.27 certainly have small black hole masses, the exact values inferred from the scaling relationship should be treated as having a larger than normal uncertainty associated with them.

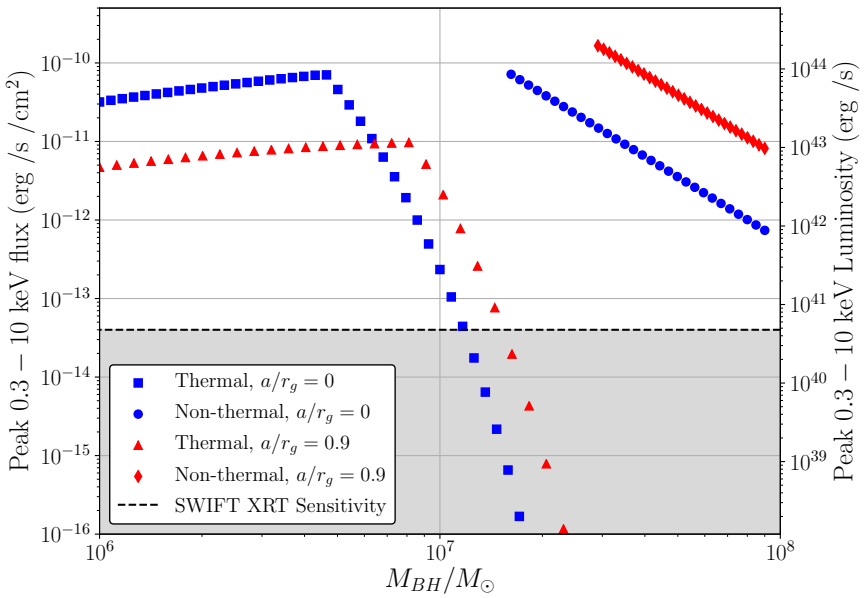

Figure 4.28: The peak observed $0.3 - 10$ keV flux, as observed from face-on accretion discs at a distance $D = 100$ Mpc, for black hole masses between 10^6 & $10^8 M_\odot$. Blue points are for a Schwarzschild black hole, and red points are for a more rapidly rotating Kerr black hole ($a/r_g = 0.9$). In the thermal emission regime the fluxes are calculated as in Figure 4.21. For sufficiently large black hole masses (when the disc's Eddington ratio is less than 10^{-2}) non-thermal X-ray emission is calculated by the model of equation 4.78, assuming all photons in the inner disc regions ($r < 12r_g$) are Compton scattered ($f_{SC} = 1$) with a photon index $\Gamma = 2$. Despite having entirely different emission mechanisms the maximum X-ray luminosities in the two regimes are comparable.

4.21 Maximum X-ray luminosity of hard state X-ray TDEs

As mentioned in the preceding sections, it is not just thermal emission which can result in a bright X-ray emission being observed from a TDE source, hard state emission may also result from the Compton up-scattering of thermal disc photons by an electron scattering corona. Using the model of nonthermal TDE X-ray emission developed in this Chapter it is possible to compute a similar upper X-ray luminosity limit for hard-state X-ray TDEs.

The brightest hard X-ray sources will result from coronae which scatter all of the soft disc photons ($f_{SC} \to 1$). While this limit is somewhat unphysical, it allows us to determine an upper luminosity scale for hard X-ray TDE sources, in addition to thermal TDEs (Figures 4.22, 4.23).

In Figure 4.28 I numerically calculate the thermal and non-thermal emission from TDE systems with either a Schwarzschild or a more rapidly rotating ($a/r_g = 0.9$) Kerr black hole. These events had a debris mass $M_{\rm deb} = 0.5 M_{\odot}$, an α-parameter $\alpha = 0.1$, and were observed face-on at a distance of $D = 100$ Mpc. If the bolometric luminosity of the resulting disc is greater than the Eddington luminosity, the disc mass is reduced according to equation 4.97. Conversely, if the Eddington ratio is lower than $l = 0.01$ emission from the compact corona was modelled with equation 4.78, with $f_{SC} = 1$, $\Gamma = 2.0$ and $R_{\rm Cor} = 12 r_g$.

A very interesting result highlighted by Figure 4.28 is that the upper X-ray luminosity scale of TDE disc systems in the non-thermal state is very similar to the maximum X-ray luminosity scale in the thermal state (Figures 4.22, 4.23). This is despite the two regimes involving very different physical emission models. These results therefore suggest that, irrespective of black hole mass and accretion state, TDEs observed at X-ray energies will always be observed at luminosity scales less than the maximum luminosity derived here

$$L_{X,\rm peak} < L_M \simeq 10^{44} \text{ erg/s}. \tag{4.106}$$

The hard state X-ray luminosity is not particularly sensitive to the underlying disc properties, scaling only as power-laws of the fundamental system parameters (equation 4.89)

$$L_X \propto f_{SC} M^2 T_p^{\Gamma+2} \propto f_{SC} L_{\rm bol} T_p^{\Gamma-2}, \tag{4.107}$$

and therefore, as is the case for thermal Eddington-limited emission, the amplitude of the hard state peak luminosities of X-ray TDEs is likely to be only weakly black hole mass dependent.

It is worth bearing in mind that the model of the disc-corona geometry and evolution presented in this Chapter do not represent the only possible description of a TDE disc in a hard accretion state. As I remarked earlier in this Chapter, the geometry, size, and precise location of the corona are still topics of significant debate. It is unlikely that this same hard state upper X-ray luminosity limit would be reproduced by all possible models of hard state TDEs, and therefore there is some additional theoretical uncertainty in this result. However, as I shall now demonstrate, the existing population of hard state TDEs do appear to be in good accord with this analysis.

4.22 X-ray TDE population analysis

To date the author is aware of 24 TDEs which have been well observed at X-ray energies at times near to the peak of the tidal disruption flare (in this section I shall not include jetted TDEs). Within this sample of TDEs there is a (potentially) surprising variety in the observed properties of individual TDE X-ray light curves. I argue here that, despite the apparent variety in observed properties, the historic population of X-ray TDEs do in fact have a unifying property: the amplitude of the peaks of their X-ray light curves correspond to the limiting luminosities derived in this Chapter.

The X-ray light curves of well observed TDE flares can be loosely split into 3 different types: 'well behaved' light curves which smoothly decay with time; flaring TDEs which show order of magnitude fluctuations over timescales as short as days to weeks; and late time re-brightening TDEs, who's X-ray luminosity grows by orders of magnitude hundreds of days after the initial flare. Some example light curves of each type are shown below. The fact that individual TDE light curves show such varied behaviour, except for the amplitude of their peak X-ray luminosities, suggests that the X-ray luminosity limit derived in this Chapter is a universal feature of these events.

4.22.1 'Well behaved' X-ray TDEs

'Well-behaved' TDEs are those which have been observed to quickly form X-ray bright accretion discs in the aftermath of the stellar disruption, which then monotonically fade with time. Perhaps the most well known example is ASASSN-14li, which underwent an X-ray flare of peak magnitude $L_X \simeq 2 \times 10^{43}$ erg/s, before fading over the next 1000 days (Holoien et al. 2016a; Bright et al. 2018; Chapter 3). The first 150 days of ASASSN-14li's X-ray light curve are shown as blue dots in Figure 4.29. A more recently discovered 'well-behaved' X-ray TDE is AT2019dsg (van Velzen et al. 2021, green squares). AT2019dsg had a peak X-ray luminosity of $L_X \simeq 3 \times 10^{43}$ erg/s, before rapidly dimming and becoming unobservable within 60 days of the first observation. The blue band in Figure 4.29 corresponds to the typical X-ray luminosity scale (a function of black hole spin) derived in this Chapter.

The very different evolutionary time scales of these two TDEs likely means that either some aspect of the disc microphysics (i.e., the α parameter or disc mass), or the black hole mass of the two sources are very different. However, both sources have peak X-ray luminosities exactly in line with the theoretical calculations presented in this Chapter.

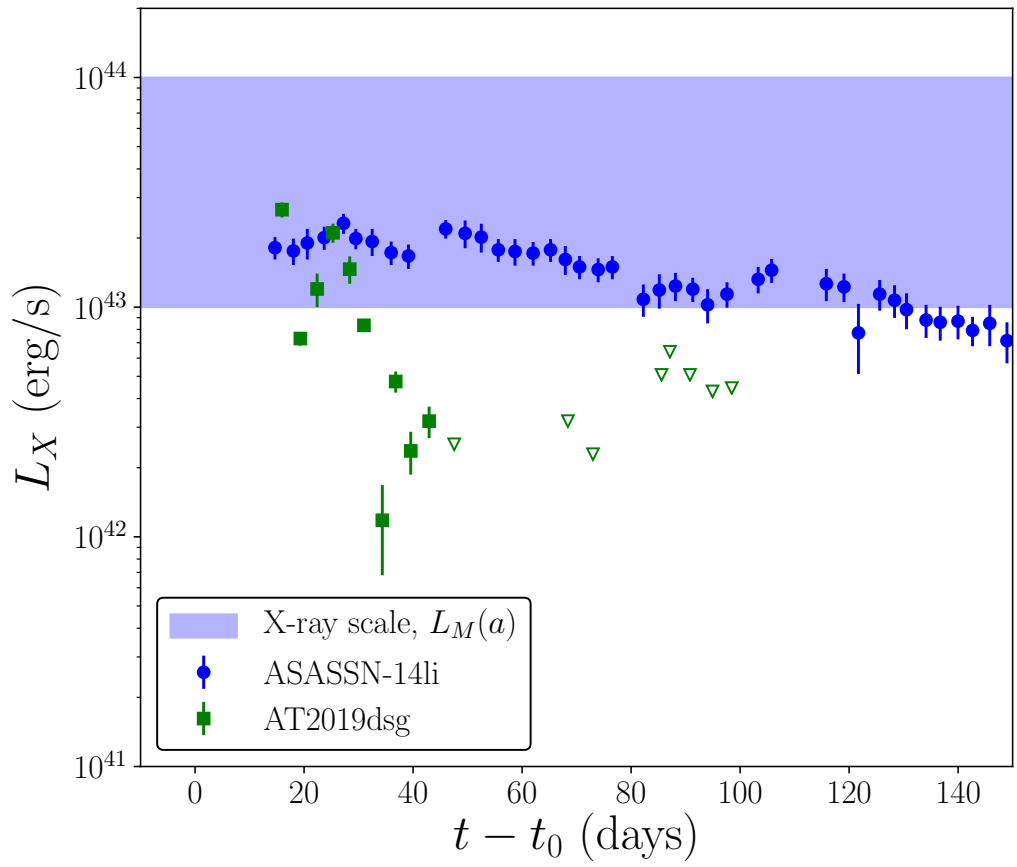

Figure 4.29: The observed light curves of two 'well-behaved' X-ray TDEs ASASSN-14li and AT2019dsg. The blue shaded region corresponds to the characteristic luminosity scale, a function of black hole spin, derived in this Chapter. Despite having very different decay timescales, both TDEs peak in the anticipated luminosity region. Upper detection limits of AT2019dsg are displayed by inverted triangles.

4.22.2 Flaring TDEs

Some X-ray TDEs show extreme X-ray variability on timescales as short as days to weeks. Three example of such events are shown in Figure 4.30, where I plot the observed X-ray light curves of AT2018fyk (Wevers et al. 2019a, blue triangles), ASASSN-18jd (Neustadt et al. 2020, red dots) and AT2019ehz (van Velzen et al. 2021, green squares) and the theoretical X-ray limiting region (blue shaded region). All three light curves, despite their extremely complex temporal behaviour, peak in the same limiting luminosity range.

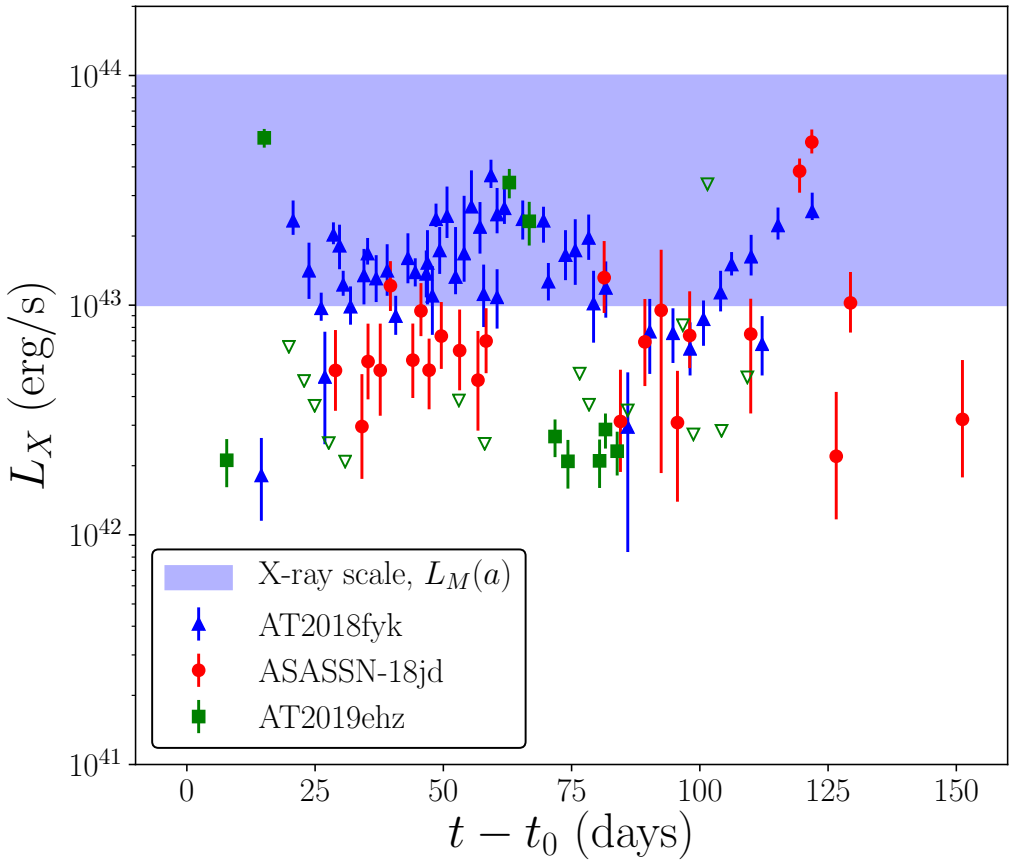

Figure 4.30: The observed light curves of three X-ray TDEs (AT2018fyk, ASASSN-18jd and AT2019ehz) which display extreme short timescale variability. The blue shaded region corresponds to the characteristic luminosity scale, a function of black hole spin, derived in this Chapter. Despite having extremely complex temporal properties, all three TDEs peak in the anticipated luminosity region. Upper detection limits of AT2019ehz are displayed by inverted triangles.

The ultimate cause of the large amplitude fluctuations in the X-ray luminosity are not at present clear: they could result from intrinsic variations in accretion rate, or by the fallback of matter scattered onto large radius orbits in the initial disruption onto the disc, or even time varying obscuration of the inner disc by other TDE debris. Irrespective of cause, the magnitude of the fluctuations are limited to the same luminosity scale as the more stably evolving discs which produce the light curves of 'well behaved' TDEs like ASASSN-14li.

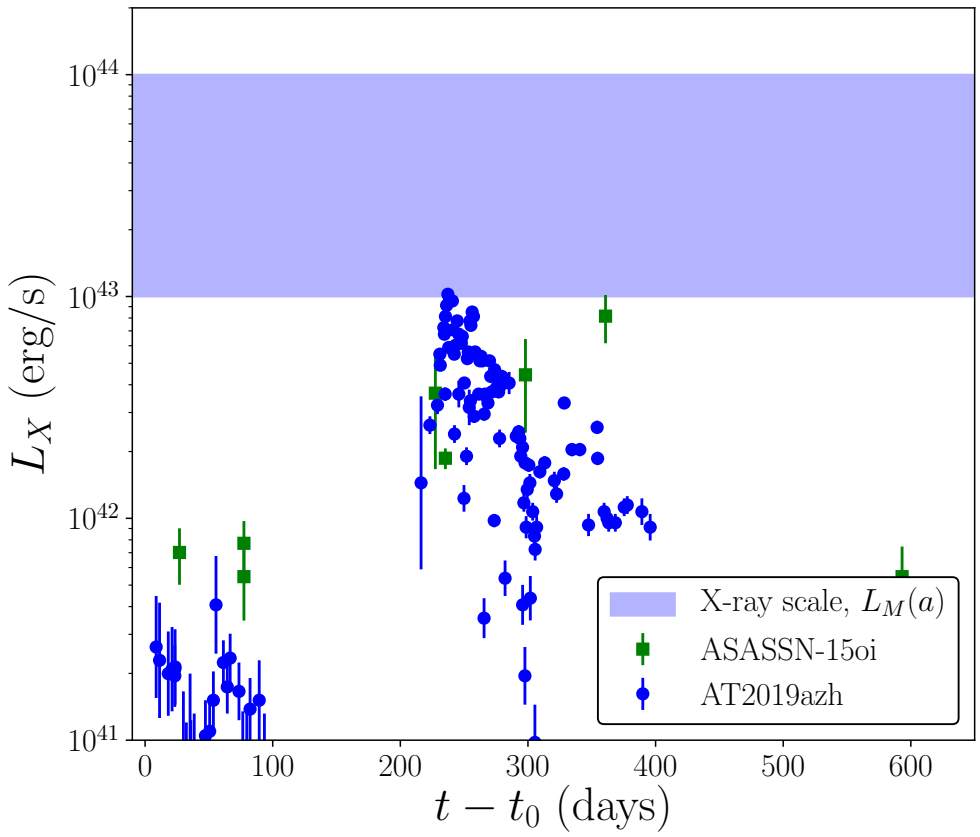

Figure 4.31: The observed light curves of two X-ray TDEs (ASASSN-15oi and AT2019azh) which re-brighten by an order of magnitude at late times. The blue shaded region corresponds to the characteristic luminosity scale, a function of black hole spin, derived in this Chapter. Although initially X-ray dim, after re-brightening these TDEs peak with luminosities at the characteristic luminosity scale.

4.22.3 Late time re-brightening TDEs

Finally, other X-ray TDEs have been observed which appear to be X-ray dim at early times, but then undergo a re-brightening by as much as two orders of magnitude at much later times. Examples of this type of X-ray TDE are ASASSN-15oi (Holoien et al. 2018) and AT2019azh (van Velzen et al. 2021, Hinkle et al. 2021), their light curves are plotted in Figure 4.31.

The physics of disc formation in TDEs which are initially X-ray dim may be very different from that of the TDEs which are X-ray bright at early times. It is therefore encouraging that when they do eventually re-brighten, the peak luminosities are again consistent with those expected of Eddington limited accretion discs.

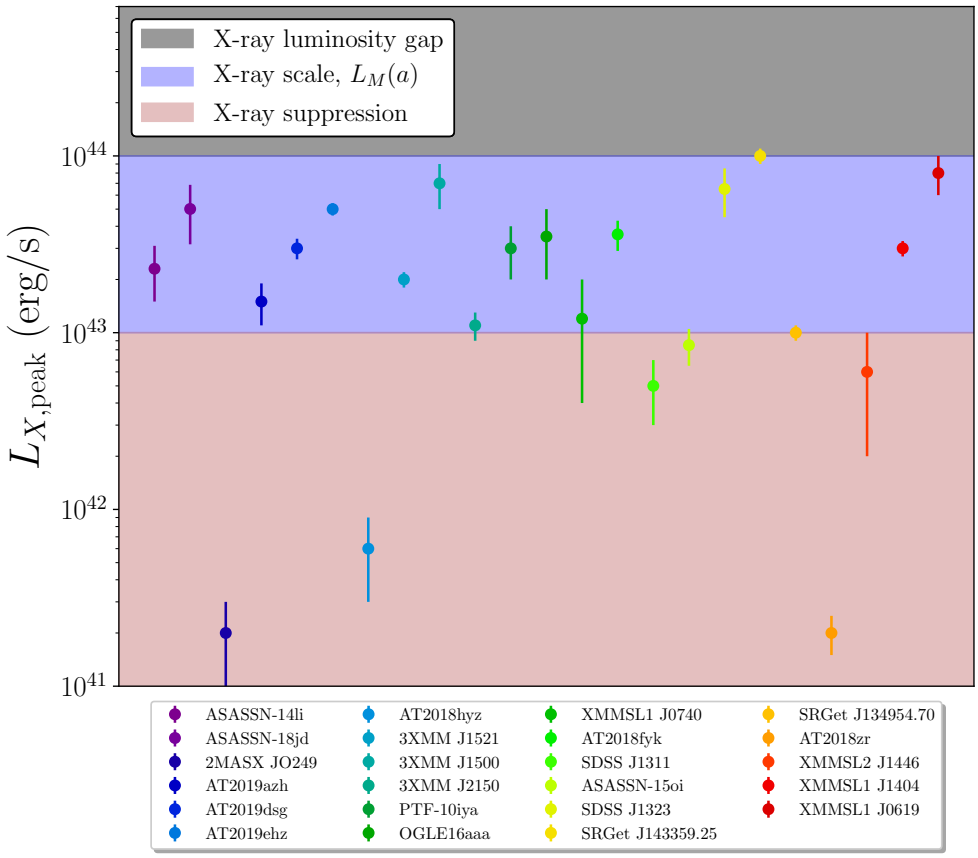

Figure 4.32: The peak observed X-ray (0.3–10 keV) luminosities of the historic TDE population (data in Table 4.4). 20 of the 24 disc-dominated X-ray TDEs lie at the black hole spin-dependent characteristic luminosity scale derived in this Chapter. No disc dominated TDEs have yet been observed in the predicted barren region of the X-ray TDE luminosity diagram, with $L_X > 10^{44}$ erg/s.

4.22.4 The total X-ray TDE population

In Figure 4.32 I plot the peak observed X-ray luminosities of the 24 disc-dominated X-ray TDEs observed to date. References and exact luminosity values can be found in Table 4.4. A final TDE NGC 247 peaked at $L_X = 2 \times 10^{39}$ erg/s and is not displayed for aesthetic reasons, but is included in Table 4.4.

The black-shaded region of the plot, defined by X-ray luminosities $L_X > 10^{44}$ erg/s is the anticipated 'barren region' of the observed TDE X-ray luminosity diagram. This region of X-ray luminosity parameter space is higher than the peak X-ray luminosities

TDE name	$L_{X,\mathrm{peak}}$ (erg/s)	Reference
ASASSN-14li	$2.3 \pm 0.8 \times 10^{43}$	Bright et al. 2018
ASASSN-15oi	$8.5 \pm 0.1 \times 10^{42}$	Holoien et al. 2018
ASASSN-18jd	$5.1 \pm 0.5 \times 10^{43}$	Neustadt et al. 2020
AT2018zr	$2 \pm 0.3 \times 10^{41}$	van Velzen et al. 2019a
AT2018fyk	$4 \pm 0.5 \times 10^{43}$	Wevers et al. 2019a
AT2018hyzj	$6 \pm 3 \times 10^{41}$	van Velzen et al. 2021
AT2019dsg	$3 \pm 0.1 \times 10^{43}$	van Velzen et al. 2021
AT2019ehz	$5 \pm 0.2 \times 10^{43}$	van Velzen et al. 2021
AT2019azh	$1.6 \pm 0.1 \times 10^{43}$	van Velzen et al. 2021
2MASX JO249	$3 \pm 0.5 \times 10^{41}$	Auchettl et al. 2017
3XMM J1521	$2.7 \pm 0.5 \times 10^{43}$	Auchettl et al. 2017
3XMM J1500	$7 \pm 0.7 \times 10^{43}$	Lin et al. 2017
3XMM J2150	$1.1 \pm 0.4 \times 10^{43}$	Lin et al. 2018
NGC 247	$2 \pm 0.1 \times 10^{39}$	Auchettl et al. 2017
OGLE16aaa	$2.2 \pm 0.4 \times 10^{43}$	Auchettl et al. 2017
PTF-10iya	$2.5 \pm 0.3 \times 10^{43}$	Auchettl et al. 2017
SDSS J1311	$7 \pm 2 \times 10^{42}$	Auchettl et al. 2017
SDSS J1323	$7 \pm 2 \times 10^{43}$	Esquej et al. 2008
XMMSL1 J0740	$1.2 \pm 1 \times 10^{43}$	Auchettl et al. 2017
XMMSL2 J1446	$6 \pm 4 \times 10^{42}$	Saxton et al. 2019
XMMSL1 J1404	$3 \pm 0.3 \times 10^{43}$	Wevers 2020
XMMSL1 J0619	$8 \pm 2 \times 10^{43}$	Saxton et al. 2014
SRGet J143359.25	1×10^{44}	Khabibullin et al. 2020b
SRGet J134954.70	1×10^{43}	Khabibullin et al. 2020a

Table 4.4: The peak observed X-ray luminosity of the 24 TDEs from the literature.

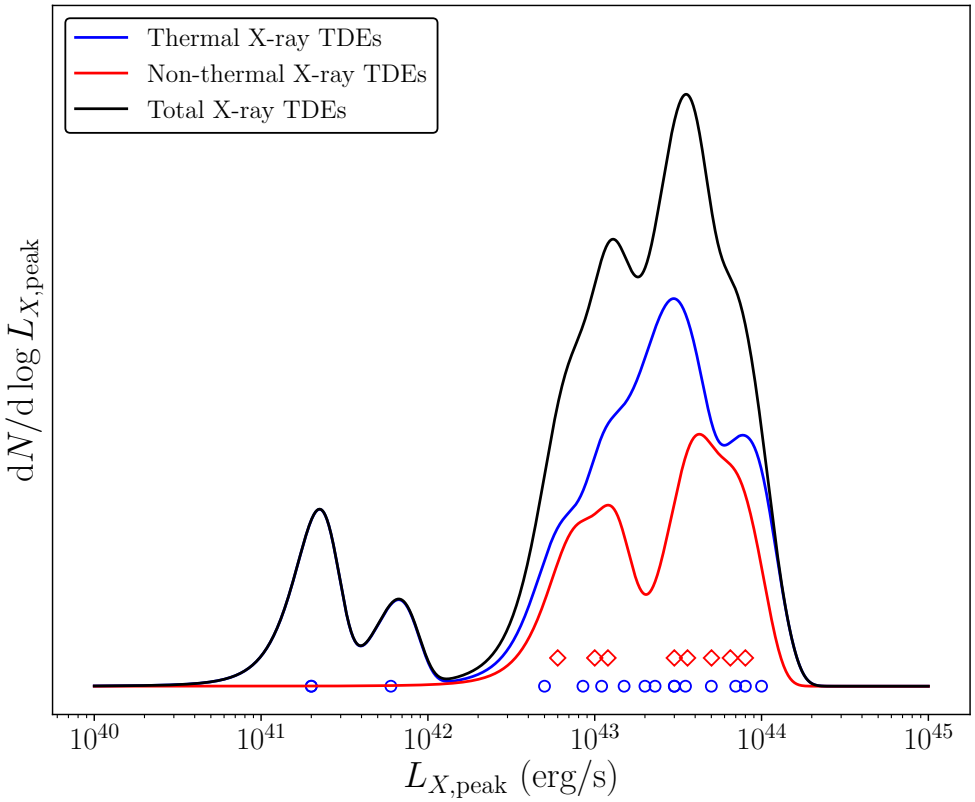

Figure 4.33: The peak observed X-ray (0.3–10 keV) luminosities of the historic TDE population (data in Table 4.4). 20 of the 24 disc-dominated X-ray TDEs lie in the black hole spin-dependent characteristic luminosity scale derived in this Chapter. No disc dominated TDEs have yet been observed in the predicted barren region of the X-ray TDE luminosity diagram, with $L_X > 10^{44}$ erg/s.

of both the thermal disc solutions in the Eddingtonization regime and the nonthermal Compton-scattered solutions (Figure 4.28), but is below the expected X-ray luminosity scale of jetted TDEs. Very few X-ray bright TDEs are therefore expected to be observed at this luminosity scale. Of the 24 TDEs detected to date not one has been observed at this luminosity scale.

The blue shaded region, $10^{43} < L_X(\mathrm{erg/s}) < 10^{44}$, corresponds to the theoretical X-ray luminosity scale, a function of black hole spin, derived in this Chapter (Figures 4.22, 4.23, 4.28). 20 of the 24 X-ray TDEs peak within this region, despite having light curves with otherwise widely varying properties. This is an extremely telling result. The inferred distribution of the X-ray luminosity of quasi-thermal (blue dots) & non-thermal (red diamonds) X-ray TDEs is displayed in Figure 4.33. The inferred

distributions (solid curves) are calculated using kernel density estimation with a kernel width equal to the uncertainty in each TDE's peak X-ray luminosity. X-ray TDEs of both spectral types peak at the same luminosity scale.

Finally, I can rule out the naive model that there exists some intrinsic relationship between the Eddington and X-ray luminosities of X-ray bright TDEs (i.e., that the X-ray luminosity is some fixed fraction of the Eddington luminosity). If the X-ray luminosity of TDEs were in some way related to the black hole's Eddington luminosity, then observed X-ray luminosity amplitudes should vary between TDEs around black holes of different masses:

$$L_{\rm edd} = 1 \times 10^{45} \left(\frac{M}{8 \times 10^6 M_{\odot}} \right) \text{ erg/s}. \tag{4.108}$$

In Figure 4.34 I plot the peak observed X-ray luminosity of the 19 X-ray TDEs which also have black hole mass estimates from galactic scaling relationships (Tables 4.2, 4.3), the black point in Figure 4.34 shows a typical uncertainty on the black hole masses resulting from intrinsic scatter in galactic scaling relationships. Different X-ray spectral types are denoted by blue diamonds (quasi-thermal emission) and red squares (non-thermal emission).

While the black hole masses of the different spectral types of X-ray TDEs are systematically different (as discussed in section 4.22), Figure 4.34 demonstrates that the peak X-ray luminosity of TDE sources is in fact effectively independent of black hole mass. This observation is strongly supportive of the disc models put forward in this chapter.

I believe that the strong agreement between the observed properties of the X-ray TDE population and the predictions of the TDE disc model (Figures 4.27, 4.33, 4.34) provide a deeper understanding of TDE evolution and compelling evidence for disc-dominated TDEs being the norm.

4.23 Discussion

In this section I have built upon and extended existing models of outflows launched from TDE discs at early times. In particular, in contrast with previous approaches, I have coupled the launching of a radiatively driven outflow directly to the bolometric luminosity of the TDE accretion disc (in Eddington units). A lack of observed TDEs in super-Eddington accretion states (e.g., Jonker et al. 2020) can be naturally explained if

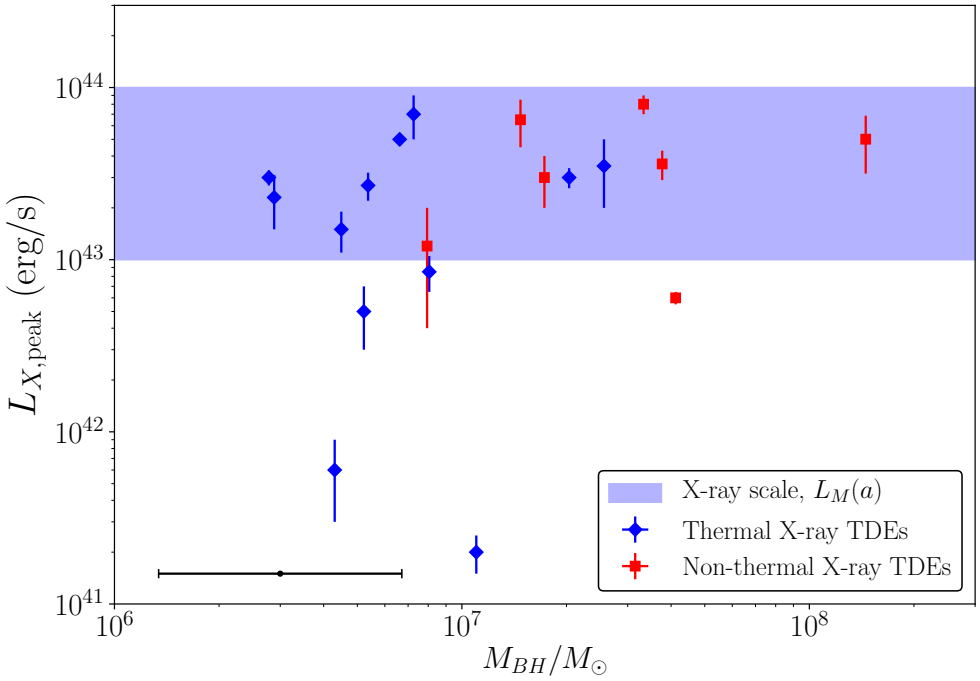

Figure 4.34: The peak observed X-ray luminosities of the 19 X-ray TDEs with black hole mass estimates from galactic scaling relationships (Tables 4.2 & 4.3). Different X-ray spectral types are denoted by blue diamonds (quasi-thermal emission) and red squares (non-thermal emission). The black point shows the typical uncertainty in the black hole masses resulting from intrinsic scatter in galactic scaling relationships. While there is a systematic difference in the black hole masses of the different X-ray spectral types, the peak X-ray luminosity is approximately independent of the central black hole mass.

TDE discs launch outflows at the earliest times in their evolution, thereby limiting the amount of the stellar debris which can form into an accretion disc in close proximity to the black hole. In this section I have assumed that the amount of material which can form into an accretion disc in the aftermath of a TDE is set such that the disc's resulting luminosity is limited by the black hole's Eddington luminosity.

This simple assumption about TDE disc formation leads to a number of quantitative and testable predictions about the properties of the populations of X-ray bright TDEs and optically bright X-ray dim TDEs. The main predictions are the following: firstly, there should exist a population of TDEs observed only at optical and UV frequencies which occur around black holes of the lowest masses $M \lesssim \mathrm{few} \times 10^6 M_\odot$. Physically this results from the strong inverse dependence of TDE disc Eddington ratio on central black hole mass (equation 4.96), meaning that TDEs around the lowest mass black holes will

result in extreme initial luminosities. The resulting large-mass outflow (Figure 4.26) will obscure the inner-most disc regions from observers, reprocessing the high energy inner disc emission to optical emission. The existing population of optical/UV-only TDEs fit exactly as predicted by this Eddingtonization model (Figure 4.27). All TDEs with inferred masses $M < 2 \times 10^6 M_\odot$ were only observed in optical and UV bands (corresponding to the 9 known TDEs with the lowest inferred masses).

The second key prediction concerns the properties of the observed amplitudes of the X-ray luminosity of the population of X-ray bright TDEs. I demonstrate analytically and numerically (equation 4.103, Figures 4.21, 4.22, 4.23) that the X-ray luminosity of TDE discs with bolometric luminosities comparable to their Eddington luminosity are approximately constant (i.e., independent of black hole mass) across the black hole mass range of interest for TDEs. The amplitude of this X-ray luminosity scale is $L_M \simeq 10^{43} - 10^{44}$ erg/s, where the primary variance results from the range of allowed black hole spins. A similar limiting X-ray luminosity exists for TDE discs evolving in harder accretion states, with additional nonthermal emission resulting from a Compton scattering corona (Figure 4.28), and so this limiting X-ray luminosity should be imprinted on the X-ray luminosity distribution of observed TDEs.

The properties of the existing population of TDEs are in excellent accord with this prediction (Figures 4.32, 4.33), with 20 of 24 TDEs having peak X-ray luminosities which lie exactly at the scale derived in this work. The remaining 4 TDEs all had peak X-ray luminosities lying below the limiting scale, meaning that no disc-dominated TDE has been observed with X-ray luminosity above this upper limit, despite the observed light curves of these 24 X-ray bright TDEs having otherwise widely varying temporal properties (Figures 4.29, 4.30, 4.31). TDEs with X-ray luminosity resulting from a powerful radio jet can comfortably exceed $L_M \sim 10^{44}$ erg/s, but normally by many orders of magnitude (Figure 4.35). An X-ray luminosity gap spanning roughly 3 order of magnitude $L_X \sim 10^{44} - 10^{47}$ erg/s, where no TDE X-ray light curves peak, is a natural prediction of the model put forward in this Chapter.

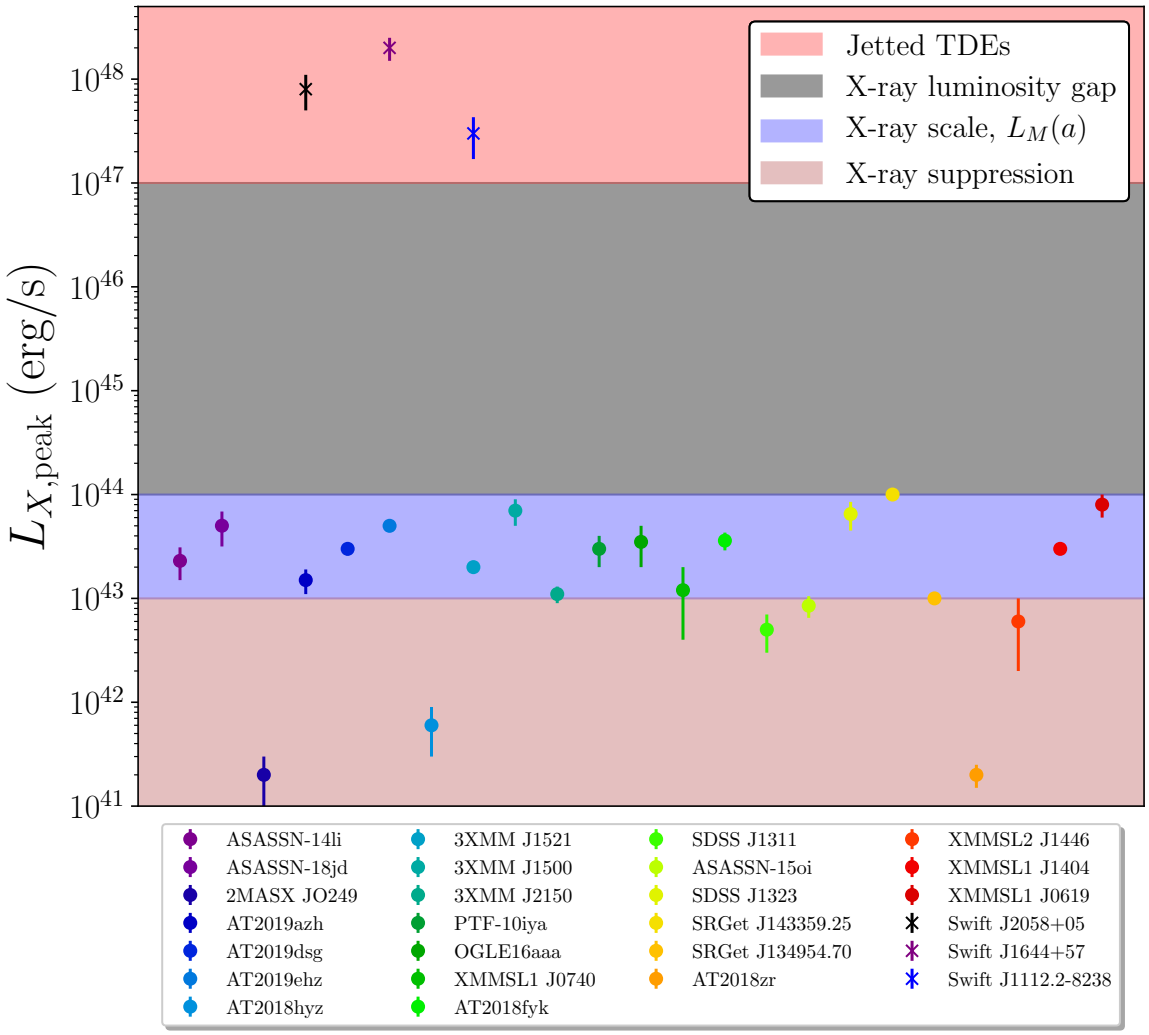

Figure 4.35: The peak observed X-ray (0.3–10 keV) luminosities of the historic TDE population, disc-dominated X-ray sources are denoted with dots (data in Table 4.4) and jetted TDEs are denoted with crosses. Also plotted are four shaded regions which denote the different luminosity scales derived in this Chapter. 20 of the 24 soft X-ray TDEs lie at the characteristic luminosity scale. No disc dominated TDEs have yet been observed in the predicted barren region of the X-ray TDE luminosity diagram, with $10^{47} > L_X > 10^{44}$ erg/s.

4.24 Conclusions

In this Chapter I have sought to model the properties of tidal disruption events, as observed at X-ray energies, across their entire physical parameter space. The X-ray bands represent a particularly interesting observing regime to target, as it probes the hottest, and therefore innermost, regions of the disc, precisely where the effects of general relativity are the most pronounced.

The analysis of the X-ray TDE population presented in this Chapter has involved a number of extensions of existing theoretical descriptions of the X-ray luminosity emergent from relativistic discs. In the first section of this Chapter I extended my analytical model of thermal emission from TDE discs, deriving closed form expressions for the observed X-ray luminosity of TDEs as a function of system parameters. By re-deriving classical α-disc scaling relationships in an out-of-equilibrium setting, I demonstrated that the thermal X-ray luminosity of TDE sources is strongly (exponentially) suppressed for TDEs around large mass black holes. This naturally leads to a maximum black hole mass at which thermal X-ray emission can be observed. This maximum mass, which may also be described fully analytically, depends on the remaining TDE system parameters, but is limited to lie below $M \sim 3 \times 10^7 M_\odot$ for nearly all TDE systems.

Not all observed TDE X-ray emission must have thermal origins however, and in the second part of this Chapter I developed the first evolutionarily self-consistent model of hard state emission resulting from the Compton up-scattering of thermal disc photons by a corona. This extension will allow the physical parameters of hard state X-ray TDEs to be extracted from detailed light curve modelling, analogous to the work presented in Chapter 3 (see two example sources in Mummery 2022). By making analogy with XRB discs, and assuming that the corona in these systems typically forms when the Eddington ratio of a TDE disc falls bellow $\sim 10^{-2}$, a characteristic black hole mass scale above which hard state TDEs will be observed is derived. For typical system parameters this mass scale lies at $M \sim 2 \times 10^7 M_\odot$, comparable to the mass scale at which thermal X-ray emission becomes unobservable. Thus, it is natural to expect these two sub-populations of TDEs to originate from distinct black hole mass distributions. In addition, I showed analytically a general property of nonthermal and thermal TDE X-ray light curves: thermal emission decays quicker than nonthermal emission. Explicitly, the leading

order late-time behaviour of the two distinct regimes are: $L_X \sim t^{-n/2}\exp(-At^{n/4})$ for thermal emission, and $L_X \sim t^{-(2+\Gamma)n/4}$ for nonthermal emission.

Finally, I examined TDE discs around the lowest mass supermassive black holes, these sources are likely to have the highest initial Eddington ratios. I extended existing models of TDE discs outflows by coupling the outflow-launching to the bolometric luminosity of the disc, rather than to the rate at which disrupted material returns to pericentre, as has previously been adopted by the community. I find that, to maintain a bolometric luminosity comparable to the Eddington luminosity, a TDE around a low mass $\sim 10^6 M_\odot$ black hole must eject a large fraction of its gravitationally bound debris in the earliest stages of disc formation. This large-mass outflow will then likely act to suppress the observed levels of X-ray luminosity, leading to the dual predictions of an upper X-ray luminosity scale of TDE discs, and a preference for optical-only detections for low-mass TDEs. The analytical work in this Chapter has been complimented by numerical solutions of the underlying disc equations (Chapter 2).

The predictions made in this Chapter can be broadly summarised as follows: the central black hole mass is the principle parameter responsible for determining the observed properties of a given TDE. In fact, the total TDE population can be split into four distinct sub-populations, separated in black hole mass space. In order of increasing black hole mass (decreasing Eddington ratio) these sub-populations are:

- A population of TDEs around black holes with the lowest masses ($M \lesssim 10^6 M_\odot$) which are observed at only optical and UV photon frequencies. This results from the inner-disc being obscured by a large mass radiatively driven outflow.

- The bright quasi-thermal X-ray TDE population to contain black holes with masses primarily between $M \sim 10^6 - 10^7 M_\odot$, with sources above $M_{\rm lim} \simeq 3\times 10^7 M_\odot$ being extremely rare.

- The existence of some optical and UV bright TDEs with black hole masses around $M \sim 10^7 M_\odot$, which are not observed at X-ray energies. These sources are insufficiently hot to produce observable levels of thermal X-ray radiation, a result of the strong dependence of the disc temperature on black hole mass.

- The bright nonthermal X-ray TDE population to contain blackholes with masses primarily in excess of $M \gtrsim 2\times 10^7 M_\odot$, with sources with masses below $M \lesssim 5\times 10^6 M_\odot$ being extremely rare.

As the black hole mass of a TDE can be estimated from galactic scaling relationships, these predictions are easily testable. In Figure 4.27 I demonstrate that the current population of TDE sources is in good agreement with this picture, with 3 distinct sub-populations clearly visible.

Furthermore, the precise X-ray luminosity distribution of the TDE population contains further information about the underlying disc physics. The model put forward in this Chapter demonstrates that

- The X-ray luminosity of quasi-thermal disc-dominated TDEs evolving with bolometric luminosities comparable to their Eddington luminosity will lie at a near universal scale $L_M(a) \sim 10^{43} - 10^{44}$ erg/s, with the variance primarily stemming from the range of allowed black hole spins.

- The nonthermal X-ray luminosity of disc-dominated hard state sources is also limited by a maximum X-ray luminosity scale $L_M(a) \sim 10^{43} - 10^{44}$ erg/s (although by completely different physics).

Which can be cast as two key observational predictions:

- The brightest quasi-thermal and nonthermal X-ray TDEs will both peak with X-ray luminosities in the range $L_X \sim 10^{43} - 10^{44}$ erg/s, meaning that the X-ray luminosity of the brightest TDEs will be independent of both black hole mass and X-ray spectral state.

- A lack of observations of disc-dominated TDEs with X-ray luminosities $L_X \gtrsim 10^{44}$ erg/s.

Again, these predictions can be tested against the observed distributions of the current TDE population. In Figures 4.33 and 4.34 I demonstrate that the properties of the current TDE population are in excellent accord with the models put forward in this Chapter.

Much of the analysis of this Chapter has, either explicitly or implicitly, assumed a connection in the properties of TDE and XRB discs. In other words, I have assumed that the properties of black hole discs are scale (mass) invariant, depending solely on the luminosity of the disc in Eddington units. As such, TDEs behave as large black hole mass analogous of XRBs. The success of many of the predictions of these models can therefore be seen as evidence in favour of this assumption, which opens up the

possibility of utilising this connection to further understand the growing populations of TDE sources. An increasing number of TDEs are detected at radio frequencies, an observational fact not thus far discussed in this thesis. The radio properties of XRB sources are strongly coupled to their disc's accretion state (Fender et al. 2004), and a natural extension of the work put forward in this Chapter would be to explore how the radio properties of TDE systems correlate with the central TDE black hole mass.

The forthcoming explosion in TDE data sets from wide field surveys like eRosita (which is expected to find $\sim$ 1000s of X-ray bright TDEs, Khabibullin et al. 2014) and LSST (which expects to find $\sim 10,000$s of TDEs at optical and UV frequencies, Bricman and Gomboc 2020), will further test the TDE-XRB connection put forward in this Chapter. Figures 4.27, 4.33 and 4.34 represent promising initial evidence for this framework, which will be rigorously tested in the coming years.

5

Towards the future of TDE and disc physics

The work in this chapter is based upon the following articles:
Mummery and Balbus, 2022, submitted.
Mummery et al., 2022, in prep.

The work in this thesis sought to answer the question posed in the introductory chapter: what if accretion in a tidal disruption event is mediated through disc like structures, rather than by direct fall-back onto the black hole? I would argue that the evidence for disc accretion dominating both the X-ray and late time optical/UV light curves of TDEs is now overwhelming. The properties of observed TDE light curves exhibit far richer behaviour than a simple $t^{-5/3}$ power-law, and the physics of relativistic accretion is central to understanding their varied properties.

In this thesis I have shown that the combined effects of TDE discs being *relativistic* systems, which are *time-dependent* and *observed over finite frequency widths*, are profound, resulting in multiple substantial modifications to the simple models used previously. In Chapter 2 I demonstrated that the global structure of relativistic discs are sensitively dependent on the properties of their very innermost regions. ISCO-stress dependent modifications to the disc structure can last for a substantial number of viscous timescales, before fading away. The detailed modelling of tidal disruption event light curves with the solutions of this relativistic theory provide both excellent fits to the data, and a deeper understanding of the physical properties of these events (Chapter 3).

A substantial refinement of previous disc treatments was introduced in Chapter 3, and extended in Chapter 4. The proper treatment of the finite frequency bandwidth over which observations are taken results in substantial modifications to the simple bolometric luminosity light curves often used in the literature. A simple power-law decay of the bolometric luminosity, when appropriately filtered by bandpass, is observed to be both near time-independent in the UV, and exponentially decaying at X-ray energies.

Finally, in Chapter 4, I demonstrated that the intrinsic time-dependence of TDE discs has profound effects on their properties as observed at X-ray energies. Rather than a simple equilibrium temperature scaling relationship $T \propto (\dot{m}/M)^{1/4}$, a time-dependent disc satisfies $T \propto M_d^{5/12}\alpha^{1/3}M^{-7/6}$, with a temperature far more sensitively dependent on the black hole mass. This sensitive dependence of the temperature on system parameters, coupled with the exponential dependence of the X-ray luminosity on temperature, results in diverse, quantitative predictions for the properties of a population of TDE sources. We are in the early days of population studies of TDEs, but the initial evidence suggests that these predictions are in good accord with the data.

In addition to seeking to answer a number of questions relating to accretion disc physics and tidal disruption events, this thesis has, I hope, highlighted a number of interesting avenues for further research. I highlight here the areas in which I believe the analysis in this thesis can be refined, or extended, and some initial progress in those directions.

5.1 The ISCO stress

The question of whether the stress of a relativistic accretion disc does or does not vanish at the ISCO has a history as long as the study of relativistic accretion discs. In a footnote of the original Page and Thorne (1974) paper on the theoretical study of relativistic discs in the steady state, the authors explicitly note: "*It is conceivable that the material might contain extremely strong magnetic fields, and that these fields might transport a torque from the infalling material at $r < r_I$, to the disc at at $r \geq r_I$. In this case the boundary condition at r_I should be modified.*" Page & Thorne went on to state "*It seems to us unlikely that the changes would be substantial, except near r_I*". The statement that the modifications to these solutions are likely to be local only to the ISCO is not particularly true in the steady-state (see e.g., Agol and Krolik 2000), but is certainly not true in time-dependent systems, as demonstrated in this thesis.

The majority of discussions regarding the properties of the ISCO stress have revolved around analysing the results of GRMHD simulations. Simulation groups invariably find a non-zero ISCO stress (e.g., Shafee et al. 2008; Penna et al. 2010; Noble et al. 2010), but the arguments about what these non-zero stresses mean, and whether they are physically important or not, remain. The finding of a non-zero stress has lead some groups to argue it is dynamically important (e.g., Noble et al. 2010), and others to argue it is not (e.g., Shafee et al. 2008). These arguments are primarily based on how much angular momentum these stresses are deemed capable of moving around.

In this thesis I have developed a number of observational predictions resulting from the presence of a finite ISCO stress, chiefly the reduced rate of luminosity decay in finite ISCO stress discs (Chapter 2). This slower luminosity decay was found to be a better fit, once filtered through the required observing bandpass, to the X-ray emission of ASASSN-14li (Chapter 3), showing that thorny theoretical questions like the properties of the ISCO stress may be decided in the future by observational data.

An additional prediction made in this thesis was discussed in Chapter 3: the modified temperature profile $T \sim r^{-7/8}$ of a finite ISCO stress disc, resulting from the additional energy sourced from the inner-disc angular momentum flux, results in a modified frequency dependence of the mid-frequency part of the disc spectrum $L_\nu \propto \nu^{5/7}$ (equation 3.32). The corresponding vanishing ISCO stress prediction is a $\nu^{1/3}$ profile (equation 3.33, Lynden-Bell 1969, Shakura and Sunyaev 1973). Recently, Weaver and Horne (2022) analysed 9,242 spectroscopically-confirmed quasars with multi-epoch and multi-band *ugriz* photometry from the SDSS Southern Survey. They decomposed their five-band spectral energy distributions into variable (disc) and non-variable (host galaxy) components. Taking into account the attenuation by dust on the line of sight through the host galaxy, and varying the assumed disc power-law spectral slope $L_\nu \propto \nu^\alpha$, Weaver & Horne found a best-fit value $\alpha = 0.71 \pm 0.02$, excluding at high confidence the canonical $L_\nu \propto \nu^{1/3}$ prediction for a steady-state accretion disc with a $T \propto r^{-3/4}$ temperature profile. Their finding was, however, consistent with $\alpha = 5/7 \simeq 0.714\ldots$, the exact prediction of the finite ISCO stress models developed in this thesis.

I believe that the question of the properties of the ISCO stress is one which will be answered by a combination of better theoretical models of the near-ISCO emission, and by ever improving datasets. A theoretical refinement of the models presented in this thesis would involve the inclusion of emission sourced from within the ISCO, this is discussed further below.

5.2 Emission from within the ISCO

In common with all analytical models of relativsitic accretion discs, in this thesis I have neglected the emission resulting from the fluid on its plunge within the ISCO, in effect cutting off the disc precisely at the ISCO. For a vanishing ISCO stress the temperature of the disc at the ISCO is of course forced to zero, but in the case of a finite ISCO stress (and those discs in GRMHD simulations) the material streaming across the ISCO is in fact still very hot. This material will continue to emit over its inspiral into the event horizon, and this emission is potentially very interesting, as it may contain imprinted signatures of the black hole's spin, resulting as it does from so close to the black hole's event horizon.

To understand the emission properties of the intra-ISCO flow, one needs to solve again the equations of mass, angular momentum and energy conservations of the flow. The equation of mass conservation in a steady flow is simple, and of the same form as in the disc proper

$$\dot{M} = 2\pi r \Sigma U^r, \tag{5.1}$$

where $\dot{M}$ is a constant radial mass flux. The determination of U^r, the radial velocity of the disc flow, is once again computed from angular momentum conservation. The exact equation of angular momentum conservation is, however, strongly modified in the intra-ISCO region: the flow is no longer diffusive, and the disc material can now accrete onto the black hole with no help required from the underlying disc turbulence. To leading order then the angular momentum of the fluid elements are themselves conserved over the inflow, and are given by their values at the ISCO.

To calculate the intra-ISCO flow velocity U^r, I start with the covariant 4-momenta U_ϕ and U_0, which are calculated in the usual manner (e.g., Hobson et al. 2006), and are proportional to the conserved angular momentum and energy, respectively ($c = 1$ in this section):

$$U_\phi = \frac{(Mr)^{1/2}}{\mathcal{D}}(1 + a^2/r^2 - 2aM^{1/2}/r^{3/2}), \quad U_0 = -\frac{1}{\mathcal{D}}(1 - 2M/r + aM^{1/2}/r^{3/2}),$$
$$\mathcal{D}^2 = 1 - 3M/r + 2aM^{1/2}/r^{3/2}. \tag{5.2}$$

The stability of circular orbits is ensured provided $\partial_r U_\phi > 0$, the relativistic analogue of the Rayleigh criterion, thus the ISCO occurs when $\partial_r U_\phi = 0$. Evaluating

this gradient leaves

$$\frac{\partial U_\phi}{\partial r} = \frac{M^{1/2}}{2r^{1/2}\mathcal{D}^3}\left(1+\frac{aM^{1/2}}{r^{3/2}}\right)\left(1-\frac{6M}{r}-\frac{3a^2}{r^2}+\frac{8aM^{1/2}}{r^{3/2}}\right). \tag{5.3}$$

The factor $\mathcal{D}^3$ is positive everywhere over the spin domain $-1 < a/M < 1$ of interest, so the expression passes through zero at $r = r_I$, where the final factor vanishes:

$$r_I^2 = 6Mr_I - 8a\sqrt{Mr_I} + 3a^2 = \frac{2Mr_I}{3} + \frac{16Mr_I}{3}\left(1-\frac{3a}{4\sqrt{Mr_I}}\right)^2 \tag{5.4}$$

The second equality will be especially convenient in what follows below. I define the constants of motion for the intra-ISCO inspiral

$$J = U_\phi(r_I), \quad \gamma = -U_0(r_I), \tag{5.5}$$

with a notation consistent with their association with the conserved angular momentum and energy of the flow. Using equation 5.4 to substitute for r_I^2 in J and γ, the resulting numerators and denominators in these expressions factor cleanly, leading to a further simplification:

$$J = 2\sqrt{3}M\left(1-\frac{2a}{3\sqrt{Mr_I}}\right), \tag{5.6}$$

$$\gamma = \frac{4}{3}\sqrt{3}\left(\frac{M}{r_I}\right)^{1/2}\left(1-\frac{3a}{4\sqrt{Mr_I}}\right) = \left(1-\frac{2M}{3r_I}\right)^{1/2}, \tag{5.7}$$

where in the final γ equality I have made use of the right hand most result of equation 5.4. General relativistic dynamics permits radial motion in orbits whose angular momentum and energy correspond to an exactly circular orbit. In particular, an infinitesimal inward displacement from the ISCO radius r_I is sufficient to launch an inward drift, extremely slowly at first, than ever more rapidly. The governing equation is easily stated in formal terms:

$$g_{rr}(U^r)^2 + U^0U_0 + U^\phi U_\phi = -1, \tag{5.8}$$

but its direct solution is a matter of no little algebraic complexity. Expanding, expressing all non-radial 4-velocities in terms of J and γ, and multiplying through by $1/g_{rr}$, leaves

$$(U^r)^2 + \frac{J}{r^2}\left(\frac{2Ma\gamma}{r}+\left(1-\frac{2M}{r}\right)J\right) - \frac{\gamma}{r^2}\left[\left(r^2+a^2+\frac{2Ma^2}{r}\right)\gamma - \frac{2MaJ}{r}\right] = -1-\frac{a^2}{r^2}+\frac{2M}{r}. \tag{5.9}$$

Equation 5.9 can be hugely simplified by noting that the ISCO radius should correspond to a triple root of U^r. This can be understood by re-writing equation 5.9 in the form $(U^r)^2 + V_{\rm eff}(r) = 0$, which defines an 'effective' potential $V_{\rm eff}$ which is cubic in $1/r$. I factorise $V_{\rm eff}$ in the following manner

$$V_{\rm eff}(r) = -V_0 \left(\frac{r_1}{r} - 1\right)\left(\frac{r_2}{r} - 1\right)\left(\frac{r_3}{r} - 1\right), \tag{5.10}$$

where r_1, r_2 and r_3 are the general (possibly complex) roots of $V_{\rm eff}$. For any circular orbit of radius $r = r_c$, both $V_{\rm eff}(r_c) = 0$ and $\partial_r V_{\rm eff}(r_c) = 0$, and there will be a double root of the polynomial. For the particular case of the last stable circular orbit, there is an additional condition, $\partial_r^2 V_{\rm eff}(r_I) = 0$. Thus, r_I must be a *triple* root of U^r. The normalisation constant V_0 may be found by going back to equation (5.9) and taking the formal limit $r \to \infty$:

$$V_0 = -(U^r)^2 \to 1 - \gamma^2 = \frac{2M}{3r_I}, \tag{5.11}$$

which leads directly to the final equation for (inward moving) U^r:

$$U^r \equiv \frac{{\rm d}r}{{\rm d}\tau} = -\sqrt{\frac{2M}{3r_I}}\left(\frac{r_I}{r} - 1\right)^{3/2}. \tag{5.12}$$

This may also be derived by a considerably more lengthy direct computation. Note that this remarkable result is universal: there is no a-dependence in this expression other than implicitly through r_I. In this sense, every Kerr orbit inspiraling from an ISCO is self-similar in its radial motion. As r_I represents a triple root of U^r, no solutions exist for $r > r_I$.

The equation of angular momentum conservation within the flow therefore exactly determines the radial velocity of the intra-ISCO flow, without any dependence on complex disc turbulence. The final equation which constrains the thermodynamics of the intra-ISCO flow is then energy conservation in the flow, which takes the same general form as equations 2.32–2.34 in Chapter 2:

$$U^\nu \nabla_\mu \left(T^\mu_\nu\right) = 0. \tag{5.13}$$

This is a classical accretion disc equation, except now the accretion velocity is given *a-priori*. Unlike in the extra-ISCO flow, conductive, adiabatic and radiative terms are all equally important within the ISCO, and this equation shall not be solved here.

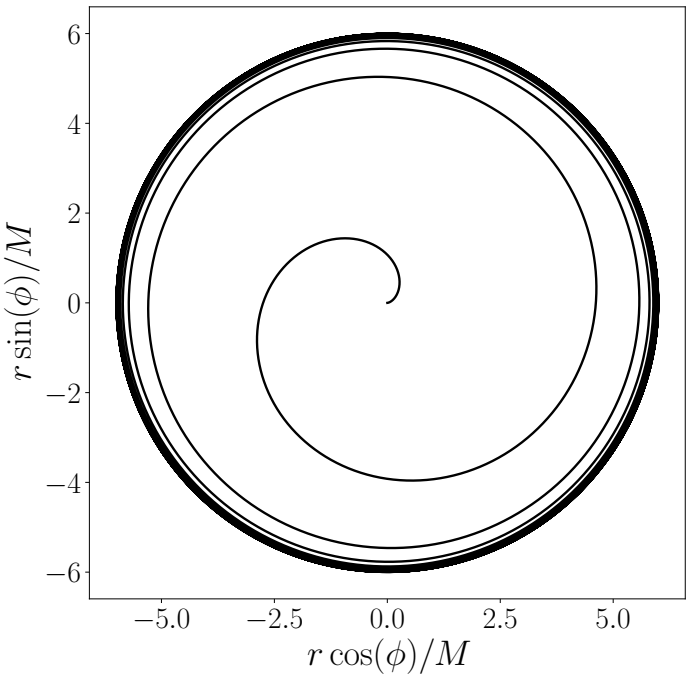

Figure 5.1: Inspiral of a test particle from the ISCO ($r = 6M$) to singularity ($r = 0$) of a Schwarzschild black hole.

The orbital dynamics of the inspiralling fluid elements are themselves fascinating however, and two illustrative examples will now be discussed. The contravariant ϕ-component of the 4-velocity is:

$$U^\phi = -g^{\phi 0}\gamma + g^{\phi\phi}J = \frac{2M\gamma a + J(r-2M)}{r(r^2 - 2Mr + a^2)}, \tag{5.14}$$

and the ratio of these velocity components U^ϕ/U^r parameterises the fluid elements inspiral $\mathrm{d}\phi/\mathrm{d}r$.

The Schawarzschild limit $a = 0$ is especially simple. Then $r_I = 6M$, $J = 2\sqrt{3}M$, and $U^\phi = 2\sqrt{3}M/r^2$. Defining $x = r/r_I$ leaves

$$\frac{\mathrm{d}\phi}{\mathrm{d}x} = 6M\frac{U^\phi}{U^r} = -\sqrt{3}\frac{1}{x^2}\left(\frac{1}{x} - 1\right)^{-3/2}, \tag{5.15}$$

which immediately integrates to

$$x = \frac{r}{6M} = \frac{1}{1 + 12/\phi^2}, \tag{5.16}$$

with the convention that ϕ increases from $-\infty$ to 0 as x goes from 1 to 0. *This is an exact orbital solution for the standard Schwarzschild metric, which is both non-circular and non-radial, extending from r_I to $r = 0$.* (Figure 5.1.) The simplicity is truly remarkable.

When $a \neq 0$, the governing spiral equations are complicated by singularities at the outer and inner Kerr event horizons $r_\pm = M \pm \sqrt{M^2 - a^2}$. While the full orbital equations are still solvable (Mummery & Balbus 2022, submitted.), they are not hugely illuminating of the various interesting physical processes at play in the vicinity of the Kerr event horizon. For extremal Kerr black holes ($a = \pm M$) the equations in fact re-simplify, as the outer and inner Kerr horizons coincide at $r_\pm = M$.

For the $a = +M$ solution, the ISCO and both event horizons actually coincide in Boyer-Lindquist coordinates. The $a = -M$ orbit is more interesting, and the $r(\phi)$ orbit can be determined exactly. I write the orbital equation, after the series of substitutions $J = 22\sqrt{3}M/9$, $\gamma = 5\sqrt{3}/9$, $r_I = 9M$, $a = -M$, and variable transformations $r = r_I \sin^2(\psi/2)$, $t = \tan(\psi/2)$, as

$$\frac{\phi}{9\sqrt{2}} = \int \frac{6t^2}{(8t^2-1)^2}\,\mathrm{d}t - \int \frac{16t^4}{(8t^2-1)^2}\,\mathrm{d}t, \tag{5.17}$$

which becomes

$$\frac{\phi}{9\sqrt{2}} = \frac{2t^3}{1-8t^2}. \tag{5.18}$$

With $t^2 = r/(r_I - r)$, this may be solved for $\phi(r)$:

$$\phi(r) = \frac{2\sqrt{2}}{3M^{3/2}} \frac{r^{3/2}}{(1-r/M)\sqrt{1-r/9M}}. \tag{5.19}$$

Inverting equation (5.18) to solve for $t(\phi)$ (and thus $r(\phi)$) is interesting, as it highlights solutions from all branches of the governing cubic equation

$$t^3 + \frac{4\phi}{9\sqrt{2}}t^2 - \frac{\phi}{18\sqrt{2}} = 0, \tag{5.20}$$

which can be found by standard trigonometric techniques. There are actually *four* branches of interest in this problem. Physically this arises from frame dragging, which produces a multi-valued $\phi(r)$. The three nominal roots of the cubic, t_j, may be written:

$$t_j = \frac{2\sqrt{2}\phi}{27}\left[2\cos\left(\frac{1}{3}\cos^{-1}\left[\frac{2187}{128\phi^2} - 1\right] + \frac{2\pi j}{3}\right) - 1\right], \tag{5.21}$$

with $j = 0, 1, 2$. The fourth branch t_3 may be formally identified with the ($j = 0$) t_0 root, but changing cos and $\cos^{-1}$ into cosh and $\cosh^{-1}$ respectively, as the argument of the $\cos^{-1}$ exceeds unity for t_3 orbits. All four branches are needed, as I now discuss.

Radial solutions which correspond to these roots are

$$r_j = \frac{9Mt_j^2}{1+t_j^2}, \tag{5.22}$$

with different roots corresponding to different "legs" of the orbit. The path of a test particle inspiralling from the retrograde ISCO of a maximally rotating Kerr black hole is as follows. The particle starts at $r = 9M$, with $\phi = -\infty$. It spirals inwards towards the event horizon, with increasing ϕ, until it crosses the special radius $r_\star = 27M/11$ at an angle

$$\phi_\star = -\frac{27\sqrt{3}}{16}, \tag{5.23}$$

whereupon frame-dragging bends the orbit backwards, and the particle begins to corotate with the black hole (Figure 5.2). Note that this location is exterior to the ergosphere $r_E = 2M$. During this initial phase the radial coordinate is given by the $r_1(\phi)$ solution (equation 5.21). Beyond this point, the orbit transitions onto the $r_2(\phi)$ branch, with ϕ once again tending towards $-\infty$ as the particle approaches the event horizon $r_H = M$. Within the event horizon, the orbit is first described by the $r_0(\phi)$ expression, with $|\phi_\star| < \phi < \infty$, and then the final branch $r_3(\phi)$ for $0 < \phi < |\phi_\star|$ (Figure 5.2).

While the exact form of the inspiralling trajectories of intra-ISCO fluid elements are themselves fascinating results, the most important result of this section for the modelling of accretion discs is equation 5.12 for $U^r(r)$, the universal form of the radial 4-velocity of a test particle insprialling from the ISCO radius of a Kerr black hole, while retaining its circular energy and angular momentum.

Interestingly, the post-ISCO acceleration will result in a rapid drop in Σ, and therefore the disc's optical depth τ, so that the hot internal radiation field will escape more easily. Offsetting this will be an adiabatic expansion which will drive global cooling, as will radiative losses. This global cooling must not be too stark however, as conductive $\mathrm{d}T/\mathrm{d}r$ terms, sourced from the reservoir of hot gas external to the ISCO, will prevent too steep a temperature gradient from developing.

Understanding the interaction between these competing effects may potentially explain recent observations which appear to show an additional hot disc component to be present in some sources, beyond the expectations of standard theory Fabian et al. (2020). It has been suggested that this additional component arises from the inner ISCO flow, which can now be directly modelled.

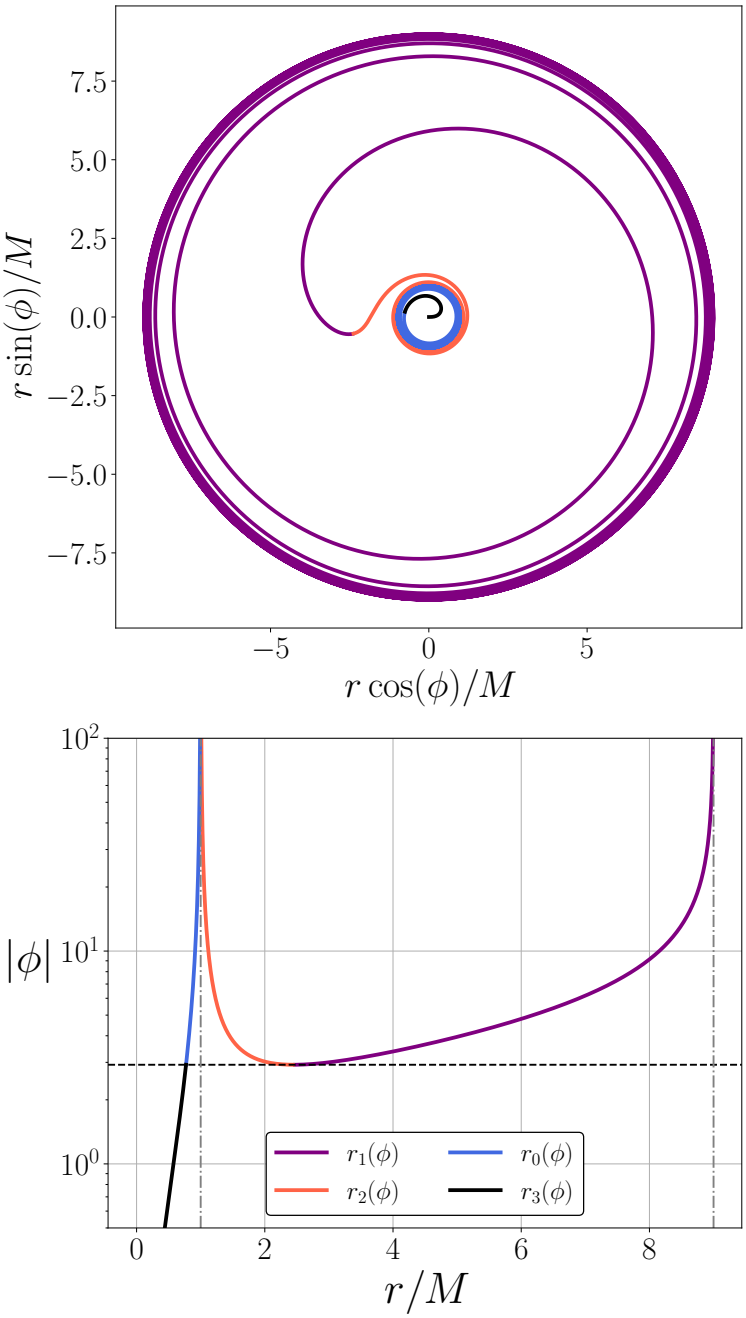

Figure 5.2: Inspiral of a test particle from ISCO ($r = 9M$) to singularity of an extremal Kerr black hole ($a = -M$). The lower figure shows the magnitude of the ϕ coordinate over the infall, with the four $r(\phi)$ branches of the solution color-coded (see text). The value of the frame-dragging angle $\phi_\star$ is shown by the horizontal dashed line. The upper figure shows the inspiral in cartesian-like coordinates with the same color-coding scheme. Note the pronounced effect of (counter rotating) frame dragging.

5.3 The UV plateau luminosity: realising the potential of TDE science

The focus of Chapter 4 of this thesis was on the X-ray emission emergent from TDE discs, and how the properties of this emission could be related to the physical parameters of the TDE system itself. The X-ray emission from a TDE has a number of fortunate properties: it is analytically simple to describe, and is extremely sensitive to the parameters of a TDE system. However, some TDE X-ray light curves are extremely complex, particularly at early times (see for example Figures 4.30 & 4.31). It may well be that in some cases large amplitude fluctuations in TDE X-ray light curves will prevent a detailed analysis from strongly constraining the TDE's physical parameters.

In Chapter 3 however I examined another key component of TDE light curves: the late-time UV plateau. Resulting from the competing effects of the spreading and cooling of the TDE's accretion disc, this light curve component has a number of fortunate qualities: it is extremely long lived, unambiguous, and can be quantified by a single number, the observed UV luminosity one year or so post discovery. If this observable can be related to the physical parameters of the TDE system, it would unlock a powerful, and simple, probe of the huge numbers of TDEs currently being discovered by optical surveys (e.g., van Velzen et al. 2021; Hammerstein et al. 2022).

Unlike the X-ray luminosity, the late-time UV plateau luminosity is not amenable to a simple analytical treatment. Contributions to the UV luminosity come from a large range of disc radii, not just the innermost regions as in the case of the X-ray flux, and the disc emission integrals (e.g., equation 3.11) do not simplify nicely. The UV plateau luminosity is simple to compute numerically however: one specifies an initial disc condition, evolves the disc forward using equation 3.2, and ray trace the resulting disc temperature profile. Therefore, the dependence of the UV plateau luminosity on system parameters is best determined by numerical experiments.

An example numerical experiment is presented in Figure 5.3, which shows the UVW1 plateau luminosity (defined as the UVW1 luminosity two years post the start of disc evolution) as a function of central black hole mass, for a sample of 10,000 TDEs. Each point represents one solution of the TDE disc equations. The distribution of the disc masses was found by randomly sampling from the Kroupa (2001) stellar mass function, with an upper limit of $1M_{\odot}$ incorporated to model the older stellar populations expected to be involved in TDEs. The observed inclination angles were

randomly distributed on a sphere, the initial disc radii are taken to be the tidal radii of the disrupted star, calculated from the sampled black hole's mass and spin, and the stellar mass and stellar radii (Kippenhahn and Weigert 1990). The (dimensionless) black hole spins were uniformly distributed between 0 and 1. Finally, the black hole masses were distributed according to the model of Stone and Metzger (2016), who relate the Schechter (1976) distribution of R-band galaxy luminosities, via the Faber-Jackson law $\sigma \approx 150\text{km/s}\ (L_R/10^{10}L_\odot)^{1/4}$, and the $M_{\rm BH} - \sigma$ relationship of McConnell and Ma (2013), to leave the black hole mass distribution

$$p(M_{\rm BH}) \propto f_{\rm occ}(M_{\rm BH}) \left(\frac{M_{\rm BH}}{10^8 M_\odot}\right)^{-1.07} \exp\left(-0.647\left(\frac{M_{\rm BH}}{10^8 M_\odot}\right)^{0.79}\right), \tag{5.24}$$

where $f_{\rm occ}$ is the "occupation fraction" of the black holes in galactic centres. This factor takes into account the fact that not every galaxy will host a black hole. In particular the lowest-mass galaxies ($M_{\rm gal} \ll 10^9 M_\odot$) in the Universe are not expected to host a central black hole. Very little is known about the functional form of $f_{\rm occ}$, other than the fact that it vanishes for low M, and is one for high M. I choose to model $f_{\rm occ}$ with the following simple form

$$f_{\rm occ}(M_{\rm BH}) = \left[\frac{1}{1 + \left(\bar{M}/M_{\rm BH}\right)^n}\right], \tag{5.25}$$

where $\bar{M}$ (loosely the most common black hole mass in the Universe), and n are free parameters ($n \geq 1.07$, so that the total number density of supermassive black holes is finite). Finally, note that the intrinsic rate of TDEs also depends on the physical parameters of the system itself. I include the analytical rate calculation of Wang and Merritt (2004)

$$\dot{N}_{\rm TDE} \propto M_{\rm BH}^{-0.38} M_\star^{-1/3} R_\star^{1/4}, \tag{5.26}$$

in the sampling procedure, so as to correctly sample the true TDE population. Figure 5.3 was computed with $\bar{M} = 5 \times 10^6 M_\odot$, $n = 3$. This value of $\bar{M}$ was chosen as it maximised the likelihood of producing the observed UV plateau luminosity distribution (Figure 5.4), as will be described in a forthcoming paper (Mummery *et al.* 2022, in prep.).

While Figure 5.3 demonstrates that the observed plateau luminosity distribution will likely have significant scatter (a result in the large ranges of values $M_\star$ and $\theta_{\rm inc}$ can take), there is a clear theoretical prediction here: the late time UV plateau luminosity will

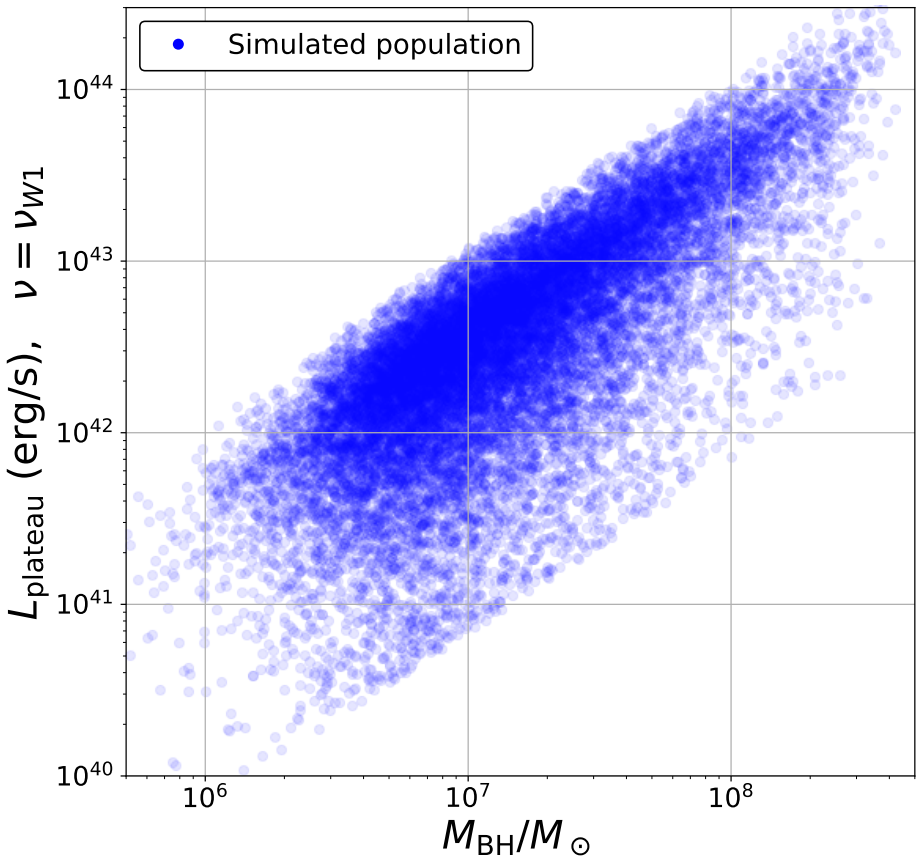

Figure 5.3: The UV plateau luminosity distribution, defined as the UV luminosity observed two years after disc evolution began, plotted as a function of black hole mass, calculated using the procedure described in the text. A clear positive correlation between TDE black hole mass and UV plateau luminosity is discovered.

correlate positively with the black hole mass at the heart of the TDE. This prediction can be tested using the current population of known optical & UV bright TDEs. I fit

$$L_{\rm UV}(t) = L_{\rm peak} \exp\left(-t/\tau\right) + L_{\rm plateau}, \tag{5.27}$$

to the 41 known TDEs with both excellent late time UV coverage, and a host galaxy mass inferred from spectral measurements. This TDE sample includes all of the new sources discovered by the ZTF survey (van Velzen et al. 2021; Hammerstein et al. 2022) which had sufficient late time coverage, as well as the historic ASASSN-discovered TDEs. Extracting $L_{\rm plateau}$, which is a simple constant in the above model, an excellent approximation over the timescales of interest, the existence of any black hole mass correlation in the observed sample of TDEs can be tested. Of course TDEs do not

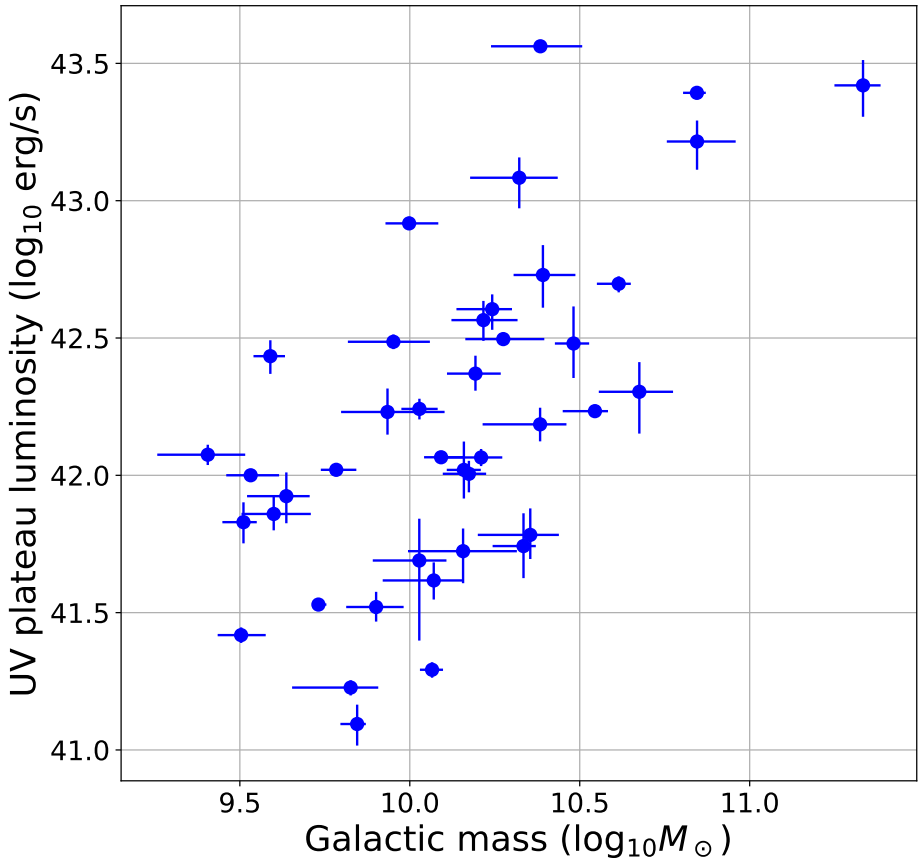

Figure 5.4: The observed UV plateau luminosity–galaxy mass correlation

generally have independent measurements of their central black hole masses, and so a proxy for the black hole mass must be used. TDEs are known to primarily occur in centrally concentrated galaxies (Hammerstein et al. 2021), with bulge mass-to-total mass factors of roughly one half (Law-Smith et al. 2017). As the bulge mass of a galaxy correlates strongly with its central black hole mass (Magorrian et al. 1998), for TDE hosts the total galactic mass should act as a good proxy for the black hole mass. The extracted UV plateau luminosity is plotted against galactic host mass in Figure 5.4, which demonstrates a clear positive correlation. This correlation is statistically significant, with a p-value of 5×10^{-5} for a Kendall-tau correlation test.

This is a result of real astrophysical importance. It suggests that with a single measurement of a TDE's late-time optical/UV luminosity strong constraints can be placed onto the value of the TDE's central black hole mass. This opens up the possibility of utilising the full power of TDE science as a probe of galactic dynamics.

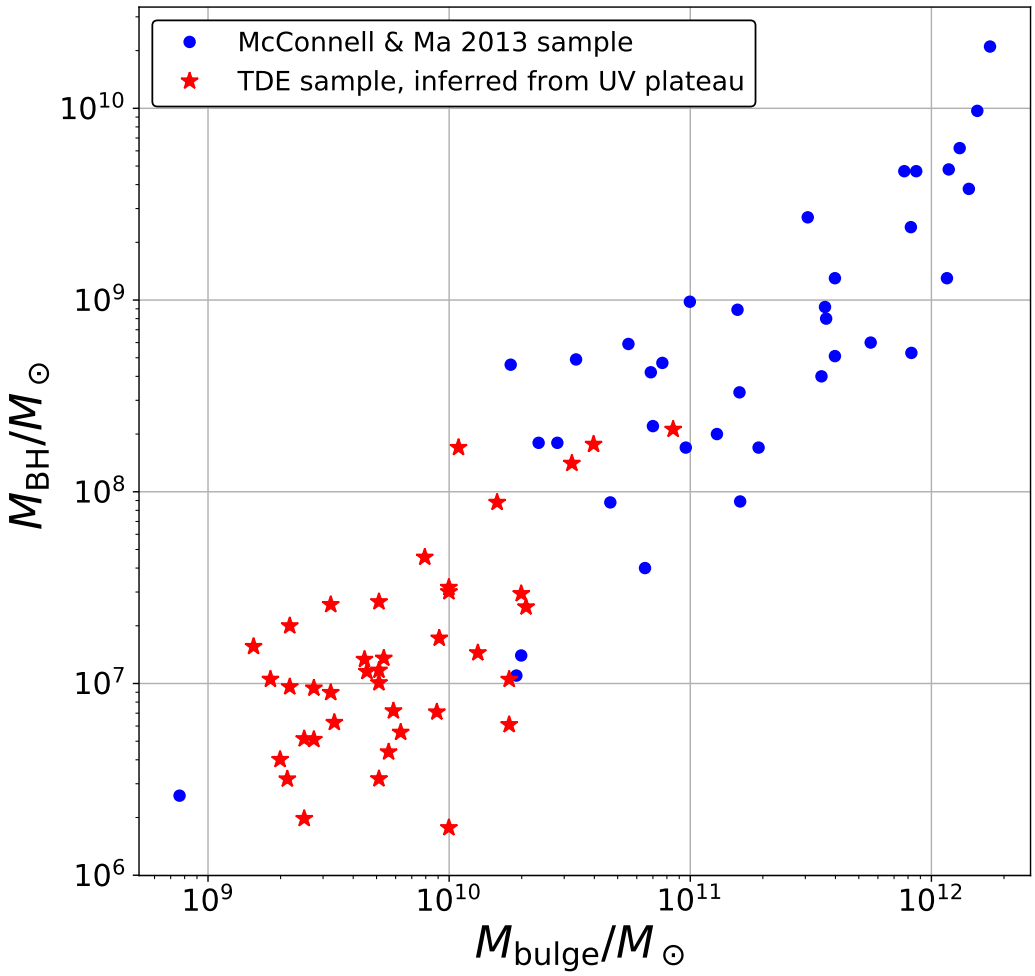

Figure 5.5: An updated 'Magorrian relationship' using the UV plateau black hole mass correlation. The TDE black hole masses are inferred from folding the observed plateau luminosities through the theoretical plateau luminosity distribution of Figure 5.3.

For example: one can ask whether the Magorrian et al. (1998) relationship between the black hole and galactic bulge mass holds down to $\sim 10^6 M_\odot$. Existing scaling relationships have been calibrated on SMBH masses typically greater than $10^8 M_\odot$ (e.g., the McConnell and Ma 2013 sample, blue points Figure 5.5), whereas TDEs will exclusively probe black hole masses below the Hills mass ($\sim 10^8 M_\odot$, e.g. Figure 3.16).

As an example of how TDEs can now 'fill in' the gaps in these scaling relationships, I present in Figure 5.5 a combined McConnell and Ma (2013) and TDE black hole mass bulge mass correlation. The TDE sample, plotted as red stars, uses the $L_{\rm plateau}$ measurements extracted from their late time light curves (Figure 5.4), combined

with the first principles theoretical plateau luminosity distribution (Figure 5.3), to determine a black hole mass probability distribution for each TDE. The median of these probability distributions are plotted. The black hole masses inferred using this method have an intrinsic scatter, typically of order ~ 0.3 dex, resulting from the breadth of the simulated distribution (Figure 5.3), which is not shown here. The bulge masses are taken to be half of the inferred galaxy mass, a factor which is in agreement with more detailed analysis (Law-Smith et al. 2017). It is clear from Figure 5.5 that the Magorrian relationship does indeed hold down to $10^6 M_\odot$, a result of real significance.

The future for tidal disruption event physics is bright, in all senses: future data streams will soon come online which will transform the study of these remarkable objects. The relativistic accretion disc models presented in this thesis have proven to be successful, and powerful, probes of the physical nature of these extreme events and, as I have argued in this final Chapter, they have much more yet to give.

Bibliography

Abbott, B. P. et al. (2016). "Observation of Gravitational Waves from a Binary Black Hole Merger". In: *Phys. Rev. Lett.* 116.6, 061102, p. 061102. DOI: 10.1103/PhysRevLett.116.061102. arXiv: 1602.03837 [gr-qc].

Abramowicz, M. A. et al. (1988). "Slim Accretion Disks". In: *ApJ* 332, p. 646. DOI: 10.1086/166683.

Abramowitz, Milton and Irene A. Stegun (1965). *Handbook of mathematical functions with formulas, graphs, and mathematical tables*.

Agol, Eric and Julian H. Krolik (2000). "Magnetic Stress at the Marginally Stable Orbit: Altered Disk Structure, Radiation, and Black Hole Spin Evolution". In: *ApJ* 528.1, pp. 161–170. DOI: 10.1086/308177. arXiv: astro-ph/9908049 [astro-ph].

Alexander, K. D. et al. (2016). "Discovery of an Outflow from Radio Observations of the Tidal Disruption Event ASASSN-14li". In: *ApJL* 819.2, L25, p. L25. DOI: 10.3847/2041-8205/819/2/L25. arXiv: 1510.01226 [astro-ph.HE].

Arnaud, K. A. (1996). "XSPEC: The First Ten Years". In: *Astronomical Data Analysis Software and Systems V*. Ed. by George H. Jacoby and Jeannette Barnes. Vol. 101. Astronomical Society of the Pacific Conference Series, p. 17.

Auchettl, Katie, James Guillochon, and Enrico Ramirez-Ruiz (2017). "New Physical Insights about Tidal Disruption Events from a Comprehensive Observational Inventory at X-Ray Wavelengths". In: *ApJ* 838.2, 149, p. 149. DOI: 10.3847/1538-4357/aa633b. arXiv: 1611.02291 [astro-ph.HE].

Bade, N., S. Komossa, and M. Dahlem (1996). "Detection of an extremely soft X-ray outburst in the HII-like nucleus of NGC 5905." In: *A&A* 309, pp. L35–L38.

Balbus, Steven A. (2014). "On the high-frequency spectrum of a classical accretion disc." In: *MNRAS* 444, pp. L54–L57. DOI: 10.1093/mnrasl/slu109. arXiv: 1407.2020 [astro-ph.HE].

Balbus, Steven A. (2017). "The general relativistic thin disc evolution equation". In: *MNRAS* 471.4, pp. 4832–4838. DOI: 10.1093/mnras/stx1955. arXiv: 1707.08884 [astro-ph.HE].

Balbus, Steven A. and John F. Hawley (1991). "A Powerful Local Shear Instability in Weakly Magnetized Disks. I. Linear Analysis". In: *ApJ* 376, p. 214. DOI: 10.1086/170270.

— (1992). "A Powerful Local Shear Instability in Weakly Magnetized Disks. IV. Nonaxisymmetric Perturbations". In: *ApJ* 400, pp. 610–621. DOI: 10.1086/172022.

Balbus, Steven A. and Andrew Mummery (2018). "The evolution of Kerr discs and late-time tidal disruption event light curves". In: *MNRAS* 481.3, pp. 3348–3356. DOI: 10.1093/mnras/sty2467. arXiv: 1809.02146 [astro-ph.HE].

Balbus, Steven A. and John C. B. Papaloizou (1999). "On the Dynamical Foundations of α Disks". In: *ApJ* 521.2, pp. 650–658. DOI: 10.1086/307594. arXiv: astro-ph/9903035 [astro-ph].

Bardeen, James M., William H. Press, and Saul A. Teukolsky (1972). "Rotating Black Holes: Locally Nonrotating Frames, Energy Extraction, and Scalar Synchrotron Radiation". In: *ApJ* 178, pp. 347–370. DOI: 10.1086/151796.

Bender, C. M. and S. A. Orszag (1978). *Advanced Mathematical Methods for Scientists and Engineers*.

Bonnerot, Clément et al. (2016). "Disc formation from tidal disruptions of stars on eccentric orbits by Schwarzschild black holes". In: *MNRAS* 455.2, pp. 2253–2266. DOI: 10.1093/mnras/stv2411. arXiv: 1501.04635 [astro-ph.HE].

Bowman, F. (1958). *Introduction to Bessel Functions*.

Bricman, Katja and Andreja Gomboc (2020). "The Prospects of Observing Tidal Disruption Events with the Large Synoptic Survey Telescope". In: *ApJ* 890.1, 73, p. 73. DOI: 10.3847/1538-4357/ab6989. arXiv: 1906.08235 [astro-ph.HE].

Bright, J. S. et al. (2018). "Long-term radio and X-ray evolution of the tidal disruption event ASASSN-14li". In: *MNRAS* 475.3, pp. 4011–4019. DOI: 10.1093/mnras/sty077. arXiv: 1801.03094 [astro-ph.HE].

Brown, J. S. et al. (2017). "The Long Term Evolution of ASASSN-14li". In: *MNRAS* 466.4, pp. 4904–4916. DOI: 10.1093/mnras/stx033. arXiv: 1609.04403 [astro-ph.HE].

Burrows, D. N. et al. (2011). "Relativistic jet activity from the tidal disruption of a star by a massive black hole". In: *Nature* 476.7361, pp. 421–424. DOI: 10.1038/nature10374. arXiv: 1104.4787 [astro-ph.HE].

Cannizzaro, G. et al. (2021). "Accretion disc cooling and narrow absorption lines in the tidal disruption event AT 2019dsg". In: *MNRAS* 504.1, pp. 792–815. DOI: 10.1093/mnras/stab851. arXiv: 2012.10195 [astro-ph.HE].

Cannizzo, John K., Hyung Mok Lee, and Jeremy Goodman (1990). "The Disk Accretion of a Tidally Disrupted Star onto a Massive Black Hole". In: *ApJ* 351, p. 38. DOI: 10.1086/168442.

Carter, B. (1971). "Axisymmetric Black Hole Has Only Two Degrees of Freedom". In: *Phys. Rev. Lett.* 26.6, pp. 331–333. DOI: 10.1103/PhysRevLett.26.331.

Cenko, S. Bradley et al. (2012). "Swift J2058.4+0516: Discovery of a Possible Second Relativistic Tidal Disruption Flare?" In: *ApJ* 753.1, 77, p. 77. DOI: 10.1088/0004-637X/753/1/77. arXiv: 1107.5307 [astro-ph.HE].

Chandrasekhar, S. (1931). "The Maximum Mass of Ideal White Dwarfs". In: *ApJ* 74, p. 81. DOI: 10.1086/143324.

Corless, R. M. et al. (1996). "On the Lambert W Function". In: *Advances in computational mathematics*, p. 329.

Dai, Lixin et al. (2018). "A Unified Model for Tidal Disruption Events". In: *ApJL* 859.2, L20, p. L20. DOI: 10.3847/2041-8213/aab429. arXiv: 1803.03265 [astro-ph.HE].

Davis, Shane W., Chris Done, and Omer M. Blaes (2006). "Testing Accretion Disk Theory in Black Hole X-Ray Binaries". In: *ApJ* 647.1, pp. 525–538. DOI: 10.1086/505386. arXiv: astro-ph/0602245 [astro-ph].

Done, Chris, Marek Gierliński, and Aya Kubota (2007). "Modelling the behaviour of accretion flows in X-ray binaries. Everything you always wanted to know about accretion but were afraid to ask". In: *A&ARv* 15.1, pp. 1–66. DOI: 10.1007/s00159-007-0006-1. arXiv: 0708.0148 [astro-ph].

Done, Chris et al. (2012). "Intrinsic disc emission and the soft X-ray excess in active galactic nuclei". In: *MNRAS* 420.3, pp. 1848–1860. DOI: 10.1111/j.1365-2966.2011.19779.x. arXiv: 1107.5429 [astro-ph.HE].

Dong, Subo et al. (2016). "ASASSN-15lh: A highly super-luminous supernova". In: *Science* 351.6270, pp. 257–260. DOI: 10.1126/science.aac9613. arXiv: 1507.03010 [astro-ph.HE].

Eardley, D. M. and A. P. Lightman (1975). "Magnetic viscosity in relativistic accretion disks." In: *ApJ* 200, pp. 187–203. DOI: 10.1086/153777.

Eddington, A. S. (1924). "A Comparison of Whitehead's and Einstein's Formulæ". In: *Nature* 113.2832, p. 192. DOI: 10.1038/113192a0.

Einstein, Albert (1915). "Die Feldgleichungen der Gravitation". In: *Sitzungsberichte der Königlich Preußischen Akademie der Wissenschaften (Berlin*, pp. 844–847.

— (1916a). "Näherungsweise Integration der Feldgleichungen der Gravitation". In: *Sitzungsberichte der Königlich Preußischen Akademie der Wissenschaften (Berlin*, pp. 688–696.

— (1916b). "Die Grundlage der allgemeinen Relativitätstheorie". In: *Annalen der Physik* 354.7, pp. 769–822. DOI: 10.1002/andp.19163540702.

Esin, Ann A., Jeffrey E. McClintock, and Ramesh Narayan (1997). "Advection-Dominated Accretion and the Spectral States of Black Hole X-Ray Binaries: Application to Nova Muscae 1991". In: *ApJ* 489.2, pp. 865–889. DOI: 10.1086/304829. arXiv: astro-ph/9705237 [astro-ph].

Esquej, P. et al. (2008). "Evolution of tidal disruption candidates discovered by XMM-Newton". In: *A&A* 489.2, pp. 543–554. DOI: 10.1051/0004-6361:200810110. arXiv: 0807.4452 [astro-ph].

Event Horizon Telescope Collaboration et al. (2019a). "First M87 Event Horizon Telescope Results. I. The Shadow of the Supermassive Black Hole". In: *ApJL* 875.1, L1, p. L1. DOI: 10.3847/2041-8213/ab0ec7. arXiv: 1906.11238 [astro-ph.GA].

— (2019b). "First M87 Event Horizon Telescope Results. IV. Imaging the Central Supermassive Black Hole". In: *ApJL* 875.1, L4, p. L4. DOI: 10.3847/2041-8213/ab0e85. arXiv: 1906.11241 [astro-ph.GA].

— (2019c). "First M87 Event Horizon Telescope Results. V. Physical Origin of the Asymmetric Ring". In: *ApJL* 875.1, L5, p. L5. DOI: 10.3847/2041-8213/ab0f43. arXiv: 1906.11242 [astro-ph.GA].

Fabian, A. C. et al. (2020). "The soft state of the black hole transient source MAXI J1820+070: emission from the edge of the plunge region?" In: *MNRAS* 493.4, pp. 5389–5396. DOI: 10.1093/mnras/staa564. arXiv: 2002.09691 [astro-ph.HE].

Fabrika, S. (2004). "The jets and supercritical accretion disk in SS433". In: *Astrophysics and Space Physics Reviews* 12, pp. 1–152. arXiv: astro-ph/0603390 [astro-ph].

Fender, Rob, T. M. Belloni, and E. Gallo (2004). "Towards a unified model for black hole X-ray binary jets". In: *MNRAS* 355.4, pp. 1105–1118. DOI: 10.1111/j.1365-2966.2004.08384.x. arXiv: astro-ph/0409360 [astro-ph].

Fender, Rob and Tomaso Belloni (2004). "GRS 1915+105 and the Disc-Jet Coupling in Accreting Black Hole Systems". In: *ARA&A* 42.1, pp. 317–364. DOI: 10.1146/annurev.astro.42.053102.134031. arXiv: astro-ph/0406483 [astro-ph].

Fragile, P. Chris et al. (2018). "Relativistic, Viscous, Radiation Hydrodynamic Simulations of Geometrically Thin Disks. I. Thermal and Other Instabilities". In: *ApJ* 857.1, 1, p. 1. DOI: 10.3847/1538-4357/aab788. arXiv: 1803.06423 [astro-ph.HE].

Frank, Juhan, Andrew King, and Derek J. Raine (2002). *Accretion Power in Astrophysics: Third Edition*.

Fromang, Sébastien, Caroline Terquem, and Steven A. Balbus (2002). "The ionization fraction in α models of protoplanetary discs". In: *MNRAS* 329.1, pp. 18–28. DOI: 10.1046/j.1365-8711.2002.04940.x. arXiv: astro-ph/0109008 [astro-ph].

Gammie, Charles F. (1999). "Efficiency of Magnetized Thin Accretion Disks in the Kerr Metric". In: *ApJL* 522.1, pp. L57–L60. DOI: 10.1086/312207. arXiv: astro-ph/9906223 [astro-ph].

Garofalo, David and Christopher S. Reynolds (2005). "Sporadically Torqued Accretion Disks around Black Holes". In: *ApJ* 624.1, pp. 94–102. DOI: 10.1086/428875. arXiv: astro-ph/0501455 [astro-ph].

Genzel, R. et al. (2003). "The Stellar Cusp around the Supermassive Black Hole in the Galactic Center". In: *ApJ* 594.2, pp. 812–832. DOI: 10.1086/377127. arXiv: astro-ph/0305423 [astro-ph].

Gezari, Suvi, S. B. Cenko, and I. Arcavi (2017). "X-Ray Brightening and UV Fading of Tidal Disruption Event ASASSN-15oi". In: *ApJL* 851.2, L47, p. L47. DOI: 10.3847/2041-8213/aaa0c2. arXiv: 1712.03968 [astro-ph.HE].

Gezari, S. et al. (2008). "UV/Optical Detections of Candidate Tidal Disruption Events by GALEX and CFHTLS". In: *ApJ* 676.2, pp. 944–969. DOI: 10.1086/529008. arXiv: 0712.4149 [astro-ph].

Ghez, A. M. et al. (2005). "Stellar Orbits around the Galactic Center Black Hole". In: *ApJ* 620.2, pp. 744–757. DOI: 10.1086/427175. arXiv: astro-ph/0306130 [astro-ph].

Gladstone, Jeanette C., Timothy P. Roberts, and Chris Done (2009). "The ultraluminous state". In: *MNRAS* 397.4, pp. 1836–1851. DOI: 10.1111/j.1365-2966.2009.15123.x. arXiv: 0905.4076 [astro-ph.CO].

Goodwin, A. J. et al. (2022). "AT2019azh: an unusually long-lived, radio-bright thermal tidal disruption event". In: *MNRAS* 511.4, pp. 5328–5345. DOI: 10.1093/mnras/stac333. arXiv: 2201.03744 [astro-ph.HE].

Gradshteyn, I. S. and I. M. Ryzhik (1980). *Table of integrals, series and products*.

Greiner, Jochen et al. (2000). "RX J1420.4+5334 - another tidal disruption event?" In: *A&A* 362, pp. L25–L28. arXiv: astro-ph/0009430 [astro-ph].

Guillochon, James and Enrico Ramirez-Ruiz (2013). "Hydrodynamical Simulations to Determine the Feeding Rate of Black Holes by the Tidal Disruption of Stars: The Importance of the Impact Parameter and Stellar Structure". In: *ApJ* 767.1, 25, p. 25. DOI: 10.1088/0004-637X/767/1/25. arXiv: 1206.2350 [astro-ph.HE].

— (2015). "A Dark Year for Tidal Disruption Events". In: *ApJ* 809.2, 166, p. 166. DOI: 10.1088/0004-637X/809/2/166. arXiv: 1501.05306 [astro-ph.HE].

Hammerstein, Erica et al. (2021). "Tidal Disruption Event Hosts Are Green and Centrally Concentrated: Signatures of a Post-merger System". In: *ApJL* 908.1, L20, p. L20. DOI: 10.3847/2041-8213/abdcb4. arXiv: 2010.10738 [astro-ph.HE].

Hammerstein, Erica et al. (2022). "The Final Season Reimagined: 30 Tidal Disruption Events from the ZTF-I Survey". In: *arXiv e-prints*. arXiv: 2203.01461 [astro-ph.HE].

Hawley, John F. and Steven A. Balbus (1991). "A Powerful Local Shear Instability in Weakly Magnetized Disks. II. Nonlinear Evolution". In: *ApJ* 376, p. 223. DOI: 10.1086/170271.

— (1992). "A Powerful Local Shear Instability in Weakly Magnetized Disks. III. Long-Term Evolution in a Shearing Sheet". In: *ApJ* 400, p. 595. DOI: 10.1086/172021.

Hawley, John F. and Julian H. Krolik (2001). "Global MHD Simulation of the Inner Accretion Disk in a Pseudo-Newtonian Potential". In: *ApJ* 548.1, pp. 348–367. DOI: 10.1086/318678. arXiv: astro-ph/0006456 [astro-ph].

Hills, J. G. (1975). "Possible power source of Seyfert galaxies and QSOs". In: *Nature* 254.5498, pp. 295–298. DOI: 10.1038/254295a0.

Hinkle, Jason T. et al. (2021). "Discovery and follow-up of ASASSN-19dj: an X-ray and UV luminous TDE in an extreme post-starburst galaxy". In: *MNRAS* 500.2, pp. 1673–1696. DOI: 10.1093/mnras/staa3170. arXiv: 2006.06690 [astro-ph.HE].

Hobson, M. P., G. P. Efstathiou, and A. N. Lasenby (2006). *General Relativity*. DOI: 10.2277/0521829518.

Hogg, J. Drew and Christopher S. Reynolds (2016). "Testing the Propagating Fluctuations Model with a Long, Global Accretion Disk Simulation". In: *ApJ* 826.1, 40, p. 40. DOI: 10.3847/0004-637X/826/1/40. arXiv: 1512.05350 [astro-ph.HE].

Holoien, T. W. -S. et al. (2014). "ASASSN-14ae: a tidal disruption event at 200 Mpc". In: *MNRAS* 445.3, pp. 3263–3277. DOI: 10.1093/mnras/stu1922. arXiv: 1405.1417 [astro-ph.GA].

— (2016a). "Six months of multiwavelength follow-up of the tidal disruption candidate ASASSN-14li and implied TDE rates from ASAS-SN". In: *MNRAS* 455.3, pp. 2918–2935. DOI: 10.1093/mnras/stv2486. arXiv: 1507.01598 [astro-ph.HE].

— (2016b). "ASASSN-15oi: a rapidly evolving, luminous tidal disruption event at 216 Mpc". In: *MNRAS* 463.4, pp. 3813–3828. DOI: 10.1093/mnras/stw2272. arXiv: 1602.01088 [astro-ph.HE].

Holoien, T. W. -S. et al. (2018). "The unusual late-time evolution of the tidal disruption event ASASSN-15oi". In: *MNRAS* 480.4, pp. 5689–5703. DOI: 10.1093/mnras/sty2273. arXiv: 1804.00006 [astro-ph.HE].

Israel, Werner (1967). "Event Horizons in Static Vacuum Space-Times". In: *Physical Review* 164.5, pp. 1776–1779. DOI: 10.1103/PhysRev.164.1776.

— (1968). "Event horizons in static electrovac space-times". In: *Communications in Mathematical Physics* 8.3, pp. 245–260. DOI: 10.1007/BF01645859.

Ivanov, P. B. and M. A. Chernyakova (2006). "Relativistic cross sections of mass stripping and tidal disruption of a star by a super-massive rotating black hole". In: *A&A* 448.3, pp. 843–852. DOI: 10.1051/0004-6361:20053409. arXiv: astro-ph/0509853 [astro-ph].

Jiang, Ning et al. (2016). "The WISE Detection of an Infrared Echo in Tidal Disruption Event ASASSN-14li". In: *ApJL* 828.1, L14, p. L14. DOI: 10.3847/2041-8205/828/1/L14. arXiv: 1605.04640 [astro-ph.HE].

Jiang, Yan-Fei et al. (2019). "Global Radiation Magnetohydrodynamic Simulations of sub-Eddington Accretion Disks around Supermassive Black Holes". In: *ApJ* 885.2, 144, p. 144. DOI: 10.3847/1538-4357/ab4a00. arXiv: 1904.01674 [astro-ph.HE].

Jiang, Yan-Fei, James M. Stone, and Shane W. Davis (2013). "On the Thermal Stability of Radiation-dominated Accretion Disks". In: *ApJ* 778.1, 65, p. 65. DOI: 10.1088/0004-637X/778/1/65. arXiv: 1309.5646 [astro-ph.HE].

Jiang, Yan-Fei, James M. Stone, and Shane W. Davis (2019). "Super-Eddington Accretion Disks around Supermassive Black Holes". In: *ApJ* 880.2, 67, p. 67. DOI: 10.3847/1538-4357/ab29ff. arXiv: 1709.02845 [astro-ph.HE].

Jonker, P. G. et al. (2020). "Implications from Late-time X-Ray Detections of Optically Selected Tidal Disruption Events: State Changes, Unification, and Detection Rates". In: *ApJ* 889.2, 166, p. 166. DOI: 10.3847/1538-4357/ab659c. arXiv: 1906.12236 [astro-ph.HE].

Kerr, Roy P. (1963). "Gravitational Field of a Spinning Mass as an Example of Algebraically Special Metrics". In: *Phys. Rev. Lett.* 11.5, pp. 237–238. DOI: 10.1103/PhysRevLett.11.237.

Kesden, Michael (2012). "Tidal-disruption rate of stars by spinning supermassive black holes". In: *Phys. Rev. D.* 85.2, 024037, p. 024037. DOI: 10.1103/PhysRevD.85.024037. arXiv: 1109.6329 [astro-ph.CO].

Khabibullin, I. et al. (2020a). "A bright X-ray TDE candidate SRGet J143359.25+400638.5 in SDSS J143359.16+400636.0". In: *The Astronomer's Telegram* 13494, p. 1.

— (2020b). "Bright X-ray source SRGet J134954.70+432859.5 in the direction of galaxy SDSS J134954.68+432856.0". In: *The Astronomer's Telegram* 13499, p. 1.

Khabibullin, I., S. Sazonov, and R. Sunyaev (2014). "SRG/eROSITA prospects for the detection of stellar tidal disruption flares". In: *MNRAS* 437.1, pp. 327–337. DOI: 10.1093/mnras/stt1889. arXiv: 1304.3376 [astro-ph.HE].

Kippenhahn, Rudolf and Alfred Weigert (1990). *Stellar Structure and Evolution*.

Kochanek, Christopher S. (1994). "The Aftermath of Tidal Disruption: The Dynamics of Thin Gas Streams". In: *ApJ* 422, p. 508. DOI: 10.1086/173745.

Komossa, Stefanie and Jochen Greiner (1999). "Discovery of a giant and luminous X-ray outburst from the optically inactive galaxy pair RX J1242.6-1119". In: *A&A* 349, pp. L45–L48. arXiv: astro-ph/9908216 [astro-ph].

Kool, E. C. et al. (2015). "Radio Non-Detection of ASASSN-15lh = SN2015L". In: *The Astronomer's Telegram* 8388, p. 1.

Krolik, J. H. (1999). "Magnetized Accretion inside the Marginally Stable Orbit around a Black Hole". In: *ApJL* 515.2, pp. L73–L76. DOI: 10.1086/311979. arXiv: astro-ph/9902267 [astro-ph].

Kroupa, Pavel (2001). "On the variation of the initial mass function". In: *MNRAS* 322.2, pp. 231–246. DOI: 10.1046/j.1365-8711.2001.04022.x. arXiv: astro-ph/0009005 [astro-ph].

Krühler, T. et al. (2018). "The supermassive black hole coincident with the luminous transient ASASSN-15lh". In: *A&A* 610, A14, A14. DOI: 10.1051/0004-6361/201731773. arXiv: 1710.01045 [astro-ph.GA].

Law-Smith, Jamie et al. (2017). "Tidal Disruption Event Host Galaxies in the Context of the Local Galaxy Population". In: *ApJ* 850.1, 22, p. 22. DOI: 10.3847/1538-4357/aa94c7. arXiv: 1707.01559 [astro-ph.HE].

Leloudas, G. et al. (2016). "The superluminous transient ASASSN-15lh as a tidal disruption event from a Kerr black hole". In: *Nature Astronomy* 1, 0002, p. 0002. DOI: 10.1038/s41550-016-0002. arXiv: 1609.02927 [astro-ph.HE].

Lemaitre, Georges (1933). "L'Univers en expansion". In: *Annales de la Scientifique de Bruxelles* 53, p. 51.

Levan, A. J. et al. (2011). "An Extremely Luminous Panchromatic Outburst from the Nucleus of a Distant Galaxy". In: *Science* 333.6039, p. 199. DOI: 10.1126/science.1207143. arXiv: 1104.3356 [astro-ph.HE].

Li, Li-Xin et al. (2005). "Multitemperature Blackbody Spectrum of a Thin Accretion Disk around a Kerr Black Hole: Model Computations and Comparison with Observations". In: *ApJS* 157.2, pp. 335–370. DOI: 10.1086/428089. arXiv: astro-ph/0411583 [astro-ph].

Lightman, Alan P. and Douglas M. Eardley (1974). "Black Holes in Binary Systems: Instability of Disk Accretion". In: *ApJL* 187, p. L1. DOI: 10.1086/181377.

Lin, Dacheng et al. (2017). "A likely decade-long sustained tidal disruption event". In: *Nature Astronomy* 1, 0033, p. 0033. DOI: 10.1038/s41550-016-0033. arXiv: 1702.00792 [astro-ph.HE].

— (2018). "A luminous X-ray outburst from an intermediate-mass black hole in an off-centre star cluster". In: *Nature Astronomy* 2, pp. 656–661. DOI: 10.1038/s41550-018-0493-1. arXiv: 1806.05692 [astro-ph.HE].

Lin, Dacheng et al. (2015). "An Ultrasoft X-Ray Flare from 3XMM J152130.7+074916: A Tidal Disruption Event Candidate". In: *ApJ* 811.1, 43, p. 43. DOI: 10.1088/0004-637X/811/1/43. arXiv: 1509.00840 [astro-ph.HE].

Liska, M. et al. (2018). "Formation of precessing jets by tilted black hole discs in 3D general relativistic MHD simulations". In: *MNRAS* 474.1, pp. L81–L85. DOI: 10.1093/mnrasl/slx174. arXiv: 1707.06619 [astro-ph.HE].

Liska, M. et al. (2021). "Disc tearing and Bardeen-Petterson alignment in GRMHD simulations of highly tilted thin accretion discs". In: *MNRAS* 507.1, pp. 983–990. DOI: 10.1093/mnras/staa099. arXiv: 1904.08428 [astro-ph.HE].

Lynden-Bell, D. (1969). "Galactic Nuclei as Collapsed Old Quasars". In: *Nature* 223.5207, pp. 690–694. DOI: 10.1038/223690a0.

Lynden-Bell, D. and J. E. Pringle (1974). "The evolution of viscous discs and the origin of the nebular variables." In: *MNRAS* 168, pp. 603–637. DOI: 10.1093/mnras/168.3.603.

Lyubarskii, Yu. E. (1997). "Flicker noise in accretion discs". In: *MNRAS* 292.3, pp. 679–685. DOI: 10.1093/mnras/292.3.679.

Maccarone, Thomas J. (2003). "Do X-ray binary spectral state transition luminosities vary?" In: *A&A* 409, pp. 697–706. DOI: 10.1051/0004-6361:20031146. arXiv: astro-ph/0308036 [astro-ph].

Maccarone, Thomas J., Elena Gallo, and Rob Fender (2003). "The connection between radio-quiet active galactic nuclei and the high/soft state of X-ray binaries". In: *MNRAS* 345.2, pp. L19–L24. DOI: 10.1046/j.1365-8711.2003.07161.x. arXiv: astro-ph/0309137 [astro-ph].

Magorrian, John and Scott Tremaine (1999). "Rates of tidal disruption of stars by massive central black holes". In: *MNRAS* 309.2, pp. 447–460. DOI: 10.1046/j.1365-8711.1999.02853.x. arXiv: astro-ph/9902032 [astro-ph].

Magorrian, John et al. (1998). "The Demography of Massive Dark Objects in Galaxy Centers". In: *AJ* 115.6, pp. 2285–2305. DOI: 10.1086/300353. arXiv: astro-ph/9708072 [astro-ph].

Maksym, W. Peter, M. P. Ulmer, and Michael Eracleous (2010). "A Tidal Disruption Flare in A1689 from an Archival X-ray Survey of Galaxy Clusters". In: *ApJ* 722.2, pp. 1035–1050. DOI: 10.1088/0004-637X/722/2/1035. arXiv: 1008.4140 [astro-ph.HE].

Margutti, R. et al. (2017). "X-Rays from the Location of the Double-humped Transient ASASSN-15lh". In: *ApJ* 836.1, 25, p. 25. DOI: 10.3847/1538-4357/836/1/25. arXiv: 1610.01632 [astro-ph.HE].

McClintock, Jeffrey E., Ramesh Narayan, and James F. Steiner (2014). "Black Hole Spin via Continuum Fitting and the Role of Spin in Powering Transient Jets". In: *Space Science Series* 183.1-4, pp. 295–322. DOI: 10.1007/s11214-013-0003-9. arXiv: 1303.1583 [astro-ph.HE].

McConnell, Nicholas J. and Chung-Pei Ma (2013). "Revisiting the Scaling Relations of Black Hole Masses and Host Galaxy Properties". In: *ApJ* 764.2, 184, p. 184. DOI: 10.1088/0004-637X/764/2/184. arXiv: 1211.2816 [astro-ph.CO].

McKinney, Jonathan C. (2006). "General relativistic force-free electrodynamics: a new code and applications to black hole magnetospheres". In: *MNRAS* 367.4, pp. 1797–1807. DOI: 10.1111/j.1365-2966.2006.10087.x. arXiv: astro-ph/0601410 [astro-ph].

McKinney, Jonathan C. and Roger D. Blandford (2009). "Stability of relativistic jets from rotating, accreting black holes via fully three-dimensional magnetohydrodynamic simulations". In: *MNRAS*

394.1, pp. L126–L130. DOI: 10.1111/j.1745-3933.2009.00625.x. arXiv: 0812.1060 [astro-ph].

Mendel, J. Trevor et al. (2014). "A Catalog of Bulge, Disk, and Total Stellar Mass Estimates for the Sloan Digital Sky Survey". In: *ApJS* 210.1, 3, p. 3. DOI: 10.1088/0067-0049/210/1/3. arXiv: 1310.8304 [astro-ph.CO].

Metzger, Brian D. and Nicholas C. Stone (2016). "A bright year for tidal disruptions". In: *MNRAS* 461.1, pp. 948–966. DOI: 10.1093/mnras/stw1394. arXiv: 1506.03453 [astro-ph.HE].

Michell, John (1784). "On the Means of Discovering the Distance, Magnitude, &c. of the Fixed Stars, in Consequence of the Diminution of the Velocity of Their Light, in Case Such a Diminution Should be Found to Take Place in any of Them, and Such Other Data Should be Procured from Observations, as Would be Farther Necessary for That Purpose." In: *Philosophical Transactions of the Royal Society of London Series I* 74, pp. 35–57.

Miller, Jon M. et al. (2015). "Flows of X-ray gas reveal the disruption of a star by a massive black hole". In: *Nature* 526.7574, pp. 542–545. DOI: 10.1038/nature15708. arXiv: 1510.06348 [astro-ph.HE].

Misner, Charles W., Kip S. Thorne, and John Archibald Wheeler (1973). *Gravitation*.

Moffatt, H. K. (1978). *Magnetic field generation in electrically conducting fluids*.

Mummery, Andrew (2021a). "A maximum X-ray luminosity scale of disc-dominated tidal destruction events". In: *MNRAS* 504.4, pp. 5144–5154. DOI: 10.1093/mnras/stab1187. arXiv: 2104.06203 [astro-ph.HE].

— (2021b). "Tidal disruption event discs are larger than they seem: removing systematic biases in TDE X-ray spectral modelling". In: *MNRAS* 507.1, pp. L24–L28. DOI: 10.1093/mnrasl/slab088. arXiv: 2108.10160 [astro-ph.HE].

— (2022). "A unified model of tidal destruction events in the disc-dominated phase". In: *arXiv e-prints*. arXiv: 2104.06212 [astro-ph.HE].

Mummery, Andrew and Steven A. Balbus (2019a). "Evolution of relativistic thin discs with a finite ISCO stress - I. Stalled accretion". In: *MNRAS* 489.1, pp. 132–142. DOI: 10.1093/mnras/stz2141. arXiv: 1908.00322 [astro-ph.HE].

— (2019b). "Evolution of relativistic thin discs with a finite ISCO stress - II. Late time behaviour". In: *MNRAS* 489.1, pp. 143–152. DOI: 10.1093/mnras/stz2142. arXiv: 1908.00348 [astro-ph.HE].

— (2020a). "The spectral evolution of disc dominated tidal disruption events". In: *MNRAS* 492.4, pp. 5655–5674. DOI: 10.1093/mnras/staa192. arXiv: 1912.06577 [astro-ph.HE].

— (2020b). "ASASSN-15lh: a TDE about a maximally rotating $10^9 M_\odot$ black hole". In: *MNRAS* 497.1, pp. L13–L18. DOI: 10.1093/mnrasl/slaa105. arXiv: 2006.00803 [astro-ph.HE].

— (2021a). "Hard X-ray emission from a Compton scattering corona in large black hole mass tidal disruption events". In: *MNRAS* 504.4, pp. 4730–4742. DOI: 10.1093/mnras/stab1184. arXiv: 2104.06195 [astro-ph.HE].

— (2021b). "An upper observable black hole mass scale for tidal destruction events with thermal X-ray spectra". In: *MNRAS* 505.2, pp. 1629–1644. DOI: 10.1093/mnras/stab1141. arXiv: 2104.06177 [astro-ph.HE].

Narayan, Ramesh and Insu Yi (1994). "Advection-dominated Accretion: A Self-similar Solution". In: *ApJL* 428, p. L13. DOI: 10.1086/187381. arXiv: astro-ph/9403052 [astro-ph].

— (1995). "Advection-dominated Accretion: Underfed Black Holes and Neutron Stars". In: *ApJ* 452, p. 710. DOI: 10.1086/176343. arXiv: astro-ph/9411059 [astro-ph].

Nathan, Edward et al. (2022). "Phase-resolved spectroscopy of a quasi-periodic oscillation in the black hole X-ray binary GRS 1915+105 with NICER and NuSTAR". In: *MNRAS* 511.1, pp. 255–279. DOI: 10.1093/mnras/stab3803. arXiv: 2201.01765 [astro-ph.HE].

Nelson, Richard P. and John C. B. Papaloizou (2003). "The interaction of a giant planet with a disc with MHD turbulence - II. The interaction of the planet with the disc". In: *MNRAS* 339.4, pp. 993–1005. DOI: 10.1046/j.1365-8711.2003.06247.x. arXiv: astro-ph/0211495 [astro-ph].

Neustadt, J. M. M. et al. (2020). "To TDE or not to TDE: the luminous transient ASASSN-18jd with TDE-like and AGN-like qualities". In: *MNRAS* 494.2, pp. 2538–2560. DOI: 10.1093/mnras/staa859. arXiv: 1910.01142 [astro-ph.HE].

Newman, E. T. et al. (1965). "Metric of a Rotating, Charged Mass". In: *Journal of Mathematical Physics* 6.6, pp. 918–919. DOI: 10.1063/1.1704351.

Noble, Scott C., Julian H. Krolik, and John F. Hawley (2010). "Dependence of Inner Accretion Disk Stress on Parameters: The Schwarzschild Case". In: *ApJ* 711.2, pp. 959–973. DOI: 10.1088/0004-637X/711/2/959. arXiv: 1001.4809 [astro-ph.HE].

Novikov, I. D. and Thorne (1973). "Astrophysics of black holes." In: *Black Holes (Les Astres Occlus)*, pp. 343–450.

Page, Don N. and Thorne (1974). "Disk-Accretion onto a Black Hole. Time-Averaged Structure of Accretion Disk". In: *ApJ* 191, pp. 499–506. DOI: 10.1086/152990.

Parfrey, Kyle, Alexander Philippov, and Benoit Cerutti (2019). "First-Principles Plasma Simulations of Black-Hole Jet Launching". In: *Phys. Rev. Lett.* 122.3, 035101, p. 035101. DOI: 10.1103/PhysRevLett.122.035101. arXiv: 1810.03613 [astro-ph.HE].

Pasham, Dheeraj R. et al. (2017). "Optical/UV-to-X-Ray Echoes from the Tidal Disruption Flare ASASSN-14li". In: *ApJL* 837.2, L30, p. L30. DOI: 10.3847/2041-8213/aa6003. arXiv: 1703.07024 [astro-ph.HE].

Pasham, Dheeraj R. et al. (2019). "A loud quasi-periodic oscillation after a star is disrupted by a massive black hole". In: *Science* 363.6426, pp. 531–534. DOI: 10.1126/science.aar7480. arXiv: 1810.10713 [astro-ph.HE].

Penna, Robert F. et al. (2010). "Simulations of magnetized discs around black holes: effects of black hole spin, disc thickness and magnetic field geometry". In: *MNRAS* 408.2, pp. 752–782. DOI: 10.1111/j.1365-2966.2010.17170.x. arXiv: 1003.0966 [astro-ph.HE].

Penrose, Roger (1965). "Gravitational Collapse and Space-Time Singularities". In: *Phys. Rev. Lett.* 14.3, pp. 57–59. DOI: 10.1103/PhysRevLett.14.57.

Piran, Tsvi et al. (2015). "?Disk Formation Versus Disk Accretion—What Powers Tidal Disruption Events?" In: *ApJ* 806.2, 164, p. 164. DOI: 10.1088/0004-637X/806/2/164. arXiv: 1502.05792 [astro-ph.HE].

Porth, Oliver et al. (2017). "The black hole accretion code". In: *Computational Astrophysics and Cosmology* 4.1, 1, p. 1. DOI: 10.1186/s40668-017-0020-2. arXiv: 1611.09720 [gr-qc].

Press, William H. et al. (1992). *Numerical recipes in FORTRAN. The art of scientific computing.*

Pringle, J. E. (1981). "Accretion discs in astrophysics". In: *ARA&A* 19, pp. 137–162. DOI: 10.1146/annurev.aa.19.090181.001033.

— (1991). "The properties of external accretion discs." In: *MNRAS* 248, p. 754. DOI: 10.1093/mnras/248.4.754.

Psaltis, Dimitrios and Tim Johannsen (2012). "A Ray-tracing Algorithm for Spinning Compact Object Spacetimes with Arbitrary Quadrupole Moments. I. Quasi-Kerr Black Holes". In: *ApJ* 745.1, 1, p. 1. DOI: 10.1088/0004-637X/745/1/1. arXiv: 1011.4078 [astro-ph.HE].

Rees, Martin J. (1988). "Tidal disruption of stars by black holes of 10^6-10^8 solar masses in nearby galaxies". In: *Nature* 333.6173, pp. 523–528. DOI: 10.1038/333523a0.

Reynolds, Christopher S. (2013). "The spin of supermassive black holes". In: *Classical and Quantum Gravity* 30.24, 244004, p. 244004. DOI: 10.1088/0264-9381/30/24/244004. arXiv: 1307.3246 [astro-ph.HE].

Ryu, Taeho, Julian Krolik, and Tsvi Piran (2020). "Measuring Stellar and Black Hole Masses of Tidal Disruption Events". In: *ApJ* 904.1, 73, p. 73. DOI: 10.3847/1538-4357/abbf4d. arXiv: 2007.13765 [astro-ph.HE].

Sądowski, Aleksander et al. (2015). "Global simulations of axisymmetric radiative black hole accretion discs in general relativity with a mean-field magnetic dynamo". In: *MNRAS* 447.1, pp. 49–71. DOI: 10.1093/mnras/stu2387. arXiv: 1407.4421 [astro-ph.HE].

Salpeter, Edwin E. (1955). "The Luminosity Function and Stellar Evolution." In: *ApJ* 121, p. 161. DOI: 10.1086/145971.

Saxton, Richard et al. (2014). "An X-ray and UV flare from the galaxy XMMSL1 J061927.1-655311". In: *A&A* 572, A1, A1. DOI: 10.1051/0004-6361/201424347. arXiv: 1410.1500 [astro-ph.HE].

— (2017). "XMMSL1 J074008.2-853927: a tidal disruption event with thermal and non-thermal components". In: *A&A* 598, A29, A29. DOI: 10.1051/0004-6361/201629015. arXiv: 1610.01788 [astro-ph.GA].

Saxton, Richard et al. (2012). "A tidal disruption-like X-ray flare from the quiescent galaxy SDSS J120136.02+300305.5". In: *A&A* 541, A106, A106. DOI: 10.1051/0004-6361/201118367. arXiv: 1202.5900 [astro-ph.CO].

Saxton, Richard et al. (2019). "XMMSL2 J144605.0+685735: a slow tidal disruption event". In: *A&A* 630, A98, A98. DOI: 10.1051/0004-6361/201935650. arXiv: 1908.01065 [astro-ph.HE].

Sazonov, S. et al. (2021). "First tidal disruption events discovered by SRG/eROSITA: X-ray/optical properties and X-ray luminosity function at z < 0.6". In: *MNRAS* 508.3, pp. 3820–3847. DOI: 10.1093/mnras/stab2843. arXiv: 2108.02449 [astro-ph.HE].

Schechter, P. (1976). "An analytic expression for the luminosity function for galaxies." In: *ApJ* 203, pp. 297–306. DOI: 10.1086/154079.

Schwarzschild, K. (1916). "On the Gravitational Field of a Mass Point According to Einstein's Theory". In: *Abh. Konigl. Preuss. Akad. Wissenschaften Jahre 1906,92, Berlin,1907* 1916, pp. 189–196.

Shafee, Rebecca et al. (2008). "Three-Dimensional Simulations of Magnetized Thin Accretion Disks around Black Holes: Stress in the Plunging Region". In: *ApJL* 687.1, p. L25. DOI: 10.1086/593148. arXiv: 0808.2860 [astro-ph].

Shakura, N. I. and R. A. Sunyaev (1973). "Black holes in binary systems. Observational appearance." In: *A&A* 24, pp. 337–355.

Shapiro, S. L., A. P. Lightman, and D. M. Eardley (1976). "A two-temperature accretion disk model for Cygnus X-1: structure and spectrum." In: *ApJ* 204, pp. 187–199. DOI: 10.1086/154162.

Shimura, Toshiya and Fumio Takahara (1995). "On the Spectral Hardening Factor of the X-Ray Emission from Accretion Disks in Black Hole Candidates". In: *ApJ* 445, p. 780. DOI: 10.1086/175740.

Short, P. et al. (2020). "The tidal disruption event AT 2018hyz - I. Double-peaked emission lines and a flat Balmer decrement". In: *MNRAS* 498.3, pp. 4119–4133. DOI: 10.1093/mnras/staa2065. arXiv: 2003.05470 [astro-ph.GA].

Sponholz, H. (1994). "Tidal Processes and Disruption of Stars near a Supermassive Rotating Black Hole". In: *Mem. Soc. Astron. It.* 65, p. 1135.

Stein, Robert et al. (2021). "A tidal disruption event coincident with a high-energy neutrino". In: *Nature Astronomy* 5, pp. 510–518. DOI: 10.1038/s41550-020-01295-8. arXiv: 2005.05340 [astro-ph.HE].

Steiner, James F. et al. (2009). "A Simple Comptonization Model". In: *PASP* 121.885, p. 1279. DOI: 10.1086/648535. arXiv: 0810.1758 [astro-ph].

Stone, James M. et al. (2008). "Athena: A New Code for Astrophysical MHD". In: *ApJS* 178.1, pp. 137–177. DOI: 10.1086/588755. arXiv: 0804.0402 [astro-ph].

Stone, Nicholas C. and Brian D. Metzger (2016). "Rates of stellar tidal disruption as probes of the supermassive black hole mass function". In: *MNRAS* 455.1, pp. 859–883. DOI: 10.1093/mnras/stv2281. arXiv: 1410.7772 [astro-ph.HE].

Strubbe, Linda E. and Eliot Quataert (2009). "Optical flares from the tidal disruption of stars by massive black holes". In: *MNRAS* 400.4, pp. 2070–2084. DOI: 10.1111/j.1365-2966.2009.15599.x. arXiv: 0905.3735 [astro-ph.CO].

Sunyaev, R. A. and L. G. Titarchuk (1980). "Comptonization of X-Rays in Plasma Clouds - Typical Radiation Spectra". In: *A&A* 86, p. 121.

Tolman, Richard C. (1939). "Static Solutions of Einstein's Field Equations for Spheres of Fluid". In: *Physical Review* 55.4, pp. 364–373. DOI: 10.1103/PhysRev.55.364.

Turner, Samuel G. D. and Christopher S. Reynolds (2021). "Investigating the theory of propagating fluctuations with numerical models of stochastic accretion discs". In: *MNRAS* 504.1, pp. 469–486. DOI: 10.1093/mnras/stab875. arXiv: 2103.09281 [astro-ph.HE].

Uttley, P., I. M. McHardy, and S. Vaughan (2005). "Non-linear X-ray variability in X-ray binaries and active galaxies". In: *MNRAS* 359.1, pp. 345–362. DOI: 10.1111/j.1365-2966.2005.08886.x. arXiv: astro-ph/0502112 [astro-ph].

van Velzen, Sjoert et al. (2016). "A radio jet from the optical and x-ray bright stellar tidal disruption flare ASASSN-14li". In: *Science* 351.6268, pp. 62–65. DOI: 10.1126/science.aad1182. arXiv: 1511.08803 [astro-ph.HE].

— (2019a). "The First Tidal Disruption Flare in ZTF: From Photometric Selection to Multi-wavelength Characterization". In: *ApJ* 872.2, 198, p. 198. DOI: 10.3847/1538-4357/aafe0c. arXiv: 1809.02608 [astro-ph.HE].

— (2019b). "Late-time UV Observations of Tidal Disruption Flares Reveal Unobscured, Compact Accretion Disks". In: *ApJ* 878.2, 82, p. 82. DOI: 10.3847/1538-4357/ab1844. arXiv: 1809.00003 [astro-ph.HE].

van Velzen, Sjoert et al. (2021). "Seventeen Tidal Disruption Events from the First Half of ZTF Survey Observations: Entering a New Era of Population Studies". In: *ApJ* 908.1, 4, p. 4. DOI: 10.3847/1538-4357/abc258. arXiv: 2001.01409 [astro-ph.HE].

van Velzen, Sjoert et al. (2016). "Discovery of Transient Infrared Emission from Dust Heated by Stellar Tidal Disruption Flares". In: *ApJ* 829.1, 19, p. 19. DOI: 10.3847/0004-637X/829/1/19. arXiv: 1605.04304 [astro-ph.HE].

Wang, Jianxiang and David Merritt (2004). "Revised Rates of Stellar Disruption in Galactic Nuclei". In: *ApJ* 600.1, pp. 149–161. DOI: 10.1086/379767. arXiv: astro-ph/0305493 [astro-ph].

Weaver, John R. and Keith Horne (2022). "Dust and the intrinsic spectral index of quasar variations: hints of finite stress at the innermost stable circular orbit". In: *MNRAS* 512.1, pp. 899–916. DOI: 10.1093/mnras/stac248. arXiv: 2201.11134 [astro-ph.GA].

Wen, Sixiang et al. (2020). "Continuum-fitting the X-Ray Spectra of Tidal Disruption Events". In: *ApJ* 897.1, 80, p. 80. DOI: 10.3847/1538-4357/ab9817. arXiv: 2003.12583 [astro-ph.HE].

Wevers, Thomas et al. (2019a). "Evidence for rapid disc formation and reprocessing in the X-ray bright tidal disruption event candidate AT 2018fyk". In: *MNRAS* 488.4, pp. 4816–4830. DOI: 10.1093/mnras/stz1976. arXiv: 1903.12203 [astro-ph.HE].

Wevers, Thomas (2020). "Fainter harder brighter softer: a correlation between α_{ox}, X-ray spectral state, and Eddington ratio in tidal disruption events". In: *MNRAS* 497.1, pp. L1–L6. DOI: 10.1093/mnrasl/slaa097. arXiv: 2006.06684 [astro-ph.HE].

Wevers, Thomas et al. (2021). "Rapid Accretion State Transitions following the Tidal Disruption Event AT2018fyk". In: *ApJ* 912.2, 151, p. 151. DOI: 10.3847/1538-4357/abf5e2. arXiv: 2101.04692 [astro-ph.HE].

Wevers, Thomas et al. (2017). "Black hole masses of tidal disruption event host galaxies". In: *MNRAS* 471.2, pp. 1694–1708. DOI: 10.1093/mnras/stx1703. arXiv: 1706.08965 [astro-ph.GA].

Wevers, Thomas et al. (2019b). "Black hole masses of tidal disruption event host galaxies II". In: *MNRAS* 487.3, pp. 4136–4152. DOI: 10.1093/mnras/stz1602. arXiv: 1902.04077 [astro-ph.HE].

White, Christopher J., James M. Stone, and Charles F. Gammie (2016). "An Extension of the Athena++ Code Framework for GRMHD Based on Advanced Riemann Solvers and Staggered-mesh Constrained Transport". In: *ApJS* 225.2, 22, p. 22. DOI: 10.3847/0067-0049/225/2/22. arXiv: 1511.00943 [astro-ph.HE].

Wilkins, D. R. and L. C. Gallo (2015). "Driving extreme variability: the evolving corona and evidence for jet launching in Markarian 335". In: *MNRAS* 449.1, pp. 129–146. DOI: 10.1093/mnras/stv162. arXiv: 1501.05302 [astro-ph.HE].

Wyrzykowski, Łukasz et al. (2017). "OGLE16aaa - a signature of a hungry supermassive black hole". In: *MNRAS* 465.1, pp. L114–L118. DOI: 10.1093/mnrasl/slw213. arXiv: 1606.03125 [astro-ph.GA].

Zabludoff, Ann et al. (2021). "Distinguishing Tidal Disruption Events from Impostors". In: *Special Science Reviews* 217.4, 54, p. 54. DOI: 10.1007/s11214-021-00829-4. arXiv: 2103.12150 [astro-ph.HE].

A

The Bessel functions

The relativistic disc equation is azimuthally-symmetric, as such, it is no surprise that its Laplace mode solutions are comprised of Bessel functions. The Bessel functions have many fascinating properties, but the most relevant for this thesis is that they are the solutions of an extremely general and common differential equation.

The Bessel functions themselves are defined as the solutions to the following equation (e.g., Bowman 1958)

$$z^2\frac{\mathrm{d}^2y}{\mathrm{d}z^2} + z\frac{\mathrm{d}y}{\mathrm{d}z} + (z^2 - \nu^2)y = 0, \tag{A.1}$$

where ν is a constant, known as the order of the Bessel equation. As a second order ordinary differential equation, the Bessel equation has two linearly independent solutions. Provided that ν is non-integer[1] these solutions are denoted

$$y = J_{\pm\nu}(z). \tag{A.2}$$

The key result of this Appendix is that equation A.1 can be manipulated into an equivalent equation of the following, more useful, form:

$$\frac{\mathrm{d}^2u}{\mathrm{d}z^2} + bz^m u = 0, \qquad (b > 0). \tag{A.3}$$

[1]If ν is an integer, the solution is given by a superposition of J_ν and Y_ν, where Y_ν is the Bessel function of the second kind. All the remaining steps in this derivation remain valid.

As such, the solutions of equation A.3 are also comprised of Bessel functions, explicitly:

$$u = z^{\frac{1}{2}} J_{\pm\frac{1}{m+2}} \left(\frac{2\sqrt{b}}{m+2} z^{\frac{m+2}{2}} \right), \tag{A.4}$$

a result I now prove.

For now I will drop the $\pm$ on the Bessel index, but it should be understood that all of the following steps hold for both positive and negative ν. Consider the following function

$$u = z^{\alpha} J_{\nu} \left(\beta z^{\gamma} \right) \equiv z^{\alpha} J_{\nu}(w), \tag{A.5}$$

which defines the variable w. Differentiating u once with respect to z leaves

$$\frac{\mathrm{d}u}{\mathrm{d}z} = \alpha z^{\alpha-1} J_{\nu} + \gamma\beta z^{\alpha+\gamma-1} J'_{\nu}, \tag{A.6}$$

and twice gives

$$\frac{\mathrm{d}^2u}{\mathrm{d}z^2} = \alpha(\alpha-1) z^{\alpha-2} J_{\nu} + \left(2\alpha\beta\gamma + \beta\gamma(\gamma-1)\right) z^{\alpha+\gamma-2} J'_{\nu} + \gamma^2\beta^2 z^{\alpha+2\gamma-2} J''_{\nu}, \tag{A.7}$$

where $'$ denotes a derivative with respect to w. Consider the particular combination

$$\frac{\mathrm{d}^2u}{\mathrm{d}z^2} + \left(\frac{1-2\alpha}{z}\right) \frac{\mathrm{d}u}{\mathrm{d}z} = \gamma^2\beta^2 z^{\alpha+2\gamma-2} J''_{\nu} + \gamma^2\beta z^{\alpha+\gamma-2} J'_{\nu} + z^{\alpha-2} \left[\alpha(\alpha-1) + \alpha(1-2\alpha)\right] J_{\nu} \tag{A.8}$$

which can be simplified to

$$\frac{\mathrm{d}^2u}{\mathrm{d}z^2} + \left(\frac{1-2\alpha}{z}\right) \frac{\mathrm{d}u}{\mathrm{d}z} = \left(\gamma\beta z^{\gamma-1}\right)^2 \left[J''_{\nu} + \frac{1}{w} J'_{\nu}\right] z^{\alpha} - \alpha^2 z^{\alpha-2} J_{\nu}. \tag{A.9}$$

The term in the square brackets can be replaced using the original Bessel equation (equation A.1):

$$\frac{\mathrm{d}^2u}{\mathrm{d}z^2} + \left(\frac{1-2\alpha}{z}\right) \frac{\mathrm{d}u}{\mathrm{d}z} = -z^{\alpha} \left[\left(\gamma\beta z^{\gamma-1}\right)^2 \left(1 - \frac{\nu^2}{\beta^2 z^{2\gamma}}\right) + \frac{\alpha^2}{z^2}\right] J_{\nu}. \tag{A.10}$$

Recalling that $u = z^{\alpha} J_{\nu}\left(\beta z^{\gamma}\right)$, and simplifying, leaves

$$\frac{\mathrm{d}^2u}{\mathrm{d}z^2} + \left(\frac{1-2\alpha}{z}\right) \frac{\mathrm{d}u}{\mathrm{d}z} + \left[\frac{\left(\gamma\beta z^{\gamma}\right)^2 + \alpha^2 - \nu^2\gamma^2}{z^2}\right] u = 0. \tag{A.11}$$

Now, I reduce this to the form A.3. Take $\alpha = 1/2$ to remove the $\mathrm{d}u/\mathrm{d}z$ term, which leaves

$$\frac{\mathrm{d}^2u}{\mathrm{d}z^2} + \left[\frac{\left(\gamma\beta z^{\gamma}\right)^2 + \frac{1}{4} - \nu^2\gamma^2}{z^2}\right] u = 0, \tag{A.12}$$

and then solve the simultaneous equations

$$\nu^2\gamma^2 = \frac{1}{4}, \quad \beta^2\gamma^2 = b, \quad 2\gamma - 2 = m. \tag{A.13}$$

The solutions are

$$\nu = \pm\frac{1}{m+2}, \quad \beta = \frac{2\sqrt{b}}{m+2}, \quad \gamma = \frac{m+2}{2}, \quad \alpha = 1/2. \tag{A.14}$$

Thus, the equation

$$\frac{\mathrm{d}^2u}{\mathrm{d}z^2} + bz^m u = 0 \tag{A.15}$$

has solution

$$u = z^{\frac{1}{2}} J_{\pm\frac{1}{m+2}}\left(\frac{2\sqrt{b}}{m+2} z^{\frac{m+2}{2}}\right), \tag{A.16}$$

a result used repeatedly in Chapter 2.

To solve the disc modal matching conditions, the radial gradients of the inner and outer disc Laplace modes must be equated. As such, another important result involves explicitly computing the derivatives of these general solutions. To simplify the z-derivatives of equation A.16, the following Bessel function recurrence relationships are useful (Bowman 1958)

$$\frac{2\alpha}{x} J_\alpha(x) = J_{\alpha-1}(x) + J_{\alpha+1}(x), \tag{A.17}$$

$$2\frac{\mathrm{d}J_\alpha(x)}{\mathrm{d}x} = J_{\alpha-1}(x) - J_{\alpha+1}(x). \tag{A.18}$$

Take the solution A.16, and define $\beta \equiv 2\sqrt{b}/(m+2)$, $x \equiv \beta z^{(m+2)/2}$, leaving

$$u\beta^{1/(m+2)} = x^{\frac{1}{m+2}} J_{\pm\frac{1}{m+2}}(x). \tag{A.19}$$

I now must treat the positive and negative Bessel orders independently. First, for the positive index solutions, take $\alpha \equiv \frac{1}{m+2}$, and thus

$$u\beta^\alpha = x^\alpha J_\alpha(x). \tag{A.20}$$

Differentiating with respect to x leaves

$$\beta^\alpha \frac{\mathrm{d}u}{\mathrm{d}x} = \frac{x^\alpha}{2}\left(\frac{2\alpha}{x} J_\alpha(x) + 2\frac{\mathrm{d}J_\alpha(x)}{\mathrm{d}x}\right) = x^\alpha J_{\alpha-1}(x), \tag{A.21}$$

where the recurrence relations have been used in going between the final two equalities.

For the negative index Bessel functions define $\alpha \equiv -\frac{1}{m+2}$, leaving

$$u\beta^{-\alpha} = x^{-\alpha} J_\alpha(x). \tag{A.22}$$

Differentiating with respect to x leaves

$$\beta^{-\alpha}\frac{\mathrm{d}u}{\mathrm{d}x} = \frac{x^{-\alpha}}{2}\left(-\frac{2\alpha}{x}J_\alpha(x) + 2\frac{\mathrm{d}J_\alpha(x)}{\mathrm{d}x}\right) = -x^{-\alpha}J_{\alpha+1}(x), \tag{A.23}$$

where again the recurrence relations have been used in going between the final two equalities. The derivative of u with respect to z is therefore

$$\frac{\mathrm{d}u}{\mathrm{d}z} = \frac{\mathrm{d}x}{\mathrm{d}z}\frac{\mathrm{d}u}{\mathrm{d}x} = \sqrt{b}z^{\frac{m+1}{2}}\left[C_+ J_{\frac{1}{m+2}-1}\left(\frac{2\sqrt{b}}{m+2}z^{\frac{m+2}{2}}\right) - C_- J_{-\frac{1}{m+2}+1}\left(\frac{2\sqrt{b}}{m+2}z^{\frac{m+2}{2}}\right)\right], \tag{A.24}$$

where C_+ and C_- are arbitrary constants which scale the $\pm 1/(m+2)$ Bessel modes in the general $u(z)$ solution. This expression simplifies to

$$\frac{\mathrm{d}u}{\mathrm{d}z} = \sqrt{b}z^{\frac{m+1}{2}}\left[C_+ J_{-\frac{m+1}{m+2}}\left(\frac{2\sqrt{b}}{m+2}z^{\frac{m+2}{2}}\right) - C_- J_{\frac{m+1}{m+2}}\left(\frac{2\sqrt{b}}{m+2}z^{\frac{m+2}{2}}\right)\right]. \tag{A.25}$$

The radial derivatives of the modal disc solutions (Chapter 2) are then computed from the above expression, with an additional multiplicative factor $\mathrm{d}z/\mathrm{d}r$, which depends on the precise definition of $z(r)$.

B

Numerical techniques for solving the relativistic disc equation

Recall that I am working in 'Boyer-Lindquist' co-ordinates in their near-equator form: t is time, as measured at infinity; r is cylindrical radius; ϕ is azimuthal angle, and z is height above equator. The line element is given by

$$ds^2 = -\left(1 - \frac{2r_g}{r}\right) \mathrm{d}t^2 - \frac{4r_g a}{r}\, \mathrm{d}t\, \mathrm{d}\phi + \frac{\mathrm{d}r^2}{1 - 2r_g/r + a^2/r^2} + \left(r^2 + a^2 + \frac{2r_g a^2}{r}\right) \mathrm{d}\phi^2 + \mathrm{d}z^2. \quad \text{(B.1)}$$

The circular orbit solutions required for the governing diffusion equation are, in the equatorial plane, given by (e.g., Hobson et al. 2006):

$$U^0 = \frac{1 + a\sqrt{r_g/r^3}}{\left(1 - 3r_g/r + 2a\sqrt{r_g/r^3}\right)^{1/2}}, \quad \text{(B.2)}$$

$$U'_\phi = \frac{\sqrt{r_g}\left(a\sqrt{r_g} + r^{3/2}\right)\left(r^2 - 6r_g r - 3a^2 + 8a\sqrt{r_g r}\right)}{2r^4\left(1 - 3r_g/r + 2a\sqrt{r_g/r^3}\right)^{3/2}}. \quad \text{(B.3)}$$

Substituting into the full evolution equation (equation 2.163), leaves

$$\frac{\partial \zeta}{\partial t} = \frac{2W^r_\phi}{\sqrt{r_g}(U^0)^2} \frac{\partial}{\partial r}\left[r^{3/2} F(r) \frac{\partial \zeta}{\partial r}\right], \quad \text{(B.4)}$$

where

$$F(r) = \frac{1 - 3r_g/r + 2a\sqrt{r_g/r^3}}{r - 6r_g - 3a^2/r + 8a\sqrt{r_g/r}}. \tag{B.5}$$

The position of the (apparently singular) ISCO is given by the solution of the equation $r_I^2 - 6r_g r_I - 3a^2 + 8a\sqrt{r_g r_I} = 0$. Numerical integration of the PDE is unstable in the vicinity of this point. This problem can be addressed by the substitution:

$$\rho = \left(r - 6r_g - \frac{3a^2}{r} + 8a\sqrt{\frac{r_g}{r}} \right)^2. \tag{B.6}$$

There is no (simple) analytic expression for the explicit inverse $r = r(\rho)$, but numerically this inversion is trivial. Using

$$\frac{\partial \zeta}{\partial r} = 2\left(1 + \frac{3a^2}{r^2} - 4a\sqrt{\frac{r_g}{r^3}}\right)\left(r - 6r_g - \frac{3a^2}{r} + 8a\sqrt{\frac{r_g}{r}}\right)\frac{\partial \zeta}{\partial \rho}, \tag{B.7}$$

the numerical singularity at the ISCO is removed. Upon full substitution of ρ for r, the equation becomes

$$\frac{\partial \zeta}{\partial t} = A(\rho)\left[B(\rho)\frac{\partial \zeta}{\partial \rho} + C(\rho)\frac{\partial^2 \zeta}{\partial \rho^2}\right], \tag{B.8}$$

with

$$A = W_\phi^r \left(\frac{1 - 3r_g/r + 2a\sqrt{r_g/r^3}}{\sqrt{r_g}\left(1 + a\sqrt{r_g/r^3}\right)^2} \right), \tag{B.9}$$

$$B = \frac{6}{\sqrt{r}}\left(r - r_g - 8a\sqrt{\frac{r_g^3}{r^3}} - \frac{a^2}{r^2}(r - 17r_g) - 8a^3\sqrt{\frac{r_g}{r^5}} \right), \tag{B.10}$$

$$C = 8r^{\frac{3}{2}}\left(1 - \frac{3r_g}{r} + 2a\sqrt{\frac{r_g}{r^3}}\right)\left(r - 6r_g - \frac{3a^2}{r} + 8a\sqrt{\frac{r_g}{r}}\right)\left(1 + \frac{3a^2}{r^2} - 4a\sqrt{\frac{r_g}{r^3}}\right)^2. \tag{B.11}$$

where r is an implicit function of ρ. The numerical solution to this equation was found using the implicit finite difference method, with centred finite difference approximations used for spatial ρ derivatives and a forward difference approximation used for the time derivative (Press et al. 1992). Numerical integration of equation B.8 is performed for the region of spacetime outside of the ISCO only ($\sqrt{\rho} > 0$), which is both mathematically self-consistent and physically sensible.

The "simple" implicit method

Assuming that the turbulent stress $W^r{}_\phi$ only depends on the disc radius (and therefore spatial variable ρ), the governing equation may be solved via the simple implicit method. The linear evolution equation in its numerically integrable form (equation B.8) will be solved on a $\rho-$grid, with space discretised into equally-spaced grid points of separation $\delta\rho$, and time discretised into time steps δt. For spatial derivatives, centred-finite-difference approximations were used

$$\frac{\partial\zeta}{\partial\rho} \approx \frac{\zeta(\rho+\delta\rho, t+\delta t) - \zeta(\rho-\delta\rho, t+\delta t)}{2\delta\rho}, \tag{B.12}$$

$$\frac{\partial^2\zeta}{\partial\rho^2} \approx \frac{\zeta(\rho+\delta\rho, t+\delta t) - 2\zeta(\rho, t+\delta t) + \zeta(\rho-\delta\rho, t+\delta t)}{\delta\rho^2}. \tag{B.13}$$

Both of these expressions have errors $O(\delta\rho^2)$. Crucially, as this is an "implicit" method, all of the spatial derivatives are evaluated at the *future* time $t+\delta t$. This approximation (which physically corresponds to the value of the ζ at a position ρ and time t affecting the value of ζ at positions ρ and $\rho\pm\delta\rho$ at $t+\delta t$), means that the numerical integration scheme is universally stable. For the time derivative, a forward-difference approximation was used

$$\frac{\partial\zeta}{\partial t} \approx \frac{\zeta(\rho, t+\delta t) - \zeta(\rho, t)}{\delta t}, \tag{B.14}$$

this has error $O(\delta t)$. I denote the time by $t = j\delta t$ and position $\rho = n\delta\rho$ and use the notation that $\zeta(\rho, t) = \zeta(n\delta\rho, j\delta t) \equiv \zeta^n_j$. The full evolution equation then becomes

$$\frac{\zeta^n_{j+1} - \zeta^n_j}{\delta t} = A_n\left[B_n\left(\frac{\zeta^{n+1}_{j+1} - \zeta^{n-1}_{j+1}}{2\delta\rho}\right) + C_n\left(\frac{\zeta^{n+1}_{j+1} - 2\zeta^n_{j+1} + \zeta^{n-1}_{j+1}}{\delta\rho^2}\right)\right], \tag{B.15}$$

where A_n, B_n, C_n are evaluated at $\rho = n\delta\rho$. This can be trivially rearranged to

$$\zeta^n_{j+1}\left(1 + 2A_nC_n\frac{\delta t}{\delta\rho^2}\right) + \zeta^{n-1}_{j+1}\left(A_nB_n\frac{\delta t}{2\delta\rho} - A_nC_n\frac{\delta t}{\delta\rho^2}\right) - \zeta^{n+1}_{j+1}\left(A_nB_n\frac{\delta t}{2\delta\rho} + A_nC_n\frac{\delta t}{\delta\rho^2}\right) = \zeta^n_j. \tag{B.16}$$

Denote the variable $\zeta(\rho, t)$ at a given time t as a spatial vector $\vec{\zeta_j}$, then the above evolution equation is simply

$$\underline{\underline{T}}\vec{\zeta}_{j+1} = \vec{\zeta}_j, \tag{B.17}$$

where $\underline{\underline{T}}$ is a tri-diagonal matrix. The numerical evolution then just becomes a problem of inverting this tri-diagonal matrix $\underline{\underline{T}}$:

$$\vec{\zeta}_{j+1} = \underline{\underline{T}}^{-1}\vec{\zeta}_j, \tag{B.18}$$

with general solution

$$\vec{\zeta}(t) = \left(\underline{\underline{T}}^{-1}\right)^n \vec{\zeta}(0). \tag{B.19}$$

There are many standard methods for inverting tri-diagonal matrices. In this thesis I implemented the Thomas algorithm. Defining

$$\underline{\underline{T}} = \begin{pmatrix} b_0 & c_0 & 0 & \cdots & 0 \\ a_1 & b_1 & c_1 & \ddots & \vdots \\ 0 & \ddots & \ddots & \ddots & 0 \\ \vdots & \ddots & a_{N-2} & b_{N-2} & c_{N-2} \\ 0 & \cdots & 0 & a_{N-1} & b_{N-1} \end{pmatrix} \tag{B.20}$$

The equation to be solved is

$$\begin{pmatrix} b_0 & c_0 & 0 & \cdots & 0 \\ a_1 & b_1 & c_1 & \ddots & \vdots \\ 0 & \ddots & \ddots & \ddots & 0 \\ \vdots & \ddots & a_{N-2} & b_{N-2} & c_{N-2} \\ 0 & \cdots & 0 & a_{N-1} & b_{N-1} \end{pmatrix} \begin{pmatrix} x_0 \\ x_1 \\ \vdots \\ \vdots \\ x_{N-1} \end{pmatrix} = \begin{pmatrix} d_0 \\ d_1 \\ \vdots \\ \vdots \\ d_{N-1} \end{pmatrix} \tag{B.21}$$

for all x_i $i \in 0, \cdots, N-1$. First define

$$g_i = \begin{cases} c_0/b_0, & \text{if } i = 0, \\ \\ c_i/(b_i - a_i g_{i-1}), & \text{else,} \end{cases} \tag{B.22}$$

and

$$r_i = \begin{cases} d_0/b_0, & \text{if } i = 0, \\ \\ (d_i - a_i r_{i-1})/(b_i - a_i g_{i-1}), & \text{else,} \end{cases} \tag{B.23}$$

then solve by back substitution

$$x_{N-1} = r_{N-1}, \tag{B.24}$$

$$x_i = r_i - g_i x_{i+1}, \quad i = N-2, N-3, \cdots, 0. \tag{B.25}$$

The "predictor-corrector" implicit method

If an α-model for the turbulent stress tensor is used, then $W^r{}_\phi$ depends explicitly on Σ, or equivalently ζ. In this regime, the above algorithm cannot be used to solve the disc evolution equation. The reason for this is that the term '$A(\rho)$' in equation B.16 now depends explicitly on ζ, and the inversion is no longer simple. As such, a modified algorithm, the so-called "predictor-corrector" method, is implemented.

In the predictor-corrector algorithm the ζ derivatives are once again expanded as in equation B.12, B.13 and B.14, and the governing equation is then re-arranged as in the previous section. However, now that the coefficient A depends on $\zeta(t)$, it is denoted $A(\rho,t) = A(n\delta\rho, j\delta t) \equiv A^n_j$. The full equation to be solved is then:

$$\zeta^n_{j+1}\left(1+2A^n_{j+1}C^n\frac{\delta t}{\delta\rho^2}\right)+\zeta^{n-1}_{j+1}\left(A^n_{j+1}B^n\frac{\delta t}{2\delta\rho}-A^n_{j+1}C^n\frac{\delta t}{\delta\rho^2}\right) - \zeta^{n+1}_{j+1}\left(A^n_{j+1}B^n\frac{\delta t}{2\delta\rho}+A^n_{j+1}C^n\frac{\delta t}{\delta\rho^2}\right)=\zeta^n_j. \quad \text{(B.26)}$$

The predictor-corrector algorithm solves the above expression in two stages. The first step, known as the "predictor" step, is to approximate $A(\rho,t+\delta t)$ by its value at the previous timestep, denoted $A(\rho,t+\delta t)\approx A(\rho,t)\equiv\widetilde{A}^n$. With this approximation, equation B.26 becomes

$$\zeta^n_{j+1}\left(1+2\widetilde{A}^nC^n\frac{\delta t}{\delta\rho^2}\right)+\zeta^{n-1}_{j+1}\left(\widetilde{A}^nB^n\frac{\delta t}{2\delta\rho}-\widetilde{A}^nC^n\frac{\delta t}{\delta\rho^2}\right)-\zeta^{n+1}_{j+1}\left(\widetilde{A}^nB^n\frac{\delta t}{2\delta\rho}+\widetilde{A}^nC^n\frac{\delta t}{\delta\rho^2}\right)=\zeta^n_j, \quad \text{(B.27)}$$

which can be solved exactly with the Thomas algorithm described above. Solving this equation gives $\widetilde{\zeta}(\rho,t+\delta t)$, the *predicted* value of ζ. The algorithm then implements the "corrector" step. The predicted value of $\widetilde{\zeta}(\rho,t+\delta t)$ is used to compute an updated estimate of $A(\rho,t+\delta t)$, denoted $A(\rho,t+\delta t)\approx A(\rho,\widetilde{\zeta})\equiv\hat{A}^n$. Substituting this updated estimator of A into equation B.26 leaves

$$\zeta^n_{j+1}\left(1+2\hat{A}^nC^n\frac{\delta t}{\delta\rho^2}\right)+\zeta^{n-1}_{j+1}\left(\hat{A}^nB^n\frac{\delta t}{2\delta\rho}-\hat{A}^nC^n\frac{\delta t}{\delta\rho^2}\right)-\zeta^{n+1}_{j+1}\left(\hat{A}^nB^n\frac{\delta t}{2\delta\rho}+\hat{A}^nC^n\frac{\delta t}{\delta\rho^2}\right)=\zeta^n_j, \quad \text{(B.28)}$$

which again is solved using the Thomas algorithm. The solution of this equation is the numerical approximation to $\zeta(\rho,t+\delta t)$ used at the beginning of the next time step.

C

Ray tracing algorithm

Equations of motion

I use the Kerr metric in Boyer-Lindquist form, with co-ordinates (t, r, θ, ϕ). This metric has non-zero components g_{00}, g_{rr}, $g_{\theta\theta}$, $g_{\phi\phi}$, $g_{0\phi} = g_{\phi 0}$. Photon trajectories through the Kerr metric are characterised by two constants of motion, the angular momentum L, and energy E. These constants of motion are related to the photon's 4-velocity u^μ by

$$L = p_\phi = g_{\phi\phi}u^\phi + g_{\phi 0}u^0, \tag{C.1}$$

and

$$E = -p_0 = -g_{00}u^0 - g_{0\phi}u^\phi. \tag{C.2}$$

The photon 4-velocities u^μ are related to the co-ordinates x^μ and invariant line element $\mathrm{d}\tau$ by

$$u^\mu = \frac{\mathrm{d}x^\mu}{\mathrm{d}\tau}. \tag{C.3}$$

These two conservation laws can be re-written as equations of motion for the photon co-ordinates t and ϕ, explicitly:

$$\frac{u^0}{E} = \frac{\mathrm{d}t}{\mathrm{d}\tau'} = -\frac{lg_{\phi 0} + g_{\phi\phi}}{g_{\phi\phi}g_{00} - g_{\phi 0}^2}, \tag{C.4}$$

and

$$\frac{u^\phi}{E} = \frac{\mathrm{d}\phi}{\mathrm{d}\tau'} = \frac{lg_{00} + g_{0\phi}}{g_{\phi\phi}g_{00} - g_{\phi 0}^2}, \tag{C.5}$$

where $\tau' \equiv E\tau$ and $l \equiv L/E$. For the r and θ co-ordinates I use the geodesic equations

$$\frac{\mathrm{d}^2 r}{\mathrm{d}\tau'^2} = -\Gamma^r_{\mu\nu}\frac{\mathrm{d}x^\mu}{\mathrm{d}\tau'}\frac{\mathrm{d}x^\nu}{\mathrm{d}\tau'}, \tag{C.6}$$

and

$$\frac{\mathrm{d}^2 \theta}{\mathrm{d}\tau'^2} = -\Gamma^\theta_{\mu\nu}\frac{\mathrm{d}x^\mu}{\mathrm{d}\tau'}\frac{\mathrm{d}x^\nu}{\mathrm{d}\tau'}, \tag{C.7}$$

where $\Gamma^\mu_{\nu\kappa} = \Gamma^\mu_{\kappa\nu}$ are the Christoffel coefficients for the Boyer-Lindquist Kerr metric. For an axi-symmetric metric the non-zero coefficients are $\Gamma^\star_{00}$, $\Gamma^\star_{rr}$, $\Gamma^\star_{\phi\phi}$, $\Gamma^\star_{\theta\theta}$, $\Gamma^\star_{\phi 0}$ and $\Gamma^\star_{\theta r}$, where $\star$ takes the place of r and θ in equations C.6 and C.7 respectively.

In addition, photons propagating through the Kerr metric posses another integral of motion, which arrises due to the vanishing norm of the photons 4-velocity

$$g_{\mu\nu}\frac{\mathrm{d}x^\mu}{\mathrm{d}\tau'}\frac{\mathrm{d}x^\nu}{\mathrm{d}\tau'} = 0. \tag{C.8}$$

This will be used as a consistency constraint to check the convergence of the algorithm.

Photon initial condition

I assume a distant observer who is orientated at an inclination angle $\theta_{\rm obs}$ from the disc plane at a distance D. I define an image plane perpendicular to the line of sight centred at $\phi = 0$ (Figure 3.1), with image plane cartesian co-ordinates (α, β). A photon at an image plane co-ordinate (α, β) has a corresponding spherical-polar co-ordinate (r_i, θ_i, ϕ_i), given by (Psaltis and Johannsen 2012)

$$r_i = \left(D^2 + \alpha^2 + \beta^2\right)^{1/2}, \tag{C.9}$$

$$\cos\theta_i = r_i^{-1}\left(D\cos\theta_{\rm obs} + \beta\sin\theta_{\rm obs}\right), \tag{C.10}$$

$$\tan\phi_i = \alpha\left(D\sin\theta_{\rm obs} - \beta\cos\theta_{\rm obs}\right)^{-1}. \tag{C.11}$$

The only photons which will contribute to the image have 3-momentum which is perpendicular to the image plane. This orthogonality condition uniquely specifies the initial photon 4-velocity (Psaltis and Johannsen 2012)

$$u_i^r \equiv \left(\frac{\mathrm{d}r}{\mathrm{d}\tau'}\right)_{\rm obs} = \frac{D}{r_i}, \tag{C.12}$$

$$u_i^\theta \equiv \left(\frac{\mathrm{d}\theta}{\mathrm{d}\tau'}\right)_{\rm obs} = \frac{D\left(D\cos\theta_{\rm obs} + \beta\sin\theta_{\rm obs}\right) - r_i^2\cos\theta_{\rm obs}}{r_i^2\left(r_i^2 - \left(D\cos\theta_{\rm obs} + \beta\sin\theta_{\rm obs}\right)^2\right)^{1/2}}, \tag{C.13}$$

$$u_i^\phi \equiv \left(\frac{\mathrm{d}\phi}{\mathrm{d}\tau'}\right)_{\rm obs} = \frac{-\alpha\sin\theta_{\rm obs}}{\left(D\sin\theta_{\rm obs} - \beta\cos\theta_{\rm obs}\right)^2 + \alpha^2}. \tag{C.14}$$

Note that the normalisation of these 4-velocity components can all be scaled by an arbitrary factor k without effecting the trajectories.

The final component of the photon's initial 4-velocity, $(\mathrm{d}t/\mathrm{d}\tau')_{\mathrm{obs}}$, can then be found from the initial 3-velocity and 3-position components (equations C.9 – C.14) by the use of equation C.8:

$$g_{00}(u_i^0)^2 + 2g_{\phi 0}u_i^0 u_i^\phi + g_{rr}(u_i^r)^2 + g_{\theta\theta}(u_i^\theta)^2 + g_{\phi\phi}(u_i^\phi)^2 = 0, \tag{C.15}$$

here the various metric components are evaluated at (r_i, θ_i, ϕ_i).

Algorithm implementation

The equations of motion (C.4, C.5, C.6 & C.7) form the basis of the ray tracing algorithm. By writing

$$\frac{\mathrm{d}^2 r}{\mathrm{d}\tau'^2} = \frac{\mathrm{d}u^r}{\mathrm{d}\tau'}, \tag{C.16}$$

and

$$\frac{\mathrm{d}^2 \theta}{\mathrm{d}\tau'^2} = \frac{\mathrm{d}u^\theta}{\mathrm{d}\tau'}, \tag{C.17}$$

equations C.4–C.7 can be expressed as four coupled first order differential equations for the variables (t, ϕ, u^r, u^θ). These four equations, together with the definitions

$$\frac{\mathrm{d}r}{\mathrm{d}\tau'} = u^r, \tag{C.18}$$

and

$$\frac{\mathrm{d}\theta}{\mathrm{d}\tau'} = u^\theta, \tag{C.19}$$

completely specify the photon's trajectory. I solve these six (C.4 – C.7, C.18, C.19) coupled first order differential equations using a fourth order Runge-Kutta integrator. The initial condition is that of a photon at the image plane with position and 4-velocity given by equations C.9 – C.15, this photon is then propagated backwards until it crosses the disc plane, at some radius r_f.

I employ a variable time step $\delta\tau'$, set as a fixed fraction h of the fastest changing variable

$$\delta\tau' = h \times \min\left[r\left(\frac{\mathrm{d}r}{\mathrm{d}\tau'}\right)^{-1}, \theta\left(\frac{\mathrm{d}\theta}{\mathrm{d}\tau'}\right)^{-1}, \phi\left(\frac{\mathrm{d}\phi}{\mathrm{d}\tau'}\right)^{-1} \right]. \tag{C.20}$$

To determine the appropriate size of the fixed step size h I require a measure of the accuracy of the algorithm. The final integral of motion (equation C.8) is useful for this purpose. Errors propagating throughout the photons trajectory will cause the norm of the photons 4-velocity to deviate from zero. I therefore define the parameter Δ by

$$\Delta = 1 + \left[g_{rr} \left(\frac{\mathrm{d}r}{\mathrm{d}\tau'} \right)^2 + g_{\theta\theta} \left(\frac{\mathrm{d}\theta}{\mathrm{d}\tau'} \right)^2 + g_{\phi\phi} \left(\frac{\mathrm{d}\phi}{\mathrm{d}\tau'} \right)^2 + 2 g_{\phi 0} \left(\frac{\mathrm{d}t}{\mathrm{d}\tau'} \right) \left(\frac{\mathrm{d}\phi}{\mathrm{d}\tau'} \right) \right] \Big/ g_{00} \left(\frac{\mathrm{d}t}{\mathrm{d}\tau'} \right)^2, \quad \text{(C.21)}$$

which should satisfy $\Delta = 0$ for an error free integration. I set the fixed step size h by requiring that $\Delta < 10^{-7}$ for all photon trajectories. This was found empirically to be satisfied by $h = 5 \times 10^{-3}$.

Photon red shift and the observed spectrum

The observed disc spectrum F_ν is given by the double integral

$$F_\nu = \frac{1}{D^2} \iint_{\mathcal{S}} f^3 B_\nu(\nu_o / f, T) \, \mathrm{d}\alpha \, \mathrm{d}\beta, \quad \text{(C.22)}$$

where the disc temperature $T(r, t)$ is given by equation 3.4, and the photon red shift factor f is given by

$$f = \frac{\nu_o}{\nu_e} = \frac{1}{U^0} \left[1 + \frac{p_\phi}{p_0} \Omega \right]^{-1}. \quad \text{(C.23)}$$

Here U^0 and $\Omega = U^\phi / U^0$ are 4-velocity components of the rotating disc fluid, and p_ϕ and p_0 are photon 4-momentum components. The ratio p_ϕ / p_0 is a constant of motion for a photon propagating through the Kerr metric, and is equal to $-l$ in the notation of this algorithm. As a conserved quantity, l can be calculated from the initial conditions and equations C.1 & C.2. The quantities U^0 and Ω are functions of the black hole spin a, and the radius at which the photon was emitted. This radius corresponds to the end point of the ray-tracing algorithm r_f.

Starting from a finely spaced grid of points (α, β) in the image plane, I trace the geodesics of each photon back to the disc plane, recording (r_f, l) for each photon. The parameter r_f allows the disc temperature T to be calculated at a given time t (equation 3.4). The parameters r_f and l together uniquely define the red-shift factor f. The integrand $f^3 B_\nu(\nu_o / f, T)$ can therefore be calculated at every grid point in the image plane. The integral C.22 was then calculated using a 2-dimensional Simpsons algorithm.

D

The relativistic TDE disc model: fitting procedure and parameter degeneracies

I fit four free parameters to the observed ASASSN-14li light curves: the time offset t_D, the viscous timescale t_v, the disc mass M_d, and the black hole mass M. The time offset and viscous timescale of the evolving disc are constrained by minimising the reduced chi-squared of the ASASSN-14li X-ray light curve, which is strongly time varying. Unlike the temporal parameters, the black hole and disc masses cannot be constrained by either the X-ray or UV observations separately. This is shown in Figures D.1 and D.3.

The black hole and disc masses may be constrained, however, by simultaneously fitting the UV and X-ray light curves. Figures D.2 and D.4 demonstrate that disc parameters which equally well fit the UV band light curve, produce X-ray light curves which differ from the observed fluxes by orders of magnitude, and vice-versa. Fitting separately to the UV and X-ray bands produce two different curves between disc and black hole mass, their unique intersection allows both to the determined (Figure D.5). To fit the black hole and disc masses I minimised the reduced chi-squared of the X-ray light curve, subject to the constraint that the late time UV flux plateau must have the correct magnitude. Note that the X-ray light curve is a more extensive data set with more complex temporal structure, and is therefore more constraining.

Fluctuations in the data mean that the best fit X-ray light curve still has a large reduced chi-squared, which makes estimating the error ranges on the best fit parameters

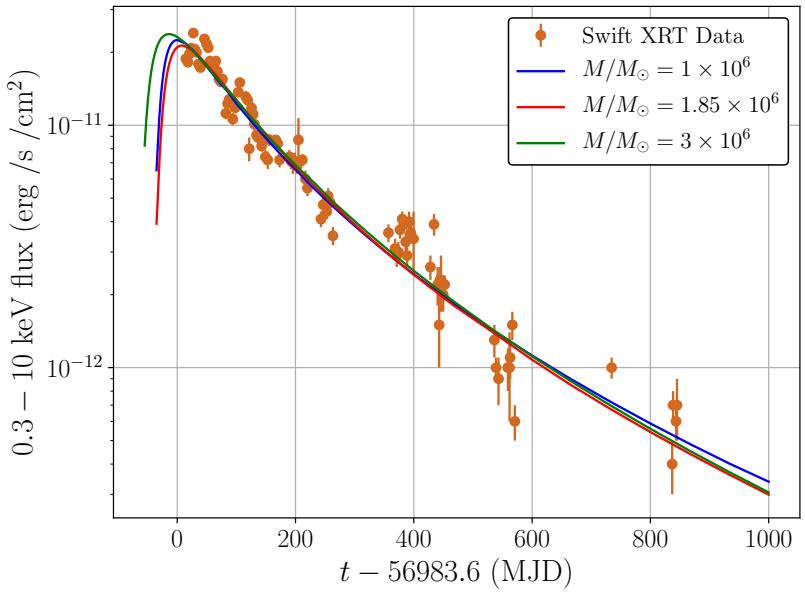

Figure D.1: Best-fit X-ray light curves for different black hole masses, ignoring the late-time ASASSN-14li UV data. The difficulty in tightly constraining system parameters exclusively with the X-ray data is evident. Black hole masses for each curve are shown.

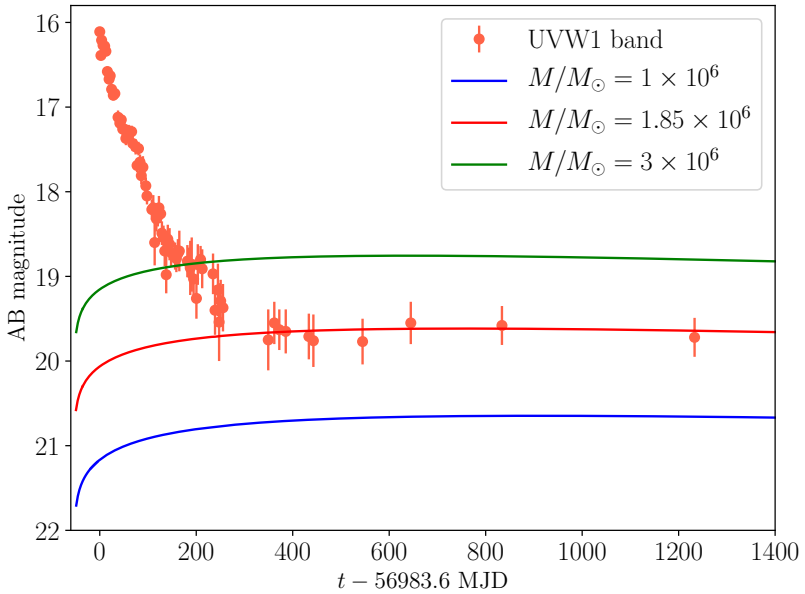

Figure D.2: The disc light curves in the UVW1 band produced by the degenerate X-ray light curve parameters of Figure D.1. Although the X-ray light curves are completely degenerate, the corresponding UVW1 fluxes significantly differ from the observed values except for narrow ranges of the black hole mass.

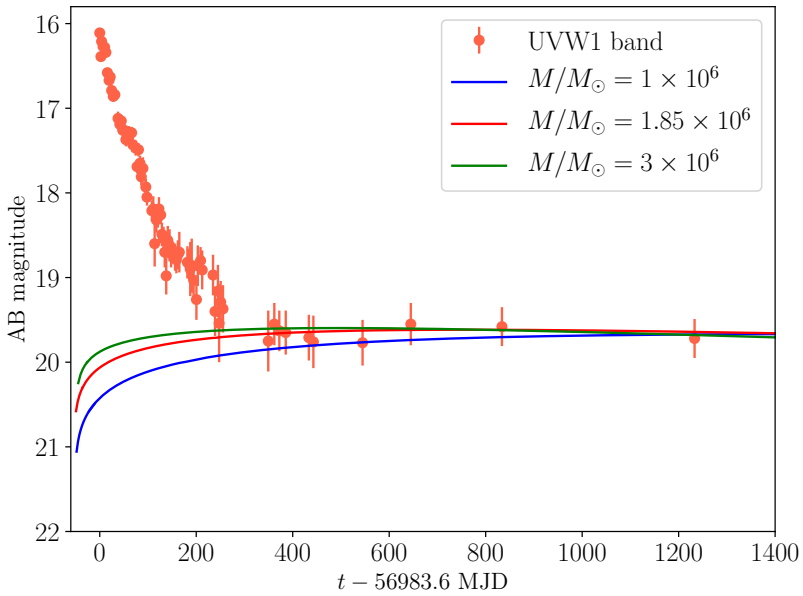

Figure D.3: Best-fit UVW1 light curves for different black hole masses, ignoring the ASASSN-14li X-ray data. The black hole masses for each curve are denoted on the plot. Like the X-ray light curves, the late-time UVW1 light curves of ASASSN-14li can individually be fit by a wide range of system parameters.

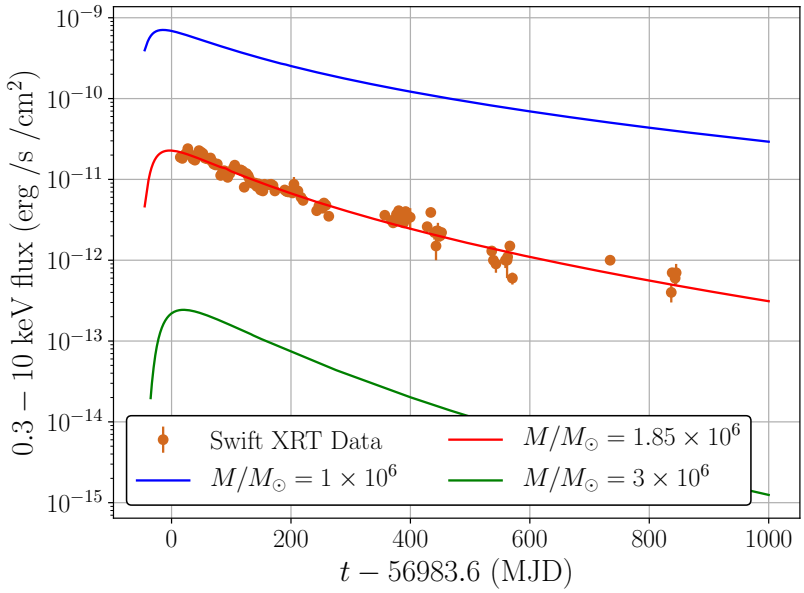

Figure D.4: The X-ray light curves produced by the degenerate UVW1 light curve parameters of Figure D.3. Degenerate UV light curves here produce orders of magnitude differences in observed X-ray fluxes.

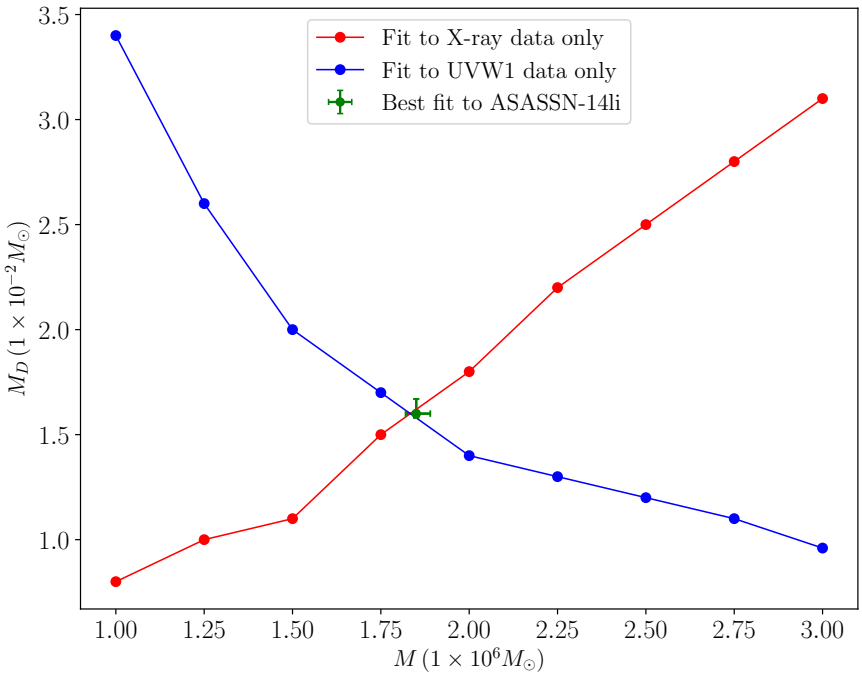

Figure D.5: The best fit disc mass as a function of black hole mass for individual light curve fits to the UVW1 band (blue curve) and X-ray band (red curve). The parameter dependencies have opposite trends for the different light curves, meaning that the system parameters can be tightly constrained by using both sets of data. The errors bars on the ASASSN-14li parameters are representative of the error bars on all the points.

problematic. Once a best fit had been found, my approach has been to formally enlarge the quoted error bars on the X-ray data (thereby accounting for the fluctuations in a statistical sense) by a constant factor until the best fit reduced chi-squared is equal to unity. Using this manipulated data, the quoted error ranges are found by computing the $\Delta\chi^2 = 3$ contours of the X-ray light curves, while ensuring that the late time UV flux was correctly reproduced. These should be considered conservative error ranges.

E

The X-ray luminosity integral for an edge on viewer orientation

I require the asymptotic solutions of the integrals I (flux integral) and J (luminosity integral), where

$$I = \iint_{\mathcal{S}} \exp\left(-h\nu_o/k_B\widetilde{T}\right)\ \mathrm{d}\alpha\,\mathrm{d}\beta, \tag{E.1}$$

and

$$J = \int_{\nu_l}^{\infty} I\,\mathrm{d}\nu_o. \tag{E.2}$$

The effective temperature is defined here, as in the text (equation 3.13),

$$\widetilde{T}(\alpha,\beta,t) = f(\alpha,\beta)\,T(r(\alpha,\beta),t). \tag{E.3}$$

In particular, I am interested in the properties of the solutions in the limit

$$h\nu_l \gg k_B\widetilde{T}, \tag{E.4}$$

when the disc is observed at an angle θ_{obs} not close to face-on. When a relativistic disc is observed at angles close to edge-on, the large rotational velocities in the innermost disc regions result in strong doppler blue shifting of the observed photons emergent from one half of the disc, and similarly strong doppler red shifting of the remaining photons. Therefore, the frequency ratio function $f(\alpha,\beta)$ will peak strongly about a 'hot spot' surrounding the most strongly blue shifted material. I must therefore

modify the asymptotic expansion techniques of sections 3.3.6 and 3.6.1 to take account of this different observing geometry.

I define the relevant function

$$K(\alpha, \beta, t) \equiv \frac{h\nu_o}{k_B \widetilde{T}}, \tag{E.5}$$

and proceed to expand K about the co-ordinates of the discs hotspot $(\alpha, \beta) = (X_0, Y_0)$, where

$$\widetilde{T}_p \equiv \widetilde{T}(X_0, Y_0) = \max_{\alpha,\beta} \left[\widetilde{T}(\alpha, \beta)\right]. \tag{E.6}$$

The exact form of the expansion will then depend on the nature of the ISCO stress. Crucially for my purposes, the leading order term in the expansion will have time dependence as in section 3.3.6

$$K_0 \equiv \frac{h\nu_l}{k_B \widetilde{T}_p} \propto t^{n/4}. \tag{E.7}$$

Finally, the effects of gravitational lensing of the observed inner disc geometry will be accounted for with

$$\mathrm{d}\alpha\, \mathrm{d}\beta = F(X, Y)\, \mathrm{d}X \mathrm{d}Y, \tag{E.8}$$

here F is an unspecified function of coordinates (but, importantly, not ν), representing the jacobian of the transformation, and $\mathrm{d}X\mathrm{d}Y$ the local area element.

Finite ISCO stress – hot spot on an inner boundary

If the stress is finite at the ISCO, then the disc temperature profile will peak at its innermost edge. The leading order expansion of K is then given by

$$K = K_0 + K_X(X - X_0) + \frac{1}{2} K_{YY}(Y - Y_0)^2 + ... \tag{E.9}$$

where X and Y have been appropriately chosen so that any cross-terms vanish. A subscript X or Y here denotes a partial derivate with respect to the relevant variable, with all other variables held constant. The spectrum integral is then

$$I = \exp(-K_0) \int_{-\infty}^{\infty} \int_{X_0}^{\infty} F(X, Y) \exp\left[-K_X(X - X_0)\right] \exp\left[-\frac{1}{2} K_{YY}(Y - Y_0)^2\right] \mathrm{d}X\, \mathrm{d}Y, \tag{E.10}$$

which has a leading order solution

$$I = F(X_0, Y_0)\frac{X_0 Y_0}{\xi_X h\nu_o}\sqrt{\frac{2\pi}{\xi_{YY} h\nu_o}}\,(k_B\widetilde{T}_p)^{3/2}\exp\left(-h\nu_o/k_B\widetilde{T}_p\right). \tag{E.11}$$

Here I have defined magnitude constants

$$\xi_X \equiv X_0 K_X, \quad \xi_{YY} \equiv Y_0^2 K_{YY}. \tag{E.12}$$

The leading order luminosity integral then simply follows

$$J \propto (k_B\widetilde{T}_p)^{-5/2}\exp\left(-h\nu_l/k_B\widetilde{T}_p\right) \propto t^{-5n/8}\exp\left(-(t/t_X)^{n/4}\right), \tag{E.13}$$

with, for a finite ISCO stress disc, $n \simeq 0.8$. The only difference resulting from changing the disc orientation from face-on to edge-on is a slight modification to the leading power-law exponent, from $4n/8$ (face-on) to $5n/8$ (edge-on).

Vanishing ISCO stress – exterior hot spot

As in section 3.6.1, when the disc stress vanishes at the ISCO, the disc temperature maximum occurs at a disc radius exterior to the ISCO. The relevant expansion is then (employing the same subscript notation as above)

$$K = K_0 + \frac{1}{2}K_{XX}(X - X_0)^2 + \frac{1}{2}K_{YY}(Y - Y_0)^2 + ... \tag{E.14}$$

This results in a leading order flux integral

$$I = \exp(-K_0)\int_{-\infty}^{\infty}\int_{-\infty}^{\infty} F(X,Y)\,\exp\left[-\frac{1}{2}\left(K_{XX}(X - X_0)^2 + K_{YY}(Y - Y_0)^2\right)\right]\,\mathrm{d}X\,\mathrm{d}Y, \tag{E.15}$$

which is solved to give

$$I = F(X_0, Y_0)X_0 Y_0\sqrt{\frac{2\pi}{\xi_{XX} h\nu_o}}\sqrt{\frac{2\pi}{\xi_{YY} h\nu_o}}\,(k_B\widetilde{T}_p)^{-1}\exp\left(-h\nu_o/k_B\widetilde{T}_p\right), \tag{E.16}$$

where

$$\xi_{XX} \equiv X_0^2 K_{XX}, \quad \xi_{YY} \equiv Y_0^2 K_{YY}. \tag{E.17}$$

The leading order luminosity integral then follows simply:

$$J \propto (k_B\widetilde{T}_p)^{-2}\exp\left(-h\nu_l/k_B\widetilde{T}_p\right) \propto t^{-n/2}\exp\left(-(t/t_X)^{n/4}\right), \tag{E.18}$$

with $n \simeq 1.2$ for a vanishing ISCO stress disc. As for a finite ISCO stress disc, modifying the disc-observer orientation angle only results in a slightly changed leading power-law exponent.

F

The opacity (in)dependence of the disc temperature scaling

The exact parameterisation of the opacity within the disc slightly modifies the dependence of the peak disc temperature on the black hole mass, disc mass, and α parameter. In this Appendix I calculate the power-law dependence of the disc surface temperature on system parameters, assuming a general bi-power-law disc opacity relationship:

$$\kappa = \kappa_0 \rho^A T_c^{-B}, \tag{F.1}$$

which may be used for a wide range of physically plausible models, including electron scattering $A = B = 0$, or a Kramers opacity: $A = 1, B = 7/2$. To aid readability I reproduce the governing equations from the main text:

$$W^r{}_\phi \equiv \alpha r c_s^2, \tag{F.2}$$

$$c_s^2 = \frac{P_g}{\rho} = \frac{k_B T_c}{\mu m_p}, \tag{F.3}$$

$$T_c^4 = \frac{3}{8}\kappa \Sigma T^4, \tag{F.4}$$

$$\sigma T^4 = -\frac{1}{2} W^r{}_\phi \Sigma \Omega'. \tag{F.5}$$

Three more relationships are required to close the set of equations for the general opacity law F.1. The density of the disc is trivially related to the disc surface density

and scale height H through:

$$\rho = \Sigma/H. \tag{F.6}$$

This scale height H is then related to the orbital frequency Ω and sound speed c_s by:

$$c_s^2 = H^2\Omega^2, \tag{F.7}$$

finally, the orbital frequency Ω is, in the Newtonian limit, given by

$$\Omega = \sqrt{\frac{GM}{r^3}}. \tag{F.8}$$

The set of equation F.1–F.8 suffice to fully determine the parameter dependence of the disc surface temperature. The substitution of equation F.2 & F.5 into equation F.4, followed by simplifications using equations F.1, F.3, F.6 & F.7 leads to

$$T_c^{3+B+A/2} = -\frac{3}{16\sigma}\kappa_0 \left(\frac{k_B}{\mu m_p}\right)^{1-A/2} \alpha r \Sigma^{2+A}\Omega^A\Omega'. \tag{F.9}$$

Equation F.8 implies that $\Omega' = -3\Omega/2r$, so that the central temperature of the disc is given by

$$T_c = \left[\frac{9}{32\sigma}\kappa_0 \left(\frac{k_B}{\mu m_p}\right)^{1-A/2} \alpha \Sigma^{2+A}\Omega^{1+A}\right]^{2/(6+2B+A)}. \tag{F.10}$$

The equations F.2, F.3 & F.5 together demonstrate that the surface temperature of the disc scales like

$$T^4 \propto \alpha T_c \Sigma \Omega \tag{F.11}$$

or in terms of the variables α, Σ & Ω:

$$T^4 \propto \alpha^{1+Q}\, \Sigma^{1+(2+A)Q}\, \Omega^{1+(1+A)Q}, \tag{F.12}$$

where $Q \equiv 2/(6 + 2B + A)$. Finally, using the general scaling relationships $\Omega \propto 1/M$, $\Sigma \propto M_d/M^2$, I am left with

$$T^4 \propto \alpha^X M_d^Y M^Z \tag{F.13}$$

with indices

$$X = (8 + 2B + A)/(6 + 2B + A), \tag{F.14}$$

$$Y = (10 + 2B + 3A)/(6 + 2B + A), \tag{F.15}$$

$$Z = -(28 + 6B + 9A)/(6 + 2B + A). \tag{F.16}$$

The system parameter dependence of the surface temperature is therefore only weakly dependent on the exact opacity specification. As reported in section 4.3 an electron scattering opacity results in

$$T_p \propto \frac{\alpha^{1/3}\, M_d^{5/12}}{M^{7/6}}, \quad A = B = 0. \tag{F.17}$$

whereas Kramers opacity would result in

$$T_p \propto \frac{\alpha^{2/7}\, M_d^{5/14}}{M^{29/28}}, \quad A = 1, B = 7/2. \tag{F.18}$$

The key results in Chapter 4 of this thesis result from the pronounced decrease in peak disc temperature as the central black hole mass is increased. Equation F.16 demonstrates that this is a general property of these thin disc solutions, and is not dependent on a particular stress or opacity parameterisation.

G

Numerical values of the X-ray luminosity fitting parameters

In this Appendix I provide the numerical values of the fitting parameters $F_0, \widetilde{M}, \psi_1$ & ψ_2. These parameters are required to analytically compute the X-ray flux and limiting black hole mass scale of Chapter 4.

Finite ISCO stress

The analytical expression for the X-ray flux (equation 4.37) has 4 free parameters, and can be written in the following form

$$F_X = F_0 \left(\frac{m}{d}\right)^2 \left[\frac{1}{\Lambda^2} + \frac{\psi_1}{\Lambda^3} + \frac{\psi_2}{\Lambda^4}\right] e^{-\Lambda}. \tag{G.1}$$

I have defined a dimensionless black hole mass $m \equiv M/\widetilde{M}$, and source-observer distance $d \equiv D/100$ Mpc. A final free parameter sets the amplitude of the important Λ parameter

$$\Lambda \equiv \frac{h\nu_l}{k_B \widetilde{T}_p} = A_1 \frac{M^{7/6}}{\alpha^{1/3} M_d^{5/12}}. \tag{G.2}$$

Defining $m_d \equiv M_d/0.5M_\odot$, then Λ may be written

$$\Lambda \equiv \frac{m^{7/6}}{\alpha^{1/3} m_d^{5/12}}. \tag{G.3}$$

It is this expression that determines the magnitude of the fitted parameter $\widetilde{M}$. The remaining fitted parameters are then found using the numerically calculated fluxes of Figure 4.1. The best fitting parameters are:

$$F_0 = 8.07 \times 10^{-9}\,\mathrm{erg/s/cm^2}, \tag{G.4}$$
$$\widetilde{M} = 2.50 \times 10^6 M_\odot, \tag{G.5}$$
$$\psi_1 = 5.5, \tag{G.6}$$
$$\psi_2 = 7.0. \tag{G.7}$$

The flux amplitude required to fit the numerically calculated upper-observable black hole mass scales (equation 4.66) differs slightly from F_0. This is a result of dropping the ψ_1 & ψ_2 correction terms in the derivation of equation 4.66. The best-fitting value f_0 used to compute Figure 4.4 is

$$f_0 = 1.21 \times 10^{-8}\,\mathrm{erg/s/cm^2}. \tag{G.8}$$

Vanishing ISCO stress

The analytical expression for the vanishing ISCO stress X-ray flux (equation 4.68) similarly has 4 free parameters, and can be written in the following form

$$F_X = F_0 \left(\frac{m}{d}\right)^2 \left[\Lambda^{-3/2} + \phi_1 \Lambda^{-5/2} + \phi_2 \Lambda^{-7/2}\right] e^{-\Lambda}. \tag{G.9}$$

An identical procedure as in the proceeding section (i.e, defining $\Lambda \equiv \alpha^{1/3} m_d^{5/12}/m^{7/6}$, before fitting to numerically calculated fluxes) leads to

$$F_0 = 2.17 \times 10^{-8}\,\mathrm{erg/s/cm^2}, \tag{G.10}$$
$$\widetilde{M} = 1.67 \times 10^6 M_\odot, \tag{G.11}$$
$$\phi_1 = 5.5, \tag{G.12}$$
$$\phi_2 = 7.0. \tag{G.13}$$

The flux amplitude relevant for calculating the upper observable black hole mass (equation 4.71) is

$$f_0 = 3.26 \times 10^{-8}\,\mathrm{erg/s/cm^2}. \tag{G.14}$$

H

TDE population black hole masses

To examine the black hole mass distributions of the different X-ray types of TDEs, I used well-established galactic scaling relationships between the black hole mass and (i) the galactic bulge mass $M : M_{\rm bulge}$, (ii) the galactic velocity dispersion $M : \sigma$, and (iii) the bulge V-band luminosity $M : L_V$ to estimate the central black hole mass as large a sample of TDEs as is currently possible. All of the scaling relationships are taken from McConnell and Ma (2013). Where available, values of $M_{\rm bulge}$, σ and L_V were taken from the literature for each TDE, and the mean black hole mass for each TDE was computed. For a full description of every $M_{\rm bulge}$, σ and L_V measurement, see Tables H.1 & H.2. As can be seen from Tables H.1 & H.2, choosing any one scaling relationship would significantly reduce the number of X-ray bright TDEs with black hole mass estimates. I therefore combine multiple scaling relationships so as to maximise the sample size of X-ray bright TDEs. Note that each scaling relationship has large intrinsic scatter, of order ~ 0.4 dex. Finally, I note that the $M : \sigma$ relationship of McConnell and Ma (2013) is not well calibrated for masses $M < 10^6 M_{\odot}$, and so while the lowest mass TDE hosts in these tables certainly have small black hole masses, the exact values inferred from the scaling relationship should be treated as having a larger than normal uncertainty associated with them.

For the optical-only TDEs, black hole masses are calculated from the velocity dispersion measurements of Wevers et al. (2019b). I include 13 of the 15 Wevers et al. TDEs, but do not include ASASSN-14li and ASASSN-15oi as they were X-ray bright.

TDE name	$M_{\rm bulge}/M_\odot$	$M_{\rm BH}/M_\odot$	σ (km/s)	$M_{\rm BH}/M_\odot$	$L_V/L_\odot$	$M_{\rm BH}/M_\odot$	References
ASASSN-18jd	$8.5^{+0.1}_{-0.5}\times10^{10}$	$2.4^{+0.7}_{-1.6}\times10^{8}$	—	—	$4.0^{+4.0}_{-2.0}\times10^{9}$	$4.7^{+13.2}_{-3.7}\times10^{7}$	[1]
AT2018fyk	$7.9^{+17.2}_{-2.9}\times10^{9}$	$2.0^{+7.4}_{-1.3}\times10^{7}$	158 ± 1	$5.5^{+1.4}_{-1.1}\times10^{7}$	—	—	[2], [3]
XMMSL1 J0740	—	—	112 ± 3	$7.9^{+4.4}_{-2.9}\times10^{6}$	—	—	[4], [3]
XMMSL2 J1446	2.9×10^{9}	$6.9^{+5.3}_{-3.0}\times10^{6}$	167 ± 15	$7.6^{+6.6}_{-4.0}\times10^{7}$	—	—	[5], [3]
SDSS J1323	—	—	80 ± 10	$1.2^{+2.2}_{-0.83}\times10^{6}$	2.5×10^{9}	$2.8^{+3.0}_{-1.4}\times10^{7}$	[6]
PTF-10iya	5.0×10^{9}	$1.2^{+0.9}_{-0.5}\times10^{7}$	—	—	$4.7^{+0.7}_{-0.6}\times10^{9}$	$5.7^{+6.6}_{-3.1}\times10^{7}$	[7]

Table H.1: The properties of the central black hole of 6 nonthermal X-ray TDEs form the literature. [1] Neustadt et al. 2020, [2] Wevers et al. 2019b, [3] Wevers 2020, [4] Saxton et al. 2017, [5] Saxton et al. 2019, [6] Esquej et al. 2008, [7] Cenko et al. 2012. The black hole masses in the third, fifth and seventh columns correspond to the black hole masses calculated using the galactic measurement in the column directly to their left.

TDE name	$M_{\rm bulge}/M_\odot$	$M_{\rm BH}/M_\odot$	σ (km/s)	$M_{\rm BH}/M_\odot$	$L_V/L_\odot$	$M_{\rm BH}/M_\odot$	References
ASASSN-14li	2.0×10^9	$4.7^{+4.0}_{-2.2} \times 10^6$	78 ± 2	$1.0^{+0.79}_{-0.45} \times 10^6$	—	—	[1], [2]
ASASSN-15oi	6.3×10^9	$1.6^{+1.0}_{-0.61} \times 10^7$	61 ± 7	$2.6^{+5.0}_{-1.7} \times 10^5$	—	—	[3], [4]
AT2018hyz	$3.5^{+0.9}_{-0.7} \times 10^9$	$8.4^{+9.8}_{-4.7} \times 10^6$	57 ± 1	$1.8^{+1.4}_{-0.8} \times 10^5$	—	—	[5], [6]
AT2019dsg	$1.4^{+0.6}_{-0.4} \times 10^{10}$	$3.8^{+4.0}_{-2.1} \times 10^7$	94 ± 1	$3.0^{+1.5}_{-1.1} \times 10^6$	—	—	[5], [7]
AT2019azh	$3.3^{+1.3}_{-1.0} \times 10^9$	$8.0^{+11.4}_{-5.0} \times 10^6$	77 ± 2	$9.5^{+7.2}_{-4.1} \times 10^5$	—	—	[5], [4]
AT2019ehz	$2.7^{+0.7}_{-0.56} \times 10^9$	$6.6^{+8.0}_{-3.8} \times 10^6$	—	—	—	—	[5]
AT2018zr	$4.5^{+1.8}_{-1.3} \times 10^9$	$1.1^{+1.4}_{-0.67} \times 10^7$	—	—	—	—	[8]
SDSS J1311	—	—	—	—	$5.5 \pm 0.5 \times 10^8$	$5.2^{+8.9}_{-3.3} \times 10^6$	[9]
XMMSL1 J1404	—	—	93 ± 1	$2.8^{+1.4}_{-1.0} \times 10^6$	—	—	[10]
OGLE 16aaa	$1.0^{+0.6}_{-0.4} \times 10^{10}$	$2.6^{+3.5}_{-1.6} \times 10^7$	—	—	—	—	[11]
3XMM J1521	4.2×10^9	$1.0^{+0.8}_{-0.4} \times 10^7$	66	$4.0^{+2.4}_{-1.5} \times 10^5$	—	—	[12]
3XMM J1500	3×10^9	$7.3^{+5.5}_{-4.2} \times 10^6$	—	—	—	—	[13]

Table H.2: The properties of the central black hole of the 12 Thermal X-ray TDEs form the literature. [1] Holoien et al. 2016a, [2] Wevers et al. 2017, [3] Holoien et al. 2016b, [4] Wevers et al. 2019b, [5] van Velzen et al. 2021, [6] Short et al. 2020, [7] Cannizzaro et al. 2021, [8] van Velzen et al. 2019a, [9] Maksym et al. 2010, [10] Wevers 2020, [11] Wyrzykowski et al. 2017, [12] Lin et al. 2015, [13] Lin et al. 2017. The black hole masses in the third, fifth and seventh columns correspond to the black hole masses calculated using the galactic measurement in the column directly to their left.

TDE name	σ (km/s)	$\log_{10}(M_{\mathrm{BH},\sigma}/M_{\odot})$
GALEX D1-9	65 ± 6	$5.85^{+0.54}_{-0.53}$
GALEX D23-H1	84 ± 4	$6.39^{+0.44}_{-0.44}$
GALEX D3-13	133 ± 6	$7.36^{+0.43}_{-0.44}$
ASASSN-14ae	53 ± 2	$5.42^{+0.46}_{-0.46}$
ASASSN-15lh	210 ± 7	$8.32^{+0.41}_{-0.41}$
PTF–09ge	82 ± 2	$6.31^{+0.48}_{-0.39}$
PTF–09axc	60 ± 4	$5.68^{+0.56}_{-0.49}$
PTF–09djl	64 ± 7	$5.82^{+0.38}_{-0.58}$
iPTF–15af	106 ± 2	$6.88^{+0.42}_{-0.38}$
iPTF–16axa	82 ± 3	$6.34^{+0.42}_{-0.42}$
iPTF–16fnl	55 ± 2	$5.50^{+0.44}_{-0.42}$
PS1–10jh	65 ± 3	$5.85^{+0.45}_{-0.44}$
SDSS TDE1	126 ± 7	$7.25^{+0.45}_{-0.46}$

Table H.3: The black hole masses of the optical TDEs inferred from the $M : \sigma$ relationship. Reproduced from Wevers et al. (2019b), their Table A1.